
Feedback in massive star-forming regions traced by integral field spectroscopy

Anna Faye McLeod



München 2016

Feedback in massive star-forming regions traced by integral field spectroscopy

Anna Faye Mc Leod

Dissertation
an der Fakultät für Physik
der Ludwig–Maximilians–Universität
München

vorgelegt von
Anna Faye Mc Leod
aus Locarno (Schweiz)

München, den 24. Mai 2016

Erstgutachter: Prof. Dr. Thomas Preibisch
Zweitgutachter: Prof. Dr. Barbara Ercolano
Tag der mündlichen Prüfung: 25. Juli 2016

To my family.

Contents

Zusammenfassung	xvii
Abstract	xix
1 Introduction	1
1.1 Introducing the culprits: formation and evolution of massive stars	2
1.2 The scientific driver of this thesis: feedback from massive stars	4
1.2.1 Momentum feedback	5
1.2.2 Explosive feedback	8
1.2.3 Thermal feedback	11
1.3 Integral field spectroscopy	12
1.3.1 Motivation and utility	12
1.3.2 General technical background	14
1.3.3 MUSE: the <i>Multi Unit Spectroscopic Explorer</i>	16
1.3.4 KMOS: the <i>K-band Multi Object Spectrograph</i>	19
1.4 The role of this thesis	21
1.4.1 Open questions and scope of the thesis	21
1.4.2 Structure of the thesis	22
2 Feedback analysed in this thesis: ionisation and HII regions	23
2.1 A brief theoretical overview	23
2.1.1 Ionisation and recombination	24
2.1.2 Heating and cooling	26
2.2 Photo-evaporation of molecular clouds due to ionisation	27
2.3 Diagnostics of ionised HII regions	29
2.3.1 Extinction	29
2.3.2 Temperatures	30
2.3.3 Densities	31
2.3.4 Ionic and elemental abundances	32
3 Observational setup: the Pillars of Creation in M 16	35
3.1 Introduction	36
3.2 Observations and simulations	38

3.2.1	IFU data	38
3.2.2	Hydrodynamical simulations	40
3.2.3	Monte Carlo radiation-transport calculations	41
3.3	Ionisation structure	42
3.3.1	Extinction correction	42
3.3.2	Integrated line maps	42
3.3.3	Electron temperature and density maps	50
3.3.4	Abundance tracers and ionic abundances	51
3.3.5	Line ratio maps and BPT diagrams	56
3.4	Emission line fitting	58
3.4.1	Velocity structure	58
3.4.2	Geometry	64
3.4.3	Mass loss rate and lifetime	68
3.5	Conclusions	69
4	Feedback in the central Orion Nebula: the classical HII region	71
4.1	Introduction	71
4.2	IFU observations	74
4.3	Abundance maps	75
4.3.1	Ionic and total abundances	75
4.3.2	Line ratios	78
4.4	Kinematics	84
4.5	Discussion of selected regions	89
4.5.1	The Orion bullet HH 201	89
4.5.2	Outflows and proplyds	96
4.6	Conclusions	102
5	Towards an observational quantification of ionising feedback	105
5.1	Introduction	106
5.2	Observations and data reduction	108
5.2.1	Carina	108
5.2.2	NGC 3603 and M 16	109
5.3	Analysis	113
5.3.1	Emission line intensity profiles	113
5.3.2	Physical parameters	117
5.3.3	Quantifying ionising feedback: relating the ionising photon flux to the photo-evaporation rate	122
5.3.4	Ionised jets	126
5.4	Conclusions	132
6	Outlook	135
6.1	Constructing evolutionary timelines from a multi-wavelength approach	135

6.1.1	An infrared study of three Galactic cloud clumps with <i>KMOS</i> and <i>Herschel</i>	137
6.2	Taking things beyond the Milky Way	147
6.2.1	A MUSE view of feedback in HII regions in the Large Magellanic Cloud	147
6.2.2	Constraining the physics of high-mass stellar feedback in NGC 300 . .	150
6.3	The next necessary step: comparing observations and simulations	152
7	Summary and conclusions	157
A	Appendix A	161
B	Appendix B	173
C	Appendix C	185
	Acknowledgments	216

List of Figures

1.1	Outflows in NGC 1333	6
1.2	Galactic HII regions with <i>Spitzer</i>	10
1.3	3-dimensional integral field data cube	13
1.4	Differential atmospheric refraction	14
1.5	Integral field image slicing techniques	15
1.6	3D rendering of MUSE	16
1.7	MUSE image splitting and slicing	18
1.8	The 24 pick-off arms of KMOS	20
2.1	Sketch of a blister-like HII region	27
2.2	Energy level diagrams of O^{++} and N^+	31
2.3	Energy level diagrams of O^+ and S^+	32
3.1	MUSE telescope pointings of the pillars in M 16	39
3.2	Emission line and continuum 3-colour composite	40
3.3	Spectrum of the M 16 HII region	43
3.4	Extinction map and histogram	44
3.5	Integrated line maps of the M 16 pillars	47
3.6	Emission line intensity profiles along the pillar/ambient interface	48
3.7	Emission line intensity profiles of simulated pillars	49
3.8	Observed and simulated electron density and temperature maps	52
3.9	Histogram of the electron density of the observed and simulated pillars	53
3.10	O_{23} vs. S_{23} and S_{23} parameter map of the tip of P2	54
3.11	S_{23} parameter map of the entire M 16 mosaic	55
3.12	Emission line ratio maps of the M 16 mosaic	57
3.13	BPT diagrams of the M 16 pillars	59
3.14	BPT diagram of the tip of P2	60
3.15	Stacked spectrum of several emission lines	60
3.16	Velocity map of the pillars in M1 6	62
3.17	Sketch of the photo-evaporative flow	63
3.18	Position-velocity plots across the pillar/ambient interface	65
3.19	Position-velocity plots across the pillar/ambient interface of simulated pillars	66
3.20	Velocity histogram	66

3.21	Sketch of the 3D geometry of the M 16 pillars	67
4.1	SII map of the Orion Nebula and its main features	72
4.2	H α continuum-subtracted integrated intensity map of the Orion Nebula	74
4.3	Orion oxygen ionic and total abundance maps	77
4.4	Orion sulphur ionic and total abundance maps	79
4.5	Orion nitrogen ionic and total abundance maps	81
4.6	Oxygen ionic and total abundance profiles	82
4.7	OII/OIII and N_e across the Orion Bright Bar	84
4.8	Continuum-subtracted S_{23} and OII/OIII maps of the Orion Nebula	85
4.9	Close-up and histograms of OII/OIII	86
4.10	Orion Nebula velocity maps of H α , OIII, SII and OI	88
4.11	Structure function slopes as a function of Gaussian noise	89
4.12	Structure functions of the Orion Nebula for H α , OIII, SII and OI	90
4.13	S_{23} map of the Orion bullet covered by MUSE	92
4.14	Integrated intensity maps of the Orion bullet covered by MUSE	93
4.15	Velocity maps of the Orion bullet covered by MUSE	94
4.16	Integrated intensity FeII map of HH 201	95
4.17	Integrated intensity maps of HH 203, HH 204 and proplyd 244-440	99
4.18	S_{23} map of the region south of the Orion Bright Bar	100
4.19	Sketch of Orion 244-440	101
4.20	Sketch of HH 204	101
5.1	RGB composites of the observes Carina pillars	110
5.2	<i>Herschel</i> RGB composite of the central Carina Nebula Complex	111
5.3	RGB composite of the pillar in NGC 3603	112
5.4	Continuum-subtracted H α integrated intensity maps of the four Carina regions	114
5.5	Emission line intensity profiles of R44 and R37	116
5.6	Emission line intensity profiles of R18 and R45	117
5.7	Simulated species abundances at the pillar/ambient interface	118
5.8	Correlations between the electron density ionising flux and distance	120
5.9	Velocity maps of the four Carina pillars	121
5.10	Correlation between the mass-loss rate and the ionising photon flux	126
5.11	Jet in R18	128
5.12	Velocity map of the R18 jet	129
5.13	Jet in R44	131
5.14	Velocity map of the jet in R44	132
6.1	Time evolution of a molecular cloud core	136
6.2	Example SED fit of BYF 73	139
6.3	Column density and temperature maps of W49	139
6.4	Feedback-driven structures in W49	142
6.5	Spitzer image of W33	143

6.6	$\text{Br}\gamma$ integrate intensity and velocity maps	144
6.7	Column density and temperature maps of BYF 73	145
6.8	RGB colour composite of BYF 73	146
6.9	Example spectra in BYF 73	147
6.10	MUSE observations of the HII region N44 in the LMC	149
6.12	The proposed MUSE observations of NGC 300	153
6.13	A schematic view of the outlook	154
A.1	Integrated line maps of NII λ 6584, SIII λ 9068	162
A.2	Integrated line maps of OI λ 6300, OI λ 5577	163
A.3	Integrated line maps of SII λ 6717, SII λ 6731	164
A.4	Integrated line maps of ArIII λ 7135, ArIII λ 7751	165
A.5	Integrated line maps of HeI λ 5876, HeI λ 6678	166
A.6	Integrated line maps of HeI λ 7065, OI λ 6363	167
A.7	Integrated line maps of OII λ 7320, OII λ 7330	168
A.8	Integrated line maps of H β , and the S_{23} parameter map	169
A.9	Star formation at the tip of a simulated pillar-like structure	170
A.10	Velocity map of P2	171
B.1	Velocity maps of H α , OIII, SII and OI	174
B.2	SII velocity maps of a simulated HII region	175
B.3	SII velocity maps of a simulated HII region, continued	176
B.4	Structure function of the simulated SII velocity map	177
B.5	Structure function of the simulated SII velocity map, continued	178
B.6	Simulated SII integrated intensity map	179
B.7	SII/H β vs. OII/OIII	180
B.8	S_{23} maps and S_{23} vs. OII/OIII scatter plots	181
B.9	S_{23} maps and S_{23} vs. OII/OIII scatter plots, continued	182
B.10	S_{23} maps and S_{23} vs. OII/OIII scatter plots, continued	183
B.11	S_{23} maps and S_{23} vs. OII/OIII scatter plots, continued	184
C.1	Continuum-subtracted integrated emission line intensity maps of R37	186
C.2	Continuum-subtracted integrated emission line intensity maps of R37, continued	187
C.3	Continuum-subtracted integrated emission line intensity maps of R44	188
C.4	Continuum-subtracted integrated emission line intensity maps of R44, continued	189
C.5	Continuum-subtracted integrated emission line intensity maps of R18	190
C.6	Continuum-subtracted integrated emission line intensity maps of R18, continued	191
C.7	Continuum-subtracted integrated emission line intensity maps of R45	192
C.8	Continuum-subtracted integrated emission line intensity maps of R45, continued	193
C.9	Continuum-subtracted integrated emission line intensity maps of NGC 3603	194
C.10	Continuum-subtracted integrated emission line intensity maps of NGC 3603, continued	195
C.11	Electron density and temperature maps of R18 and R37	196

C.12 Electron density and temperature maps of R44 and R45	197
C.13 Electron density and temperature maps of RNGC 3603	198
C.14 RGB composite of HH 1124	199

List of Tables

1.1	MUSE specifications	17
1.2	KMOS specifications	19
3.1	Central coordinates of the MUSE mosaic pointings	38
3.2	Emission lines in the MUSE M 16 data set	45
3.3	Emission line peaks across the pillar/ambient interface	50
3.4	Derived ionic and total oxygen and sulphur abundances	55
3.5	Line of sight velocities of the M 16 pillars relative to the HII region	67
4.1	Atomic data used for the ionic abundance determination	76
4.2	Ionic and total abundances	80
4.3	Electron densities and temperatures extracted from the Orion Nebula	81
4.4	Best fit parameters of the Gaussian fitting to the FeII line in HH 201	96
4.5	Orion proplyds	97
5.1	MUSE observations of pillar-like structures in the Carina Region	109
5.2	Emission line intensity profile peaks	115
5.3	Properties and physical parameters of the considered pillars	124
5.4	Emission line fitting to the jet in R18	130
6.1	KMOS target selection	138
6.2	H ₂ lines identified in the KMOS K-band spectra	140
6.3	MUSE LMC large program target selection	150

Zusammenfassung

Während ihrer gesamten Lebensdauer haben massereiche Sterne Auswirkungen auf ihre Umgebung (z.B. durch protostellare Ausströmungen, starke Winde, ionisierende Strahlung, Supernovae). Dies kann zwar konzeptuell erklärt werden, jedoch fehlt noch ein detaillierteres Verständnis sowohl der genauen Rolle dieser Feedback-Mechanismen auf den gesamten Prozess der Sternentstehung und des stellaren Umfelds als auch im Hinblick auf deren Abhängigkeit von den Eigenschaften der Regionen, in welchen massereiche Sterne entstehen. In dieser Doktorarbeit wird der Effekt des ionisierenden Feedbacks massereicher Sterne mittels einer Beobachtungstechnik namens integraler Feldspektroskopie analysiert. Diese liefert dreidimensionale Informationen, indem sie es erlaubt, die gewählten Zielobjekte nicht nur in einem einzigen Frequenzbereich sondern über die gesamte Bandbreite des beobachteten Wellenlängenbereichs abzubilden. Hierfür werden zunächst eine Beobachtungskonfiguration und neue Analysetechniken entwickelt. Diese werden dann angewandt, um eine Korrelation zwischen den Feedback-treibenden, ionisierenden massereichen Sternen und den vom Feedback betroffenen umgebenden Gasstrukturen abzuleiten, nachdem das Verfahren zunächst anhand einer klassischen Sternentstehungsregion getestet wurde. Die integrale Feldspektroskopie erweist sich dabei als ideales Instrument um Feedback von massereichen Sternen zu verfolgen. Zudem können die von solchen Instrumenten beobachteten Datensätze auch zur Identifizierung und Klassifizierung Feedback-treibender, massereicher Sterne dienen.

Die hier entwickelten Methoden haben es ermöglicht, (i) den Massenverlust von Molekülwolkenstrukturen anhand von Photoevaporation, bedingt durch die ionisierende Strahlung der nahen massereichen Sterne zu berechnen; (ii) den Effekt von ionisierendem Feedback durch eine Korrelation zwischen Massenverlust und dem ionisierendem Photonenfluss zu bestimmen; (iii) den relativen Beitrag von Schock- und ionisierendem Feedback zur Anregung von Emissionslinien zu analysieren; (iv) Jets von jungen, in den umliegenden Molekülwolkenstrukturen eingebetteten, Sternen zu identifizieren, und deren Morphologie und Kinematik in Bezug auf die nahe gelegenen massereichen Sterne zu analysieren. Diese Ergebnisse zeigen, dass die hier entwickelten Methoden der Untersuchung der Effekte von ionisierendem Feedback massereicher Sterne dienen und eine beobachtungsbedingte Quantifizierung dieser Effekte ergeben.

Diese Arbeit bereitet den Boden für zukünftige Untersuchungen, welche zusammen mit laufenden und geplanten Beobachtungen auf die Charakterisierung und Quantifizierung massereicher stellaren Feedbacks während aller evolutionärer Stadien Feedback-treibender Sterne und ihres Umfelds abzielen. Dies wird zu entscheidenden Kenntnissen führen um den gesamten Prozess der Sternentstehung zu verstehen, d.h. wie Galaxien Gas in Sterne wandeln und wie

dies vom Feedback selbst abhängt.

Abstract

Throughout their entire lives, massive stars have a deep impact on their surroundings (e.g. via protostellar outflows, strong winds, ionising radiation, supernovae events). Conceptually this is well understood, but the exact role of these feedback mechanisms on the global star formation process and the stellar environment, as well as their dependence on the properties of the regions in which massive stars form, are yet to be understood in detail. In this thesis, the effect of ionising feedback from massive stars is analysed with an observational technique called integral field spectroscopy, which yields 3-dimensional information by allowing one to image the target sources not only in one band or wavelength, but across an entire wavelength range. For this purpose an observational setup and novel analysis techniques are first developed, which are then used to derive a correlation between the feedback-driving, ionising massive stars and the feedback-affected surrounding gas structures, after having tested them on a classical star-forming region. It is found that integral field spectroscopy is ideal to trace feedback from massive stars, and that datasets from such instruments can also be used to identify and classify the feedback-driving massive stars.

The novel methods and techniques developed in this thesis allowed (i) the computation of the mass-loss rate of molecular cloud structures due to photoionisation from the nearby massive stars; (ii) an observationally-derived quantification of the effect of photoionisation by correlating the mass-loss rate of the cloud structures to the photon flux emitted by the feedback-driving stars; (iii) the analysis of the relative contribution of shock and ionising feedback to the excitation of the cloud matter; (iv) the identification of jets originating from young stars embedded in the molecular cloud structures surrounding the massive stars and the analysis of their kinematics and morphologies with respect to the nearby ionising stars. These results demonstrate that the developed methods allow the study of the effect of ionising feedback from massive stars, and that they deliver an observational quantification of these effects.

This thesis sets the ground for future investigations, which, together with ongoing and planned observational campaigns, are aimed at characterising and quantifying high-mass stellar feedback throughout the evolutionary stages of the feedback-driving stars and their environments. This can lead to crucial insight needed to understand the global process of star formation, i.e. how galaxies turn their gas into stars and how this depends on feedback itself.

1

Introduction

One of the fundamental problems in modern astrophysics is to constrain the physics driving the baryon cycle in galaxies – i.e. how galaxies turn their gas into stars, how the feedback from these stars regulates the growth of galaxies, and how these processes may have changed with galactic environment and across cosmic time. The (re)distribution of mass, energy, photons, and metals by stellar feedback represents the main missing ingredient to connect the observed galaxy population to Λ CDM cosmology (e.g. Vogelsberger et al. 2014, Schaye et al. 2015). In order to make progress, the field requires a direct observational link between the feedback-driving sources and the feedback-affected interstellar medium. This in turn requires a systematic observational census of the small (cloud-) scale quantities describing feedback (i.e. the cloud lifetime, the size and expansion velocity of HII regions, the photo-evaporation rates and structure of the ionisation fronts), as well as a systematic census of the feedback-driving sources (O-, B- and WR-type stars, supernovae). Until recently, it was not possible to obtain these quantities outside the limited sample of nearby star-forming regions. However, thanks to the arrival of new observing techniques such as integral field spectroscopy, as well as recent developments of novel analysis techniques, it is now possible to systematically obtain both the quantities describing the effect of feedback on the interstellar medium and the stars responsible for driving the feedback from a single dataset for large samples of star-forming regions across nearby galaxies.

This thesis aims at testing these new observing techniques and instruments, and at finding and developing the best observing strategies and data analysis tools to set the ground for large-scale surveys of massive star formation feedback across molecular cloud evolution (from starless massive molecular cloud clumps to fully evolved HII regions). For this, initial data sets in the near-infrared and optical wavelength regimes, sampling molecular cloud evolution from the relatively early, embedded stages of star and cluster formation to exposed HII regions respectively, are analysed in this work. The three main chapters of this thesis describe the progress from a pilot study testing the observational set up (Chapter 3) to the development of new analysis techniques via the expertise gained in the pilot study and by applying this to a well-studied star-forming region (Chapter 4), and finally the application of the two previous works to deliver a first quantification of the effect of feedback from massive stars (Chapter 5).

The long-term goals of the projects derived from this thesis are aimed at determining and

quantifying the role of massive star formation feedback, both on large (galaxy-wide) and on small (cloud-) scales, and the methods and techniques obtained from this thesis are the first necessary fundamentals on which the future studies will be based. Indeed, projects and plans expanding on the work presented in this thesis are discussed in Chapter 6. To set the scene, this introduction first describes massive stars and feedback mechanisms associated with their formation and evolution, and then describes the new observational instruments used for the analysis of the work presented here. Finally, these two threads will be brought together to motivate the work of this thesis via introducing the main open questions and the scope of this work.

1.1 Introducing the culprits: formation and evolution of massive stars

Massive stars have profound repercussions both on large, kpc-scales (galactic scales) and on small, pc-scales (molecular cloud scales) via various different mechanisms throughout their entire lifetime. They are responsible for enriching the interstellar medium (ISM) with heavy elements, for injecting great quantities of energy (radiative and mechanical) into the ISM, and they play a crucial role in galaxy evolution models. Before understanding exactly how massive stars influence their environments, it is important to first understand what massive stars are, how and where they form, as well as how they will evolve. A *brief* overview of massive star formation and evolution is given in this section.

It is generally accepted that stars form via the gravitational collapse of dense, cold subregions of hierarchical molecular clouds (so-called molecular cloud cores). These self-gravitating subregions, created via fragmentation of the turbulent giant molecular cloud (GMC) they are embedded in, will undergo gravitational collapse when the internal gas pressure is no longer able to support it, and form a central object which will accrete matter until the critical mass for the onset of hydrogen burning is reached. This mechanism, here explained in a few simple words (for the interested reader, comprehensive and exhaustive descriptions and reviews are given in Shu et al. 1987, McKee & Ostriker 2007 and Zinnecker & Yorke 2007), is generally valid when considering so-called low-mass stars, i. e. stars with masses $\lesssim 8 M_{\odot}$, which do not form elements heavier than carbon during their lifetime because they never reach the necessary temperatures for carbon burning and will not end their lives as supernovae.

With the term *massive stars*, objects with masses greater than the above mentioned $\sim 8 M_{\odot}$ are referred to, and one of the fundamental problems in modern astrophysics is the formation of these stars. Observationally speaking, massive star formation is very challenging, since the formation regions are typically affected by high extinction, large distances and therefore low spatial resolution, and confusion due to crowded (clustered) regions.

From the theoretical approach, there are two main contending scenarios for the formation of massive stars: *core accretion* (high-mass stars form via the collapse of massive molecular cloud cores, thus a scaled-up version of low-mass star formation), and *competitive accretion* (massive stars form via continued accretion in the centres of high-density star-forming clumps where they

have access to the necessary matter). However, both theories suffer from the same weak point: according to the physics of gravitational collapse and radiation, accretion should be halted by the strong radiation originating from the forming central object. By comparing the inward-directed gravitational forces acting on a forming star to the outward-directed radiative pressure, Larson & Starrfield (1971) compute that at masses around $\sim 20 M_{\odot}$, further infall of material onto the proto-star should be halted due to the strong radiation pressure acting on a dust shell surrounding the star formed via increasing temperatures and subsequently evaporating dust grains. Indeed, Wolfire & Cassinelli (1987) find that by using a dust grain size distribution and composition derived from observations as described in Mathis et al. (1977), massive stars could only form under circumstances in which shocks or ionisation could lower the dust abundance.

Numerous numerical simulations have been performed in the decades since these early publications addressing the formation of massive stars from various different perspectives, and at least numerically, massive stars up to about $80 M_{\odot}$ can be formed despite the radiation pressure problem by including accretion disks (Yorke & Sonnhalter 2002, Kuiper & Yorke 2013), Rayleigh-Taylor instabilities (Krumholz et al., 2009) and bipolar outflows (Krumholz et al., 2005), all of which lead to shielding from radiation pressure or anisotropies in the radiation field. Reviews of the various efforts in simulating massive star formation are given in Hennebelle & Commerçon (2014) and Tan et al. (2014).

Once a massive star has formed, the further evolution mainly depends on its mass, as this will determine important factors such as the mass-loss rate by stellar winds (which increases with mass, de Jager et al. 1988). In general, stars with $M \lesssim 25 M_{\odot}$ never reach the Wolf-Rayet phase and will evolve from the super-giant phase to a supernova, while stars more massive than that do undergo the Wolf-Rayet stage in which they lose most of their progenitor mass, before resulting in a supernova event. The mass of the progenitor star determines the type of supernova event a massive star will undergo: stars with $M \lesssim 25 M_{\odot}$ will result in a supernova type II (spectrum shows hydrogen lines), stars with $25 M_{\odot} \lesssim M \lesssim 60 M_{\odot}$ typically result in a type Ib or Ic supernova (no hydrogen lines), stars with $M \gtrsim 60 M_{\odot}$ end their lives as a type IIn supernova (presence of narrow lines).

Stars in hydrostatic equilibrium follow a relation between their mass and luminosity such that $L \propto M^{\alpha}$, with $1 < \alpha < 3$ (Kippenhahn & Weigert, 1990), and their lifetime t is proportional to the mass-luminosity ratio M/L . It therefore follows that $t \propto M^{1-\alpha}$, constraining the lifetimes of massive stars to a few 10^6 years. The lifetime however depends on several factors, such as the star's mass, chemical composition, multiplicity, magnetic properties or rotation. For example, stars with $M > 40 M_{\odot}$ produce very strong winds (which are even stronger if the star is metal-rich, see Section 1.2.2) and strong radiation pressures, rapidly losing mass as they evolve. The mass-loss rate of a massive star during its lifetime will therefore also determine the supernova-type, as described in the previous paragraph. The effects of massive stars on their environment will be discussed hereafter.

1.2 The scientific driver of this thesis: feedback from massive stars

Massive stars act on their environment through various different mechanisms, depending on their evolutionary stage. As will be discussed in more detail in the next pages, feedback (FB) from massive stars is observed throughout cosmic time and distance. One of the prime examples for this is the star-forming region 30 Doradus in the Large Magellanic Cloud, the largest and most massive HII region in the Local Group. In 30 Doradus, thousands of OB stars have shaped the complex morphology of this region that consists of ionised filaments, wind- and radiation blown cavities, supernova-driven shell-like structures and dense, cold molecular gas complexes. Clearly 30 Doradus is under the influence of several FB mechanisms, but observationally disentangling these from one another is very challenging (Lopez et al., 2011), as the various FB mechanisms often act at the same time. In general, both observations and simulations show that star formation is a slow and rather inefficient process in which the available molecular gas is never fully converted into stars (Zuckerman & Evans 1974, Williams & McKee 1997). Indeed simulations of star-forming molecular clouds demonstrate that if FB is not included, star formation is too fast and too efficient (Klessen & Burkert 2000, Klessen & Burkert 2001, Bate 2009). Another argument which both observations and simulations support is that while stars tend to form in clusters (Lada & Lada 2003, Beuther et al. 2007, Bressert et al. 2010), most stars are no longer part of a star cluster after 10 -100 Myr (Silva-Villa & Larsen 2011, Fall & Chandar 2012), and simulations without FB recipes tend to form clusters which are and remain bound (Bate et al. 2003, Bonnell et al. 2003). FB is therefore a potential solution, as it can disperse the gas and inject turbulence and therefore halt the further formation and collapse of potential star-forming molecular cloud cores. However, none of the current simulations include all FB mechanisms, and a better understanding will be only possible if numerical improvements are made towards this. Observationally speaking, the challenge for the future is to obtain observations of extragalactic, more extreme environments at better angular resolution. This will help determining whether the increasingly complex simulations are able to reproduce the structures and dynamics generated at GMC scales by feedback, and how the different feedback mechanisms interact with each other. A first step towards the last point will be described in Chapter 6.

In this section the various types of feedback mechanisms will be presented and briefly discussed. Feedback can be classified in different ways, for example according to the amount of energy input as in Bally (2011), where the various mechanisms are put on the so-called *feedback ladder*, or according to the type of feedback as in Krumholz et al. (2014). The latter is adopted here: there are three main categories of feedback, namely *momentum feedback*, *explosive feedback* and *thermal feedback*. These will be discussed one by one in the next sections. Furthermore, to avoid misunderstandings, molecular cloud terminology is used as in Williams et al. (2000): molecular cloud *clumps* correspond to star cluster-scaled condensations, while molecular cloud *cores* are single (star-scaled) condensations.

1.2.1 Momentum feedback

As the terminology already suggests, this kind of feedback injects momentum into the surrounding medium, with the general effect of forcing the nearby clouds back (and disrupting them if the injected momentum is large enough) and driving turbulence within them. There are two main types of feedback mechanism which inject momentum: protostellar outflows and radiation pressure.

Protostellar outflows

Outflows are associated with both high- and in low-mass stars throughout star-forming regions. They occur at the earliest stages of star formation when the forming object is still accreting matter. The launching mechanism of jets and outflows is a long-lasting and not yet solved astrophysical problem, but this will not be discussed in this thesis as the focus is on the effect of these mechanisms rather than their origin. The most important theoretical measure of outflows is the amount of momentum injected per unit stellar mass, V_{out} (Krumholz et al., 2014), where $V_{\text{out}} = p/M_{\star}$ and therefore corresponds to the amount of momentum carried by the outflow divided by the mass of the star launching the outflow. As most of the mass in star clusters is located in low-mass stars, it is clear that outflow feedback is not dominated by massive stars, but rather by large numbers of low-mass stars in the same region.

The effect of outflow FB depends on the timescale on which it acts: if all the stars in low-mass cluster were to inject momentum from their outflows roughly simultaneously, the combined V_{out} can be enough to unbind the native molecular cloud, while if the momentum injection occurs gradually, the main effect is the maintenance of a certain level of turbulence which results in stabilising the surrounding matter against gravitational collapse and therefore in regulating further star formation by slowing it down. This is demonstrated by several numerical simulations (Li & Nakamura 2006, Matzner 2007, Nakamura & Li 2007, Cunningham et al. 2009, Carroll et al. 2009). These models also show that because of the injected turbulence, outflows from low-mass stars can hinder high infall rates towards massive stars and therefore regulate the formation of these. The scales on which outflows act range from 0.01 pc to some tens of pc and therefore affect molecular clouds on cloud scales, while they do not have an impact on larger, giant molecular cloud scales (Bally, 2011).

Observationally speaking, protostellar outflows can be identified by various tracers. Where outflows with supersonic velocities hit the surrounding matter, shocks arise which can be traced by emission line wings in the sub-mm and mm regime, as well as by radiative shocks from the near-UV to the near-infrared. Examples for collisionally-excited emission lines deriving from outflow shocks are [OI] and [SII] in the visible wavelength range and [FeII] in the near-infrared (Bally et al. 2015, McLeod et al. 2015, McLeod et al. 2016). One of the prime examples of a region where several low-mass stellar outflows are observed is the star-forming region NGC 1333 (e.g. Gutermuth et al. 2008, Curtis et al. 2010, Plunkett et al. 2013), shown in Fig. 1.1.

The quantification, or at least evaluation, of the effect of outflow FB is, in observational terms, not trivial. The main methods for this are (i) the comparison between the kinetic energy of the outflow-affected gas and the turbulent energy of the gas in the cluster (e.g. Arce et al.

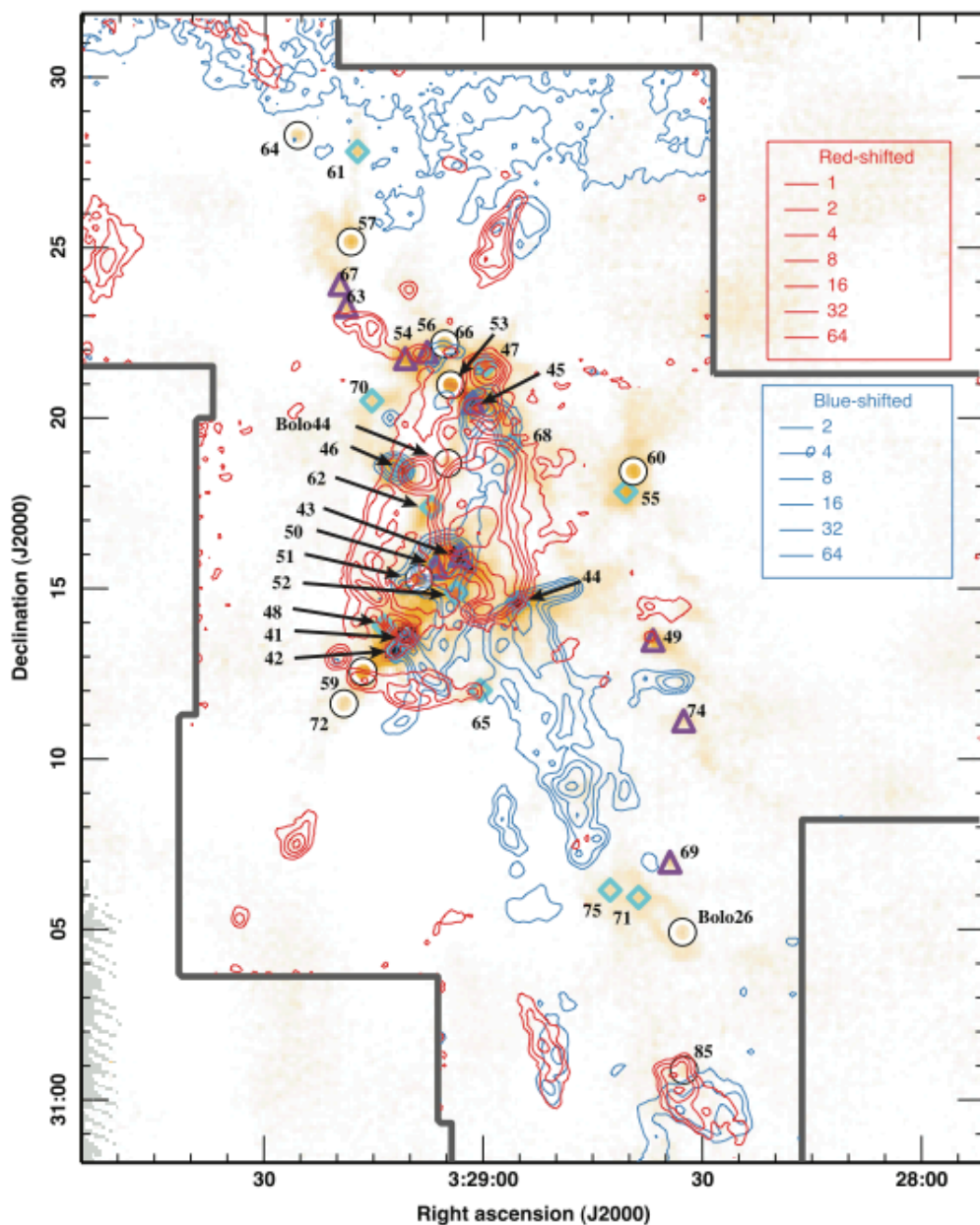


Figure 1.1: Protostellar outflows in NGC 1333 (figure from Curtis et al. 2010): red and blue contours trace the CO outflows on a SCUBA 850 μm map. Red contours are from 12 to 18 km s^{-1} , blue contours are from -5 to 3 km s^{-1} . The identified outflows are marked with numbers.

2010, Duarte-Cabral et al. 2012, Narayanan et al. 2012), and (ii) the comparison between the total mechanical outflow luminosity and the turbulent energy dissipation rate (e.g. Williams et al. 2003, Maury et al. 2009, Nakamura et al. 2011, Nakamura et al. 2011). The uncertainties of these studies are large because of the difficulty in determining the above mentioned quantities, and in general observations support what simulations predict, namely that outflows are capable of maintaining turbulence on local, clumps-cales, but not on larger, molecular cloud complex scales.

The main limitation of current observations of outflows is that the resolution needed to disentangle single outflows can currently only be achieved in nearby (and predominantly low-mass) star-forming regions. To fully understand outflow feedback, high angular resolution observations of more distant but high-mass star-forming regions are needed, where the challenge will be disentangling outflow FB and the other mechanisms at hand.

Radiation pressure

Radiation pressure is the injection of momentum into the surrounding matter by stellar radiation (which of course also injects energy, but this will be discussed later). While momentum FB driven by protostellar outflows is dominated by the low-mass stars, momentum FB driven by radiation pressure is dominated by the high-mass stars, since for $2 M_{\odot} < M < 20 M_{\odot}$ the luminosity scales with $\sim M^{3.5}$, while for $0.43 M_{\odot} < M < 2 M_{\odot}$ it scales as $\sim M^4$, and the momentum injected by radiation pressure can be computed analogously to the outflows as $V_{\text{rad}} = p/M_{\star}$. Because of this, radiation pressure only becomes important when the initial mass function (IMF) is fully sampled and a cluster has a mass of $\sim 10^{3.5} M_{\odot}$ or higher (Krumholz & Thompson, 2012), or for stars with masses starting from $\sim 20 M_{\odot}$ (Krumholz et al., 2009).

In analysing radiation pressure, simulations are far ahead of observations, and simulations of radiation pressure in single stars need to be distinguished from those that model radiation pressure on larger scales. In both cases however, results are contradictory. In the former, work by Krumholz et al. (2009, 2010) (and earlier publications) conclude that gravitational and Rayleigh-Taylor instabilities that form in the gas surrounding a forming star are able to funnel matter to the star and create escape routes for the radiation, and therefore stop radiation from halting accretion, while Kuiper et al. (2011, 2012) conclude that these kind of instabilities which can help circumvent the radiation pressure problem do not have the time to form before radiation pressure expels the matter. As described in Section 1.1, the enigma of the formation of massive stars and the radiation pressure problem are yet to be solved.

An observational quantification of radiation pressure has not been attempted in many studies, and these find rather contradicting results. An example is the already cited work by Lopez et al. (2011) on 30 Doradus, where the bolometric luminosity of all the stars is computed and subsequently related to the radiation pressure. These authors find that radiation pressure dominates within 75 pc of the central massive cluster R136. Pellegrini et al. (2011) use the same approach, but do not consider radiation pressure reprocessed by dust, and conclude that radiation pressure is not a dominant FB mechanism in 30 Doradus.

1.2.2 Explosive feedback

Although supernova events are included in this category, *explosive* feedback also originates from mechanisms which are not *per se* deriving from an explosive event. Rather, the terminology underlines the ability of these FB mechanisms to heat the surrounding gas to such high temperatures, that radiative cooling is no longer efficient and a part of the injected energy is responsible for a rapid expansion of the heated material into the cold surrounding molecular clouds.

Stellar winds

In order to produce strong stellar winds, stars need to have surface temperatures of $\sim 2.5 \times 10^4$ K (Vink et al., 2000) or higher, which (for main sequence stars) corresponds to a mass of about $40 M_{\odot}$. These are truly massive stars, which start their main sequence life while still accreting matter. The wind momentum flux strongly depends on metallicity, because the reduced presence of heavy elements reduces the efficiency of stars in driving stellar winds* (Vink et al., 2000), while stellar rotation can lead to the opposite effect (e.g. Maeder & Meynet 2010).

The amount of injected momentum via stellar winds depends on the specific kinetic energy of the wind, most of which thermalises when the wind collides with the ISM. The reason for this is that the high terminal velocity of hot winds (which can be of several 10^3 km s $^{-1}$, Castor et al. 1975, Leitherer et al. 1992) can produce shocks when colliding with the ISM, heating the matter to very high temperatures ($T > 10^7$ K) at which point radiative cooling is not very efficient (e.g. Weaver et al. 1977), leading to an expanding flow of matter (unless the wind is not confined and can leak out of the bubble). Yeh & Matzner (2012) defined the relative strength of stellar winds in an HII region via the so-called wind parameter Ω ,

$$\Omega = \frac{P_w V_w}{PV - P_w V_w}$$

where P and V are the thermal pressure and volume of the outer edge of the HII region (therefore of the 10^4 K gas), while P_w and V_w are the thermal pressure and volume of a hot (10^7 K), X-ray emitting gas which has been shock-heated by hot stellar winds. If $PV \gg P_w V_w$ and therefore $\Omega \ll 1$, winds are dynamically speaking irrelevant, while the opposite is true for $\Omega \gg 1$.

Two are the current observational methods used to constrain Ω , the first exploring the X-ray emission from the shocked gas (e.g. Townsley et al. 2003, Lopez et al. 2011, Pellegrini et al. 2011), and the second using wind-sensitive optical and infrared emission line ratios (e.g. [NII]/H α , [SII]/H α , [OIII]/H β and so-called BPT diagrams, see Chapter 3, Verdolini et al.

*A brief explanation for the metallicity dependance of stellar winds. Gas streams outwards from the atmospheres of stars via radiation and gas pressure. Stellar atmospheres, where winds originate, consist of highly ionised matter; if an atom is excited by the encounter with a photon, the decay into the lower excitational state will give rise to emission lines, and furthermore, the redistribution of momentum and energy couples these atoms or ions to the surrounding matter, dragging it along. An accelerating gas will therefore be accelerated even more as it absorbs the Doppler-shifted photons. As the line force is dominated by ions of heavy elements, the abundance of these will determine the net line force driving the wind.

2013). Despite the varying methods and uncertainties, the general observational consensus is that $\Omega < 1$, meaning that the effect of stellar winds is minimal. From the numerical perspective, the results strongly depend on whether wind leakage is included or not, and whether other FB mechanisms are considered in the same simulations. Indeed, if leakage is considered and stellar winds are modelled alone (Dale & Bonnell, 2008) or followed by supernova events Rogers & Pittard (2013), wind FB seems to be quite relevant in dispersing matter and slowing star formation. However, when modelled with other FB mechanisms which act roughly at the same evolutionary stage such as photoionisation (Dale et al., 2014), the effect of stellar winds is modest at most except at very early evolutionary stages. Until further numerical models that include a more detailed physical description and therefore produce a more realistic description of the phenomenon are available, the relative importance of stellar winds over other FB mechanisms will remain under debate.

Photoionisation

The main effect of photoionisation from massive stars is the inflation of HII regions, thus heating and ionising the surrounding matter, where the degree of ionisation depends on the balance between the processes of photoionisation and radiative recombination (in which thermal electrons produced via ionisation recombine with protons to produce neutral hydrogen), and the temperature depends on the balance between photoionisation and radiative cooling. The details of photoionisation will be discussed in Chapter 2, while this section is limited to a more qualitative discussion.

The high temperature ($\approx 10^4$ K) of the ionised gas, its sound speed $c_s \approx 10$ km s⁻¹ and the resulting overpressure lead to an expansion of the HII region into the surrounding neutral/molecular matter. The main ways through which HII regions are observable are free-free emission (thermal bremsstrahlung due to free electrons scattering with ions and remaining free after the scattering event) and recombination lines in the radio (and optical) regime, dust-reprocessed radiation in the infrared, and ionised emission lines in the optical regime. HII regions are ubiquitous throughout star-forming galaxies, and appear in a wide range of sizes and morphologies as is shown in Fig. 1.2.

The main effects of photoionisation are, to date, not well understood, and include the triggering (or suppression) of the formation of new generations of stars, the driving of turbulence at scales of giant molecular clouds, and the disruption of these. However, the exact mechanisms with which photoionisation interacts with the surrounding neutral and molecular matter are highly complex. One of these effects is photo-evaporation (Hester et al., 1996): as the strong ionising radiation from the nearby O- and B-type stars hits the matter of the molecular cloud rims, the pressure of the matter increases and it is photo-ionised, leading to a photo-evaporative flow of matter streaming away from the cloud surface. Observationally quantifying these effects is therefore very important in order to establish their relative importance in the global FB budget. This thesis is mainly focused on the effects of photoionisation, and is aimed at a first observational quantification of photo-evaporation (see Chapter 5).

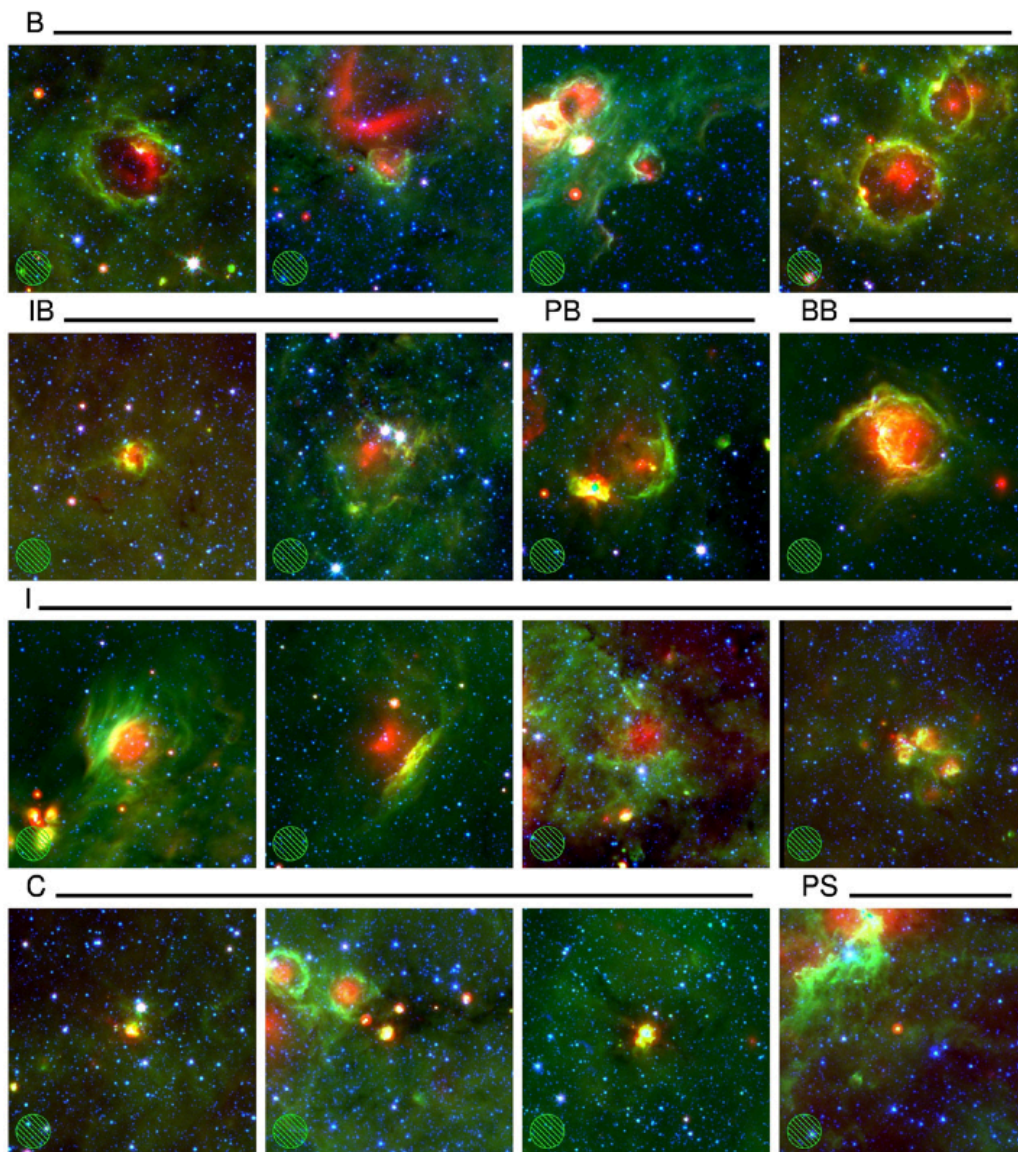


Figure 1.2: RGB-composites of Galactic HII regions imaged by *Spitzer* from Anderson et al. (2011): red is $24 \mu\text{m}$, green is $8.0 \mu\text{m}$ and blue is $3.6 \mu\text{m}$. The morphological classification is as follows: B = bubble, BB = bipolar bubble, PB = partial bubble, IB = irregular bubble, C = compact, PS = point source, I = irregular. The $82''$ Green Bank Telescope beam is shown in the lower left corners.

Supernovae

As already mentioned in Section 1.1, when a $M > 8 M_{\odot}$ star comes to the end of its stellar evolution, it undergoes an explosive *supernova* event during which it expels up to $\sim 60\%$ of its mass at velocities of several 10^4 km s^{-1} and energies of some 10^{51} erg (Tielens, 2010). Supernovae are responsible for heating the ISM to its hottest phase ($T > 10^6 \text{ K}$, McKee & Ostriker 1977) and driving ISM turbulence (e.g. Norman & Ferrara 1996, Gent et al. 2013). The relative contribution of supernova FB with respect to the other FB mechanisms discussed here is, however, not well understood (e.g. Tamburro et al. 2009, Gatto et al. 2015).

On small scales, the expansion of supernova ejecta crucially depends on the density and structure of surrounding matter, as in the low-density ISM a supernova can expand rapidly, and the low-velocity shocks can lead to the surrounding clouds to be crushed. Furthermore, the conduction of energy from the hot remnant-gas to the surrounding molecular clouds can result in an evaporative flow streaming away from the latter and leading to their destruction. Observations show that supernova remnants are typically small compared to the surrounding bubbles, if present at all (Lopez et al. 2011, Munro et al. 2006), hinting at the fact that previous FB mechanisms have already expelled most of the gas.

On large (galactic) scales, the effects of supernovae in the ISM have been probed by many numerical simulations in which the basic varying assumption is the localisation of the supernova events: clustered, random or correlating with density (e.g. de Avillez & Breitschwerdt 2004, Joung & Mac Low 2006, Hennebelle & Iffrig 2014). Iffrig & Hennebelle (2015) find that supernovae only have relevant effects when occurring in a higher-density environment of a molecular cloud, where a significant amount of the cloud's mass can be removed, thus halting star formation in that region and globally affecting the star formation history of the galaxy. However, if the density of the surrounding matter is too high, the effect of the supernova FB will be quickly quenched (Whalen et al., 2008).

1.2.3 Thermal feedback

Thermal feedback is not to be confused with the heating from the above described explosive FB mechanisms. The temperature of the affected matter is increased, but not to such high values which lead to explosive expansion. Thermal FB originates during the very first stages of star formation when a molecular cloud core undergoes gravitational collapse and the central forming object accretes matter. The sources for this kind of feedback are the (i) luminosity produced by the stellar core, (ii) the luminosity produced via accretion onto the core, and (iii) the luminosity produced via the sustained collapse and accretion processes.

The luminosity produced by general collapse and accretion is not relevant. For low- and intermediate-mass stars, the importance of thermal feedback of the stellar core luminosity or from accretion luminosity depends both on the mass and the accretion rate of the stellar core. For massive stars however, the intrinsic luminosity always (for all accretion rates) dominates over accretion luminosity.

There is observational evidence for thermal FB in massive star-forming regions. For example, Longmore et al. (2011) infer the initial conditions of the massive star-forming region G8.68-

0.37 by combining sub-mm observations and radiative transfer modelling to replicate the present conditions of the region. They find evidence for gas-heating by a previous generation of low-mass stars which resulted in the fragmentation of the cloud matter into cores which can only form O-type stars if these are fed with matter via infall from the massive gas reservoir of the region. These observations not only support the presence of thermal FB, but also a scenario of competitive accretion, rather than core accretion (see Section 1.1). The precise consequences of thermal FB have been thoroughly explored with numerical simulations which include radiative transfer, and it is found that it profoundly affects the cloud assembly into stars and the IMF (Krumholz et al. 2007, Bate 2009, Offner et al. 2009, Urban et al. 2010) because of thermal FB reducing fragmentation.

1.3 Integral field spectroscopy

Observational astronomy is an ever growing and fast advancing field, with new instruments and observing facilities being developed and constructed. The work presented in this thesis makes use prevalently of data from so-called *integral field spectrographs*. These kind of spectrographs are instruments which originate in the last one or two decades and are becoming more and more popular. The final data product, rather than being a single spectrum or a single 2-dimensional image, is a 3-dimensional data cube consisting of a stack of 2-dimensional images across a certain wavelength range, meaning that for each pixel in an integral field data cube there is a spectrum covering that wavelength range. The motivation for these kind of instruments and their basic technical setup will be presented in the next subsections, as well as details about the two main instruments used for the research described in this thesis.

1.3.1 Motivation and utility

Certainly the major advantage of integral field spectroscopy (IFS henceforth) is that the observed objects are measured both spatially and spectrally. This addresses the major disadvantage of traditional long-slit spectroscopy where an object can only be resolved by moving the slit across the observed field and then combine the multitude of slit observations to reconstruct a spatially resolved image. This means that for spatially extended sources, slit spectroscopy is very time-consuming, and IFSs overcome this problem by delivering spatially measured spectral cubes within one telescope pointing (in the case of a non-mosaic mode observation). In this respect IFS is also more advantageous than Fabry-Perot spectroscopy, which permits a large field of view and can therefore resolve spatially extended sources, but only at a single wavelength. Fig. 1.3 illustrates the 3-dimensionality of IFS data cubes: the final data product consists of a series of 2-dimensional images across the entire covered wavelength range. This of course corresponds to a much more efficient observing strategy over long slit and Fabry-Perot scans, and it leads to a much better continuum subtraction.

Another advantage of IFS over slit spectroscopy is that it solves the issue of differential atmospheric refraction, illustrated in Fig. 1.4: as the light from a target located low on the horizon passes through the atmosphere, it will suffer from refraction, the blue part of the

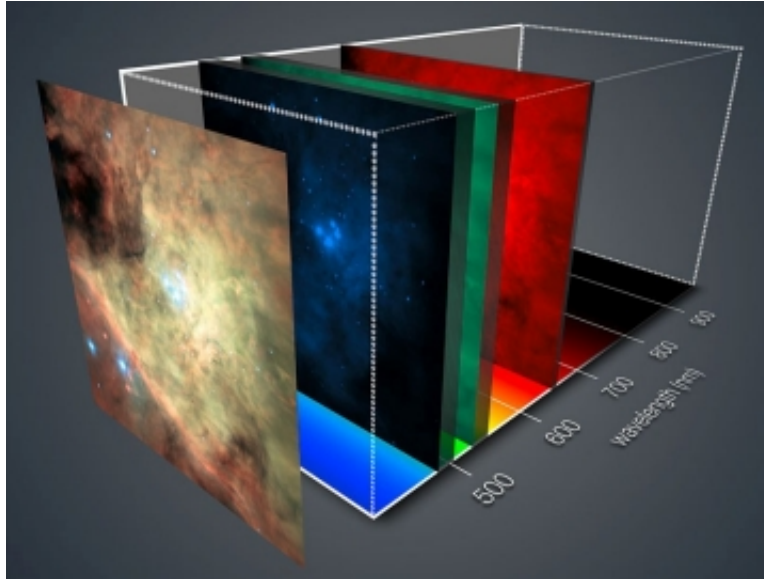


Figure 1.3: Integral field spectrographs deliver a 3-dimensional data cube as final product, which consists of a series of 2-dimensional images across the entire covered wavelength range, meaning that for each pixel there is a spectrum covering that wavelength range. Image credit: ESO/MUSE consortium/R. Bacon/L. Calçada.

spectrum being more deviated than the red part. In the case of broadband filters and spectra over a wide wavelength range, this will cause the observed position of the target to deviate from its actual position, unless the slit is positioned at the parallactic angle. IFS circumvents this problem by taking a spectrum of each spatial sample of the extended source, and the atmospheric diffraction can be corrected for *a posteriori* (Arribas et al., 1999).

The wealth of information obtained with a single exposure of an integral field spectrograph is truly unique, as this technique not only offers imaging, but it also yields the kinematical information from the spectral axis of the data cube. Depending on the wavelength range of the instrument, it is therefore possible to cover many emission/absorption lines simultaneously and therefore perform analyses on a homogeneous data set. For the scope of this thesis, IFS is a crucial new development in the field of star formation feedback especially in the optical and near-infrared regimes: it offers the possibility to obtain information about different phases of the FB-affected ISM from the same uniform data set and with single exposures instead of multiple scans of the same regions.

An example is the near-infrared K-band coverage of the integral field spectrograph KMOS mounted on the Very Large Telescope (and discussed in more detail in Section 1.3.4). KMOS covers the wavelength range 1.934 - 2.460 μm in the K-band grating, and therefore the ionised gas line $\text{Br}\gamma$ at 2.1655 μm and several different [HeI] lines, as well as a multitude of molecular hydrogen lines originating from different transitions (e. g. $\text{H}_2(1-0) \text{S}(1)$ at 2.122 μm , $\text{H}_2(2-1) \text{S}(1)$ at 2.247 μm). Molecular cloud clump data from KMOS will be presented and discussed in Section 6.1. Also of great importance is the capability of IFS to deliver simultaneous

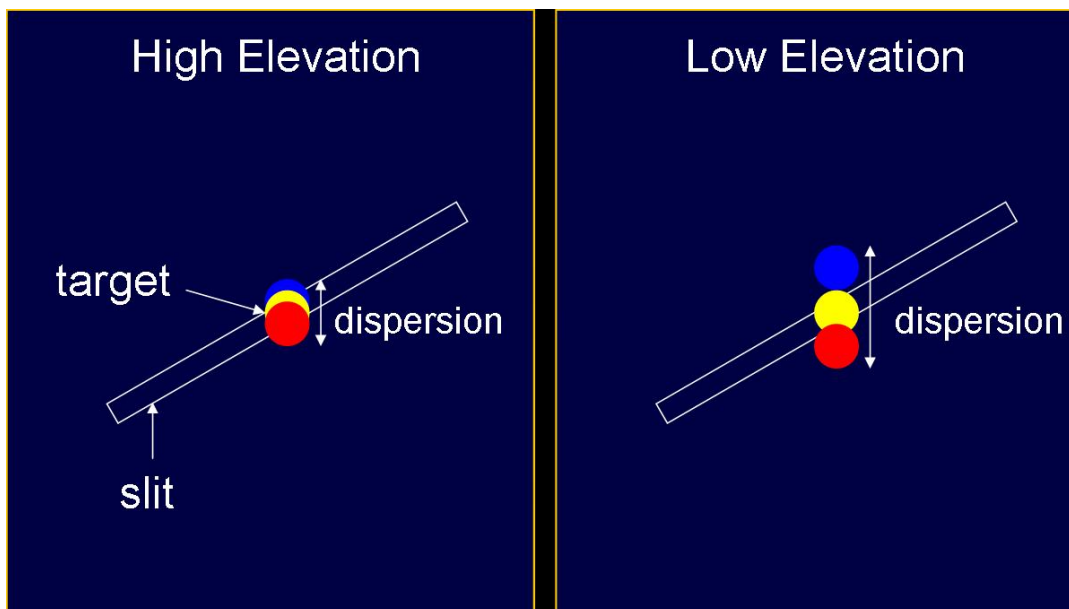


Figure 1.4: Illustration of differential atmospheric refraction in slit spectroscopy: if a source is situated low on the horizon, the passage of the light through the atmosphere will cause the observed position of the source to deviate from its actual position, as blue light is more strongly deviated than red light. Image credit: W. M. Keck Observatory.

information about the FB-driving stars and the FB-affected gas observed in the imaged region. This capability allows one to spectrally classify the FB-driving stars from the same data set used to analyse the affected matter. This kind of simultaneous analysis cannot be performed with any other observing technique, and preliminary applications in the field of massive star formation FB will be discussed in further detail in Section 6.2.1.

1.3.2 General technical background

There are two main components in an integral field instrument: the spectrograph, which splits the incoming light into the desired wavelength range, and the integral field unit (IFU), which slices the acquired image into an array of single slices. To achieve this, there are three main techniques, as illustrated in Fig. 1.5. The *lenslet array* segments the images and projects the light from each element onto single images of the telescope pupil (Allington-Smith & Content, 1998). The single small images are then fed through the spectrograph, and to avoid the single spectra overlapping, the direction of dispersion is tilted, as is shown in the upper right panel of Fig. 1.5. The overlap of the spectra naturally leads to a maximum length of the wavelength range, which is the main disadvantage of this technique. Examples for lenslet IFUs are TIGER and OASIS on the Canada-France-Hawaii Telescope (Bacon et al., 1995), as well as SAURON on the William Herschel Telescope (Bacon et al., 2001).

The *fibre* setup (which can be combined with lenslets), consists in a tight bundle of fibres that sends the collected light to a slit (or set of slits), which are then fed through the spec-

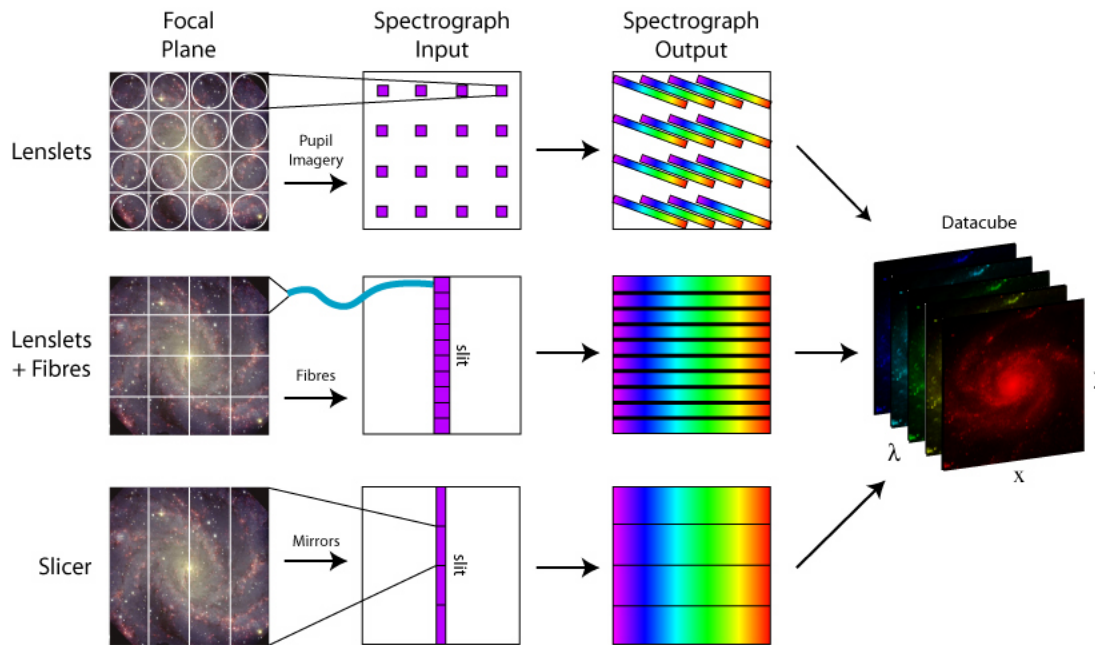


Figure 1.5: Illustration of the three main integral field image slicing techniques: lenslet arrays, lenslet + fibre combination, and the image slicer (see text Section 1.3.2). Image credit: M. Westmoquette, adapted from Allington-Smith & Content (1998).

trograph and arranged in a horizontal array. The main weak point of this method is the fact that the spatial sampling is not contiguous because of the fibres having gaps between them. This is the main reason for combining the fibre-fed IFU with lenslets positioned before the fibres, such that the light collected from the fibres comes from the contiguous sampling of the lenslets. Examples for this are GMOS on Gemini (Hook et al., 2004), the Very Large Telescope (VLT) VIMOS IFU (Le Fèvre et al., 2003), and INTEGRAL on the William Herschel Telescope (García-Lorenzo et al., 2000).

In *image slicers* the light collected by the telescope is directed onto a segmented mirror, where each mirror segment is positioned at slightly different angles and the slices of the image are therefore sent into different directions. Through a second mirror the slices are rearranged onto a rectangular field. In this case, the spatial sampling is however limited to that of the telescope. Also, the designs tend to be bulky and difficult to combine with existing spectrographs. Examples for this are SINFONI on the VLT (Eisenhauer, 2003) and NIFS for Gemini (McGregor et al., 2003).

Integral field units are not the only instruments capable of integral field spectroscopy. Because of their capability of producing a spatially measured 2-dimensional image at a single wavelengths, one can use Fabry-Perot instruments to scan through a wavelength range and therefore obtain the 3-dimensional data cube. Despite the fact that high angular and spectral resolution can be obtained by Fabry-Perot scanning, the main disadvantages are the necessary telescope time, the restricted wavelength range and the difficulties posed by the data reduction. Another technique is offered by *multi-object spectroscopy*, in which IFS is obtained by imaging

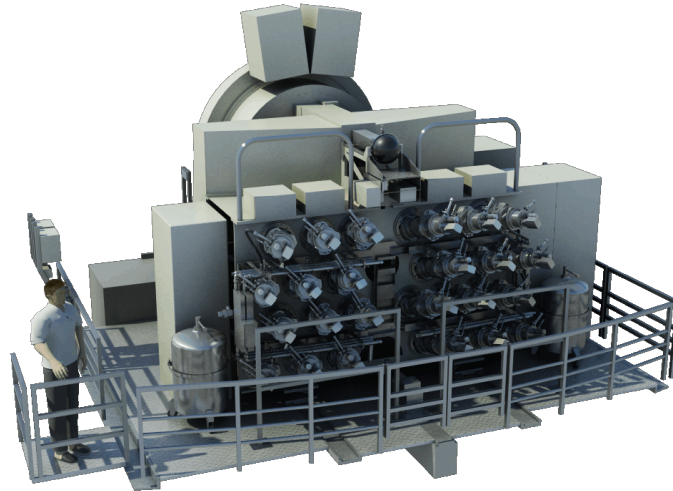


Figure 1.6: A 3D rendering of the instrument MUSE mounted on the VLT. Image credit: ESO.

multiple small targets over the instrument's field of view, and the spectra are typically obtained via fibres or fibre/lenslet combinations. An example for a multi-object spectrograph is KMOS on the VLT, which will be discussed separately later in this section.

1.3.3 MUSE: the *Multi Unit Spectroscopic Explorer*

The *Multi Unit Spectroscopic Explorer* MUSE (Bacon et al. 2014, Fig. 1.6) is an integral field spectrograph based on image slicing mounted on the VLT in Paranal, Chile. It is composed of 24 IFU modules on a 1×1 arcmin field of view in the Wide Field Mode (WFM). MUSE can also operate in a Narrow Field Mode with a small field of view of about 7.4×7.4 arcsec and a spatial sampling of $0.025''$ per pixel, but this mode is not yet being offered, and it is therefore not discussed in this thesis. MUSE covers almost the entire visible wavelength range between 4800 \AA and 9300 \AA , a resolving power of 1770 and 3590 at the blue and red end respectively, and a spectral sampling of $0.2''$ per pixel. The main characteristics of MUSE are reported in Table 1.1.

The instrument encompasses four main components: a *calibration unit*, which holds a set of calibration lamps used for the wavelength calibration of MUSE; the *fore optics* which adapt and resize the incoming image from the telescope to be projected on the splitting system; the *splitting and relay optics*, responsible for dividing the field of view into 24 horizontal sub-fields to be fed to the IFUs; and the single 24 IFUs which slice the image into 48 slices each, run these slices through a spectrograph and send these to a detector. The detectors onto which

Table 1.1: Technical specifications of MUSE for the Wide Field Mode, table adapted from the MUSE User Manual.

No. of IFU modules	24
Wavelength range	4800 - 9300 Å (nominal mode) 4650 - 9300 Å (extended)
Spatial pixel scale	0.2" / pixel
Spectral sampling	0.125 nm / pixel

the single 24 spectrographs send the light have about 4000 × 4000 pixels and a pixel size of 24 μm . The image reconstruction then occurs in the data reduction pipeline. A schematic view of the image splitting and slicing of MUSE is shown in Fig. 1.7. As the technical description of the single electronics and optics which make up these four main components is beyond the scope of this thesis, the interested reader is referred to the MUSE User Manual available on the website of the European Southern Observatory[†].

With its unique capabilities in terms of simultaneous spatial and spectral resolution, MUSE was designed to tackle questions from numerous research fields, such as the formation and evolution of galaxies, nearby galaxies, stars and resolved stellar populations, supermassive black holes in nearby galaxies, the early stages of stellar evolution and studies of the Solar System. Since its first light at the end of January 2014, MUSE quickly became one of the most requested VLT instruments, and for the instrument's science verification run, a total of 50 proposals were allocated time in the period June 20th to 29th, 2014. Examples of the scientific highlights obtained with MUSE are the detection of gas which is being stripped from its galaxy as the latter moves towards a galaxy cluster (Fumagalli et al., 2014); a 3D view of the *Hubble* Deep Field South (Bacon et al., 2015) in which the authors compute redshifts for the detected galaxies, identify previously undetected Ly α -emitting galaxies and exploit the 3-dimensional properties of the data to disentangle background-confused sources; the first observations of interacting dark matter halos (Massey et al., 2015); and the 3-dimensional analysis of the iconic Pillars of Creation in M 16, which demonstrated the capability of MUSE of yielding new insights even to well studied star-forming regions (published in McLeod et al. 2015, to appear in the ESO Annual Report 2015, described in Chapter 3).

Many star-forming regions, especially those at very early stages of their evolution, are still shrouded in the molecular cloud they originally formed from, and due to the subsequent high extinction towards these regions, it is almost impossible to observe them in the optical wavelength regime. However, when the young stars have started to clear away the surrounding matter, expose the stars and star clusters formed, and inflated HII regions, MUSE becomes a powerful tool in characterising these regions in terms of physical parameters and kinematics of the ionised and atomic gas. Indeed, MUSE covers all of the main ionised emission lines in the optical regime (i.e. H β , [OIII] λ 4959,5007, [SII] λ 6717,31, [SIII] λ 9069, [NII] λ 6548,84, [OI] λ 6300, [OII] λ 7320,30) which can be used to compute physical parameters such as the interstellar extinction and electron temperature and density, but also to derive the the kinematics

[†]<https://www.eso.org/sci/facilities/paranal/instruments/muse/doc.html>

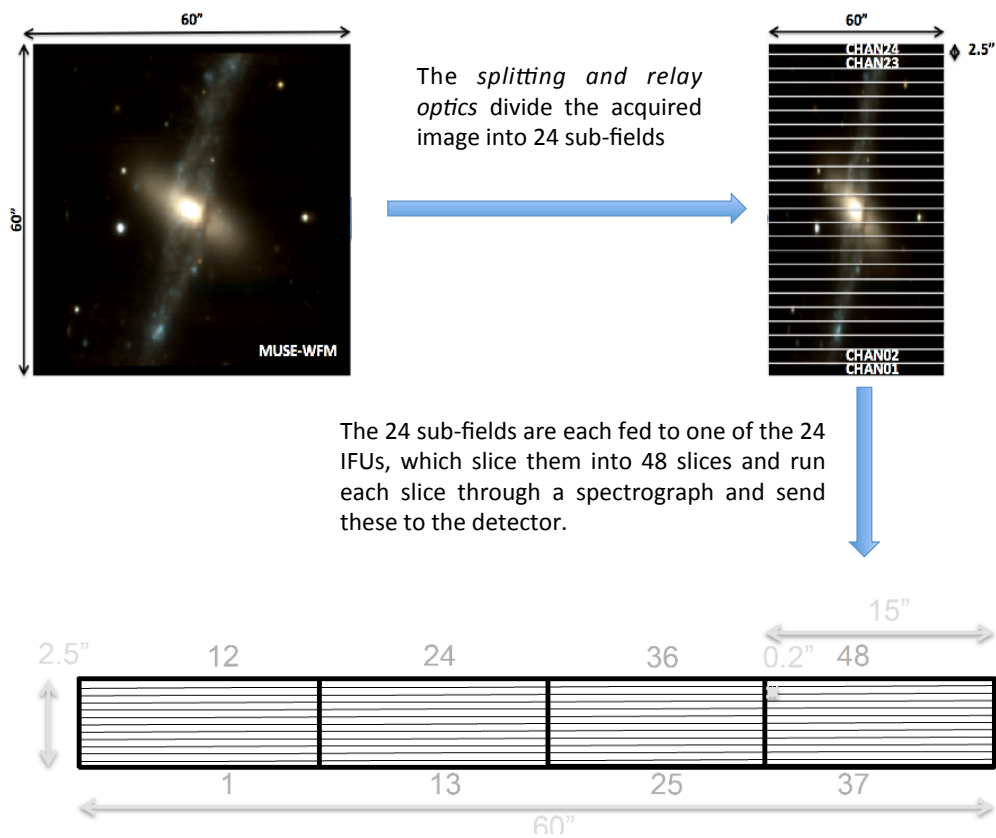


Figure 1.7: Illustration of the MUSE image splitting and slicing, adapted from the MUSE User Manual. See text Section 1.3.3.

Table 1.2: Technical specifications of KMOS, table adapted from the KMOS User Manual.

No. of IFU modules	24
Wavelength range	0.8 - 2.5 μm
Spectral bands	IZ, YZ, H, K, HK
Spatial pixel scale	0.2" / pixel

of the different stages of the ionised gas components (see Chapters 2, 3 and 4).

MUSE observations of Galactic and extragalactic HII regions already delivered new insights in open questions in the field of star formation and feedback in general, such as whether feedback mechanisms can actively trigger the formation of new stars, the dependence of star-formation feedback on physical parameters in HII regions across entire galaxies, the connection between the feedback-driving massive stars and the surrounding affected gas. Examples of extragalactic star formation observations with MUSE are (i) Cresci et al. (2015), who analyse the ionised gas in the central region of the Seyfert galaxy NGC 5643; these authors identify HII regions at the terminus of an outflow originating from the nuclear region of the galaxy, and suggest that the star formation that lead to these HII regions was triggered by the compression of matter due to the nuclear outflow, yielding the first hint at feedback-induced star formation in such an environment; (ii) by imaging the spiral galaxy NGC 6754 with MUSE, Sánchez et al. (2015) obtain a complete census of HII regions in the galaxy, which was used to derive the distribution of electron densities and oxygen abundances across the entire galaxy. These observations are extremely valuable, as they are a first step to understanding how star formation feedback depends on the physical parameters of the star-forming regions (see also Section 1.4.1).

Examples of Galactic observations of star-forming regions are Weilbacher et al. (2015), McLeod et al. (2015) and McLeod et al. (2016), where the first presents the MUSE commissioning data of the central part of the Orion Nebula, and the latter two represent the first Galactic star formation analyses works derived from MUSE data. These will be presented in Chapters 3 and 4.

1.3.4 KMOS: the *K-band Multi Object Spectrograph*

The technical setup of the *K-band Multi Object Spectrograph* (also mounted on the VLT) differs slightly from that of MUSE, where the entire field of view is imaged and subsequently divided into 24 sub-fields which are fed to the 24 IFUs: indeed, KMOS has 24 configurable arms (shown in Fig. 1.8) which can be positioned throughout the field of view and which therefore directly pick the 24 sub-fields. The most important specifications of KMOS are listed in Table 1.2. The pick-off arms, which are set out in two different planes of 12 arms each to avoid interference between adjacent arms, contain the relay optics, which feed the acquired and adjust images to the 24 IFUs. These slice the 24 sub-fields into 14 slices each, which are then reformatted into a single slit and fed in 3 groups to the three spectrographs, which in turn send the light to the three identical detectors of the instrument. The five offered gratings (see Table 1.2) are mounted on a wheel and can be switched according to user needs.

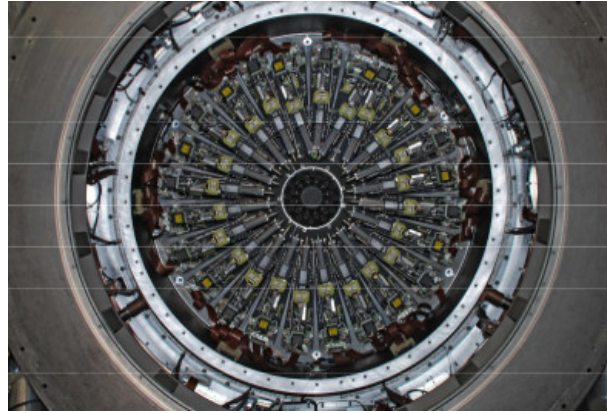


Figure 1.8: The 24 pick-off arms of KMOS mounted on the VLT. Image credit: ESO.

Each of the 24 pick-off arms has a field of view of 2.8×2.8 arcsec, and KMOS can be used either as a single-pointing instrument, where each arm covers a source across the retarget field, or in mosaic mode. The mosaic mode has two different setups, a large mosaic of 16 pointings or a small mosaic of 9 pointings, with which rectangular fields of 64.9×43.3 and 32.5×16.3 arcsec can be covered. KMOS also allows these rectangular fields to be combined as a mosaic.

First light on KMOS occurred on November 21st, 2012. Since then, KMOS has been exploited for projects across many different research fields, ranging from star formation to high-redshift galaxies. By combining deep KMOS observations of over 200 star-forming galaxies in a redshift range from 0.6 to 2.6 with molecular gas (carbon-monoxide) observations, Wuyts et al. (2016) find that the baryonic matter fraction in the inner parts of the galaxies increases with redshift, and that at $z \sim 2$ galaxy disks tend to be baryon-dominated. These findings are of great importance for galaxy formation and evolution models, as the baryonic mass fraction is well constrained for the local Universe but less so for higher redshifts, and connecting these yields information on mass growth with cosmic time. Another representative use of KMOS is presented in Gazak et al. (2015), where about 30 red supergiants in the nearby star-forming galaxy NGC 300 were targeted in the J-band: by analysing the spectra, these authors determine the metallicity distribution of the galaxy, yielding important insight on the chemical enrichment of NGC 300. In Feldmeier-Krause et al. (2015) KMOS data is used to extract spectra of early-type stars of the Milky Way nuclear star cluster; the main results of this study show that the young stars at the centre of our Galaxy are found in a compact distribution, indicating that these most probably formed *in situ*, contradicting a scenario in which gas migrated to the Galactic centre from larger radii.

For the scope of this thesis, KMOS delivers observations of the younger and still embedded sources which cannot be observed in the optical with MUSE: with KMOS we target massive star-

forming regions in which the stellar population has not yet fully emerged from the natal molecular cloud. As will be discussed in Chapter 6, by combining the MUSE and KMOS observations with far-infrared and radio data it is possible to construct a timeline of the evolution of molecular clouds, from young, collapsing clouds in the radio/mm regime to exposed star clusters and HII regions in the optical. The K-band grating of KMOS is of particular interest, as both emission lines from the ionised as well as the molecular gas components are covered in this band, detected i.e. via the Brackett- γ and excited H₂ lines.

1.4 The role of this thesis

1.4.1 Open questions and scope of the thesis

As discussed above, from simulations of massive star-forming molecular clouds (MCs) that include FB recipes, a quantification of the star formation FB mechanisms is possible, and their qualitative morphological predictions are in agreement with observations. But, while the simulations become more realistic, they still fail to reproduce the observed star formation efficiencies and rates, and to date no simulation includes all the fundamental physics of star formation. From an observational point of view, the quantification of star formation FB is one of the greatest challenges of modern astronomy, as on small scales the FB-affected environments and the FB-driving stars need to be directly related to one another, and on large scales the impact of FB on galaxy evolution needs to be addressed. To date, the main open questions in the field of FB in massive star formation are:

1. what are the dominant feedback mechanisms, and can they be quantified?
2. how does this role change when the perspective changes from small (cloud) scales to large (galactic) scales?
3. what is the role feedback from massive stars plays in regulating star formation?
4. how does the effect of FB depend on the physical properties of star forming regions?

Answering all of these questions would require a lifetime of studies, large collaborative efforts and both new observational and new theoretical approaches working strictly hand in hand. However, with the advent of new observational techniques made possible by integral field spectroscopy, it is possible to start tackling these questions, starting from the very basics. The research presented in this thesis exploits these new integral field instruments, which have the unique advantage of offering both spectrally and spatially measured observations, with *the main aim being the determination and quantification of the link between ionising feedback from massive stars and the disruption of the nearby molecular clouds via ionisation-induced photo-evaporation*. This research is meant to set the ground for future observational investigations, in which the quantification of the effect of ionising FB will be extended to the other previously discussed FB mechanisms. As will be discussed in Chapter 6, observational campaigns to lead research in tackling the effects of FB mechanisms other than ionisation have already been planned and

started, such as a large campaign targeting a sample of HII regions in the Large Magellanic Cloud. With these observations, the relative importance of ionising FB to supernovae FB will be quantified. The question this thesis is designed to answer therefore is: **is it possible, with the unprecedented spatial and spectral coverage of integral field spectroscopy, to quantify the effects of ionising feedback and therefore deliver a quantitative observational study of high-mass stellar feedback?** This question will be tackled by observing HII regions and the FB-driven structures within these with the integral field spectrograph MUSE and by subsequently comparing the results for each of these regions to each other to sample FB in a variety of different environments and conditions.

1.4.2 Structure of the thesis

After describing the physical backgrounds of ionising feedback (Chapter 2), this thesis is divided into four main parts. In the first part, Chapter 3, we present the observational setup required to answer the main question this thesis aims to address. In this observational setup we cover the Pillars of Creation in the Eagle Nebula (M 16) with MUSE, and develop the data reduction and analysis methods used for the following analyses which will lead to the ultimate results. In the second part, Chapter 4, the observational setup and analysis techniques are tested by observing one of the most observed and best studied objects in the sky: the Orion Nebula. With the firm observational and analytical background obtained in these first two steps, the acquired skills are used in the third part of this thesis (Chapter 5) to determine an observational quantification of the effects of ionising feedback. The fourth part of the thesis (Chapter 6) then gives an outlook onto the natural evolution this groundbreaking, preliminary work, towards the use of the gained expertise to tackle the main open questions in the field of massive star formation feedback posed in Section 1.4.1. A summary and the main conclusions are given in Chapter 7.

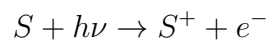
2

Feedback analysed in this thesis: ionisation and HII regions

The term *ionisation* stands for the physical process in which atoms and molecules acquire an electrical charge due to gain or loss of electrons. This effect is anything but rare, and technology exploits it widely, for purposes ranging from illumination to medical treatments. In nature, we experience ionisation e.g. during thunderstorms or aurorae. In astrophysical terms, this effect occurs when gas is exposed to strong ionising radiation, which can be the case e.g. in star-forming regions, active galactic nuclei or X-ray binaries. For the purpose of this thesis, the interest lies in ionisation occurring in HII regions, where massive stars have been formed and ionise their surrounding molecular clouds. The effect of photoionisation in HII regions is that of heating and eroding the neutral and molecular material via photo-evaporation. This effect, if strong enough, therefore destroys molecular clouds and could lead to their disruption. The process of photo-evaporation will be discussed in Section 2.2 after a brief physical description of the process of ionisation in Section 2.1, and followed by a description of the computation of the main physical parameters of HII regions will be given in Section 2.3.

2.1 A brief theoretical overview

Through the process of ionisation atoms or molecules acquire or lose an electron by interaction with light or via collisional processes to form an ion, which can be positively or negatively charged. The astrophysical mechanism of interest for this thesis is photoionisation: the formation of ions via the interaction of atoms or molecules with photons. The probability of an atom/molecule to be photoionised is given by the photoionisation cross-section, which relates the energy of a photon to the target particle: a photon can only ionise the particle if its energy is greater than the energy needed to strip an electron from the target particle. Typically, photoionisation of an atomic or molecular species S can be written as



where $h\nu$ is the energy of the incoming photon and e^- the free electron produced by the interaction. Therefore, ionisation only occurs if $h\nu > E_{\text{ion}}$, where E_{ion} is the ionisation energy of the species S .

Photoionisation is the mechanism which couples the ISM gas to the radiation field the ISM matter is exposed to, and it is the principal heating mechanism, as the emitted electron carries away a part of the incident photon's energy and transfers it to the surrounding gas. In this thesis photoionisation in HII regions is considered, in which the dominant species being ionised consists of course of hydrogen atoms. In other regions, such as neutral HI regions, gas heating is dominated by ionisation of dust grains and molecules. When considering a mean photon-intensity $N(\nu)$, the photoionisation cross-section of hydrogen $\sigma(\nu_{\text{H}})$ and the ionisation energy of hydrogen $h\nu_{\text{H}^0}$ ($= 13.6$ eV), the average energy carried away by the liberated electron that heats the gas then equals

$$\frac{3}{2}kT_{\text{H}} \int_{\nu_{\text{H}}}^{\infty} N(\nu)\sigma_{\text{H}}(\nu)d\nu = \int_{\nu_{\text{H}}}^{\infty} N(\nu)\sigma_{\text{H}}(\nu)h(\nu - \nu_{\text{H}})d\nu$$

where the integral over the frequency represents the heating term. If T_{eff} is the effective stellar temperature, then typically $T_{\text{H}} \simeq 0.5 - 0.7 T_{\text{eff}}$ (Tielens, 2010). The redistribution of the energy carried away by the electron heats the gas, and thermal electrons can excite the ISM species which will lead to cooling via radiative transitions.

In HII regions, photoionisation is balanced by recombination (*photoionisation equilibrium*), and heating due to photoionisation is balanced by cooling (*thermal balance*). To understand the physics governing ionised HII regions, it is therefore important to understand these two processes, and a simple consideration is made in the next two sections in the simplified case of a nebula consisting only of hydrogen atoms.

2.1.1 Ionisation and recombination

If J_{ν} is the ionising photon flux, $\sigma_{\nu} \approx \sigma_0(\nu/\nu_0)^{-3}$ the ionisation cross-section of hydrogen (with $\sigma_0 = 6 \times 10^{-18}$ cm² the ionisation cross-section of neutral hydrogen in the ground state) and n_{H} the volume density of hydrogen atoms, then the rate per unit volume at which ionisation occurs is given by

$$n_{\text{H}^0} \int_{\nu_0}^{\infty} \frac{4\pi J_{\nu}}{h\nu} \sigma_{\nu} d\nu \quad (2.1)$$

where hydrogen can only be ionised if $h\nu > 13.6$ eV. Likewise, the rate per unit volume at which hydrogen atoms are recombined is given by

$$n_{\text{e}}n_{\text{p}}\alpha(T) \quad (2.2)$$

where n_{e} and n_{p} are the densities of electrons and protons respectively, and α the temperature-dependent recombination coefficient. The electron and proton densities are related to the density of neutral hydrogen n_{H} via the *hydrogen neutral fraction* ξ , therefore the degree of ionisation: $n_{\text{e}} = n_{\text{p}} = (1 - \xi)n_{\text{H}}$, with $\xi n_{\text{H}} = n_{\text{H}^0}$, and in this parametrisation the matter is fully ionised if $\xi = 0$ and fully neutral if $\xi = 1$. The **photoionisation equilibrium** is therefore

given by setting the two rates equal,

$$\xi n_{\text{H}} \int_{\nu_0}^{\infty} \frac{L_{\nu}}{4\pi r^2} \frac{\sigma_{\nu}}{h\nu} d\nu = (1 - \xi)^2 n_{\text{H}}^2 \alpha(T) \quad (2.3)$$

where the ionising photon flux from an ionising star at a distance r is related to the luminosity of a star and given by

$$4\pi J_{\nu} = \frac{L_{\nu}}{4\pi r^2}$$

The ionisation balance of Equation 2.3 is of great importance, as it determines the ionisation fraction and therefore the structure of the ionised nebula. This becomes clear when inserting example values and working out a numerical solution for a hydrogen nebula with a density of $n_{\text{H}} = 10 \text{ cm}^{-3}$ at a distance $r = 5 \text{ pc}$ from an ionising star of spectral type O6.5V ($T_{\star} \approx 4 \times 10^4 \text{ K}$)*. In this case, the nebula is almost fully ionised, the neutral fraction is very small, and the mean free path of an ionising photon is

$$l_{\nu_0} = \frac{1}{\sigma_{\nu_0} n_{\text{H}^0}}$$

meaning that at the location where 50% of the matter is neutral ($\xi = 0.5$), $n_{\text{H}^0} = \xi n_{\text{H}} = 5 \text{ cm}^{-3}$, yielding $l_{\nu_0} \approx 3 \times 10^{16} \text{ cm} \approx 0.01 \text{ pc}$. The mean free path, which sets the transition region between neutral and ionised matter, is (in this case) only $0.01/5 \approx 0.2\%$ of the size of the nebula, implying very sharp transition regions (ionisation fronts).

HII regions do not consist of pure hydrogen. Enrichment by previous stellar populations leads to heavier elements being present, prevalently helium, carbon, nitrogen, oxygen, neon, iron and silicon. The ionisation equilibrium is therefore rewritten in consideration of every species X^s , relating its number density to that of the next highest ionisation state X^{s+1} , with a recombination coefficient α_{G} as

$$n(X^s) \int_{\nu_0}^{\infty} \frac{4\pi J_{\nu}}{h\nu} a_{\nu}(X^s) d\nu = n(X^{s+1}) n_e \alpha_{\text{G}}(X^s, T) \quad (2.4)$$

Because of their low abundances, heavy elements do not contribute significantly to the opacity of the nebula, and the liberated electrons mainly originate from hydrogen atoms (this is not the case for the high-density stellar atmospheres, where the presence of the metals needs to be taken into consideration when modelling the radiative transfer of these regions). Furthermore, dust does affect the optical depth and therefore the radiation field and structure of the nebula, as it absorbs radiation and therefore needs to be taken into account when considering the ionisation equilibrium. By absorbing photons, dust grains are heated and subsequently emit far-infrared continuum photons which escape the nebula. However, dust grains can also be photo-evaporated in the case of radiation from very hot O-type stars, liberating otherwise frozen-out heavy elements and molecules into the gas phase.

*For this simple quantification of ionisation, the assumption was made that all photo-ionising events occur from hydrogen atoms in the ground state, without considering ionisation from higher excitation states (*nebular approximation*). This approximation is quite good, since the lifetimes of the higher excited states is much smaller than the photoionisation time, which leads to the ground state being the dominant state for ionisation.

2.1.2 Heating and cooling

Ionisation is the main heating source in HII regions. As for the previous discussion, a first approach is made considering a pure hydrogen nebula, and the heating rate per unit volume due to photoionisation is given by

$$G(H) = n_{\text{H}} \int_{\nu_0}^{\infty} \frac{4\pi J_{\nu}}{h\nu} h(\nu - \nu_0) a_{\nu}(H) d\nu$$

where the term $h(\nu - \nu_0)$ represents the energy input per ionising event. With equations 2.1 and 2.2, the heating rate per unit volume can be written as

$$G(H) = \frac{3}{2} k T_i n_e n_p \alpha(H, T)$$

with T_i the initial (non-thermalised) electron temperature.

Cooling can occur in several different ways: cooling by *recombination*, cooling by *free-free emission*, and cooling via *collisionally excited line emission*. Recombination cooling involves a free electron recombining with a proton to form atomic hydrogen under emission of a photon which carries away part of the energy. The recombination cooling rate will be proportional to a recombination coefficient which depends on the relative velocities of the recombining electron and proton. Free-free cooling is obtained when a thermal electron is scattered by an ion and subsequent emission of radiation in the radio regime (i.e. Bremsstrahlung). The energy that can be removed by free-free emission depends on the nuclear charge of the scattering ion, as well as on the density of ions. Cooling via collisionally excited line emission is the dominant cooling mechanism, and it is mediated via ions of the heavy elements present in the nebula which have excitation energies of the order of the energy of the thermal electrons. The impact of the thermal electrons with ions leads to an excited ionic state, whose re-radiation cools the gas. The efficiency of this process leads to the fact that lower metallicity nebulae have higher temperatures, since the elemental abundances are lower and therefore collisionally excited cooling is less efficient.

Without going into details (a thorough explanation is given in Tielens 2010), **thermal equilibrium** is therefore reached when the heating rate G equals the sum off all cooling contributions

$$G = L_{\text{R}} + L_{\text{ff}} + L_{\text{C}} \quad (2.5)$$

where L_{R} , L_{ff} and L_{C} are the cooling rates for recombination, free-free emission and collisional excitation. The important information obtained from this is that the temperature of a nebula is therefore dependent on (i) the density of electrons and the various species; (ii) the initial photon input from the radiating source; (iii) the elemental abundances; (iv) and the presence of dust. These factors need to be taken into account when modelling the radiative transfer of HII regions. For this thesis, together with the ionisation balance from the previous section, this is an important aspect to grasp, since a preliminary and qualitative comparison with radiative transfer post-processed simulated HII regions will be performed (see Chapter 3), and a thorough quantitative comparison is part of ongoing work (see Chapter 6). Furthermore, understanding how ionised nebulae are cooled helps in understanding their characteristic optical

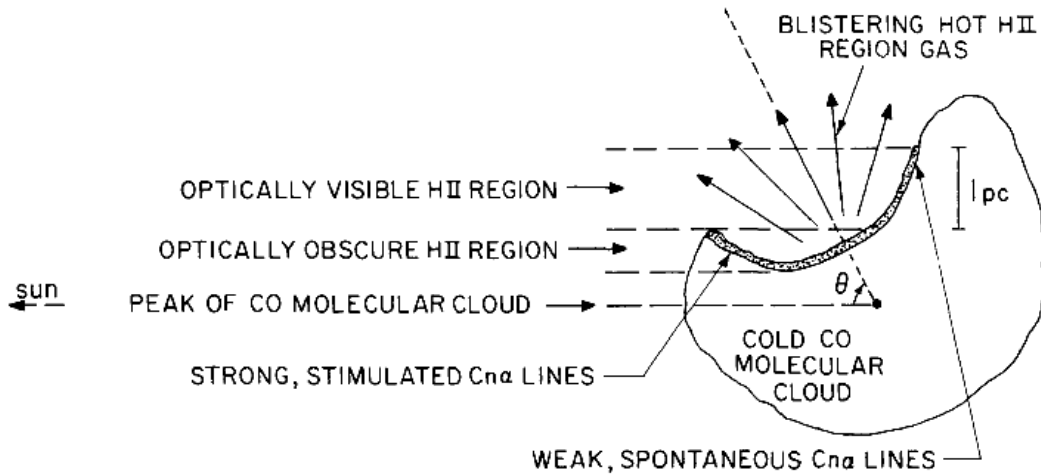


Figure 2.1: Sketch of a blister-like HII region showing the hot, ionised gas streaming out of an opening of the HII region. Image from Vallee (1987).

spectra analysed in this thesis, as these will be dominated by recombination and collisionally excited lines.

2.2 Photo-evaporation of molecular clouds due to ionisation

The effect of ionising radiation from O-type stars on the surrounding ISM has been subject to pioneering works such as that by Oort & Spitzer (1955), in which the “rocket effect,, of the asymmetrically off-streaming gas would cause a small cloud to accelerate away from the ionising source while losing mass. Later works found that photo-evaporation of large clouds would lead to the so-called *champagne flow* (Tenorio-Tagle, 1979) or *blister HII region* models (Icke, 1979), in which ionised gas escapes from the FB-driven cavity in a flow-like manner (see Fig. 2.1).

The incident extreme-ultraviolet radiation (EUV, $h\nu > 13.6$ eV) from the nearby stars ionises the gas, while the far-ultraviolet photons (FUV, $6 < h\nu < 13.6$ eV) heat and pressurise the gas at the surface layers of the surrounding clouds, which consequently expands and streams away from the cloud surfaces. The off-streaming gas can then be ionised by the EUV field, leading to an ionised photo-evaporation flow. On GMC scales, the general effect of photo-evaporation might lead to the destruction of potentially star-forming cloud clumps and cores, therefore suppressing star formation; on smaller scales, star-forming molecular cores might be stripped off their outermost envelope, therefore limiting the mass of the forming star, while shocks driven into a cloud could lead to gravitational collapse and therefore trigger star formation (Gorti & Hollenbach, 2002).

A thorough analytical picture of cloud ionisation and photo-evaporation by EUV photons

is given in a series of two papers by Bertoldi (1989) and Bertoldi & McKee (1990). These authors analyse the evolution of a neutral cloud which is being ionised by a young OB-type star. They find that (i) the ionised gas expands into the HII region with $v > c_s$ (where c_s is the ionised gas sound speed); (ii) the ionisation front drives a shock into the neutral cloud material, compressing it and shaping it into cometary-shaped (or globule-like) structures; (iii) the evolution of the neutral cloud is set by the initial column density and the local ionisation parameter; (iv) the cometary-shaped cloud will accelerate away from the ionising source as a consequence of the rocket effect. In a more recent analytical work, Gorti & Hollenbach (2002) study the effect of different FUV fields varying in strength on molecular clumps of different sizes to determine their lifetimes and structural evolution via hydrodynamical calculations. They find that the FUV photons induce photo-evaporation of the surface layers of the analysed clumps. The evolution of their cloud clumps depends on the initial column density, the strength of the FUV field and the ratio of the timescale for the FUV field to be turned on and the sound crossing time of the clump. The timescales for photo-evaporation found by these authors are typically $10^4 - 10^5$ yr.

Observations of photo-evaporative flows are numerous. A prime example are the iconic Pillars of Creation in the Eagle Nebula (M 16), imaged by the *Hubble Space Telescope* (HST) and analysed in Hester et al. (1996) (and later in McLeod et al. 2015, see Chapter 3). Hester et al. argue that the fact that the photo-evaporative flow is perpendicular to the pillar surface indicates that the pressure gradient driving the flow does not depend on the direction of the incident radiation, nor on the orientation of the pillars, resulting in flow dynamics which are independent of the interaction of the flow with the ambient HII region matter. They also find a stratified ionisation structure at the pillar/ambient interface (a well known phenomenon generally observed at ionisation fronts, e.g. Hester et al. 1991, Scowen et al. 1998, O'Dell et al. 2001, McLeod et al. 2016), interpreting this as a photo-evaporative flow which is being ionised as it streams off the pillars. Because of the stratification being observed throughout ionisation fronts in HII regions, the authors also argue that the emission coming from the photo-evaporative flow might dominate the optical emission from the HII region.

Observations of photo-evaporative flows have been used by many authors to estimate the mass-loss rate and remaining lifetime of the ionised gas structures, in various different ways. For example, Pound (1998) use a geometrical approach in which the ionised tips of pillar-like structures are treated as half spheres with surface area $2\pi r^2$ and assuming that these are composed of hydrogen and lose mass at a velocity corresponding to the isothermal sound speed in the ionised gas. They determine the mass-loss rate of the M 16 pillars as

$$\dot{M} = 2\pi r_c^2 c_i m_p n_i$$

where r_c is the curvature radius of the pillar tips, c_i the isothermal sound speed, m_p the proton mass, and n_i the volume density. Westmoquette et al. (2013) use the numerically-derived expression given in Lefloch & Lazareff (1994),

$$\dot{M} = 10.4 \left(\frac{\Phi}{10^7 \text{cm}^{-2} \text{s}^{-1}} \right)^{1/2} \left(\frac{r}{1 \text{pc}} \right)^{3/2} \text{M}_\odot \text{Myr}^{-1}$$

where Φ is the ionising photon flux at the pillar tip and r the radius of the pillar tip. As will be discussed in Chapter 3, a further method consists in computing the mass of the [SII] emitting matter, M_{SII} , and compute the mass-loss rate as

$$\dot{M} = \frac{M_{SII}v}{l}$$

where l is the size of the line-emitting region and v the velocity of the photo-evaporative flow. In this last method, the fact that the [SII] line is optically thin is used to compute the mass of the matter being ionised at the pillar tips by exploring the proportionality between the line-luminosity and number of line-emitting atoms along the line of sight. For details, see Hartigan et al. (1995) and Chapter 3.

2.3 Diagnostics of ionised HII regions

The spectra of HII regions are dominated by hydrogen (and helium) recombination lines, as well as collisionally excited emission lines from the main heavy elements (e.g. oxygen, sulphur, nitrogen, argon, silicon, iron, chlorine). The emission from each species depends on their abundance (and therefore on the star formation history) and on the radiation field of the region. Most of the relevant emission lines used to determine physical parameters such as temperatures and densities are in the optical and near-infrared regime, but the spectra of ionised nebulae span the entire electromagnetic spectrum. As discussed earlier, hydrogen recombination lines arise from the downward cascades of electrons from excited levels (initiated by recombination of a proton and an electron into a higher level) into the ground level via emission of photons. Collisionally excited lines (also called forbidden lines[†]) arise when collisions between ions and thermal electrons excite ionic electrons into energy levels within a few eV from the ground state.

A brief description of the computation of the main physical parameters from the emission lines in the optical spectra of HII regions is given here. These methods will be used later on in this thesis for the analysis of the observed regions.

2.3.1 Extinction

An important factor to determine when studying ionised nebulae is the level of extinction, i.e. the amount of radiation that is absorbed by the ISM lying between the source and the observer. Dust scatters the light coming from the observed source along the line of sight, and because in this process the shorter wavelengths are scattered more than the longer wavelengths, the observed source appears *redder* than it intrinsically is. Prior to the computation of physical parameters from the emission lines in the observed spectra, it is therefore imperative to correct these for extinction.

[†]Historically, these lines are called forbidden because they are not allowed by the common selection rules for normal transitions that occur e.g. via absorption of a photon. However, they do not arise via photon absorption, but via collisions between ions and thermal electrons, and the energy levels so populated can only be populated by collisional excitation.

If I_{λ_0} is the intensity of the light emitted at the source, then dust reduces the light coming from a source according to

$$I_{\lambda} = I_{\lambda_0} \exp(-\tau_{\lambda})$$

and τ_{λ} is the optical depth. Empirical measurements showed that $\tau_{\lambda} = Cf(\lambda)$, where $f(\lambda)$ is the wavelength-dependent extinction curve and C a constant factor. The intensity ratio of two emission lines then becomes

$$\frac{I_{\lambda_1}}{I_{\lambda_2}} = \frac{I_{\lambda_1,0}}{I_{\lambda_2,0}} \exp[-(\tau_{\lambda_1} - \tau_{\lambda_2})] = \frac{I_{\lambda_1,0}}{I_{\lambda_2,0}} \exp[-C(f_{\lambda_1} - f_{\lambda_2})]$$

The determination of interstellar extinction of ionised nebulae is, in the optical regime, usually done via the so-called *Balmer decrement*, where the ratios of the main hydrogen Balmer lines (i.e. those originating from the downward cascade and emission of a photon from higher energy levels to the second level) are exploited to determine the amount of extinction. The theoretical value of $I_{H\alpha,0}/I_{H\beta,0}$ is known and approximately equal to 2.86 for $T = 10^4$ K and $N_e = 10^4 \text{ cm}^{-3}$, and with an empirically measured extinction curve one can determine C and therefore apply an extinction correction to all the observed emission lines. For the Milky Way, the generally used extinction curve is used such that $f_{\lambda_1} - f_{\lambda_2} = -0.35$ (Osterbrock, 1989).

2.3.2 Temperatures

The fact that some ionic species (e.g. [OIII], [NII]) show emission lines in the optical regime which originate from different energy levels can be exploited to determine the temperature of the nebula, as the population of these energy levels strongly depend on temperature. Fig. 2.2 shows the energy level diagrams of [OIII] and [NII]: the relative rates of the different energy levels, e.g. the 1S level which gives rise to the [NII] $\lambda 5755$ line and the 1D level which gives rise to the [NII] $\lambda 6548$ line, depend on the temperature, and the relative strengths of the emission lines from the two levels can therefore be used as a temperature probe, as long as the density is $< 10^5 \text{ cm}^{-3}$ and collisional deexcitation is negligible.

Since the downward transitions from the 1S and 1D levels to the 3P levels depend on their transition probabilities, the ratio of the emissivities can be written as

$$\frac{j(^1D - ^3P_1) + j(^1D - ^3P_2)}{j(^1S - ^1D)} = \frac{\gamma(^3P, ^1D)}{\gamma(^3P, ^1S)} \left[\frac{A_{1S,1D} + A_{1S,3P}}{A_{1S,1D}} \right] \frac{\bar{\nu}(^3P, ^1D)}{\bar{\nu}(^1D, ^1S)} e^{-h\nu/kT}$$

where γ is the collision strength of the various levels, $\bar{\nu}$ the mean emission line frequency and A the transition probabilities. By inserting numerical values, the ratio of the [NII] lines is

$$\frac{j_{\lambda 6548} + j_{\lambda 6583}}{j_{\lambda 5755}} = \frac{8.23 e^{2.5 \times 10^4/T}}{1 + 4.4 \times 10^{-3} n_e / T^{1/2}}$$

where n_e is the electron density. As MUSE does not cover the [OIII] $\lambda 4363$ line, an example for the temperature determination from the [OIII] lines is not given here, for this as well as a

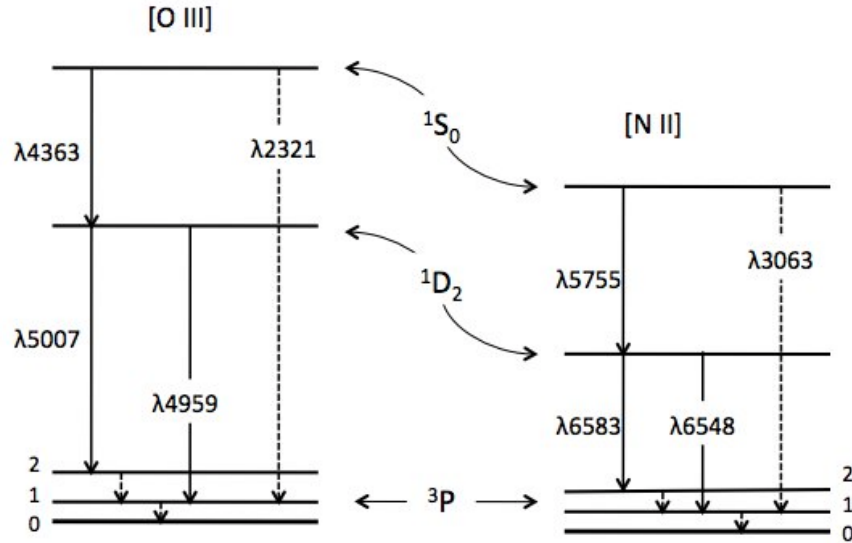


Figure 2.2: Energy level diagrams of [OIII] and [NII], from Osterbrock (1989).

full derivation, consult Osterbrock (1989). One of the major problems in the determination of the temperature via the [NII] lines is that [NII] $\lambda 5755$ is typically very faint compared to the other two nitrogen lines, and the derived errors in temperature therefore depends on the errors in determining [NII] $\lambda 5755$.

2.3.3 Densities

In a similar way to the determination of the nebular temperature, the electron density can be derived from the ratio of collisionally excited emission lines. However, what is exploited here are the intensities of emission lines which originate from transitions from energy levels with very similar excitation potentials, so that the excitation of these levels only depends on the ratio of the collision strengths. Examples for this are the [OII] $\lambda 3729, 3726$ and the [SII] $\lambda 6717, 6731$ lines, as is shown in Fig. 2.3: the energy difference between the $^2D_{3/2}$ and the $^2D_{5/2}$ is so small, the dependence on temperature is very weak, and the population of the levels only depends on the density.

Electron densities in this thesis are derived via the [SII] $\lambda 6717, 6731$ lines, while the [OII] $\lambda 3729, 3726$ lines are not covered by MUSE. If the $^2D_{5/2}$ level is labeled with the subscript 2a, and the $^2D_{3/2}$ level is labeled with the subscript 2b, the ratio of the emissivities is

$$\frac{j_{\lambda 6717}}{j_{\lambda 6731}} = \frac{n_{2a} A_{2a1} h \nu_{2a1}}{n_{2b} A_{2b1} h \nu_{2b1}} \approx \frac{n_{2a} A_{2a1}}{n_{2b} A_{2b1}}$$

Assuming a high-density gas in which collisional deexcitation from a higher energy level 2 to a lower energy level 1 is not negligible and occurs in the equilibrium $n_2(N_e q_{21} + A_{21}) = N_e n_1 q_{12}$, where q_{21} is the collisional deexcitation probability for the $2 \rightarrow 1$ transition, q_{12} the collisional

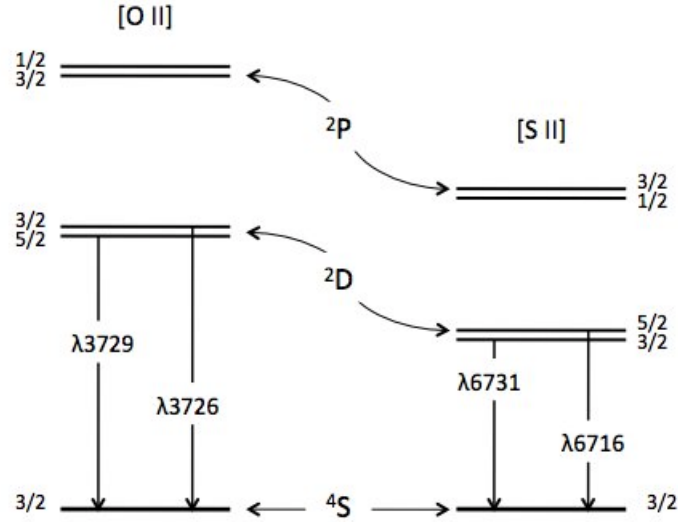


Figure 2.3: Energy level diagrams of [OII] and [SII], from Osterbrock (1989).

excitation probability for the $1 \rightarrow 2$ transition and $n_{1,2}$ the level populations. With this, the above equation becomes

$$\frac{j_{\lambda 6717}}{j_{\lambda 6731}} = \frac{q_{12a}}{q_{12b}} \times \left[\frac{1 + \frac{N_e q_{2b1}}{A_{2b1}}}{1 + \frac{N_e q_{2a1}}{A_{2a1}}} \right]$$

An analytical solution for this is given in McCall (1984), and the electron density can be calculated from the line ratio as

$$\frac{[SII]\lambda 6717}{[SII]\lambda 6731} \equiv R_{[SII]} \simeq 1.49 \frac{1 + 3.77 \times 0.01 N_e / T^{1/2}}{1 + 12.8 \times 0.01 N_e / T^{1/2}}$$

where the assumption of $T \approx 10^4$ K is made.

2.3.4 Ionic and elemental abundances

The abundance of any given species in the gas phase of a nebula is typically given relative to hydrogen. *Ionic abundances* are those tracing the relative abundances of certain ionic species (e.g. S^{++} , S^+ , O^+) relative to H^+ , which result as a consequence of the varying ionisation conditions throughout the region. The sum over the abundances of all ions of a given species yields the *total elemental abundance* relative to H (e.g. S/H , O/H). If abundances are obtained throughout star forming regions in a galaxy, abundance variations can yield insight on the chemical enrichment history of the galaxy.

Ionic abundances are traced by the ratio of the emission line of a given ionic species to that of H^+ , typically $H\beta$

$$\frac{I_{\text{ion}}}{I_{\text{H}\beta}} = \frac{\int n_e n_i \epsilon_i(T_e) ds}{\int n_e n_p \epsilon_{\text{H}\beta}(T_e) ds}$$

where n_i is the ionic density and $\epsilon_{i,\text{H}\beta}$ the emissivity of the lines, which depends on the electron temperature T_e . If it is assumed that the observed nebula is homogeneous along the line of sight, then the ionic density relative to the hydrogen density, i.e. the proxy for the ionic abundance, is simply given by

$$\frac{n_i}{n_p} = \frac{I_{\text{ion}} \epsilon_{\text{H}\beta}(T_e)}{I_{\text{H}\beta} \epsilon_i(T_e)}$$

Ionic abundances derived in this thesis rely on the homogeneity assumption. However, as will be discussed in Chapter 4, the derived ionic abundance maps (in this work for O^{++} , O^+ , S^{++} , S^+ and N^+) show a certain degree of structuring, which comes from the fact that the line ratios used to determine the abundances are sensitive to local temperature and density variations, which therefore need to be taken into account when analysing these maps.

Total elemental abundances are derived by summing over the ionic abundances of a given element. However, one must consider the fact that not all ionic species per element can be observed, and an assumption for these *unobserved* species needs to be made using an empirical *ionisation correction factor* (ICF). Oxygen is particularly abundant in ionised nebulae and several emission lines from the different ions are easily observed in the optical regime. Because of this, most ICFs rely on the ionic oxygen abundances as well as similarities of the ionisation potential E_{ion} of different species to account for the unseen ions of other elements (therefore assuming that emission lines with similar ionisation energies are produced in the same region because of the same ionising conditions). For example, $E_{\text{ion}}(\text{O}^+) = 35.1$ eV and $E_{\text{ion}}(\text{S}^{++}) = 34.8$ eV are used to correct for the unseen S^{3+} ion,

$$\frac{n(\text{S}^{++})}{n(\text{S}^{3+})} \approx \frac{n(\text{O}^+)}{n(\text{O}^{++})}$$

and the resulting total abundance of sulphur would then be

$$\frac{\text{S}}{\text{H}} = \left(\frac{\text{S}^+ + \text{S}^{++}}{\text{H}^+} \right) \times \text{ICF} \approx \left(\frac{\text{S}^+ + \text{S}^{++}}{\text{H}^+} \right) \times \left(\frac{\text{O}^+ + \text{O}^{++}}{\text{O}^+} \right)$$

Total elemental abundances in this work rely on the ICFs empirically derived in Esteban et al. (1998) for nitrogen and Hägele et al. (2008) for sulphur.

3

Observational setup: the Pillars of Creation in M 16

*Published as McLeod, Dale, Ginsburg, Ercolano et al., MNRAS, 2015, 450, 1057;
“The Pillars of Creation revisited with MUSE: gas kinematics and high-mass stellar feedback traced by optical spectroscopy”**

Abstract

Integral field unit (IFU) data of the iconic Pillars of Creation in M16 are presented. The ionisation structure of the pillars was studied in great detail over almost the entire visible wavelength range, and maps of the relevant physical parameters, e.g. extinction, electron density, electron temperature, line-of-sight velocity of the ionised and neutral gas are shown. In agreement with previous authors, we find that the pillar tips are being ionised and photo-evaporated by the massive members of the nearby cluster NGC 6611. They display a stratified ionisation structure where the emission lines peak in a descending order according to their ionisation energies. The IFU data allowed us to analyse the kinematics of the photo-evaporative flow in terms of the stratified ionisation structure, and we find that, in agreement with simulations, the photo-evaporative flow is traced by a blueshift in the position-velocity profile. The gas kinematics and ionisation structure have allowed us to produce a sketch of the 3D geometry of the Pillars, positioning the pillars with respect to the ionising cluster stars. We use a novel method to detect a previously unknown bipolar outflow at the tip of the middle pillar and suggest that it has an embedded protostar as its driving source. Furthermore we identify a candidate outflow in the leftmost pillar. With the derived physical parameters and ionic abundances, we estimate a mass loss rate due to the photo-evaporative flow of $70 M_{\odot} \text{ Myr}^{-1}$ which yields an expected lifetime of approximately 3 Myr.

*This work is the result of collaborative efforts of the authors of the paper. Specifically, I was responsible for the entire data reduction, analysis and interpretation, as well as the manuscript preparation. Furthermore, I am Principal Investigator of the observing proposal which led to the acquisition of the data. Dale, Gritschneider and Ercolano provided the radiative transfer post-processed simulations, and the other co-authors contributed with valuable insight on the interpretation of the results and in proof-reading the manuscript. This publication is accompanied by a combined ESO and Monthly Notices of the Royal Astronomical Society press release appeared on the ESO/MNRAS websites.

3.1 Introduction

Throughout their entire lifetime, massive stars influence their immediate surroundings via strong stellar winds, potent ionising radiation and powerful supernovae events. Simulations show that their feedback is responsible for clearing vast bubble-shaped gas voids, inflating expanding HII regions, exposing pillar-like dust and gas lanes and regulating the formation of new stellar populations in their surrounding natal molecular clouds (Gritschneider et al. 2010a, Peters et al. 2011, Bisbas et al. 2011, Tremblin et al. 2012, Walch et al. 2013, Dale et al. 2013a, Dale et al. 2013c, Ngoumou et al. 2015). The simplified and idealised conditions of the simulations can yield important insight on feedback mechanisms, but even the state of the art simulations fail to represent the complexity of reality, and the details of this feedback have yet to be fully understood. Furthermore, massive star formation dominates the energetics and feedback in star forming galaxies, and properly accounting for the star formation feedback is a critical ingredient of galaxy evolution models. This is the first publication from our FuSIOn (Feedback in massive star forming regions: from Simulations to Observations) study in which we seek to test the predictions of the above mentioned numerical simulations, to put better constraints on their initial conditions and to ultimately understand feedback mechanisms by comparing them with observations of high mass stellar feedback.

Pillar-like structures are a common morphological phenomenon in star forming regions where massive O- and B-type stars shape the surrounding material via ionisation and stellar winds, and they arise naturally in simulations of cluster formation and evolution that include radiative feedback (Gritschneider et al. 2010a, Dale et al. 2012a, Tremblin et al. 2012, Walch et al. 2013). Such structures are found to host young stellar objects and are observed to be between the hot and hostile environment created by massive stars and the material of the parent molecular cloud that has not yet been reached by the stellar feedback. The nearby massive stars compress, ionise and photo-evaporate the top layers of gas that face directly toward them (Hester, 1991), and therefore ultimately cause the pillars to be destroyed over time. Whether indeed the massive stars are able to trigger star formation at the pillar-ambient medium interface, and how efficient their photo-evaporating effect really is are still open questions that need to be addressed.

One of the prime examples of pillars in a massive star forming region is the Pillars of Creation in the Eagle Nebula (M16), which can be seen as protruding from a molecular cloud into a vast HII region inflated by the 2-3 Myr old and ~ 2 kpc distant (Hillenbrand et al., 1993) massive cluster NGC 6611, whose brightest and most massive object (the O3-O5 V star W205) lies - in projection - just short of 2 pc North-East of the Pillars. The Pillars can be divided into three main structures, all of them pointing towards the cluster stars of NGC 6611. In this work we will refer to them as P1 (the easternmost and biggest pillar, subdivided into P1a and P1b), P2 (middle pillar) and P3 (the westernmost pillar), as is shown in Fig. 3.1. This pillar-like shape seems to have its origin in the fact that the low-density material in the bodies of the pillars could be easily removed, but it is capped by much denser cores which shield the pillars from the intense ionising sources in NGC 6611 (Oliveira, 2008).

These Pillars have been studied by many authors in the past two decades since they were first captured in spectacular detail with the Hubble Space Telescope (HST) by Hester et al. (1996)

(hereafter referred to as H96), and as it is too great a task to collect and cite all publications regarding these famous structures, we can here only give a brief historical research overview. H96 first described the morphology in great detail and analysed the stratified ionisation structure in terms of a photo-evaporative flow and identified star forming cometary globules currently emerging from the Pillars with the HST images obtained in the $H\alpha$, $[\text{SII}]\lambda 6717,6731$ and $[\text{OIII}]\lambda 5007$ filters. By comparing the optical observations with near-IR images, these authors suggest the presence of a population of YSOs in the pillars and so called evaporating gaseous globules (EGGs), indicating active star formation in the region. McCaughrean & Andersen (2002) however find that only about 15 % of the EGGs show signs of active star formation, while the rest appear not to host young stellar objects. For completeness we show the spectrum of an EGG not covered by the HST data of H96 which is located to the left of P1 (the spectrum is shown in Fig. 3.3c and its location is shown in Fig. 3.12a). A molecular line and continuum emission study, combined with mid-IR observations, was presented by White et al. (1999a), who reported that the pillars are capped by dense and relatively cold ($\sim 10\text{-}60 M_{\odot}$) cores in a pre-protostellar evolutionary stage. These authors detected no embedded IR sources or molecular outflows at the pillar tips, found very small (~ 1.7 km/s) velocity gradients along the pillar bodies and estimated the total mass of the Pillars to be $\sim 200 M_{\odot}$. Fukuda et al. (2002) used millimetre data to analyse the age sequence of CO cores, finding a linear age gradient with more evolved objects closer to NGC 6611 and less evolved ones closer to the Pillars, suggesting the propagation of star formation. Whether this corresponds to triggered star formation is debated, as suggested by Indebetouw et al. (2007), but the presence of young stellar objects (YSOs) and water masers near or in the pillar tips is discussed by several different authors (Thompson et al. 2002, Healy et al. 2004, Linsky et al. 2007). In the more recent years, much effort has been invested in the simulation of such objects to better understand the extent of the stellar feedback, the physical effects occurring at the pillar-ambient interface and their kinematic structure (Miao et al. 2006, Mizuta et al. 2006, Ercolano et al. 2012). To celebrate Hubble's 25th anniversary, the NASA/ESA/Hubble Heritage Team recently released a new, revisited HST image of the Pillars with a much higher spatial resolution and a bigger field of view than H96, bringing new media attention to these structures.

As part of the science verification of the optical integral field spectrograph MUSE at the Very Large Telescope (VLT), we obtained a 3×3 arcmin mosaic of the Pillars. In this work we analyse the ionisation structure of these objects in greater detail than ever before, and tie their evaporation and active star formation directly back to the members of NGC 6611. Following the theme of our FuSIO project, we seek to compare our observations with the results obtained by Ercolano et al. 2012, who created synthetic observations of pillars under the influence of ionising O- and B-type stars in their immediate neighbourhood. They computed line profiles as a function of position within the pillars for $H\alpha$, $[\text{OIII}]\lambda 5007$, $[\text{NII}]\lambda 6584$ and $[\text{SII}]\lambda 6717$, as well as line ratios for the just mentioned emission lines.

This paper is organised as follows. We introduce both the observations and simulations in Section 3.2; we compute the main physical parameters such as electron density and temperature, emission line and ratio maps, as well as analyse the ionisation structure in Section 3.3. In Section 3.4 we describe the velocity structure obtained via emission line fitting and compute the expected lifetime of the Pillars. Conclusions are presented in Section 3.5.

Table 3.1: Central coordinates of the MUSE mosaic pointings shown in Fig. 3.1. The number of spaxels (spectral pixels) corresponds to the number of valid spaxels in the $H\alpha$ slice of the data cube.

Field no.	RA (J2000)	Dec (J2000)	No. of spaxels
1	18:18:51.918	-13:48:45.90	94586
2	18:18:48.892	-13:49:23.52	93936
3	18:18:45.866	-13:50:01.18	94129
4	18:18:48.493	-13:50:45.96	94746
5	18:18:51.519	-13:50:08.34	94723
6	18:18:54.545	-13:49:30.58	94034
7	18:18:57.172	-13:50:15.50	94207
8	18:18:54.146	-13:50:53.12	94690
9	18:18:51.120	-13:51:30.78	94610

3.2 Observations and simulations

3.2.1 IFU data

The optical IFU observations of the Pillars of Creation in M16 were obtained with the Multi Unit Spectroscopy Explorer MUSE instrument (Bacon et al., 2010) mounted on the VLT. The data was obtained during the instrument’s science verification run in service mode on June 21 and June 22 (2014) for the proposal 60.A-9309(A) (PI Mc Leod), using the nominal wavelength range spanning from 4750 Å to 9350 Å (and a wavelength-dependent spectral resolution of ~ 75 and 150 km s^{-1} respectively). The Wide Field Mode of MUSE has a field of view of $1 \times 1 \text{ arcmin}^2$, and we obtained two $3 \times 3 \text{ arcmin}^2$ mosaics with an exposure time of 30 and 130 seconds each, thus requiring 9 pointings per mosaic. The nine fields of the two mosaics are shown in Fig. 3.1 overlaid on the HST $H\alpha + [\text{NII}]$ image, and their central coordinates and number of spaxels (spectral pixels) are listed in Table 3.1. Each field was observed three times via a dither pattern by rotating the instrument position angle by 90 degrees at each exposure. The full dataset thus consists of two subsets of 27 exposures each, where the subsets differ in exposure time only. The effective spatial resolution of the presented data is about $0.2''$, which corresponds to $\sim 1.9 \times 10^{-3} \text{ pc}$ (or $\sim 390 \text{ AU}$).

The 54 exposures were reduced using the standard recipes of the MUSE pipeline (v0.18.2) and the required calibrations. To make the integrated line maps of the entire mosaic discussed in Section 3.1, the integrated line maps of the single pointings were combined using Montage. After this step of making the mosaic a fault in the world coordinate system (WCS) of the single fields, resulting from the rotating dither pattern, manifested itself. This led to the single fields being shifted and rotated with respect to one another, and an updating of the WCS of each field by comparing observed stellar coordinates with a catalog was required. This was done with the IRAF tasks MSCTPEAK and MSCSETWCS of the MSCRED package.

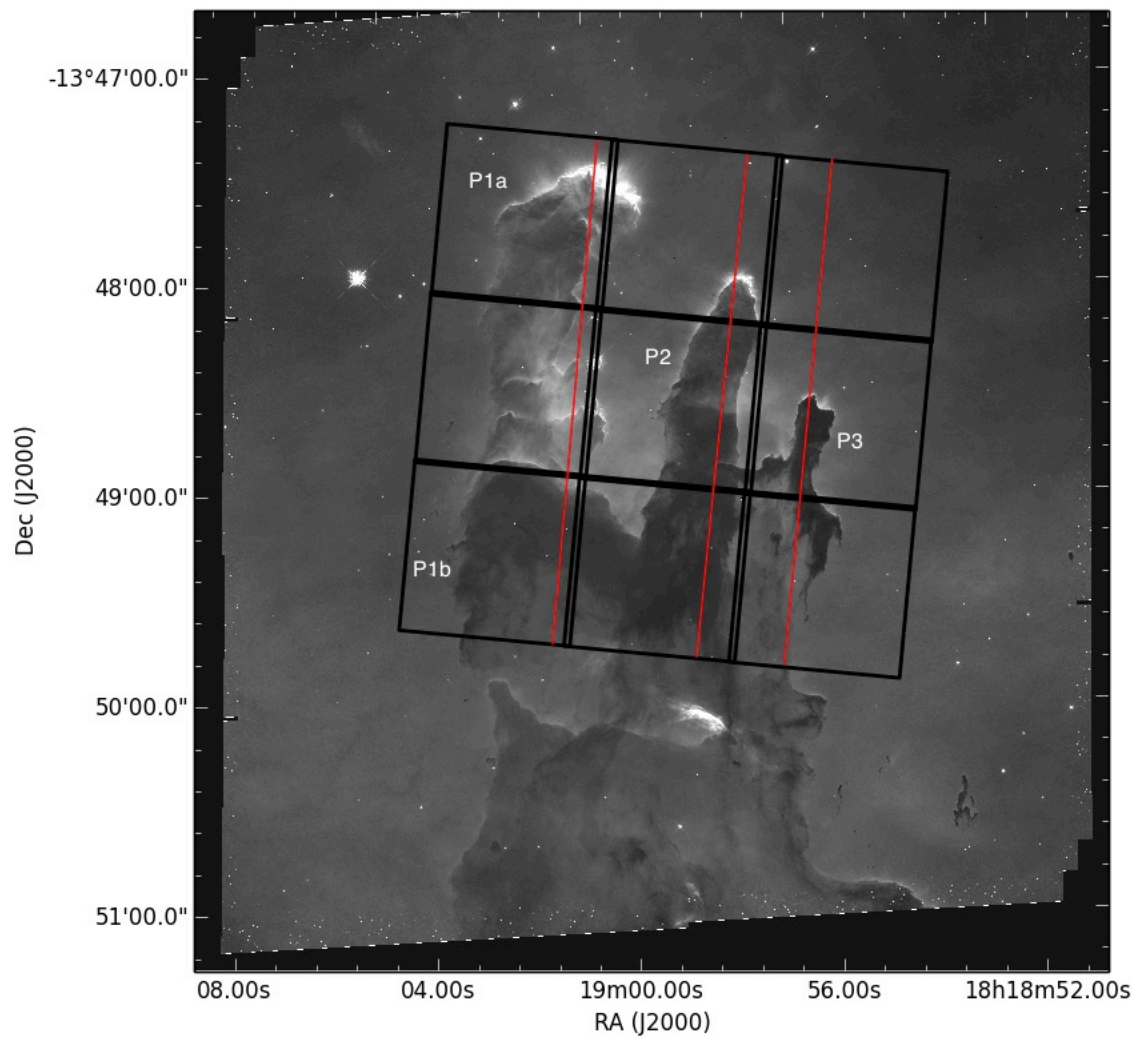


Figure 3.1: The nine MUSE pointings overlaid on the Hubble Space Telescope $H\alpha + [\text{NII}]$ image (credit: STScI). Each pointing spans approximately 1×1 arcmin². The red lines represent the cuts along which the line intensity profiles were computed (Section 3.2).

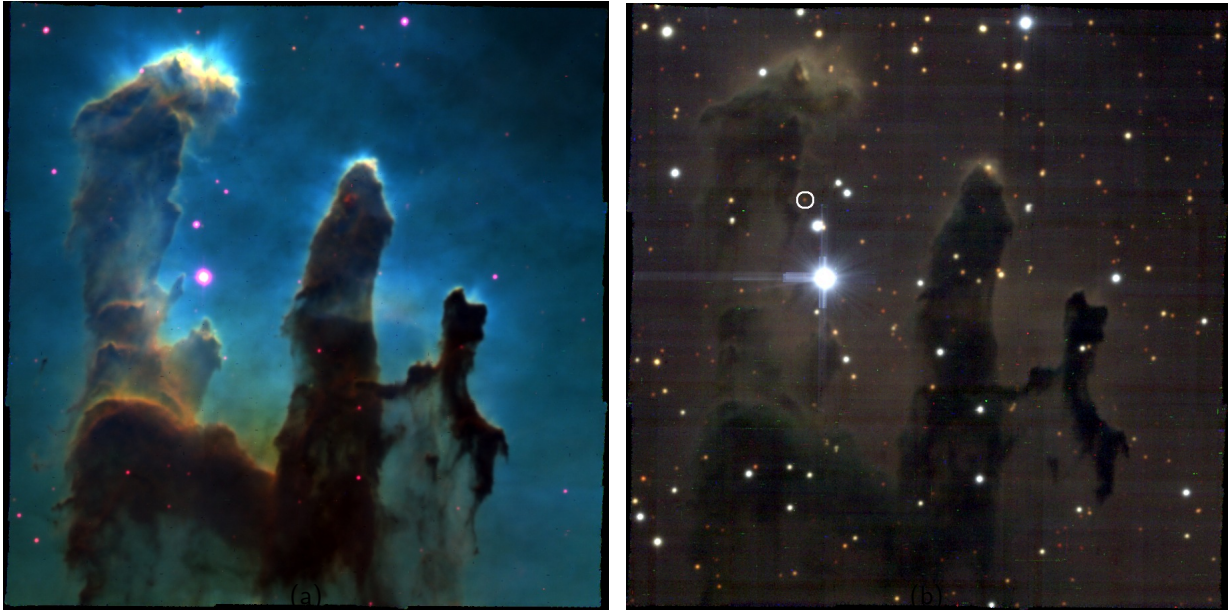


Figure 3.2: RGB composite (panel a): red is $[\text{SII}]\lambda 6717$, green is $\text{H}\alpha$, and blue is $[\text{OIII}]\lambda 5007$. Continuum RGB composite (panel b, red 8050 - 8250 Å, green 6850 - 7000 Å, blue 5200 - 5400 Å). The tips of P1 and P2 are to be seen as reflection nebulae illuminated by the nearby stars. The white circle in panel b indicates the continuum source discussed in Section 4.1.

As a counterpart to the iconic and very well known HST 3-color composite by Hester et al. (1996) and the recently released 25th HST anniversary image, the RGB composite (where red is $[\text{SII}]\lambda 6717$, green is $\text{H}\alpha$, and blue is $[\text{OIII}]\lambda 5007$) of the 30 second exposure is shown in Fig. 3.2a. This RGB composite clearly shows the structure and evaporation of the Pillars and their tips which are being illuminated and ionised by the nearby cluster NGC 6611, and also clearly to be seen are the dust lanes at the lower end of the Pillars that point towards their natal molecular cloud, as well as several detached globules to the left of P1 (better appreciable in the digital version if this article).

Figure 3.2b shows a continuum 3-color composite of the region: the pillar tips (P1 and P2) are to be seen as reflection nebulae illuminated by the nearby stars. The star at the tip of P2 corresponds to a known T Tauri star (Sugitani et al. 2002, Indebetouw et al. 2007).

3.2.2 Hydrodynamical simulations

We compare our observations with three-dimensional radiation-hydrodynamical simulations performed with the smoothed-particle hydrodynamics (SPH) code `DIVINE`. The code is able to model the plane-parallel irradiation by ionising photons of an arbitrary gas distribution, as described by Gritschneider et al. (2009), and also includes the effects of the diffuse ionising field resulting from recombinations (Ercolano & Gritschneider, 2011).

Ercolano & Gritschneider (2011) simulated the photoionisation of a $(4\text{pc})^3$ turbulent box initially containing $474 M_{\odot}$ of neutral gas at 10K and with a turbulent RMS Mach number of 5.

The box is illuminated with a Lyman continuum flux of 5×10^9 photons $\text{cm}^{-2} \text{s}^{-1}$ and allowed to evolve for ≈ 500 kyr, corresponding to ≈ 0.17 freefall times. The turbulent density field is sculpted by the photoevaporation flows and the pressure in the HII region into a complex morphology which includes three prominent pillar structures pointing roughly in the direction from which the photons are propagating. It is these structures which form the basis for our comparative work.

The SPH simulations and subsequent MOCASSIN (described in Section 2.3) calculations do not specifically reproduce the pillars in M16, as they have smaller mass and the radiation field is not as strong as the one produced by NGC 6611 (see Section 3.3). The comparison we seek to do is more of a qualitative one which helps us to see whether the characteristic ionisation structure of the pillar tips is recovered in the simulations after running them through the radiative transfer calculation, ultimately testing our numerical computations.

3.2.3 Monte Carlo radiation-transport calculations

Since the SPH simulations described above are only intended to reproduce the dynamical effects of photoevaporation and ionised gas pressure, they do not lend themselves to detailed comparison with observations. For this purpose, we post-processed the SPH simulation output with the 3D Monte Carlo photoionisation code MOCASSIN (Ercolano et al., 2003a, 2005, 2008). MOCASSIN uses a Monte Carlo formalism, enabling the self-consistent treatment of the direct and diffuse radiation field.

We mapped a $1 \times 3 \times 1$ pc cutout of the hydrodynamical simulation snapshot onto a uniform $128 \times 384 \times 128$ pixel grid. We assumed typical HII region gas-phase abundances as follows: $\text{He}/\text{H} = 0.1$, $\text{C}/\text{H} = 2.2 \times 10^{-4}$, $\text{N}/\text{H} = 4.0 \times 10^{-5}$, $\text{O}/\text{H} = 3.3 \times 10^{-4}$, $\text{Ne}/\text{H} = 5.0 \times 10^{-5}$, $\text{S}/\text{H} = 9.0 \times 10^{-6}$. The gas is heated mainly by photoionisation of hydrogen and other abundant elements. Gas cooling is mainly via collisionally excited lines of heavy elements, although contributions from recombination lines, free-bound, free-free and two-photon continuum emission are also included. To compute the emission line flux from each cell, MOCASSIN solves the statistical equilibrium problem for all atoms and ions, given the local temperature and ionisation state.

These MOCASSIN calculations were already used by Ercolano et al. (2012) to create synthetic observations of the simulations of Ercolano & Gritschneider (2011). Here, for the first time, we make use of the very rich new dataset provided by MUSE to compare the hydrodynamic simulations in detail to the Pillars of Creation.

3.3 Ionisation structure

3.3.1 Extinction correction

The extinction toward M16 has been studied by many authors in the past and has been found to vary significantly over the members of NGC 6611. Chini & Wargau (1990) found that for $\lambda < 5500 \text{ \AA}$ the extinction law deviates from the standard galactic extinction law ($R_V = 3.1$, Seaton 1979), this effect is caused by the dust grains being larger than those found in the standard interstellar medium (Orsatti et al., 2006). Indeed, Hillenbrand et al. (1993) find a typical value of $R_V \sim 3.75$ for NGC 6611. Therefore, to correct for extinction along the line of sight toward M16 we computed the reddening coefficient C via the Balmer decrement method:

$$C = 3.1 \times \left(\log \frac{F(H\alpha)}{F(H\beta)} - \log \frac{I(H\alpha)}{I(H\beta)} \right)$$

assuming a reddening curve parametrised by Cardelli et al. (1989) with $R_V = 3.1$ for $\lambda > 5500 \text{ \AA}$, and $R_V = 3.75$ for shorter wavelengths. An intrinsic flux ratio of $I(H\alpha)/I(H\beta) = 2.86$ (corresponding to a case B Balmer recombination decrement, Osterbrock & Ferland 2006) was adopted, and the measured $F(H\alpha)/F(H\beta)$ flux ratio used to compute C was taken to be the mean value obtained from the map of that particular line ratio, thus obtaining $\langle F(H\alpha)/F(H\beta) \rangle \cong 5.93$ and therefore $C \cong 0.98$. We find extinction values between ~ 1.5 and ~ 3.2 mag, which agree with literature values (Guarcello et al., 2010). Fig. 3.3 shows co-added spectra of the HII region (top panel), the pillar-ambient interface (the pillar tips, middle panel) and an EGG (bottom panel). The prominent features in the 8000 \AA to 9000 \AA range are OH sky lines that have not been removed from the spectra). Table 3.2 lists the detected emission lines together with their observed wavelength (column 2), the adopted reddening curve (column 4) and the flux ratio prior and after correcting for extinction (columns 3 and 5) for the example spectrum of the HII region shown in Fig. 3.3. The integrated line intensity maps were de-reddened according to the appropriate reddening curve value for each wavelength. The $[OII]\lambda 7320,30$ as well as the $[NII]\lambda 5755$ have intensities (relative to $H\beta$) < 0.07 and were not included in the fit used to derive the parameters in Table 3.2.

A clear gradient can be seen in the extinction map shown in Fig. 3.4a where P1a shows a higher overall extinction, P3 the lowest, and P2 values in between. This is quantified in Fig. 3.4b, where the normalised histograms of circular regions ($r \sim 3$ arcsec, white circles in panel a) in the three pillar tips are shown together with the best fit values to each histogram. We therefore believe that P3 is the pillar closest along the line of sight, behind that lies P2, and behind P2 lies P1. A description of the 3D geometry of the Pillars is given in Section 3.4.

3.3.2 Integrated line maps

The extinction-corrected integrated line maps were created using the moment map subroutine of the PYTHON package SPECTRAL_CUBE*. All line and line ratio maps shown in this paper

*spectral-cube.readthedocs.org

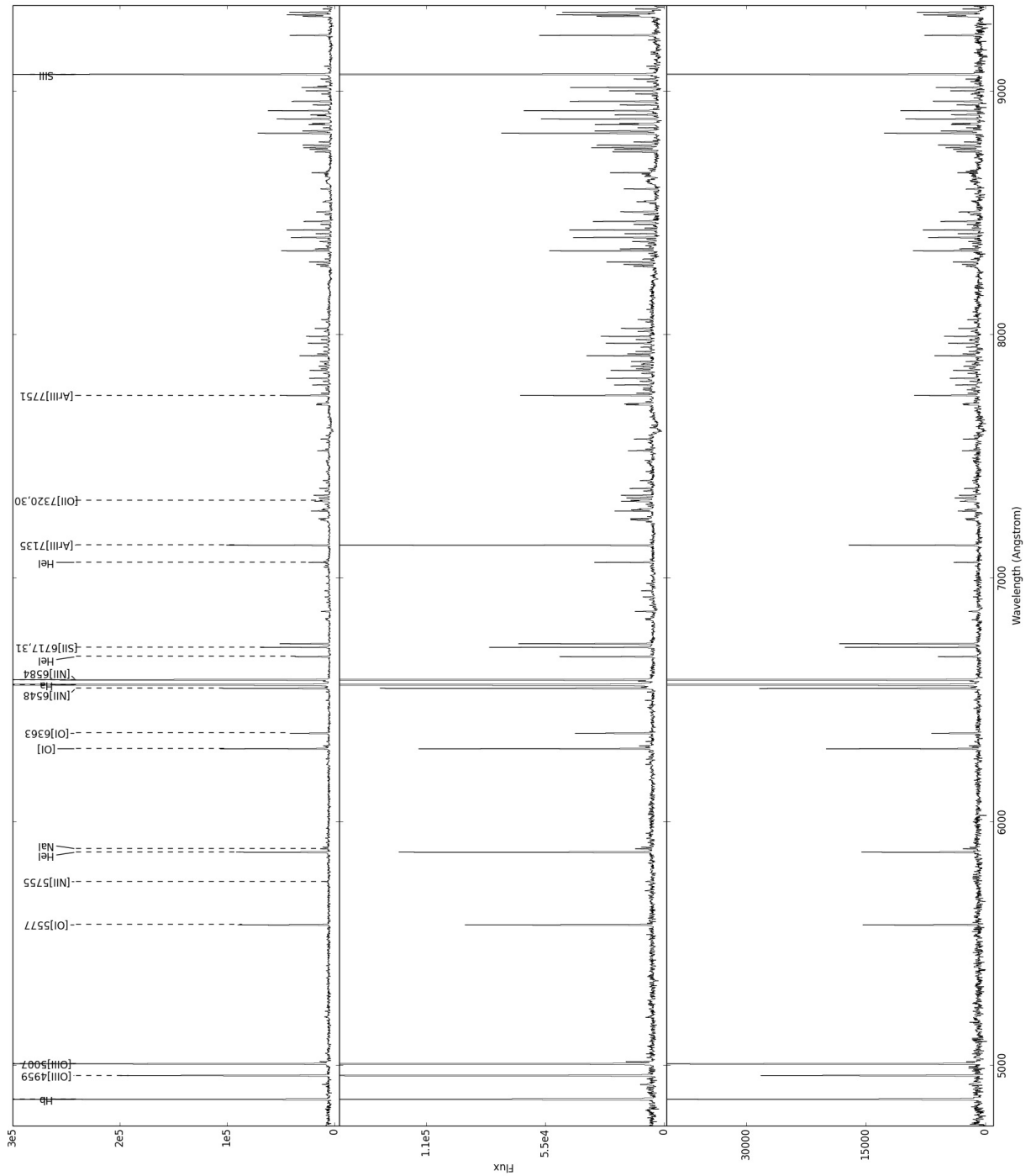


Figure 3.3: Example spectra of the HII region (top panel), the pillar-ambient matter interface (middle panel) and the EGG (bottom panel) extracted from the positions marked in Fig. 3.12a (see text Section 3.1). The flux is measured in $10^{-20} \text{ ergs s}^{-1} \text{ cm}^{-2} \text{ \AA}^{-1} \text{ pixel}^{-1}$.

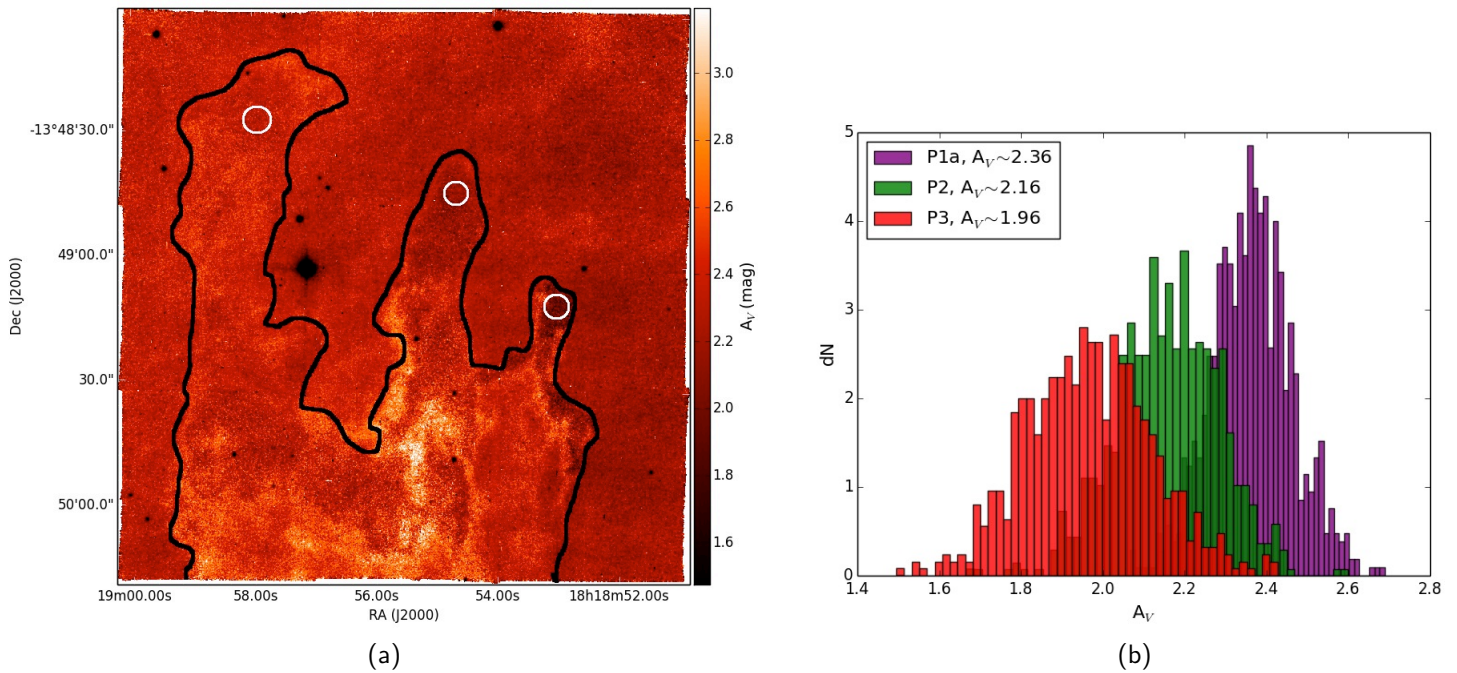


Figure 3.4: Left: extinction map in terms of A_V (linear scale to maximum/minimum). To help the reader identify the location of the Pillars, these have been marked with a schematic black contour. The white circles in panel (a) correspond to the regions used to quantify the extinction for the three Pillars (panel b and text Section 3.1). Right: normalised extinction histograms of circular regions ($r \sim 3$ arcsec) at the tip of the three pillars.

Table 3.2: Detected emission lines (column 1) and line centroids obtained via gaussian line fitting (column 2), line fluxes relative to the observed $H\beta$ flux prior (column 3) and after (column 5) correcting for extinction, and the reddening curve for each line (column 4).

Line	λ_{obs}	$F(\lambda)/F(H\beta)$	$f(\lambda)$	$F(\lambda)/F(H\beta)_{\text{corr}}$
4861 $H\beta$	4861.42	1.0 ± 0.019	0.0	1.000
4959 [OIII]	4959.01	0.433 ± 0.015	-0.025	0.419
5007 [OIII]	5006.93	1.36 ± 0.023	-0.036	1.297
5577 [OI]	5577.42	0.298 ± 0.014	-0.153	0.244
5876 HeI	5875.76	0.233 ± 0.015	-0.203	0.179
6300 [OI]	6300.39	0.382 ± 0.015	-0.267	0.269
6363 [OI]	6363.86	0.121 ± 0.014	-0.276	0.084
6548 [NII]	6548.12	0.312 ± 0.015	-0.303	0.21
6563 $H\alpha$	6562.89	6.476 ± 0.088	-0.305	4.343
6584 [NII]	6583.5	0.975 ± 0.019	-0.308	0.552
6678 HeI	6678.24	0.083 ± 0.015	-0.322	0.055
6717 [SII]	6716.56	0.197 ± 0.015	-0.327	0.129
6731 [SII]	6730.94	0.144 ± 0.015	-0.329	0.093
7065 HeI	7065.37	0.047 ± 0.015	-0.377	0.029
7135 [ArIII]	7135.89	0.231 ± 0.015	-0.387	0.139
7751 [ArIII]	7751.19	0.129 ± 0.014	-0.475	0.069
9068 [SIII]	9068.69	0.521 ± 0.015	-0.531	0.272

(included in the appendix) are linearly scaled to minimum/maximum. The $H\alpha$, $[\text{NII}]\lambda 6548$, $[\text{SII}]\lambda 6717,31$ and $[\text{OIII}]\lambda 5007$ maps are shown in Fig. 3.5, the maps of the other detected lines are shown in Appendix A, available as supplementary online material. H96 discussed the normal-oriented striations coming from the pillar-ambient interface in the context of photo-evaporation: as the strong ionising radiation from NGC 6611 hits the dense molecular material of the pillars, the matter is ionised and the pressure at the pillar-ambient matter interface is increased causing matter to flow away from the latter, creating a photo-ionised flow. The fact that the evaporation is normal to the pillar-ambient interface is an indication that neither the interaction between the flow and the ambient matter, nor the interaction of the impinging photons with the outflowing material are able to influence the direction of the photo evaporative flow (see H96). The photo-evaporative striations can be clearly seen in the $H\alpha$ maps (and slightly in the $[\text{SIII}]\lambda 9068$ and $[\text{ArIII}]\lambda 7135$ maps). The emission from the other species is either very diffuse ($[\text{OIII}]$, $H\beta$) or very localised (rest).

The strongest emission is the $H\alpha$ emission coming from the tip of P1. In general we identify two types of emission: a more or less localised line emission that traces the tips of the pillars as well as the protrusions on the inner side of P1 can be seen in the $H\alpha$, $[\text{ArIII}]$, HeI , $[\text{NII}]$, $[\text{OI}]$, $[\text{OII}]$, $[\text{SII}]$, $[\text{SIII}]$ maps, and a more diffuse emission that surrounds the pillars in a halo-like manner ($[\text{OIII}]$ and $H\beta$). In the first type the emission peak of some lines is sharper and more localised than others, e.g. $[\text{SII}]$ compared to $H\alpha$, and we furthermore see a spatial shift in the peak emission of different lines corresponding to a stratified ionisation structure which correlates with the ionisation energy of the identified species. This stratification was already discussed in H96, who modelled the scenario with CLOUDY84 (see Ferland et al. 2013a for the latest release of the code) and found a very good agreement between the model and the data. While these authors were limited to three emission lines ($H\alpha$, $[\text{SII}]$ and $[\text{OIII}]$), MUSE now offers the possibility of investigating this stratified ionisation structure in great detail across almost the entire optical regime and thus covering almost all of the optical ionisation-tracing emission lines. Fig. 3.6 shows the intensity profiles of the emitting line species listed in Table 3.2 for the three pillars along the cuts marked in Fig. 3.1 as a function of distance from the top of the image (wherever two lines of the same ionised state and atom were present these were averaged): the stratified ionisation structure is clearly seen from the fact that the lines from the ions/atoms with higher ionisation energy peak first, followed by the ones with lower and lower ionisation energy. The locations of the peaks with respect to the $[\text{OIII}]$ peak are listed in Table 5.2: it is clear that MUSE is not able to spatially resolve the ionisation front, as for some lines (especially in P2 and P3 where the emission is weaker compared to P1) it is impossible to spatially separate the maxima.

Fig. 3.7 shows the line intensity profiles obtained from our simulations, and although we cannot resolve the separation between the $H\alpha$, $[\text{SII}]$ and $[\text{NII}]$ peaks, the shape and trend of the profiles is in good agreement. The distance between the $[\text{OIII}]$ maximum and the maxima of the other three lines is about $d \approx 0.015$ pc, which agrees with what we find from the observations of P1 where $d_{H\alpha, [\text{NII}]} \approx 0.019$ and $d_{[\text{SII}]} \approx 0.022$. Our models therefore quantitatively predict the ionisation structure of pillar-like objects.

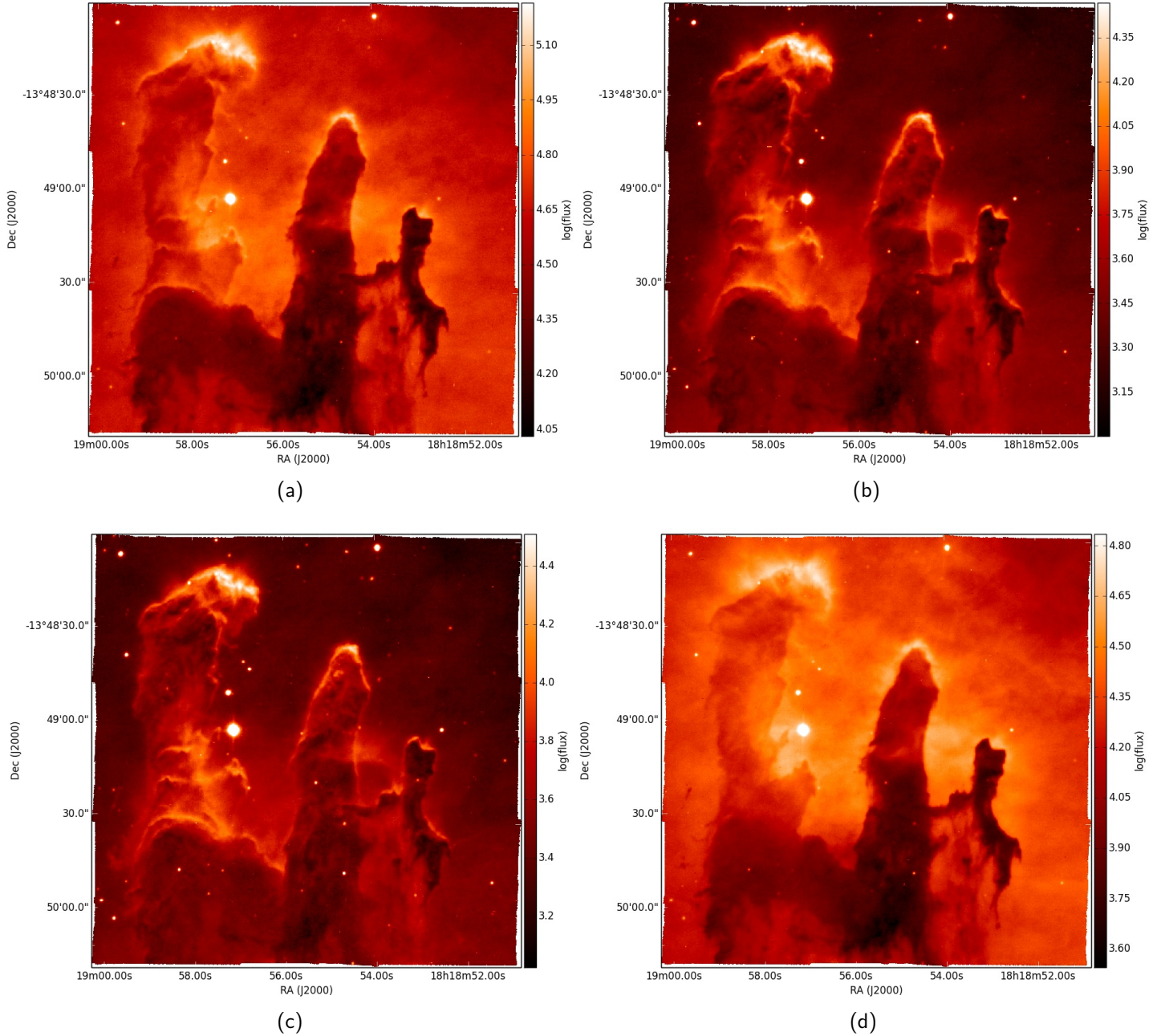


Figure 3.5: Integrated line maps derived from the MUSE data: $\text{H}\alpha$ (a), $[\text{NII}]\lambda 6548$ (b), $[\text{SII}]\lambda 6717,31$ (c) and $[\text{OIII}]\lambda 5007$ (d). The flux scale bar is in $10^{-20} \text{ erg s}^{-1} \text{ cm}^{-2} \text{ pixel}^{-1}$, all maps are linearly scaled to minimum/maximum. See Section 3.2 for discussion.

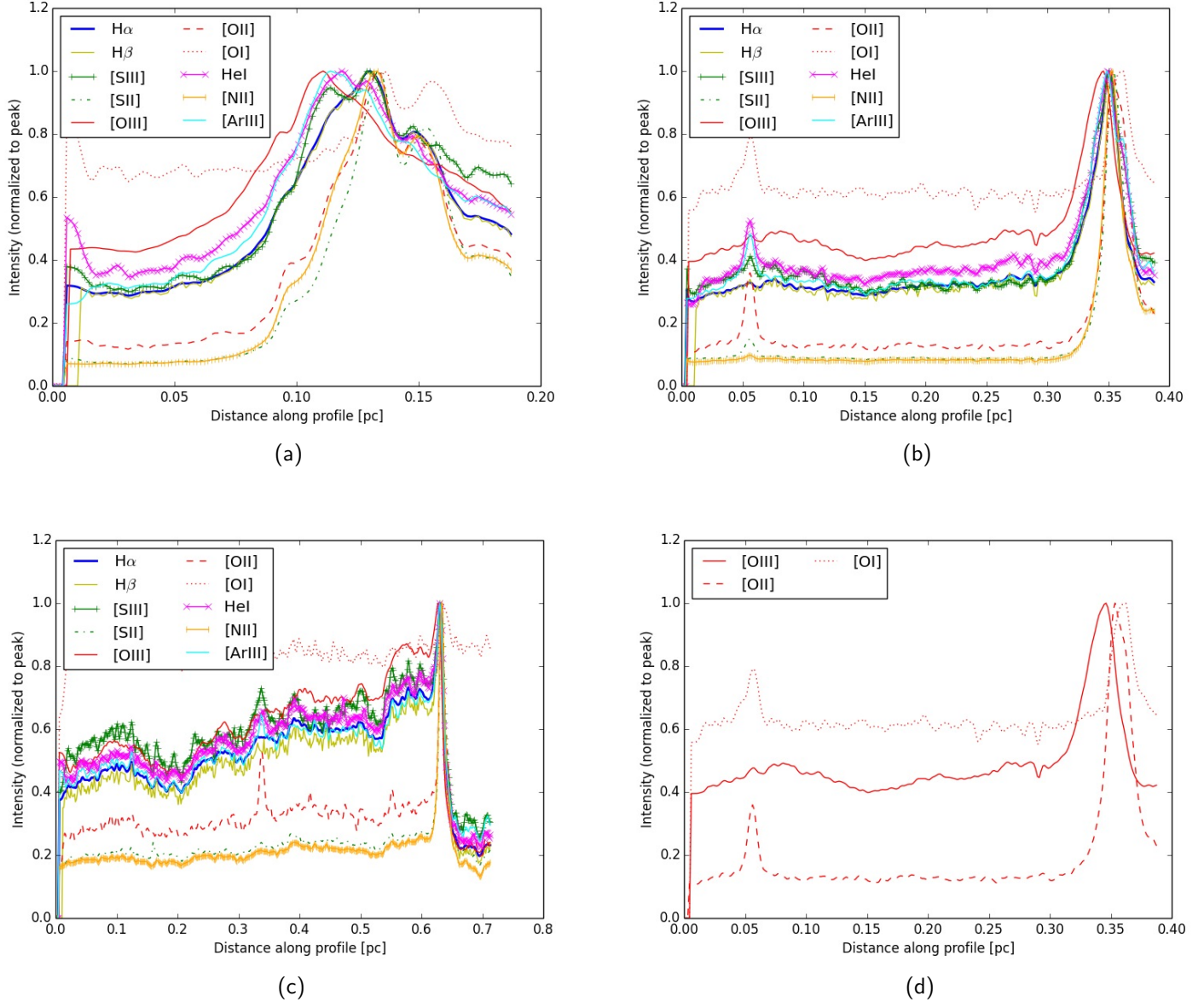


Figure 3.6: Line intensity profiles for the emission lines listed in Table 3.2 for P1, P2 and P3 (panels a, b, and c respectively, see text Section 3.2 for discussion). The lines are the same in the first three panels: H α (blue), H β (yellow), [SIII] λ 9068 (solid green), [SII] λ 6717,31 (dashed green), [OIII] λ 4969,5007 (solid red), [OII] λ 7320,30 (dashed red), [OI] λ 5577,6300 (dotted red), HeI λ 5876,6678 (magenta), [ArIII] λ 7135,7751 (cyan), [NII] λ 6548,6584 (orange). Panel d shows the oxygen lines only for P2: [OIII] (solid line), [OII] (dashed line) and [OI] (dotted line). The profiles in these figures only cover the pillar tips; they do not follow the whole length of the slits shown in Fig. 3.1.

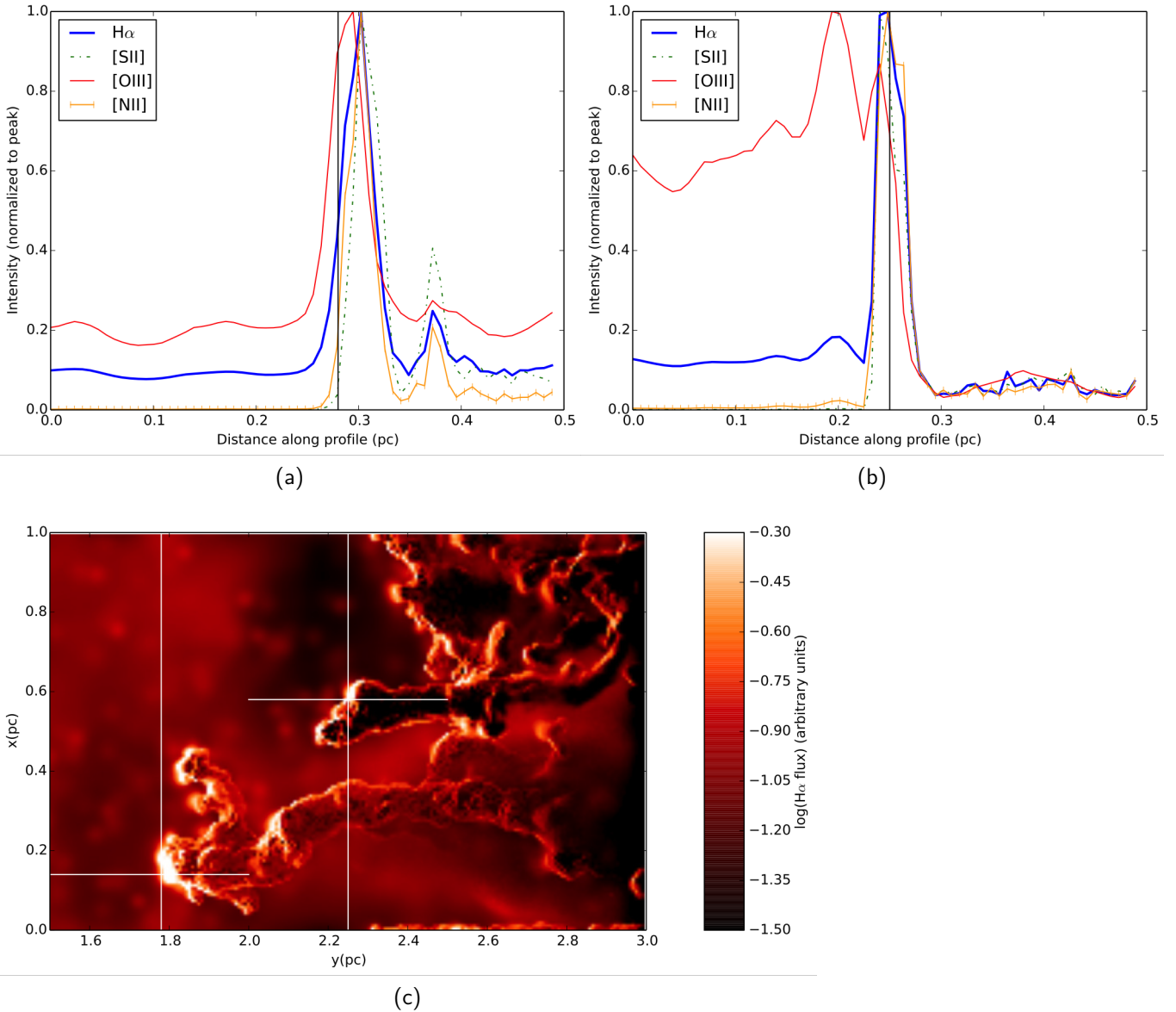


Figure 3.7: Line intensity profiles for the emission lines obtained from our simulations (panels a and b) along the (horizontal) slits shown in the $H\alpha$ intensity map (panel c). The colour-coding is the same as in Fig. 3.6. See text Section 3.2 for discussion.

Table 3.3: Location of the peaks (in 10^{-2} pc) of the lines seen in Fig. 3.6a, 3.6b and 3.6c with respect to the position of the [OIII] peak ($E_{\text{ion}} = 35.12$ eV) and their ionisation energy (see text Section 3.2).

	[ArIII]	HeI	[SIII]	$H\alpha, \beta$	[NII]	[SII]	[OII]	[OI]
P1	0.296	0.739	1.775	1.923	2.218	2.218	2.218	2.514
P2	0.296	0.296	0.444	0.444	0.592	0.739	0.739	1.627
P3	0.296	0.296	0.296	0.296	0.592	0.592	0.592	0.887
E_{ion} (eV)	27.63	24.59	23.23	13.59	14.53	10.36	13.62	-

3.3.3 Electron temperature and density maps

The electron density was estimated via the ratio of the [SII] λ 6717 and [SII] λ 6731 lines. The sulfur ion has a single ground level, and two first excited levels are energetically very close and their ratio is thus sensitive to density but not temperature. We used the analytical solution given in McCall (1984) for a three-level atom:

$$\frac{[\text{SII}]\lambda 6717}{[\text{SII}]\lambda 6731} \equiv R_{[\text{SII}]} \simeq 1.49 \frac{1 + 3.77x}{1 + 12.8x} \quad (3.1)$$

where $x = 0.01N_e/T^{1/2}$ and assuming that $T = 10^4$ K, so that the electron density N_e in cm^{-3} is given by

$$N_e = \frac{R_{[\text{SII}]} - 1.49}{5.6713 - 12.8R_{[\text{SII}]}} \times 10^4 \quad (3.2)$$

The tips of the pillars show the highest densities with values $> 2000 \text{ cm}^{-3}$ and we find decreasing density values along the pillar bodies, while the surrounding gas is at densities $< 250 \text{ cm}^{-3}$ (Fig. 3.8a). The pillar tips having the highest electron densities is a consequence of them also having a much higher column density than the pillar bodies (White et al., 1999a): the dense tips act like caps that shield the pillar bodies from the stellar feedback. Fig. 3.8c shows the electron density map of our simulations, derived via Eq. 2. The density of the HII region is comparable to what we observe, as is the fact that the exposed pillar protrusions that are being ionised display the highest density values. These are lower by a factor of ~ 2 , which is consistent with the fact that the radiation field implemented in the simulations is weaker than what is observed in M16. Another factor adding to this is that the simulated pillars, while roughly the same size as the M16 Pillars, are only about 1/10th the mass. Fig. 3.9a shows that the histogram of the electron density follows a lognormal distribution with a slight tail toward the low-density regime. The lognormal density distribution is well recovered in our simulations as is shown in Fig. 3.9b, where the electron density as measured from the SPH grid (real) is plotted together with the electron density derived via the [SII] line ratio (derived). In the real electron density histogram it appears that in the simulations the high and low density values are

both washed out by the line-ratio calculation, an effect arising from smoothing along the line of sight. A lognormal electron density distribution has been observed for the ionised interstellar medium (Redfield & Falcon 2008, Hill et al. 2007) where the driver for the shape is isothermal turbulence. In the case of the Pillars of Creation we suggest that shocks could produce such a distribution. The presence of shocks could in principle be inferred from emission line ratios, but, as we show in Section 3.5, these shock indicators may be washed out - and therefore not detected - by the dominant influence of photoionisation.

The electron temperature is usually determined via the forbidden line ratio ($[\text{OIII}]\lambda 5007 + [\text{OIII}]\lambda 4959 / [\text{OIII}]\lambda 4363$), but the $[\text{OIII}]\lambda 4363$ is not covered by MUSE and we therefore derived the electron temperature T_e via the $[\text{NII}]$ doublet according to equation 5.5 in Osterbrock & Ferland (2006) (assuming that the term in the denominator of the Osterbrock & Ferland equation is negligible)

$$T_e = \frac{2.5 \times 10^4}{\ln(0.164R)} \quad (3.3)$$

where $R = [\text{NII}]\lambda 6548, 8584 / [\text{NII}]\lambda 5755$. From the electron temperature map shown in Fig. 3.8 it is clear that the high density regions at the tip of the pillars and the arc-like structures in P1 display lower temperatures with respect to the surrounding ambient gas, although the map presents a certain level of noise coming from the weak $[\text{NII}]\lambda 5755$ line.

3.3.4 Abundance tracers and ionic abundances

Among abundance parameters the most used are the oxygen R_{23} and the sulfur S_{23} parameters, which are defined as $R_{23} = ([\text{OII}]\lambda 3726, 3729 + [\text{OIII}]\lambda 4959, 5007) / H\beta$ (Pagel et al. 1979) and $S_{23} = ([\text{SII}]\lambda 6717, 31 + [\text{SIII}]\lambda 9068, 9532) / H\beta$ (Vilchez & Esteban 1996a), and have been extensively used to determine galactic as well as extragalactic chemical abundances, since these differ as a function of position within a galaxy and can therefore be used to study star formation histories and evolutionary scenarios. Other authors have used these parameters, together with the excitation measured by the ratio of $[\text{OII}]/[\text{OIII}]$, to study the ionisation structure of HII regions (García-Benito et al. 2010, Monreal-Ibero et al. 2011). Here, we exploit these parameters to distinguish between the various regions in our data (pillars, surrounding HII region, stars, young stellar objects, and protostellar outflows). This is demonstrated in Fig. 3.10, where S_{23} (defined as $S_{23} = ([\text{SII}]\lambda 6717, 31 + [\text{SIII}]\lambda 9068) / H\beta$ because of the lacking coverage of the $[\text{SIII}]\lambda 9532$ line) is plotted versus $[\text{OII}]/[\text{OIII}]$ (panel a) for a sub-region that highlights the tip of P2 (panel b): the clearly recognisable different populations in the scatter plot correspond to ambient matter (red), the pillar-ambient interface (green), the pillar matter (blue), a known T Tauri star (magenta, see Section 4.1) and a sulfur-abundant region (orange) of panel b. The brushed S_{23} map of the entire mosaic is shown in Fig. 3.11, the stars have been intentionally left white. Fitting in the picture where P1a lies behind NGC 6611 and the other two pillars along the line of sight (see Section 4.2), we see the pillar body of P1a (marked in blue) contaminated by the HII region (marked in red). The sulfur-abundant region is clearly visible in the S_{23} parameter map (Appendix A) and is visible as a slight over-density of the order of $\sim 2000 \text{ cm}^{-3}$ in the electron density map. As will be discussed in Section 4.1, we suggest that this region corresponds to

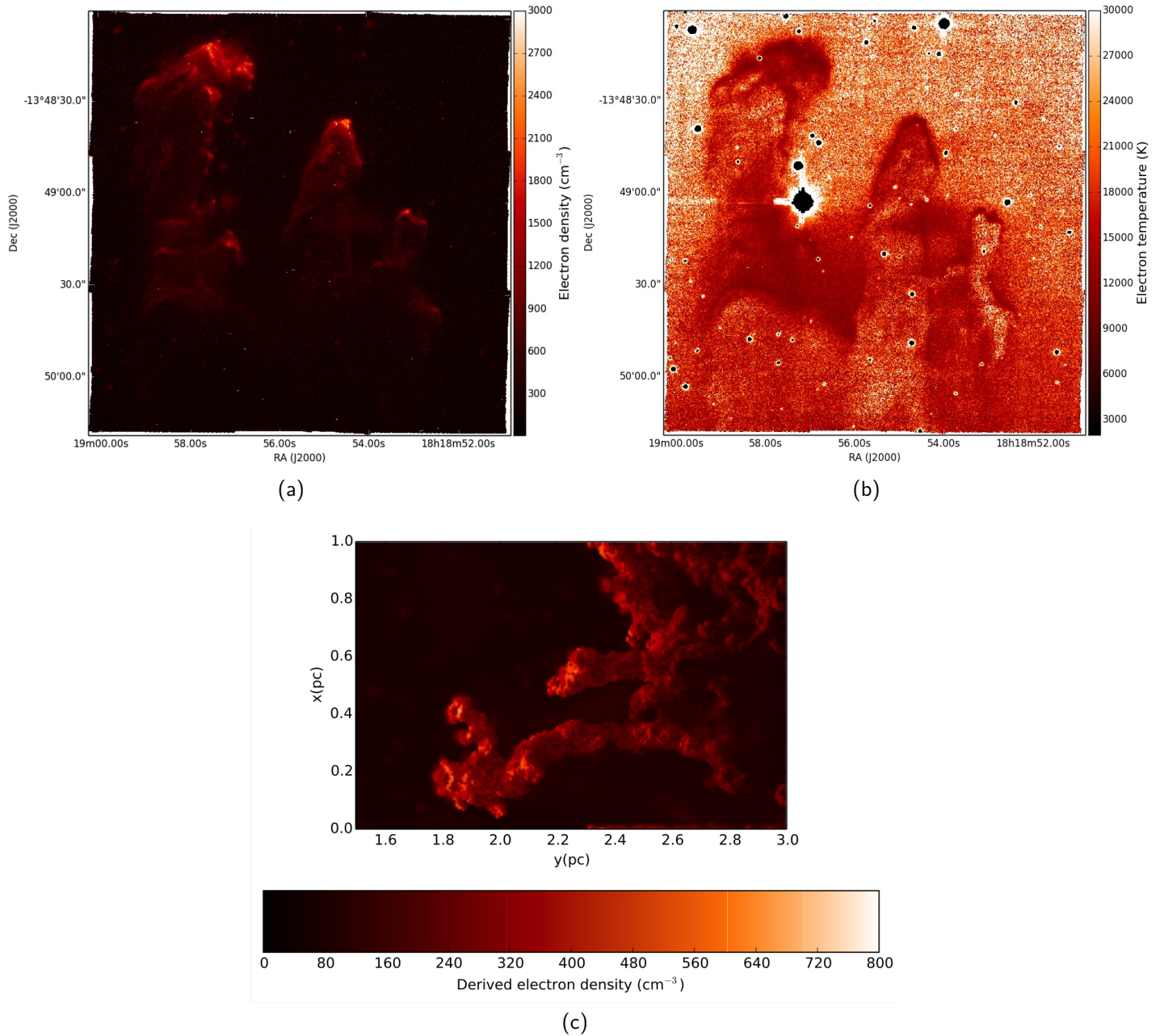


Figure 3.8: The electron density map derived via Eq. 3.2 (a), the electron temperature derived via Eq. 3.3 (b), and the electron density of the simulation computed with the sulfur line ratio (c) (see text Section 3.3).

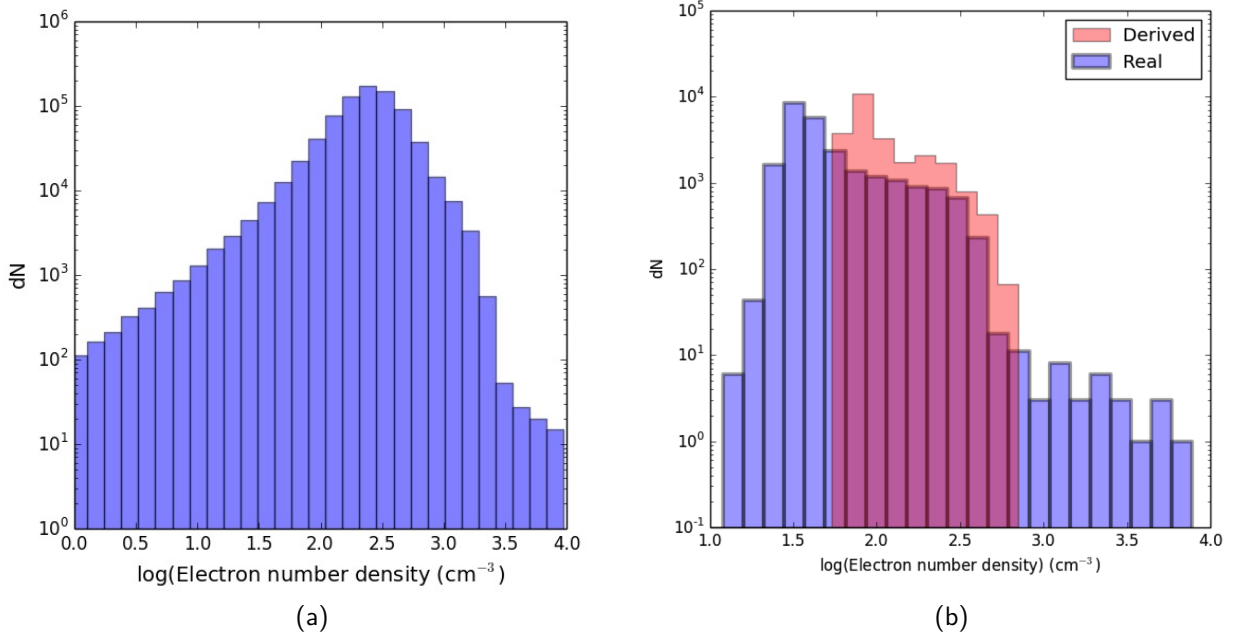
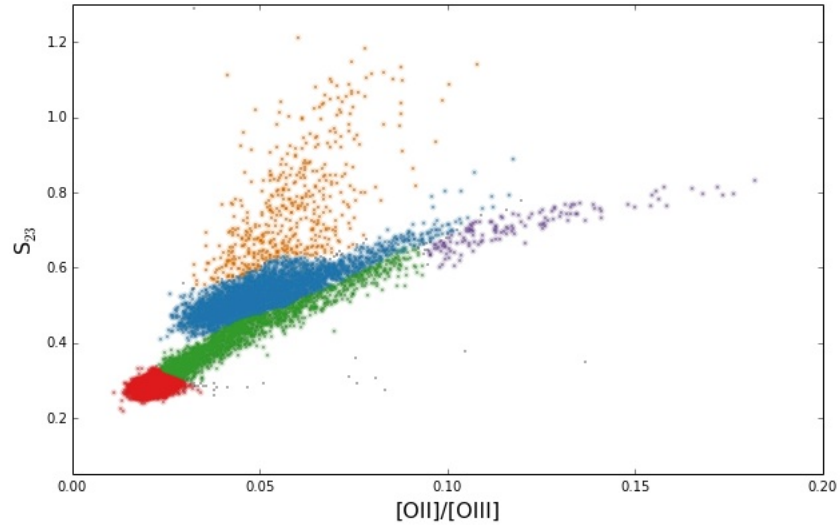


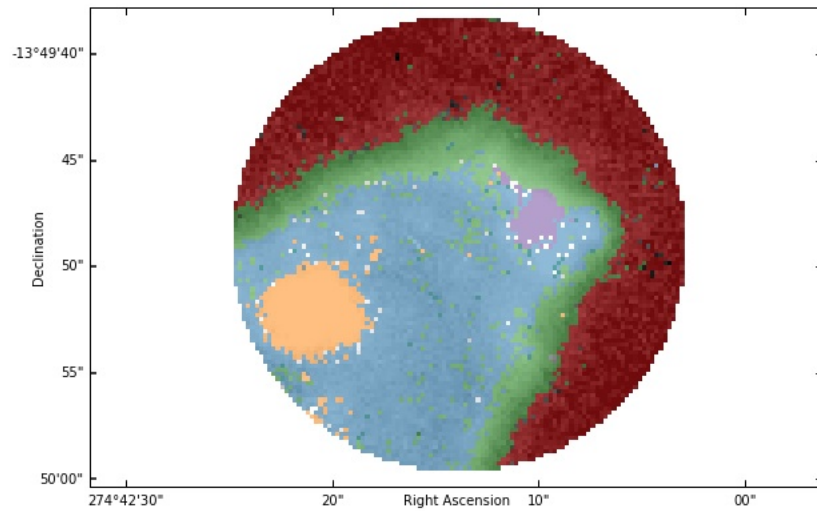
Figure 3.9: Histogram of the electron density of the observed data (panel a) and the simulated pillars (panel b). See text Section 3.3 for discussion.

where the blue-shifted lobe of a bipolar jet originating from a deeply embedded protostar is pushing its way out through the pillar material. The fact that it is only visible in the integrated intensity maps of the [SII] lines and in [OI] λ 6300 indicates that the outflow is not energetic enough to ionise the detected atoms with $E_{\text{ion}} \geq E_{\text{ion, [SII]}} = 10.36$ eV.

Furthermore, we derived ionic and total abundances of the HII region and the pillar tips via the IRAF task `ionic`. For this, we produced co-added spectra of a region representative of the HII region matter and a region representative of the pillar tips (see Fig. 3.3), which were fitted with a gaussian routine to determine emission line intensities. The electron density was computed via equation 2, and this was then used to derive ionic abundances and the electron temperature with IRAF. The derived ionic and total abundances are listed in Table 4.2. The oxygen ionic abundance ratios O^+/H^+ and O^{2+}/H^+ were obtained with the [OII] λ 7320,30 and [OIII] λ 4959,5007 lines respectively and assuming $T([\text{OII}]) \approx T([\text{NII}])$ and $T([\text{OIII}]) \approx T([\text{SIII}])$, as we do not have the wavelength coverage for the [OII] λ 3727,29 and the [OIII] λ 4363 lines to determine $T([\text{OIII}])$ and $T([\text{OII}])$. The total S/H abundance was determined by taking into account the unobservable ionisation stages and therefore using the ionisation correction factor (ICF) for $\text{S}^+ + \text{S}^{2+}$ as in Hägele et al. (2008). As is expected from the fact that molecular material is being ionised at the pillar tips, these present higher ionic abundance values when compared with the HII region.



(a)



(b)

Figure 3.10: $O_{23} = [OII]/[OIII]$ vs. S_{23} for the tip of P2 (panel a) and the S_{23} parameter map of the same region (panel b). The colours in panel a highlight different populations in the scatter plot of panel a which correspond to the same coloured regions in panel (b), as is discussed in Section 3.4.

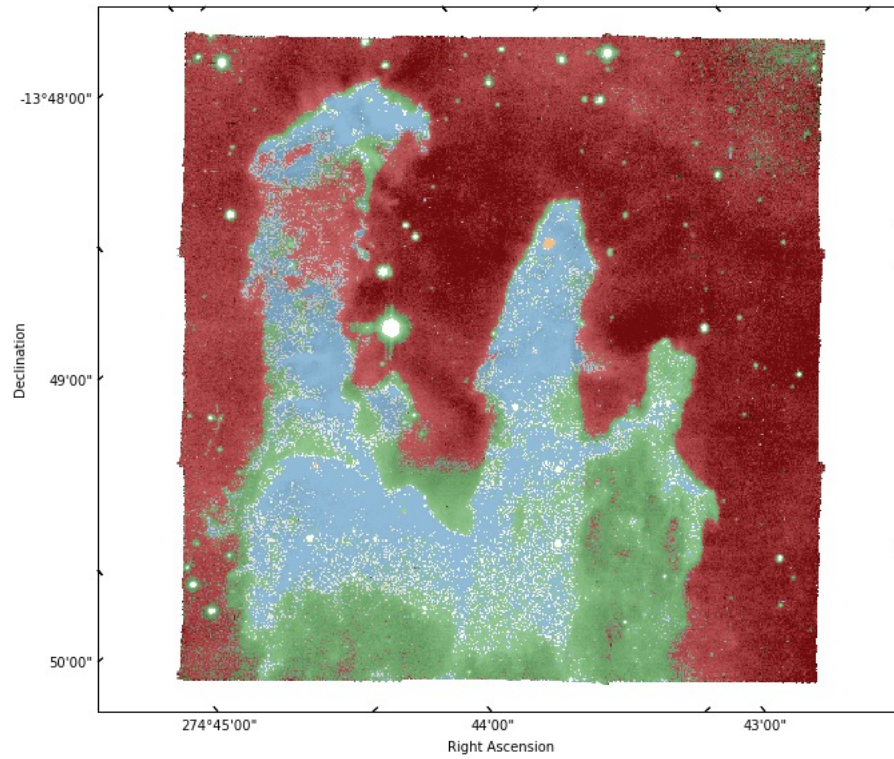


Figure 3.11: S_{23} parameter map of the entire mosaic, the colour-coding is the same as in Fig. 3.10.

Table 3.4: Derived ionic and total abundances of O and S (see Section 3.4).

Region	$12+\log(\text{O}^+/\text{H}^+)$	$12+\log(\text{O}^{2+}/\text{H}^+)$	$12+\log(\text{O}/\text{H})$	$12+\log(\text{S}^+/\text{H}^+)$	$12+\log(\text{S}^{2+}/\text{H}^+)$	$12+\log(\text{S}/\text{H})$
HII	8.00	8.16	8.39	6.05	7.53	7.59
Pillar tip	8.76	8.22	8.87	6.79	7.65	7.77

3.3.5 Line ratio maps and BPT diagrams

BPT (Baldwin et al. 1981) diagrams compare collisionally excited lines like $[\text{OIII}]\lambda 5007$, $[\text{NII}]\lambda 6584$ and $[\text{SII}]\lambda 6717, 31$ to hydrogen recombination lines ($\text{H}\alpha$, $\text{H}\beta$) and use the forbidden/recombination line ratios as indicators of the number of ionisations per unit volume. The position of an object on a BPT diagram is used for classification purposes, e.g. to distinguish star forming galaxies from active galactic nuclei (AGN), as gas excited by photoionisation rather than shock ionisation occupies different regions in such a diagram. Kewley et al. (2001) combined photoionisation and stellar population synthesis models to put an upper limit on the location of star-forming sources in the BPT diagram. This upper limit is given by a maximum starburst line (labelled as Ke01 in Fig. 3.13, from Kewley et al. 2001) of pure stellar photoionisation models, and galaxies lying above this line are considered AGN dominated because for them to be found here an additional excitation mechanism other than stellar photoionisation is required. Kauffmann et al. (2003) modified the Ke01 plot to account for galaxies that have contribution from both star formation and AGN (labelled as Ka03 in Fig. 3.13, from Kauffmann et al. 2003).

The position on the BPT diagram as a diagnostic tool is widely used for spatially unresolved observations of galaxies or nebulae where the integrated emission of the whole source is used to compute the emission line ratio. BPT diagrams have been used for IFU observations of HII regions (Monreal-Ibero et al. 2011, García-Benito et al. 2010) as well, but since these are spatially resolved observations caution is advised: one is comparing a 3D structure with a 1D photoionisation model, and in a 2D projection of a 3D structure the line ratio will show variations from pixel to pixel because of the local gas conditions along the line of sight on each pixel (Ercolano et al. 2012). Maps of the $[\text{NII}]\lambda 6584/\text{H}\alpha$, $[\text{SII}]\lambda\lambda 6717, 6731/\text{H}\alpha$ and $[\text{OIII}]\lambda 5007/\text{H}\beta$ line ratios are shown in Fig. 3.12.

Here we investigate the commonly used line ratios as indicators of the ionisation structure: $[\text{OIII}]\lambda 5007/\text{H}\beta$ is a tracer of the highly ionised gas and $[\text{NII}]\lambda 6584/\text{H}\alpha$ as well as $[\text{SII}]\lambda\lambda 6717, 6731/\text{H}\alpha$ are tracers of the less ionised gas. The $[\text{NII}]/\text{H}\alpha$ and $[\text{SII}]/\text{H}\alpha$ line ratio maps are quite similar and show significantly higher line ratios at the tip of the pillars as well as on the edges of the wave-like structures in the pillars' main bodies, correlating with the position of the peaks of the localised emission; the $[\text{OIII}]/\text{H}\beta$ ratio on the other hand has its lowest values at the positions of the $[\text{SII}]/\text{H}\alpha$ and $[\text{NII}]/\text{H}\alpha$ peaks, as one would expect in an ionisation picture where the double ionised elements are found in the less dense material more exposed to the ionising radiation rather than in the dense molecular environment shielded from the stellar influence.

Fig. 3.13 shows the $[\text{OIII}]\lambda 5007/\text{H}\beta$ versus $[\text{NII}]\lambda 6584/\text{H}\alpha$ and $[\text{SII}]\lambda\lambda 6717, 6731/\text{H}\alpha$ diagnostic diagrams for the entire observed region (panel a) and for a circular region containing the tip of P2 (panel b), the lines correspond to the maximum starburst lines from Kewley et al. (2001) and Kauffmann et al. (2003) (to better identify structures in panel a, panel c shows a normalised 2D histogram of the panel a). From these diagrams it is clear that the line ratios lie in the the region below Ke01 and therefore in the region where HII regions are expected to be found. Also taking into account the fact that if shocks were strongly contributing to the excitation one would expect $[\text{NII}]/\text{H}\alpha > -0.1$ and $[\text{SII}]/\text{H}\alpha > -0.4$ (Allen et al., 2008) but we do not see values that high, we suggest that the dominant excitation mechanism at the pillar tips is

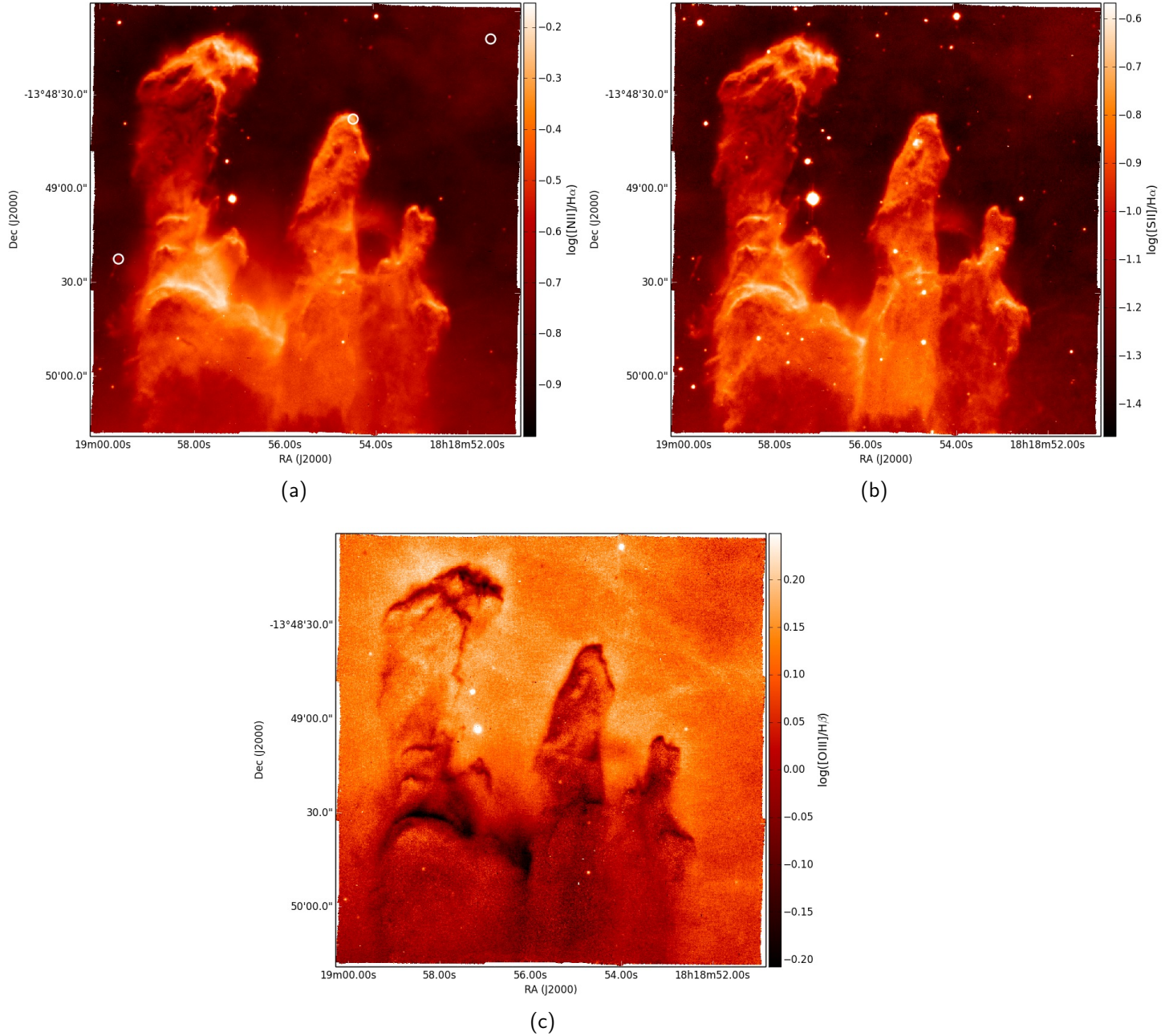


Figure 3.12: Line ratio maps linearly scaled to maximum/minimum: $[\text{NII}]\lambda 6584/\text{H}\alpha$ (a), $[\text{SII}]\lambda\lambda 6717,6731/\text{H}\alpha$ (b) and $[\text{OIII}]\lambda 5007/\text{H}\beta$ (c). The white circles in panel (a) indicate the regions where the co-added spectra were extracted. The leftmost circle also corresponds to the location of the EGG discussed in Section 1.

photoionisation. This agrees very well with the BPT diagrams of our SPH simulations (see Fig. 4 and 5 in Ercolano et al. 2012), where the majority of data points lie in the photoionisation region. The simulated BPT diagrams (Figures 4 and 5 in Ercolano et al. 2012) do however show a small percentage of points lying in the shock-dominated region, but as the simulations do not include shock models these line ratios are due to 3D effects. Fig. 3.14 shows the BPT diagram of the tip of P2 color coded according to the regions identified in Fig. 3.10b.

3.4 Emission line fitting

MUSE's detectors undersample the line spread function, and we therefore proceeded by first normalising and stacking several emission lines in each single pixel (thus assuming that all the lines in one pixel originate from the same emitting gas) and then by fitting the resulting velocity spectrum in each pixel with a gaussian function to produce a velocity map[†]. The lines used for the stacked spectrum are $H\alpha$, the two [NII] lines, the two [SII] lines, [OI] λ 6300,6363 and $HeI\lambda$ 6678. The undersampling of single lines is shown in Fig. 3.15, where the stacked spectrum and spectra of single lines ($H\alpha$, [NII] λ 6548 and [NII] λ 6584 in panel a, $H\beta$ and [SIII] λ 9068 in panel b) are shown, together with the resolution at 4600 Å ($\Delta v = 150 \text{ km s}^{-1}$) and at 9300 Å ($\Delta v = 75 \text{ km s}^{-1}$). The early version of the data reduction pipeline we used did not include a radial velocity correction, and the derived velocities are therefore topocentric. Furthermore, during the observations the sky lines at λ 5577 Å and λ 6300 Å are calibrated with a set of arc lamps, calibration that yields an offset between the arc and observed lines; this offset is then propagated to the rest of the spectrum, but in a linear way such that the wavelength dependency of the correction is lost. This leads to a velocity offset of the red (e.g. [SIII]) and blue (e.g. [OIII], $H\beta$) lines with respect to the lines close to the calibration wavelength which can be seen in Fig. 3.18 (a) and (b), where the topocentric velocities of single emission line species are plotted along the slits shown in Fig. 3.1. Furthermore, when computing local standard of rest velocities from the MUSE data with IRAF and comparing them to velocities obtained from CO observations (Pound 1998, $v_{\text{LSR}} \sim 20 - 30 \text{ km s}^{-1}$), we find that the two are offset by about 20 km s^{-1} , an offset we cannot attribute to a physical origin. Further investigation of the science verification data and the early version of the used data reduction pipeline is needed. Because of these problems we only report relative velocities: for each line emitting species the mean velocity of the HII region was computed, a value which was then subtracted from the whole velocity map of that line. The relative velocities reported are therefore velocities relative to the HII region.

3.4.1 Velocity structure

Based on CO J=3-2 data White et al. (1999a) report complex velocity fields within the pillars and a systematic large scale velocity gradient of about 1.7 km s^{-1} along P2. The resolution of MUSE does not allow the detection of such a small velocity gradient, but Fig. 3.16a shows the

[†]The PYTHON packages SPECTRAL_CUBE (spectral-cube.readthedocs.org) and PYSPECKIT (Ginsburg & Mirocha, 2011) were used for the fitting routine.

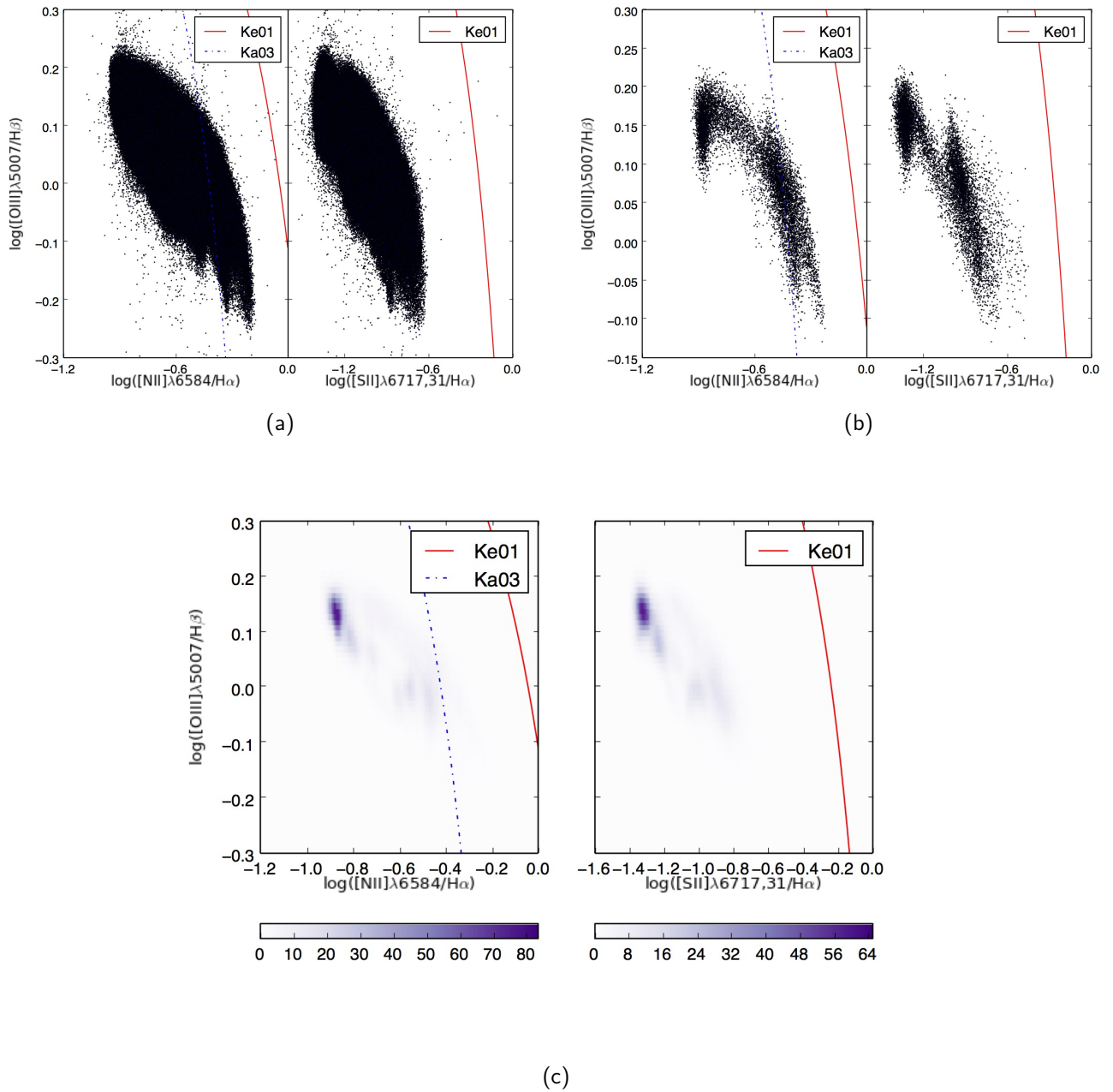


Figure 3.13: Diagnostic BPT diagrams for the entire observed area (panel a) and the tip of P2 only (panel b). Panel c shows a normalised 2D histogram of panel a. See text Section 3.5 for discussion. The Ke01 and Ka03 lines separate regions where photoionisation (below the lines) and AGN feedback (above the lines) dominate. Ka03 accounts for a mixed feedback of both AGN and photoionisation.

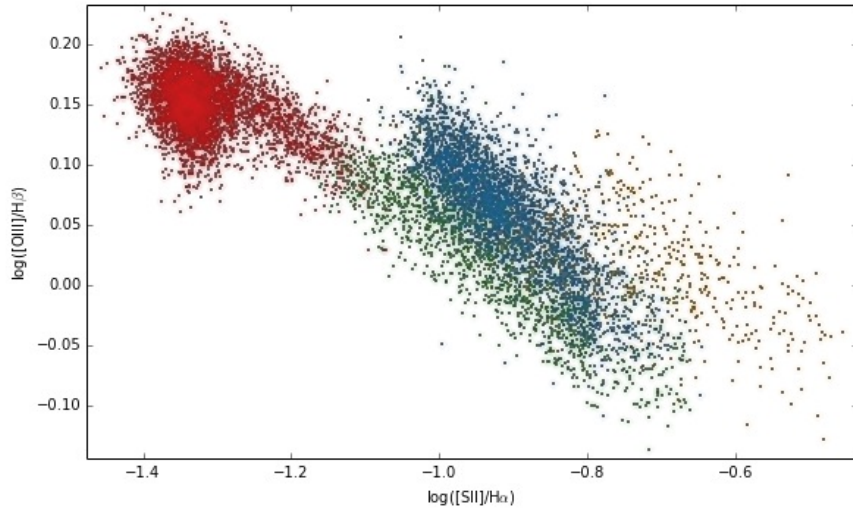


Figure 3.14: BPT diagram of the tip of P2. The colours in panel (a) highlight different populations in the BPT diagram which correspond to the same coloured regions in panel (b).

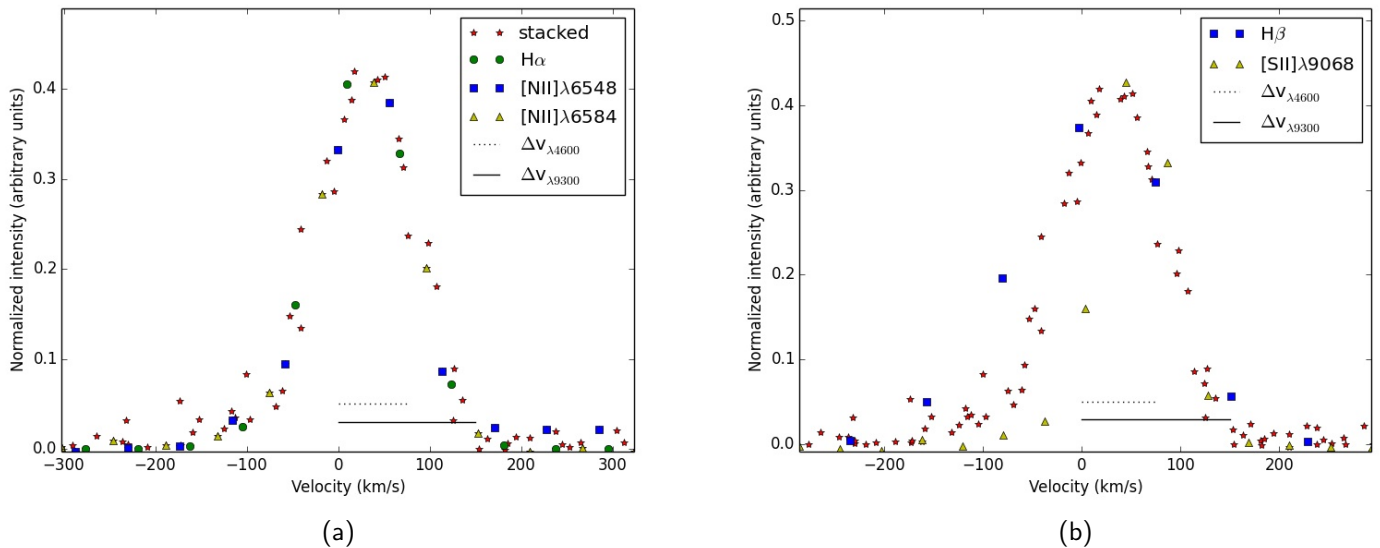


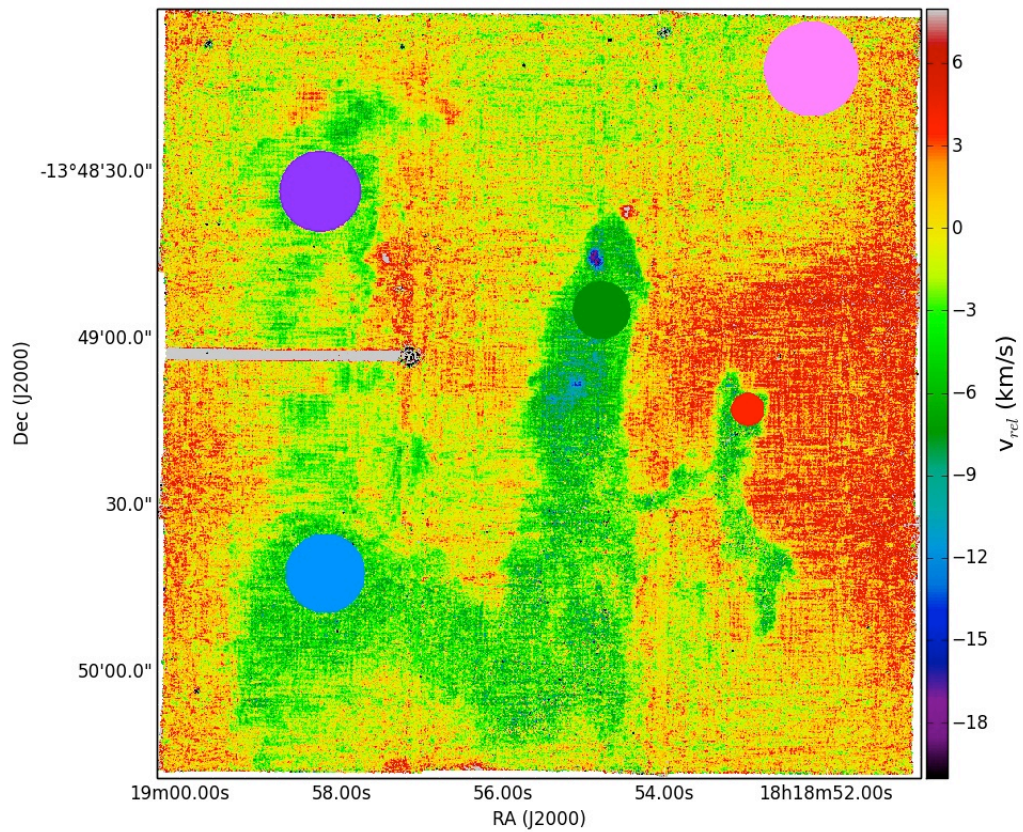
Figure 3.15: Stacked spectrum (red in both panels), shown together with the $H\alpha$ (green circles), $[NII]\lambda 6548$ (blue squares) and $[NII]\lambda 6584$ (yellow triangles) spectra (panel a), as well as the $H\beta$ (blue squares) and $[SIII]\lambda 9068$ (yellow triangles) (panel b). See Section 4 for discussion.

velocity map obtained with the above mentioned emission line fitting. The pillars are clearly distinguishable from the ambient gas, and indeed the pillars are blue-shifted with respect to the surrounding gas because of the photo-evaporative flow along the line of sight that is moving radially away from the pillar surfaces. This means that, when moving from the pillar bodies facing our way along the line of sight to the pillar-ambient interface, we see the pillar border redshifted with respect to the pillar body as a geometrical consequence of the normal vector moving out of the line of sight (this is seen best in P3, and is illustrated in Fig. 3.17). The velocities of the Pillars and the HII region were estimated first by extracting circular regions for each of them via *brushing*[‡] (Fig. 3.16a), and by then fitting the velocity histograms of these regions with Gaussian distributions (Fig. 3.20). They are listed in Table 3.5.

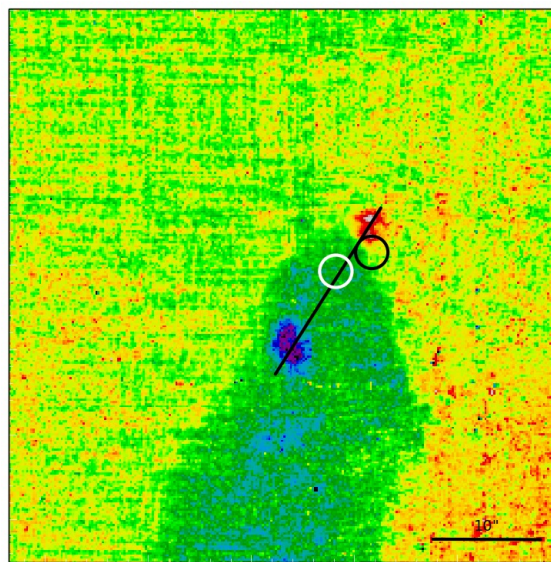
The sulfur-abundant region identified at the tip of P2 via the S_{23} parameter is blueshifted ($v_{\text{rel}} \approx -20 \text{ km s}^{-1}$) with respect to the main pillar body ($v_{\text{rel}} \approx -7 \text{ km s}^{-1}$), as can be seen in Fig. 3.16b, and at the very tip of the same pillar a redshifted region is identified ($v_{\text{rel}} \approx 10 \text{ km s}^{-1}$). The red and blue-shifted regions can be connected with a line with a position angle of approximately 107.3 degrees, on which a source identified as a candidate T Tauri star with a disk-like structure (Sugitani et al. 2002, Sugitani et al. 2007, source M16 ES-2 in Thompson et al. 2002), as well as a water maser (Healy et al., 2004) are found. We suggest that the blue- and redshifted regions trace the two counterparts of a bipolar outflow originating from an accreting protostar or young stellar object. As discussed by Healy et al. (2004), the water maser is too far away from the candidate T Tauri star to be excited by the latter and the two are therefore not associated. With these observations we are unable to say whether the bipolar outflow originates from the T Tauri star or from a deeply embedded object, but considering the fact that the T Tauri star seems to lie somewhat off the hypothetical direction of the jet, we tentatively suggest that the latter is the case. Healy et al. (2004) suggest that the excitation source of the maser is a Class 0 protostar due to the lack of a detected near-IR source, but high angular resolution sub-mm observations are required to identify the maser driving protostar. Optical protostellar jets generally have observed radial velocities from a few tens up to hundreds km s^{-1} (Bally et al., 2007), implying that the one detected here is a low-velocity outflow with $v_{\text{rel, jet}} \approx 20 \text{ km s}^{-1}$. The blue-shifted counterpart is tunnelling its way through the pillar material and is only now starting to emerge, and the redshifted counterpart on the other hand is flowing out from the pillar tip but is immediately dispersed in the strong ionising and unfavourable conditions of the HII region.

We also identify a candidate outflow on the inner side of P1, which is shown in Fig. A10 of the appendix. Also in this case we identify both a blueshifted and a redshifted counterpart in the velocity map that have relative velocities of $\sim -10 \text{ km s}^{-1}$ and $\sim 16 \text{ km s}^{-1}$ respectively. This candidate outflow does not appear to correspond to a sulfur-abundant region and is not seen in the S_{23} map. If this is indeed an outflow, we suggest that the absence of the sulfur-indicator comes from the fact that the blue lobe is only just starting to emerge from the pillar body and did not yet have the time to ionise atoms with $E_{\text{ion}} \geq E_{\text{ion, [SII]}} = 10.36 \text{ eV}$. Healy et al. (2004) do not detect water masers in P1, but Sugitani et al. (2002) identify candidate T Tauri star

[‡]The technique of *brushing*, also known as *graphical exploratory data analysis* allows the user to manually select specific data points or subsets from an image or a plot by interactively drawing regions on the latter two.



(a)



(b)

Figure 3.16: Map of relative velocity (to the the HII region) of the entire mosaic (panel a) and a zoom-in on P2 (panels 2). The coloured circles in panel (a) correspond to the regions used for the histograms in Fig. 3.20. The black line in panel (b) corresponds to a hypothetical orientation of the bipolar outflow with position angle 107.3 degrees, the black circle is centred on the coordinates of the candidate T Tauri star, while the white circle corresponds to the water maser detected in March 2002 by Healy et al. 2004 (see text Section 4.1).

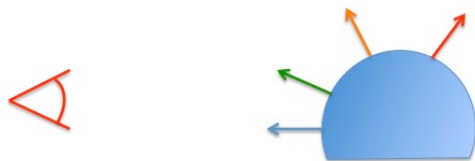


Figure 3.17: Sketch of the normal velocity vector, corresponding to the photo-evaporative flow, to demonstrate that the pillar tips appear redshifted with respect to the main pillar bodies because of the geometrical effect of the vector component along the line of sight (see text Section 4.1).

right outside the pillar which corresponds to a continuum source in Fig. 3.2.

The presence of ongoing star formation is also observed in our SPH simulations (Gritschneider et al. (2010a) and Fig. A9), where 4 objects have formed at the pillar tips and are still present 0.5 Myr into the simulation. These objects all have angles of 20-50 degrees between the disk (or accretion feature) and the direction of radiation (which in the simulations is roughly perpendicular to the long axis of the pillars). Raga et al. (2010) simulated outflows from stars forming at the tips of pillars and find that the orientation of the outflows depends on the orientation of the pillars along the line of sight. For pillars that are seen face on, the projected outflow orientations are found to be perpendicular to the main pillar axes. Then again, Smith et al. (2010a) report that in their HST Herbig-Haro jet sample the outflows are not preferentially found to be perpendicular to the pillars. Here, the projected outflow orientation with respect to the P.A. of $\sim 137^\circ$ of P2 is $\sim 30^\circ$, which corresponds to an angle of only $\sim 7^\circ$ between outflow and the direction of radiation. The disk of the jet-driving source is thus supposedly perpendicular to the incident radiation, which contradicts what is found from the simulations, where the accretion disks of the forming sources are preferentially aligned with the direction of radiation (Gritschneider, in preparation).

Knowing that the ionisation structure of the photo-evaporative flow is (spatially) stratified, the question whether these emission lines are also offset in position-velocity space occurs naturally. Fig. 3.18 (panels c and d) shows the relative velocity[§] of the single atomic species (obtained by simultaneously fitting all the detected lines for each species) of P2 and P3 along the same slits used for the intensity profiles shown in Fig. 3.6. The pillar-ambient interface is clearly recognisable from the dip in velocity of ~ 7 and 10 km s^{-1} for P3 and P2 respectively, the dip toward bluer velocities occurring because we are probing the radially outward directed photo-evaporative flow which is thus moving toward us along the line of sight. The neutral [OI] line does not follow the same rise-and-fall profile as the ionisation-tracing lines, while the [OII] lines are not shown, as their weak intensity to produce a reliable velocity map. Panels (a) and (b) of Fig. 3.18 show the uncorrected (topocentric) line of sight velocity: the redshift of the [SIII] line and the blueshift of the $H\beta$ and [OIII] lines are due to the wavelength calibration in the MUSE pipeline, as described at the beginning of this section. Fig. 3.19 shows the

[§]relative to the HII region

analogous plot for a synthetic pillar: the profile seen in the observations is well recovered by our simulations, but the magnitude of the blueshift is of the order of about $3 - 5 \text{ km s}^{-1}$. As already discussed, we don't expect the simulations and the observations to agree quantitatively because of the different physical conditions.

3.4.2 Geometry

Another interesting open question is the 3D geometry of the Pillars and their spatial orientation with respect to NGC 6611, and because for the first time we have the velocity information combined with an extinction map and integrated line intensities for the entire structures, this can now be addressed. In our attempt to understand the geometry of the Pillars, we consider the following:

- from the integrated intensity and electron density maps it is clear that ionisation mainly occurs at the tip of P1 and P2, that P3 seems to be less exposed to the ionising radiation on the side we can see, and that the exposed protrusions along P1 are also being (though somewhat less than the tip) ionised
- the extinction map (Fig. 3.4b) shows a gradient from P1 (most extinction) to P3 (least extinction)
- the tips of P1 and P2 are seen as reflection nebulae in the continuum 3-color composite (Fig. 3.2), while P3 is more seen as a silhouette illuminated from behind
- the three pillars have different velocities, as is shown in Fig. 3.20 and Table 3.5
- the velocity of the lower part of P1 is consistent with the velocity of P2 and P3, and seems inconsistent with the upper part of P1

With molecular line data, Pound (1998) find that P1 is in reality composed of two separate parts, the upper part (P1a) being behind the ionising stars of NGC 6611 with a tail inclined away from us and the lower part (P1b) being in front of them with its tail is inclined toward us. P2 is a single structure with its tail pointing toward us, while for P3 their data is inconsistent and inconclusive. From our observations it is clear that P1a is the least blue-shifted and the most extinguished of the three pillars, and its tip shows the highest degree of ionisation. Together with the positive velocity gradient reported in Pound (1998) and the fact that the protrusions along its body show weak signs of ionisation, we confirm that P1a is behind the ionising O stars and its tip is pointing toward us along the line of sight, while P1b is in front of the stars and inclined with its tip pointing away from us. Because of the lack of ionisation along their bodies, we suggest that both P2 and P3 are also in front of the ionising sources, that P3 is closer to the observer but because it is slightly less blue-shifted and its tip shows less ionisation than P2, it is inclined with its tip pointing toward us, while the opposite is true for P2. We sketch this in Fig. 3.21 to make it easier for the reader to visualise.

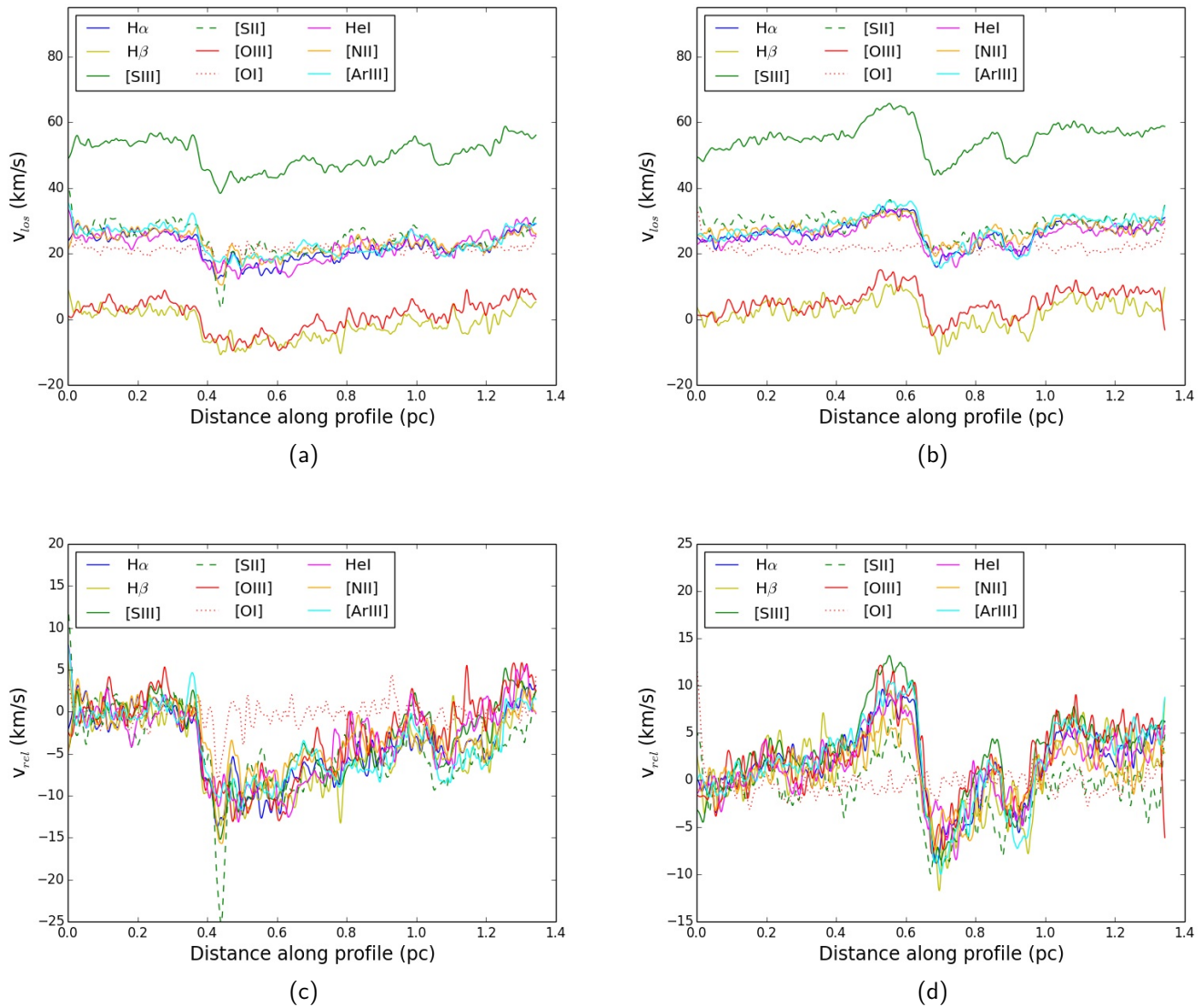


Figure 3.18: Velocity profile of P2 (panels a and c) and P3 (panels b and d) along the same slits as Fig. 3.6. The lines are: $H\alpha$ (blue), $H\beta$ (yellow), $[SIII]9068$ (solid green), $[SII]6717,31$ (dashed green), $[OIII]4969,5007$ (solid red), $[OI]5577,6300$ (dotted red), HeI 5876,6678 (magenta), $[ArIII]7135,7751$ (cyan), $[NII]6548,6584$ (orange). Panels (a) and (b) show the observed line of sight velocity (not corrected for radial velocity) with the wavelength-dependent offset between the red ($[SIII]$), blue ($[OIII]$, $H\beta$) and green (rest) lines originating from the wavelength calibration applied during the observations (see text). Panels (c) and (d) are the same as the other two, but the velocities are now relative to the mean velocity of the region between 0 and 0.2 pc (corresponding to the HII region). See text Section 4.1 for discussion.

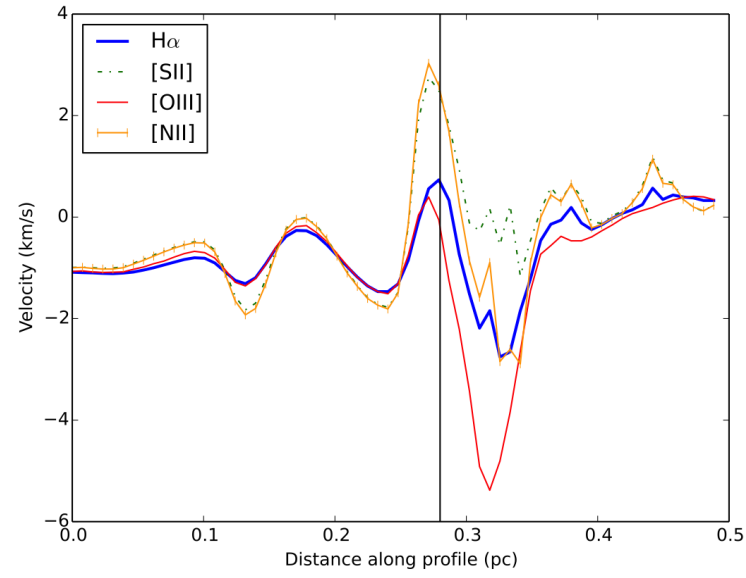


Figure 3.19: Velocity profile of a simulated pillar along the same slit as Fig. 3.7b.

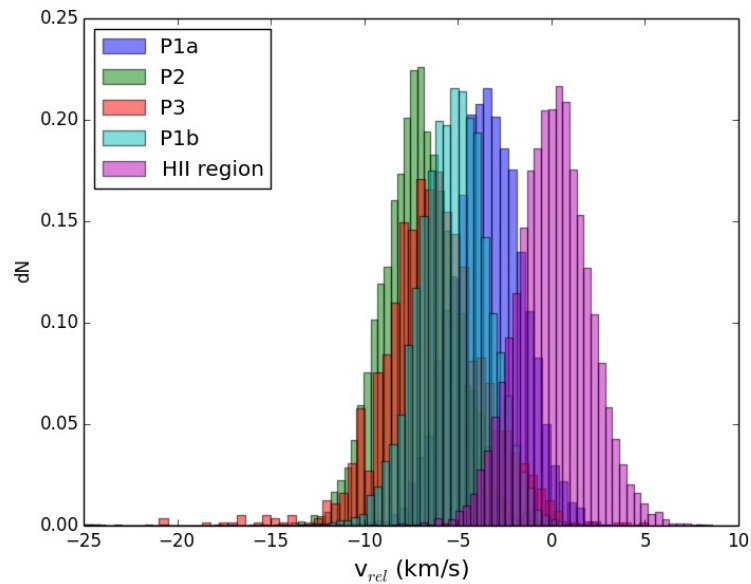


Figure 3.20: The histograms of the velocity (relative to the HII region, see Section 4.1) of the pillars and the HII region obtained from circular regions extracted from the velocity map.

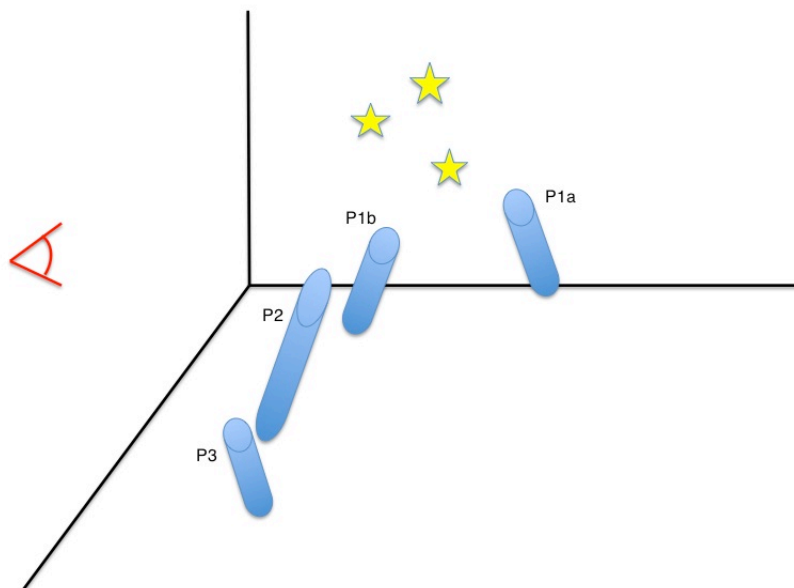


Figure 3.21: Sketch of the 3D geometry of the Pillars of Creation with respect to the ionising stars in NGC 6611 (not to scale). See text Section 4.2.

Table 3.5: Line of sight velocities relative to the HII region derived from fitting gaussian distributions to the histograms in Fig. 3.20 (see Section 4.1).

	P1a	P1b	P2	P3
$v_{\text{rel}} \text{ (km s}^{-1}\text{)}$	-3.43	-5.34	-7.14	-6.62

3.4.3 Mass loss rate and lifetime

Because forbidden lines such as [OI] λ 6300 or [SII] λ 6731 are optically thin they can be used to estimate the mass of the line emitting matter, since the line luminosity is proportional to the number of line emitting atoms along the line of sight. For the pillar-ambient interface region ($T_e \approx 11870$ K, $N_e \approx 2800$ cm $^{-3}$, Fig. 3.8), the ionisation fraction is $f_{\text{ion}} \sim 0.01$ and the critical density is $N_{c,[\text{SII}]\lambda 6731} \cong 3.9 \times 10^3$ cm $^{-3}$, and therefore $N > N_c$. Because the signal-to-noise ratio is much higher for the [SII] line than for the [OI] line, we use the former to derive the mass loss rate of the pillars. This line originates from the transition from the $^2\text{D}_{3/2}$ (level 1) to the $^4\text{S}_{3/2}$ (level 2) transition which occurs with a rate $A_{21} = 8.8 \times 10^{-4}$ s $^{-1}$ (Osterbrock & Ferland, 2006). Following the method described in Hartigan et al. (1995), we compute the mass of the line emitting matter with expressions for the luminosity L_{6731} of the [SII] λ 6731 line and the total number of sulfur atoms in the lower level, η_1

$$L_{6731} = \frac{g_2}{g_1} \eta_1 \exp\left(-\frac{h\nu_{12}}{kT}\right) \left(1 + \frac{N_c}{N_e}\right)^{-1} A_{21} h\nu_{21}$$

and

$$\eta_1 = \left[\frac{\eta_1}{\eta(\text{S})} \right] \left[\frac{\eta(\text{S})}{\eta(\text{H})} \right] \left[\frac{\eta(\text{H})}{\eta_{\text{tot}}} \right] \frac{M_{\text{tot}}}{\mu m_{\text{H}}}$$

which correspond to equations A2 and A5 in Hartigan et al. (1995) and where $g_1 = g_2 = 4$ are the statistical weights of the two levels, $h\nu_{12} = 2.95 \times 10^{-12}$ erg is the energy of the transition, $\eta(\text{S})/\eta(\text{H}) = 5.88 \times 10^{-5}$ (Table 4.2), $\eta_1/\eta(\text{S}) \approx 0.9$ (computed with the IRAF task `ionic`), and assuming $\eta(\text{H})/\eta_{\text{tot}} \approx 0.921$ and $\mu = 1.24$ (Allen, 1973). With an electron density of 2800 cm $^{-3}$ and a temperature of about 10 4 K characteristic for the pillar tips, the mass of the line emitting matter then becomes

$$M \simeq 2.69 \times 10^{-4} \left(1 + \frac{N_c}{N_e}\right) \left(\frac{L_{6731}}{L_{\odot}}\right) M_{\odot}$$

The mass loss rate can then be computed via $\dot{M} = Mv/l$, where v is the velocity of the photo evaporative outflow and l the average size of the line emitting region. In order to estimate the total luminosity of the [SII] λ 6731 line we subtracted the stellar continuum in the [SII] λ 6731 integrated intensity map and summed the line intensity of all pixels to obtain $L_{6731} \cong 130 L_{\odot}$. With $v \approx 8$ km s $^{-1}$ from the velocity map in Fig. 3.16 and $l \cong 3 \times 10^{16}$ cm (measured from the SII intensity map), $\dot{M} \approx 70 M_{\odot} \text{ Myr}^{-1}$. With a total mass of the pillars of $M_{\text{tot}} \sim 200 M_{\odot}$ (White et al., 1999a), we estimate the lifetime of the pillars to be approximately 3 Myr. This however is an upper limit, as the [SII] line may not be tracing the bulk flow and we therefore might be underestimating the mass loss rate. Pound (1998) estimated the expected lifetime of the Pillars to be about 20 Myr, but as suggested by Westmoquette et al. 2013 (who find a lifetime of about 2 Myr for pillars near NGC 3603) we believe that the used value of the curvature radius was too small, so they overestimated the lifetime.

We suggest that the identified outflow will not contribute significantly to the mass loss rate. Indeed, we compute the mass of the outflow to be $\dot{M} \cong 0.29 M_{\odot} \text{ Myr}^{-1}$ (with $N_e \sim 1400 \text{ cm}^{-3}$, $L_{6731} \simeq 0.18 L_{\odot}$), which is only $\sim 0.4 \%$ of the total mass loss rate.

3.5 Conclusions

For the first time the Pillars of Creation were imaged using optical integral field spectroscopy. This technique allowed us to map the entire structures and obtain medium resolution spectra for each pixel in the 3x3 arcmin mosaic, which were fitted with Gaussian profiles to produce integrated line and line of sight velocity maps in many spectral lines. Also, we computed physical parameters such as the electron density, the electron temperature and the extinction for the entire mosaic.

In agreement with Pound (1998), we find that the three Pillars are actually 4 distinct structures that lie at different distances along the line of sight and have different inclination angles, some pointing away and others pointing toward the observer. The consequence of their position and inclination is a different degree of ionisation not only of the pillar tips, but also of the pillar bodies. We therefore see the strongest emission from ionised species from the tip of P1a, which is pointing toward us but lies behind the ionising O stars of NGC 6611 and we therefore see weak emission coming from the exposed structures along its body as well. This we do not see in P1b, P2 and P3, as these all lie in front of the ionising stars, and furthermore for P1b and P2 because they are inclined with their tips facing away from the observer and their tails pointing to us. The effect of their different inclination angles is that the 4 structures show different velocities: all of them are blue-shifted with respect to the ambient HII region because we are tracing the photo-evaporative flow, but because this flow is normal to their surfaces, we will see them at different velocities.

The kinematic analysis also allowed us to reveal a possible protostellar outflow at the tip of P2. Of this outflow, we can identify both lobes as a blue and a redshifted counterpart. The jet seems to be almost parallel to the incident ionising radiation, in fact it is inclined by only 7 degrees with respect to the pillar body and the radiation. This does not seem to agree with what we find in our smoothed particle hydrodynamic simulations, in which we also find stars forming at the pillar tips, but their accretion disks are preferentially aligned with the direction of radiation. We explain this by arguing that the angle between the outflow and the pillar bodies is the consequence of projection effects, as is discussed in Raga et al. (2010). The outflow is clearly traced by the S_{23} parameter, which, if plotted against an indicator of the degree of ionisation such as $[\text{OII}]/[\text{OIII}]$, can be used in future studies with IFU data of star forming regions to detect outflows in dense molecular material. In our data this is the only outflow we can detect in both the velocity map and via the S_{23} parameter. From the kinematics we also identify a candidate outflow on the inner side of P1, which however does not show a sulfur abundance. Using IFU data it would be interesting to apply this method to other star forming regions that have an embedded young stellar population to look for outflows that have not yet fully emerged from the molecular material and would therefore have been missed in previous studies. Furthermore, the outflow and its driving source would be an interesting target for the

Atacama Large Millimeter/submillimeter Array, which has the required high sensitivity and the frequency coverage to analyse the velocity field and the outflow in great detail.

The Pillars show a classical stratified ionisation structure in which line emitting species peak in a sequential manner throughout the ionisation interface of the molecular material, in agreement with previous authors. Typical electron densities at the pillar tips are $> 2000 \text{ cm}^{-3}$, whereas the electron temperature in this region is in the 8000 K - 10 000 K range. The comparison with our SPH+radiative transfer computations is encouraging, as we are able to reproduce the ionisation structure, the kinematics and physical parameters. Finally, by computing the mass of the [SII] line-emitting gas, we estimate the mass loss rate to be of about $70 M_{\odot} \text{ Myr}^{-1}$, which, assuming the total mass of the Pillars to be $\sim 200 M_{\odot}$, yields an expected lifetime of about 3 Myr, timescale which does not depend of the presence of an outflow at the tip of the middle pillar.

4

Feedback in the central Orion Nebula: the classical H II region

*Published as McLeod, Weilbacher, Ginsburg, Dale et al., MNRAS, 2016, 455, 4057;
"A nebular analysis of the central Orion nebula with MUSE",**

Abstract

A nebular analysis of the central Orion Nebula and its main structures is presented. We exploit MUSE integral field observations in the wavelength range 4595-9366 Å to produce the first O, S and N ionic and total abundance maps of a region spanning 6' × 5' with a spatial resolution of 0.2". We use the S_{23} ($= ([\text{SII}]\lambda 6717,31 + [\text{SIII}]\lambda 9068)/\text{H}\beta$) parameter, together with $[\text{OII}]/[\text{OIII}]$ as an indicator of the degree of ionisation, to distinguish between the various small-scale structures. The only Orion Bullet covered by MUSE is HH 201, which shows a double component in the $[\text{FeII}]\lambda 8617$ line throughout indicating an expansion, and we discuss a scenario in which this object is undergoing a disruptive event. We separate the proplyds located south of the Bright Bar into four categories depending on their S_{23} values, propose the utility of the S_{23} parameter as an indicator of the shock-contribution to the excitation of line-emitting atoms, and show that the MUSE data is able to identify the proplyds associated with disks and microjets. We compute the second order structure function for the $\text{H}\alpha$, $[\text{OIII}]\lambda 5007$, $[\text{SII}]\lambda 6731$ and $[\text{OI}]\lambda 6300$ emission lines to analyse the turbulent velocity field of the region covered with MUSE. We find that the spectral and spatial resolution of MUSE is not able to faithfully reproduce the structure functions of previous works.

4.1 Introduction

The Orion Nebula (M 42) is the closest Galactic H II region and corresponds to one of the most observed objects in the sky. It therefore not only serves as a template for the comparison with observations of other (Galactic and extragalactic) H II regions, but also as a very good

*This work is the result of collaborative efforts of the authors of the paper. Specifically, I was responsible for the entire data analysis and interpretation, as well as the manuscript preparation. Weilbacher is responsible for the data reduction (see also Weilbacher et al. 2015), and the other co-authors contributed with valuable insight on the interpretation of the results and in proof-reading the manuscript.

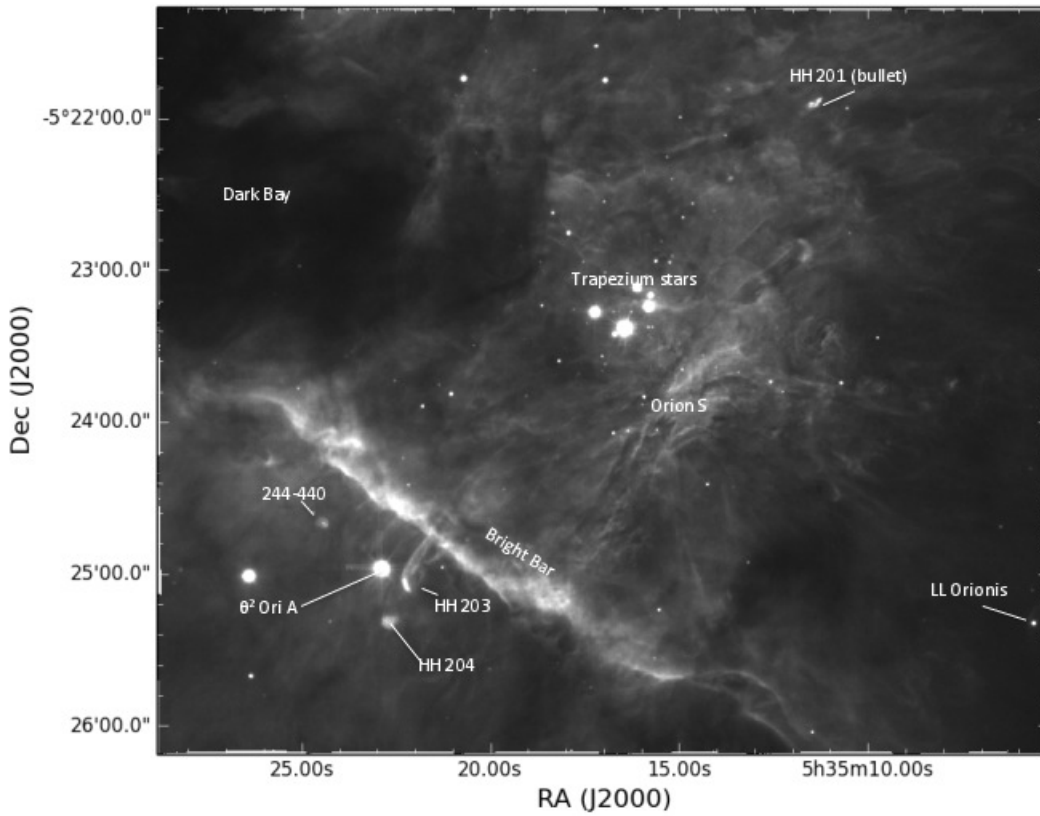


Figure 4.1: The most commonly discussed features of the central Orion Nebula on a MUSE non-continuum subtracted, integrated intensity map of $[\text{SII}]\lambda 6717$.

testing ground for new instruments. The number of papers written about M 42 in the last six decades is in the three digit regime, demonstrating how important and how well studied this region is. A thorough review of the main features, the geometry, the population of stars, the outflows and the main physical aspects of the H II region conditions is given in O'Dell (2001).

The central part of M 42 is a treasure chest for star formation feedback studies: it is home to four massive stars (one O- and three B-type stars) that make up the so called Trapezium cluster, of which θ^1 Ori C (of spectral type O7 Parenago 1954, van Altena et al. 1988) is the most luminous. These stars are ionising the surrounding material and giving rise to the vast number of detected nebular emission lines which trace ionisation fronts such as the Bright Bar and the Orion S cloud. Furthermore, because of the ongoing star formation in the region, it hosts many optical Herbig-Haro (HH) and molecular outflows, as well as a large population of young stellar objects called *proplyds* (short for protoplanetary disk, O'Dell & Wen 1994). The three-dimensional structure of this region is that of a blister-like H II region in front of the Orion Molecular Cloud (OMC-1), where the emitting region is ~ 0.1 pc thick and 1 pc in lateral dimension (O'Dell, 2001). The most common features of this region are shown in Fig. 4.1, in an integrated $[\text{SII}]\lambda 6717$ map.

Because of its vicinity (~ 420 pc, Schlafly et al. 2014), in combination with the fact that it is associated with recent star formation and a comparatively high surface brightness, it is the perfect object to study elemental abundances and therefore help understand not only the chemical evolution of the interstellar medium (ISM), but also the process of nucleosynthesis. Many studies have been dedicated to the elemental abundances in the Orion Nebula using slit spectroscopy (e.g. Osterbrock et al. 1992, Esteban et al. 1998, Esteban et al. 2004, Mesa-Delgado et al. 2008), finding that the abundances of heavy elements in Orion are only somewhat higher than solar ones. In the era of integral field spectroscopy, new studies have emerged that exploit the combination of simultaneous imaging and spectroscopy on large spatial and spectral scales (e. g. Sánchez et al. 2007, Mesa-Delgado et al. 2011). A common analysis in the study of H II regions is given by line ratios of nebular emission lines which are used as abundance tracers (e.g. [NII]/H α , [SII]/H α tracing the nitrogen and sulphur abundances respectively) or as tracers of the degree of ionisation (e.g. [OII]/[OIII]). Another sulphur abundance parameter computed for both Galactic and extragalactic H II regions is given by $S_{23} = ([SII] + [SIII])/H\beta$ (Vilchez & Esteban, 1996a), which is commonly used to determine star formation histories and evolutionary scenarios, as this parameter is found to vary as a function of position within a galaxy. Together with [OII]/[OIII], S_{23} can also be used to analyse the ionisation structure of H II regions (García-Benito et al., 2010). Together with a spatially resolved velocity map, the combination of the S_{23} parameter and [OII]/[OIII] has been used by McLeod et al. (2015) (MC15 henceforth) to detect a previously unknown outflow in the famous Pillars of Creation in the Eagle Nebula (M 16) in MUSE science verification observations, as the location where the outflow is currently emerging from the pillar material has distinctively high S_{23} and low [OII]/[OIII] values. Future MUSE observations will determine whether this new method can be used to detect outflows in molecular cloud structures. In this work, we exploit this method to characterise the outflow and propylid population in M 42.

The same nebular emission lines used to determine ionic and total abundances have also been used to study the turbulent motions in M 42 with a statistical approach by computing the second order velocity structure function, generally defined as $S_2(\mathbf{r}) = \langle |\mathbf{v}(\mathbf{r}') - \mathbf{v}(\mathbf{r}'')|^2 \rangle$ (where $\mathbf{r} = \mathbf{r}' - \mathbf{r}''$ is the separation between any given pair of points), and comparing the shape of the structure function to that of theoretical models of turbulence (e. g. Kolmogorov 1941, von Hoerner 1951). The main studies about structure functions in Orion used the [OIII] (Castaneda, 1988), the [OI] (O'Dell & Wen, 1992) and later the [SIII] lines (Wen & O'Dell, 1993), which show that the structure function has a steep slope at small values of r and a transition scale after which the slope is shallower for larger values of r , except for [OI] where the slope is seen to remain constant over almost all measured scales. In general, the cited studies indicate similarities between the observations and the von Hoerner predictions (see Section 4 and O'Dell (2001)).

The new optical integral field unit (IFU) MUSE at the VLT offers, for the first time, a very powerful combination of sub-arcsecond spatial resolution and medium spectral resolution over a field of view of $1' \times 1'$ and a large spectral range. With this instrument it is now possible to compute not only ionic and elemental abundance maps, but also compute velocity information from the same observations in an unbiased manner for a very large field. In this work we derive the abundance maps of oxygen, nitrogen and sulphur, analyse how the S_{23} and

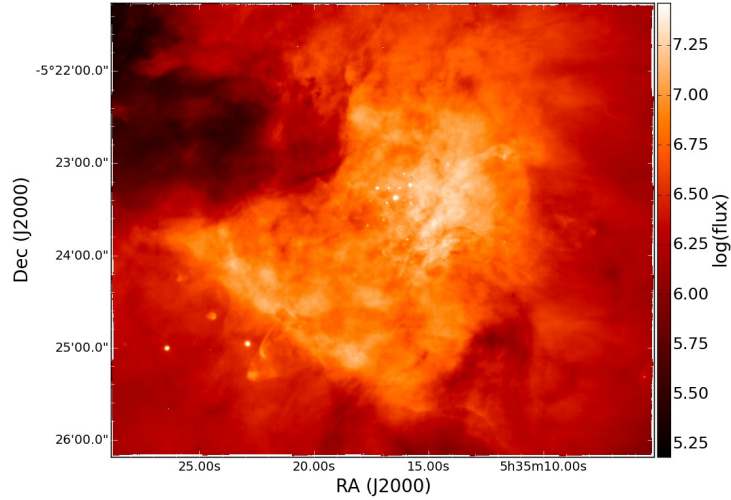


Figure 4.2: $H\alpha$ continuum-subtracted integrated intensity map, linearly auto-scaled (the flux is measured in $10^{-20} \text{ erg s}^{-1} \text{ cm}^{-2} \text{ pixel}^{-1}$).

$[\text{OII}]/[\text{OIII}]$ emission line ratios vary across the central part of the Orion Nebula and how one can use them to distinguish between the different types of outflows. Furthermore, we attempt a kinematical analysis by computing the second order structure function. This work demonstrates the potential of IFU spectroscopy to probe different types of feedback mechanisms (ionisation, jets/outflows) with a combination of line ratios, kinematics and physical properties. The paper is organised as follows: we briefly present the observations in Section 4.2, compute and discuss the abundance and line ratio maps of the entire mosaic in Section 4.3; the structure functions are discussed in Section 4.4, while in Section 4.5 we present detailed studies of several selected regions. Finally, the conclusions are presented in Section 4.6.

4.2 IFU observations

The MUSE integral field observations of the Orion Nebula were taken during the instrument's commissioning run (Bacon et al., 2014) on February 16th, 2014. The $6' \times 5'$ mosaic consists of 60×5 seconds exposures, where each of the 30 mosaic pointings was observed twice with a 90 degree rotation dither pattern. The data reduction was carried out in the ESOREX environment with the MUSE pipeline (Weilbacher et al., 2012a). For a detailed description of the data reduction we refer to Weilbacher et al. 2015 (W15 henceforth). The observations were carried out in the Wide Field Mode with a field of view of $1' \times 1'$, in the wavelength range 4595 - 9366 Å and a sampling of $0.2'' \times 0.2'' \times 0.85 \text{ Å}$. An integrate intensity map of $H\alpha$ is shown in Fig. 4.2. Maps of other emission lines, as well as maps of the most relevant physical parameters (e. g. electron density, electron temperature, extinction) are shown and discussed in W15.

4.3 Abundance maps

4.3.1 Ionic and total abundances

Abundance determination in the Orion Nebula is supported by a long record of publications dating back to the last century (e. g. Peimbert & Torres-Peimbert 1977, Rubin et al. 1993, Baldwin et al. 1991, Esteban et al. 1998, Sánchez et al. 2007, Mesa-Delgado et al. 2011), and it serves as the comparison ground for abundances in other extra- and galactic H II regions. One of the major problems in determining abundances is the dependence of line emissivity on the electron temperature T_e : the emissivity of recombination lines (RLs) decreases with increasing T_e , while the emissivity of collisionally excited lines (CELs) increases with T_e in an exponential manner (O'Dell, 2001). This means that in the case of temperature inhomogeneity along lines of sight (as is the case for Orion, Peimbert 1967) different regions will be more or less sensitive to RLs or CELs, and ratios of RLs are therefore preferentially used to determine abundances because of their weaker dependence on temperature. As the RLs covered by MUSE ($\text{OII}_{\lambda 4650}$ and $\text{OII}_{\lambda 4661}$) tend to be very weak and noise-dominated, in this work we only make use of CEL line ratios to determine abundances.

The large spatial and spectral coverage of MUSE offers the first unbiased possibility of computing ionic abundance maps for many atoms simultaneously. For this, we used integrated intensity maps, corrected for extinction as described in MC15 with $R_V \approx 5.5$, using the python package PYNEB (Luridiana et al., 2015a) together with the electron density and temperature maps derived in W15. The atomic data used for the computations are shown in Table 4.1. The oxygen abundance ratios O^+/H^+ and O^{++}/H^+ were computed from the $[\text{OII}]\lambda 7320,30$ and $[\text{OIII}]\lambda 4959,5007$ lines respectively and assuming $T([\text{OII}]) \sim T([\text{NII}])$ and $T([\text{OIII}]) \simeq T([\text{SIII}])$, as MUSE does not cover the $[\text{OII}]\lambda 3727,29$ and $[\text{OIII}]\lambda 4363$ lines to compute $T([\text{OII}])$ and $T([\text{OIII}])$. The $[\text{SII}]$ electron density map was used for the abundance determination. The $[\text{OII}]\lambda 7320,30$ lines are generally low in intensity and can suffer from the contamination of OH rotational line emission at 7330 Å, and, as stated in W15, the MUSE Orion data cube was not corrected for sky background. However, the nebular emission in the central Orion Nebula is very bright compared to the sky, and the maximal contribution of sky emission to the measurements is of 5% to the $[\text{OII}]$ lines. Because in the outer regions (e.g. the Dark Bay) the $[\text{OII}]$ lines, as well as the $[\text{SII}]$ and the $[\text{NII}]\lambda 5755$ lines are significantly weaker and the level of noise very high, we masked the emission line maps used to compute the abundance based on the flux of the weakest lines of the three species ($[\text{OII}]\lambda 7330 > 4 \times 10^{-16} \text{ erg s}^{-1} \text{ cm}^{-2} \text{ pixel}^{-1}$, $[\text{SII}]\lambda 6717 > 4 \times 10^{-16} \text{ erg s}^{-1} \text{ cm}^{-2} \text{ pixel}^{-1}$, $[\text{NII}]\lambda 5755 > 4 \times 10^{-17} \text{ erg s}^{-1} \text{ cm}^{-2} \text{ pixel}^{-1}$). The sulphur abundance was computed with $[\text{SII}]\lambda 6717$, $[\text{SII}]\lambda 6731$ and $[\text{SIII}]\lambda 9068$, while for nitrogen we made use of the $[\text{NII}]\lambda 5755$, $[\text{NII}]\lambda 6548$ and $[\text{NII}]\lambda 6584$ lines. To account for undetected lines corresponding to higher ionisation states we adjust the abundance determination with the appropriate ionisation correction factors (ICF), according to Hägele et al. (2008) for sulphur and Esteban et al. (1998) for nitrogen.

The abundance maps are shown in Fig. 4.3 through Fig. 4.5 (the stellar emission has been removed from these maps by fitting and subtracting the continuum on a pixel-by-pixel basis, stars that were saturated appear as white in the images because they are masked out). Mean

Ion	Transition probability	Collision strength
O ⁺	Zeippen (1982)	Pradhan et al. (2006)
	Wiese et al. (1996)	Tayal (2007)
O ⁺⁺	Wiese et al. (1996)	Aggarwal & Keenan (1999)
	Storey & Zeippen (2000)	
S ⁺	Podobedova et al. (2009)	Tayal & Zatsarinny (2010)
S ⁺⁺	Podobedova et al. (2009)	Tayal & Gupta (1999)
N ⁺	Galavis et al. (1997)	Tayal (2011)

Table 4.1: Atomic data used in PYNEB for the ionic abundance determination.

values for circular regions (with a radius of 2.5") of the Trapezium cluster and the Bright Bar, as well as of a 8.5"x3" box as to match the slit Position 2 in Esteban et al. (1998) are shown in Table 4.2 (to distinguish between our extraction and the actual slit used in Esteban et al. 1998, we label the latter as P2E and the region used for this work as P2). Also shown in the same table are ionic and total abundances obtained by Esteban et al. (2004) (henceforth referred to as E04) for P2.

The total abundance maps computed from the MUSE data show a certain degree of structure: the Bright Bar, the Orion S region, the HH 203 and 204 objects, as well as some of the proplyds are clearly seen in the maps. The fact that the abundances are not constant across the nebula but show a certain degree of structure has already been discussed in Mesa-Delgado et al. (2011) (henceforth referred to as MD11) and Núñez-Díaz et al. (2012). Specifically, MD11 find that for the Bright Bar (BB) their mean value of 8.49 ± 0.03 for the O/H ratio agrees with previous estimates of 8.50 (e.g. Esteban et al. 1998, Blagrove et al. 2006), that the spatial variation of O/H in the BB varies within the computed typical error, while the range of O/H values is slightly higher for the Orion S region. They also find a coincidence of the lowest O⁺⁺/H⁺ values with the largest electron temperature uncertainties, the highest total oxygen abundance values in spatial agreement with the higher ionic O⁺/H⁺ abundance values, and a structural similarity of O⁺/H⁺ and O/H to the electron density (N_e) map, indicating a strong dependence of the oxygen abundance on the physical parameters. They suggest two possible explanations for this: (i) possibly, the N_e derived from the [SII] lines is not appropriate for the determination of O⁺/H⁺, as it does not reflect the true density of the O⁺ zone; (ii) although reflecting the physical conditions of both S⁺ and O⁺, the computed N_e values do not correspond to the true values in regions like the BB or Orion S, as in these regions the density approaches the critical density of the [SII] and [OII] lines, and higher N_e values are computed. In fact, these authors discuss how, by correcting the N_e to lower values, they recover the mean value for the O abundance. Without any additional information about specifically where to apply such correction, we show uncorrected maps.

To test the reliability of the abundances obtained in this work, we extract a 16"x16" sub-region of the BB, matching the observations of MD11. For the entire sub-region, we find a mean O/H ratio of 8.60 ± 0.09 , which is higher than the typical Orion O/H ratio of 8.50. We also compare our temperature, density, O⁺/H⁺ and O⁺⁺/H⁺ of the sub-region with MD11, and find that our N_e map (derived from the [SII] lines) shows: (i) lower values, typically of

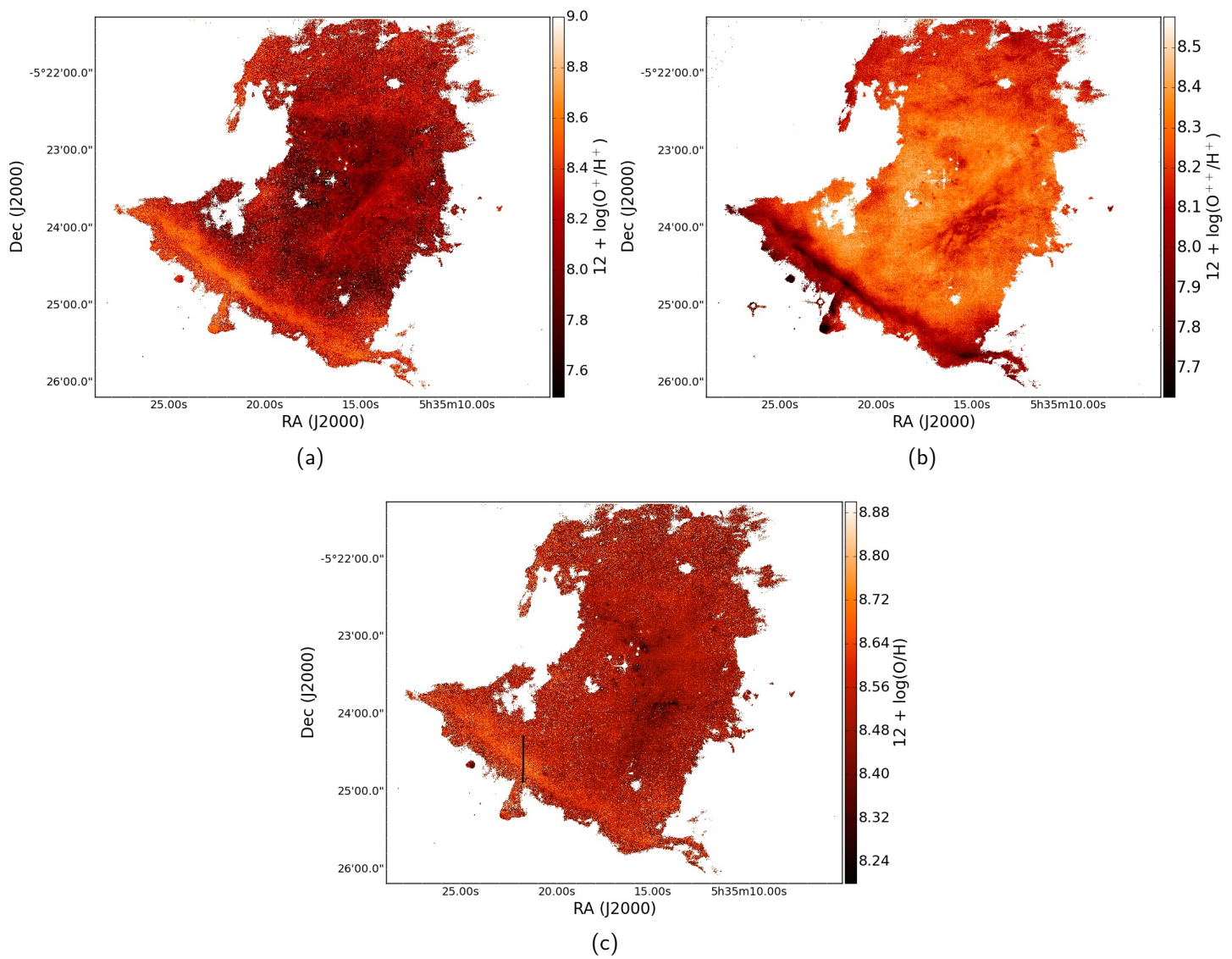


Figure 4.3: Maps of the O^+ (panel a), O^{++} (panel b) and total O (panel c) abundances, see text Section 3.1. The black line in panel (c) marks the position of the slit used to compute the profiles shown in Fig. 4.6.

about 1000-2000 cm^{-3} ; (ii) a noise-affected T_e ([NII]) map; (iii) a comparable O^{++}/H^+ map; (iv) and higher O^+/H^+ as well as O/H values. We speculate that the higher O^+/H^+ values found for the BB in this work are a result of the noisy T_e and [OII] maps. This could be tested with data with higher S/N.

To demonstrate the strong dependence of the ionic and total abundances on the electron density, in Fig. 4.6 we plot profiles (smoothed with a Gaussian kernel) of these along a slit positioned on the Bright Bar (the slit is shown in Fig. 4.3c, the profile is computed in direction from north to south): the O^+ and the O abundances show higher values in correlation with the higher N_e values, while the opposite trend is the case for O^{++} . However, we cannot resolve this issue by artificially lowering N_e . Furthermore, the structuring is also seen in S^+/H^+ , N^+/H^+ and N/H: we therefore suggest that the dominant mechanism that leads to the structures seen in the abundance maps is (as already discussed in MD11) that in regions like the Bright Bar and the Orion S cloud, densities approach the critical densities of [SII], [NII] and [OII] lead to untrustworthy artefacts.

Table 4.2 shows that the abundances found in this work do not agree with E04 (Table 4.3 specifies the electron density and temperatures extracted from the same regions listed in Table 4.2: for P2 we find a lower N_e as the assumed density of E04, but higher T_e values): in this work, O^+ is overestimated by about 0.22 dex, while O^{++} and O are underestimated by about 0.15 and 0.04 dex respectively; S^+ is overestimated by 0.16 dex, S^{++} and S are underestimated by 0.09 and 0.04 dex respectively; for nitrogen, N^+ is overestimated by 0.10 and N underestimated by 0.17 dex. Summarising this, we see how the abundances computed via PYNEB from the MUSE data overestimate the low ionisation potential ions (O^+ , S^+ , N^+), and they underestimate the ions with high ionisation potential as well as the total abundances (O^{++} , O, S^{++} , S, N). However, within the margin of errors, the MUSE *total* abundance maps are able to recover literature total O and S abundance measurements. This is not the case for N, as only one ionisation state is observed and the total abundance computation relies on the ICF.

4.3.2 Line ratios

In our MUSE observations of pillar-like structures in the the Eagle Nebula (see MC15), the S_{23} ($= ([\text{SII}]\lambda 6717,31 + [\text{SIII}]\lambda 9068)/\text{H}\beta$) parameter was used in combination with $[\text{OII}]\lambda 7320,30 / [\text{OIII}]\lambda 5007$ (as an indicator of the degree of ionisation) and a velocity map obtained from the same dataset to identify a previously unknown outflow in one of the pillars. However, in MC15 we did not attempt a physical explanation of the empirical fact that S_{23} can be used to trace outflows. Here, we repeated the S_{23} vs. $[\text{OII}]/[\text{OIII}]$ analysis, motivated by the fact that the central Orion Nebula hosts a very peculiar combination of massive ionising stars and a wealth of outflows, forming stars in the form of proplyds, and HH objects. We therefore refine the empirical S_{23} vs. $[\text{OII}]/[\text{OIII}]$ analysis of MC15 by exploring the rich environment of the Orion Nebula. Because the relative importance of photoionisation and shocks to the production of sulphur emission lines is different for different kind of objects (the Bar, HH outflows and proplyds), it can be used, together with $[\text{OII}]/[\text{OIII}]$, to distinguish between them (as will be discussed in Section 5.2). The S_{23} map is shown in panel (a) of Fig. 4.8, panel (b) shows the

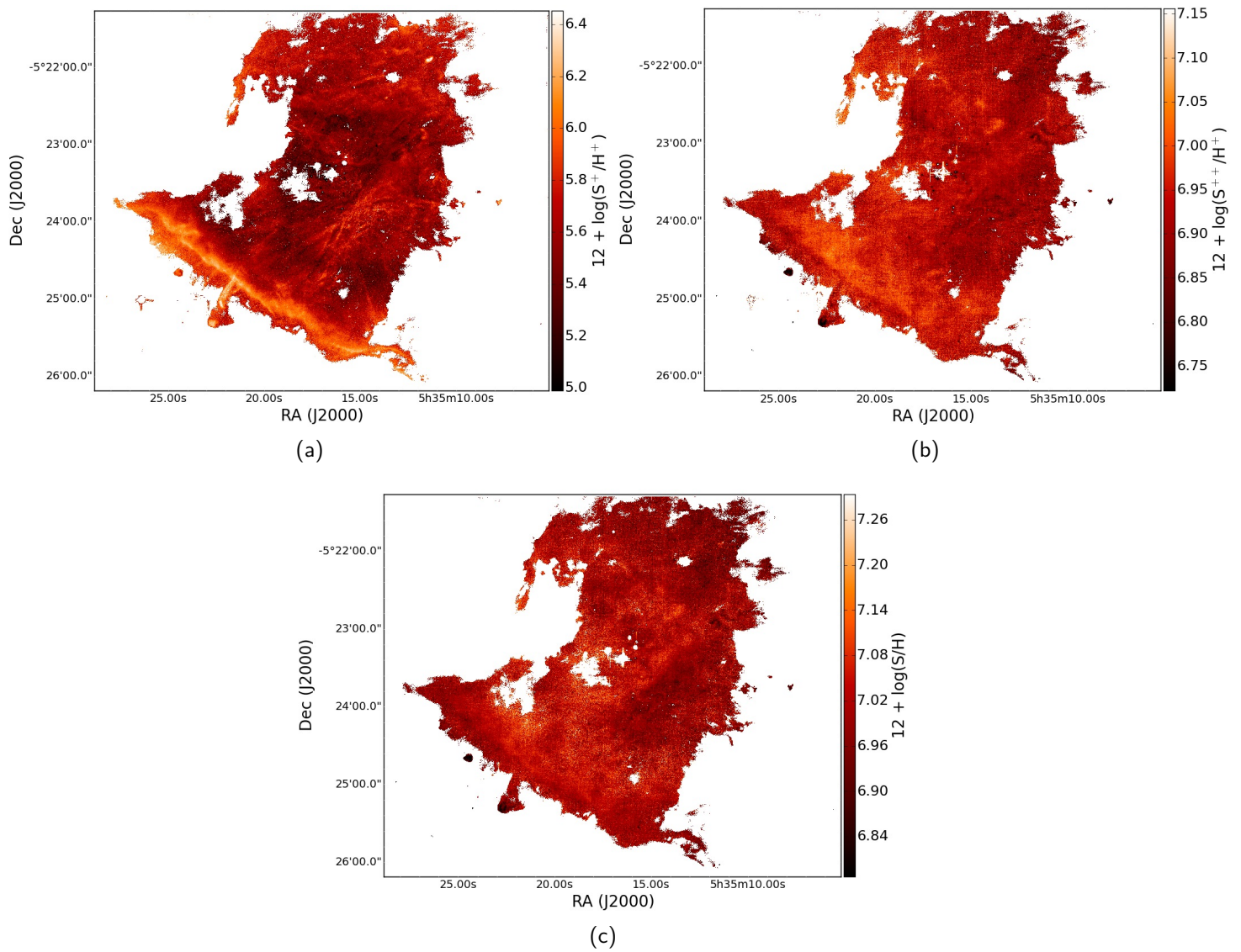


Figure 4.4: Maps of the S^+ (panel a), S^{++} (panel b) and total S (panel c) abundances, see text Section 3.1.

Table 4.2: Ionic and total abundances. Mean values for circular regions with 2.5" radius centred on selected regions as well as slit Position 2 from Esteban et al., 2004, obtained in this work (P2) and abundances computed in Esteban et al. (P2E) for $t^2=0.000$. The last line indicates the approximate ranges of abundance values found in MD11 from integral field observations of a sub-region of the Bright Bar. See text Section 3.1.

Region	Coordinates (J2000)		O ⁺	O ⁺⁺	O	S ⁺	S ⁺⁺	S	N ⁺	N
Bright Bar	5 35 21.91	-5 24 38.20	8.56±0.08	7.93±0.05	8.65±0.06	6.11±0.06	6.98±0.03	7.04±0.03	7.51±0.04	7.60±0.03
Trapezium	5 35 16.4	-5 23 11.9	8.09±0.14	8.31±0.04	8.52±0.06	5.53±0.09	6.92±0.03	7.01±0.04	7.01±0.07	7.44±0.05
P2	5 35 14.54	-5 23 33.86	7.98±0.12	8.28±0.05	8.47±0.04	5.56±0.15	6.92±0.02	7.02±0.03	7.00±0.10	7.48±0.05
P2E, $t^2=0.000$	5 35 14.54	-5 23 33.86	7.76±0.15	8.43±0.01	8.51±0.03	5.40±0.06	7.01±0.04	7.06±0.04	6.90±0.09	7.65±0.09
P2-P2E			0.22	-0.15	-0.04	0.16	-0.09	-0.04	0.10	-0.17
MD11	Bright Bar		8.00-8.47	7.86-8.24	8.41-8.58					

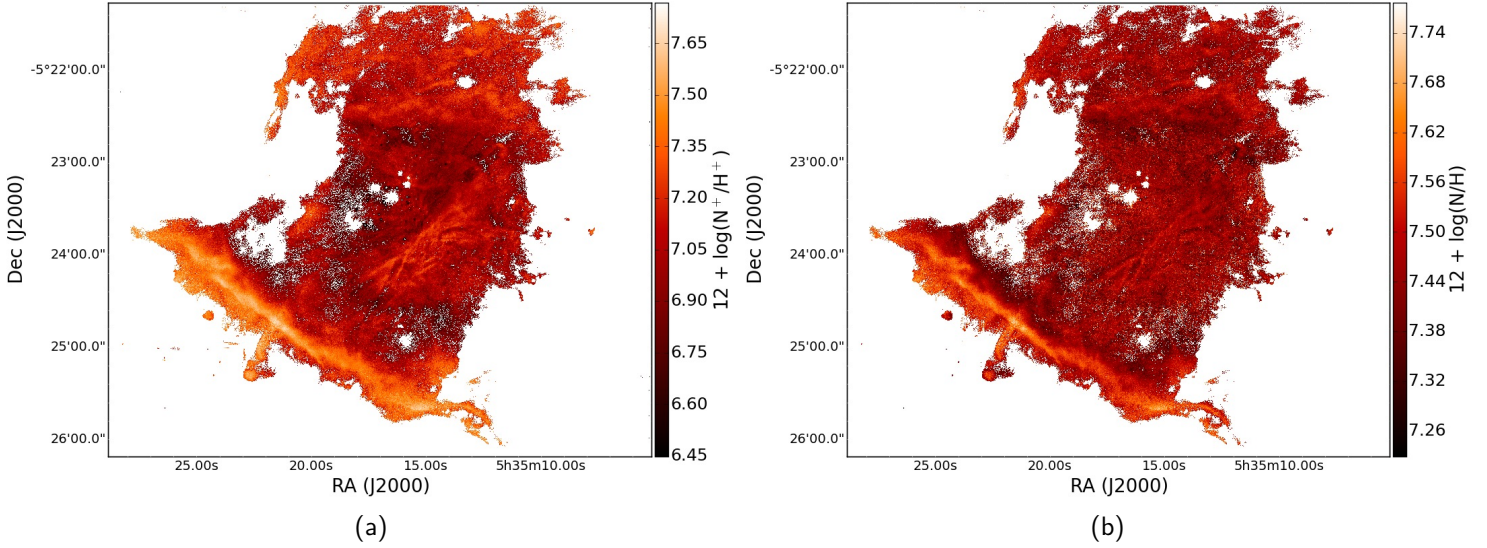


Figure 4.5: Maps of the N^+ (panel a) and total N (panel b) abundances, see text Section 3.1.

Table 4.3: Electron densities and temperatures extracted from the same regions listed in Table 4.2 for this work and slit position 2 in Esteban et. al 2004 (P2E).

Region	N_e ([SII]) (cm^{-3})	T_e ([NII]) (K)	T_e ([SIII]) (K)
Bright Bar	3430 ± 430	9410 ± 260	8870 ± 190
Trapezium	4530 ± 1080	10090 ± 525	8780 ± 210
P2 (this work)	7310 ± 3320	10535 ± 520	8950 ± 180
P2E, $t^2 = 0.000$ (Esteban et al. 2004)	8900 ± 200	10000 ± 400	8320 ± 40

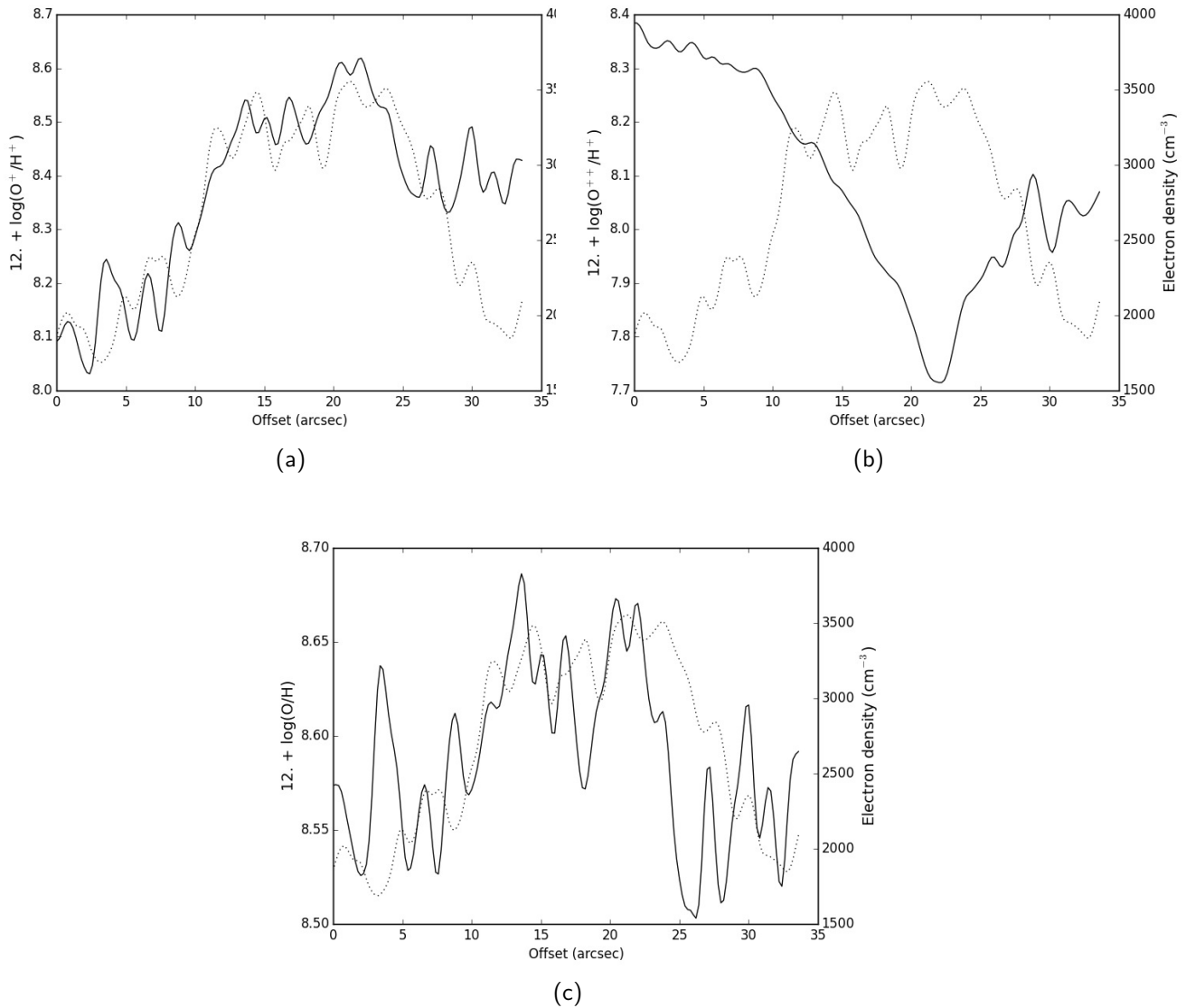


Figure 4.6: Profiles of the O^+ (top), O^{++} (middle) and O abundances along the slit (along the north-south direction) shown in Fig. 4.3 (solid lines), together with the profile of the electron density derived from the $[\text{SII}]$ lines (dotted lines) along the same slit (marked in Fig. 4.3c). The originally very noisy profiles were smoothed with a Gaussian kernel. See text Section 3.1.

[OII]/[OIII] map, and panel (c) corresponds to a scatter plot of the two parameters. The maps and scatter plot shown in Fig. 4.8 are continuum-subtracted: the strong stellar residuals of the saturated stars appear as white in the images because they are masked. Furthermore, the white line in Fig. 4.8b shows the slit used to compute the profile shown in Fig. 4.7 and discussed below.

We applied a technique called *brushing** to analyse the spatial correspondence of the data points in the scatter plot of S_{23} vs. [OII]/[OIII] and trace them back to their position in the maps. Both in the [OII]/[OIII] and the S_{23} maps the structures of the nebulosity are clearly distinguishable, e.g. the Bright Bar shows high values of both parameters, while the central part of the H II region is marked with lower values of both parameters, meaning that in the vicinity of the Trapezium cluster we find lower S_{23} values and higher degrees of ionisation, as is expected.

In Fig. 4.8c S_{23} vs. [OII]/[OIII] is shown, and several of the main features are (indicatively) highlighted†: the Orion bullet HH 201 (yellow ellipse) covered by the MUSE field shows high S_{23} values as well as a high degree of ionisation, while the proplyds in the vicinity of the Trapezium stars (dark red ellipse) are found in a region with very low S_{23} values but a rather high degree of ionisation; the HH objects and proplyds south of the Bright Bar clearly stand out, displaying a wide range in S_{23} and ionisation values; furthermore, they can be divided into four distinct classes (described in Section 5.2), marked by the orange, blue, green and cyan ellipses; the Bright Bar is marked by the red ellipse.

Fig. 4.9a is a zoom-in on the region of the S_{23} vs [OII]/[OIII] parameter space where most of the data points lie. The [OII]/[OIII] histogram is bimodal, the spatial correspondence of the two distributions is shown in Fig. 4.9, panels (b) and (c). From this Figure, it is clear that the region immediately around the Trapezium stars, as well as the Orion S region, do not show the highest degree of ionisation, while the highly ionised matter surrounds these inner regions like a ring. This goes against the naive picture, where matter with the lowest [OII]/[OIII] values (i.e. the highest degree of ionisation) should be found in the immediate vicinity of the ionising stars. The reason for the higher [OII]/[OIII] values is not immediately clear. Because the strong dependence of [OII]/[OIII] on the electron density (as can be seen in Fig. 4.7, where [OII]/[OIII] and N_e are plotted along the slit marked in Fig. 4.8b), the following two scenarios can be a possible explanation for this empirical fact:

- density variations: in regions of higher density the ionisation parameter is quenched and the emission from low-ionisation lines (e.g. [OII], [SII]) enhanced
- shocks: the above reasoning for density variations holds if shocks are present as well, as shocks locally compress matter, producing density enhancements

A further possibility is a combination of these two scenarios, as the central Orion Nebula,

*This method was also applied in MC15. It is also known as *graphical exploratory data analysis*, and it allows the user to manually select specific data points from an image or a plot by interactively drawing regions on the latter of the two.

†Because of the large number of data points, we refrained from properly colour-coding single points in the scatter plot and trace them back to their spatial origin in the S_{23} map as was done for HH 201 in Fig. 4.13.

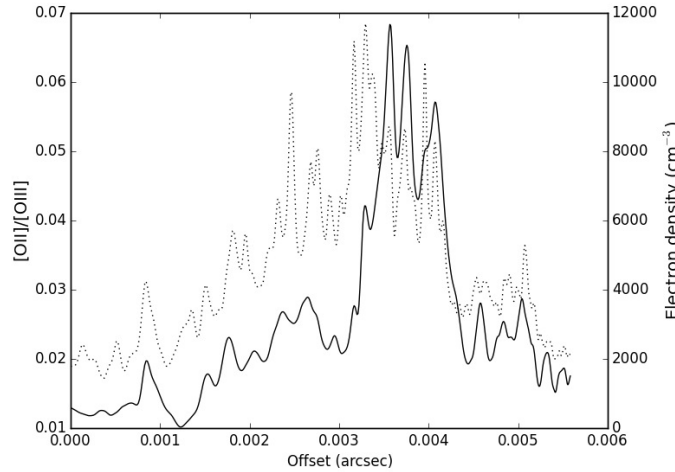


Figure 4.7: $[OII]/[OIII]$ and N_e along the slit shown in Fig. 4.8 (see text Section 3.2).

where the Orion S cloud is located, hosts a wealth of HH outflows and shocks such as HH 529, HH 269, HH 202 (O'Dell, 2001).

We will discuss selected subregions of the mosaic and the scatter plot in Section 5 in order to disentangle the very large number of data points and distinguish between the different populations.

4.4 Kinematics

Turbulence generates a velocity field characterised by stochastic hierarchical fluctuations, and because of this, a statistical approach such as the second order structure function has been widely used to analyse turbulent motions in both extragalactic (e.g. Medina Tanco et al. 1997, Lagrois & Joncas 2011) and galactic (e.g. O'Dell 1986, Wen & O'Dell 1993, Miville-Deschenes et al. 1995, Chakraborty & Anandarao 1999) H II regions. For Orion, this has been done, e.g. with the $[OIII]\lambda 5007$ line in Castaneda (1988), with the $[OI]\lambda 6300$ line in O'Dell & Wen (1992) and with the $[SIII]\lambda 6312$ line in Wen & O'Dell (1993).

Following the method of Boneberg et al. (2015), we compute the second order structure function $S_2(dr)$ as the squared velocity difference between each pair of pixels. As the total number of pixels in the MUSE dataset is $> 2 \times 10^6$, we compute the structure function for a randomly selected sample of 10^3 pixels j , around which we radially bin all other pixels i . The size of the random pixel sample was chosen such that the optimum combination between computing time and smoothness was obtained. The structure function then corresponds to the mean of each radial bin,

$$S_2(dr) = \langle (v_i - v_j)^2 \rangle_{\text{bin}} \quad (4.1)$$

According to the predictions of von Hoerner (1951), for a homogenous slab of emitting material

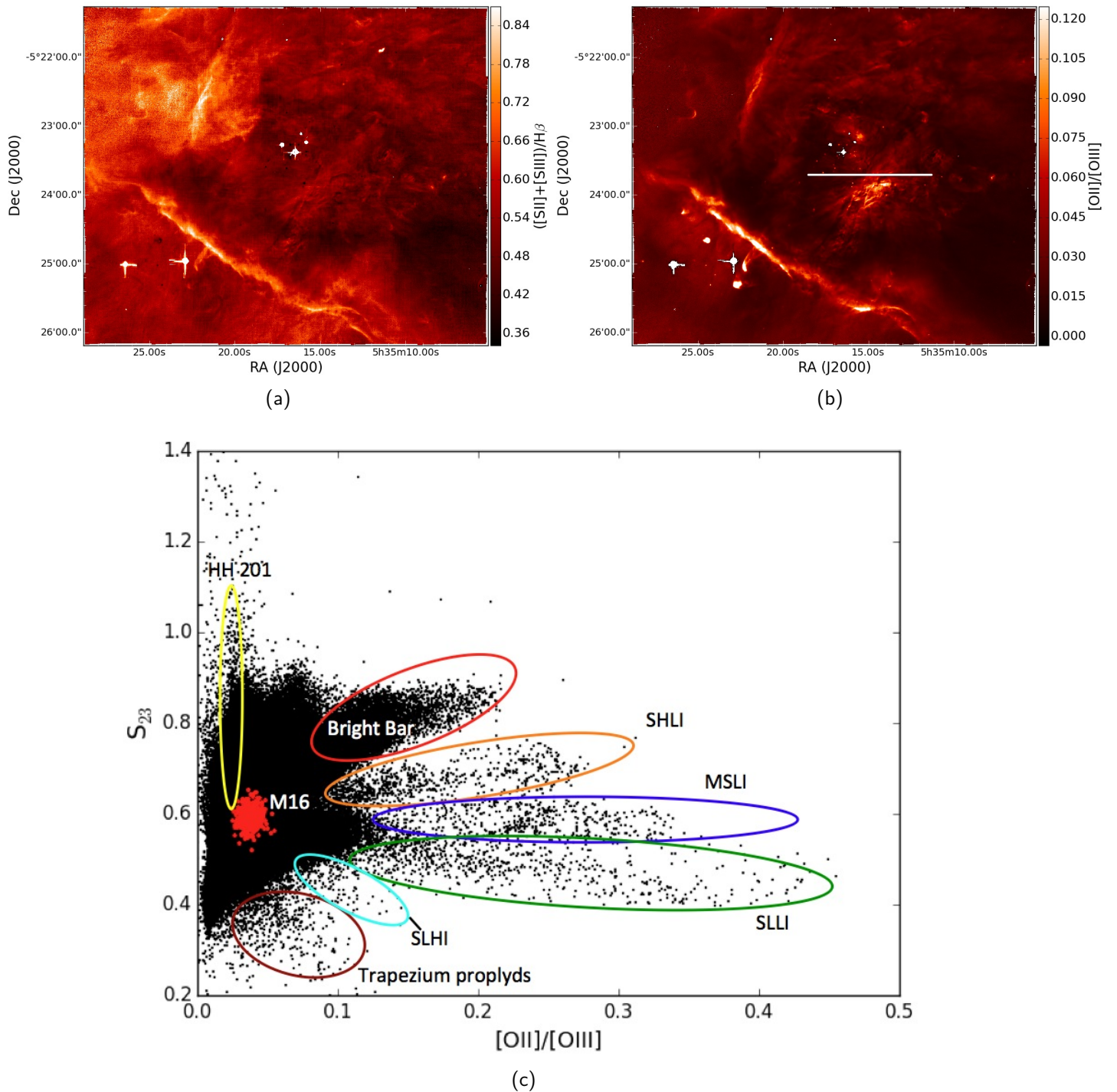


Figure 4.8: Continuum-subtracted maps of the S_{23} ($= ([SII] + [SIII])/H\beta$, panel a) and $[OII]/[OIII]$ (panel b) parameters, linearly scaled. The white line in panel (b) indicates the slit used for Fig. 4.7. Scatter plot of the two (black points, panel c) and the indicative positions of the following structures: the M 16 outflow (from MC15, red dots), the Bright Bar (red), HH 201 (yellow), the proplyds in the Trapezium cluster region (dark red), and the four classes of proplyds and outflows south of the Bright Bar (SHLI = S_{23} -high and low ionisation, MSLI = medium S_{23} values and low ionisation, SLLI = S_{23} -low and low ionisation, SLHI = S_{23} -low and high ionisation, see text Section 5.2).

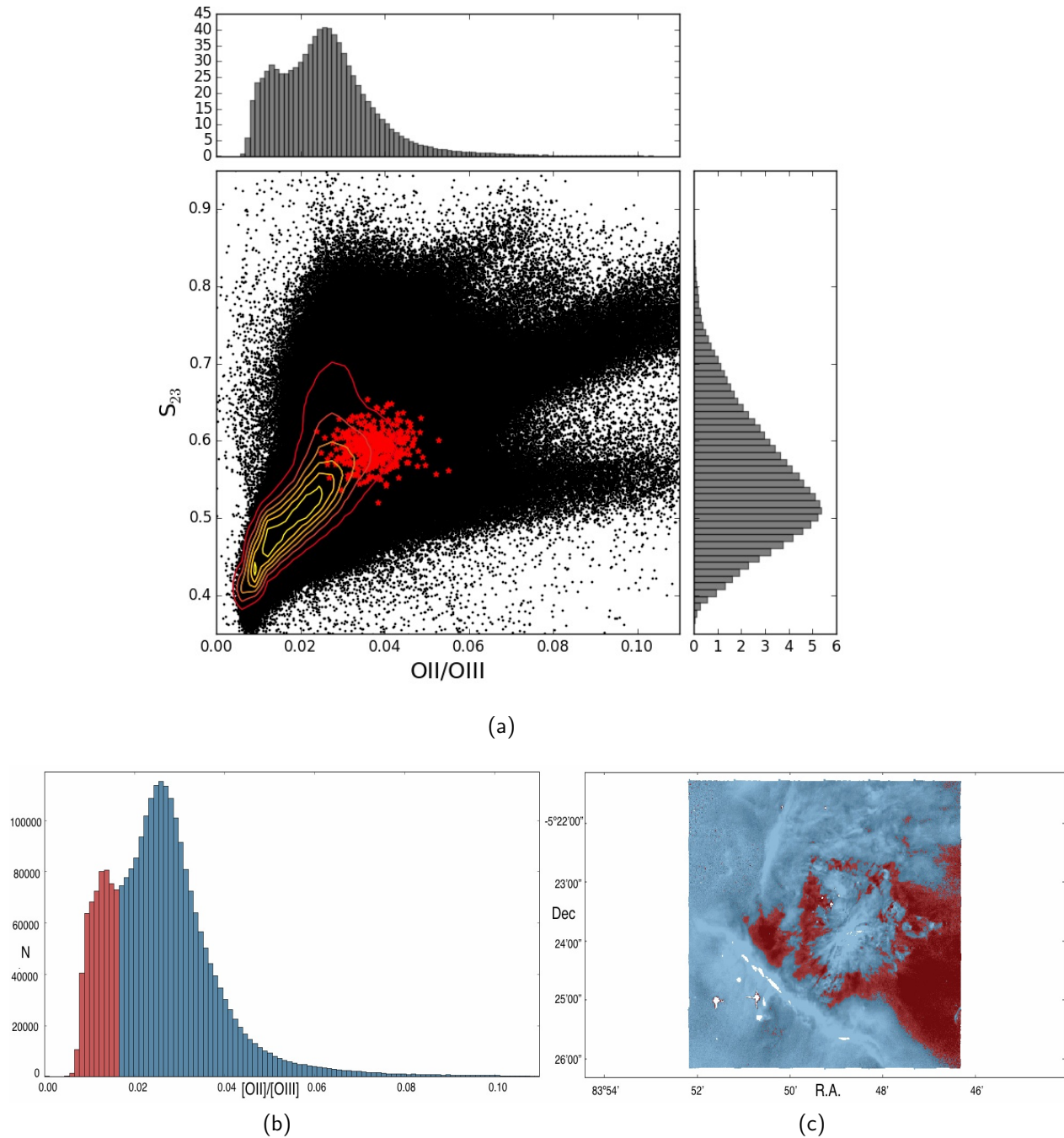


Figure 4.9: Panel (a) zoom-in on the dense region of Fig. 4.8c the contours correspond to the number of data points, the first contour level is $N = 3000$ and the increment is 3000, and the red stars correspond to the M 16 outflow (MC15). The histograms are normalised counts. Panels (b) and (c) illustrate the spatial origin of the bimodal distribution of the $[OII]/[OIII]$ histogram highest (red) and lower (blue) degree of ionisation (the background $[OII]/[OIII]$ histogram in panel (b) is the same as at the top of panel (a), the red and the blue are the normalised histograms corresponding to the same-shaded areas in panel c). See text Section 3.2.

of thickness s the structure function should behave as

$$S(r) \propto \begin{cases} r^{n+1} & \text{if } r < s \\ r^n & \text{if } r > s \end{cases} \quad (4.2)$$

where $n = 2/3$ in the case of Kolmogorov turbulence. We computed S_2 for the velocity maps of $H\alpha$, $[O\text{I}]\lambda 6300$, $[O\text{III}]\lambda 5007$ and $[S\text{II}]\lambda 6731$. When comparing the shape of S_2 with the velocity map from which each was derived (Fig. 4.10 and red curves in Fig. 4.12 respectively), it is clear that for $[O\text{I}]\lambda 6300$ and $[S\text{II}]\lambda 6731$ the slope of S_2 is dominated by noise.

In order to quantify the effect of noise on the S_2 slope, we used the MOCASSIN code (Ercolano et al. 2003a, 2005, 2008) to create synthetic emission line maps from a snapshot of the Run UP simulation of an expanding H II region in a turbulent cloud from Dale et al. (2013c). We selected a 5×5 pc subregion of the cloud containing a relatively simple isolated bubble, 0.38 Myr after ionisation was enabled (see Fig. A6). We then created first-moment maps by convolving the emission line maps with the smoothed-particle hydrodynamics (SPH) velocity field, as shown in Fig. A2a. This map has low intrinsic noise, thus it can be used as a baseline. We then added Gaussian noise with increasing values for the standard deviation σ ($\sigma = 0.01, 0.05, 0.1, 0.5, 1, 5, 10$ in panels b to h, not shown are $\sigma = 0.03, 0.15, 0.2, 0.3, 0.75, 2, 3$). For each of these maps we then computed S_2 , fitted power laws to the resulting structure functions and analysed the dependence of the slope α on σ . The result can be seen in Fig. 4.11, where a quadratic dependence of the slope on the level of noise is shown.

Because of this, we computed a mask based on the intensity of the mean value of the $[O\text{I}]\lambda 6300$ line ($\sim 10^{-16}$ erg s $^{-1}$ cm $^{-2}$ pixel $^{-1}$), discarding all pixels below this threshold, and applied this to all the above mentioned velocity maps (see Fig. A1)[‡]. The resulting structure functions are shown in Fig. 4.12, where S_2 for both the unmasked (red circles) and the masked (blue squares) velocity maps for the four lines are plotted (to visualise the two on the same scale, the ordinate is always normalised to peak). By masking out some of the noise, the slopes of the structure functions are clearly steeper, but because we have no way of effectively getting rid of the noise and therefore computing unbiased structure function slopes both for the $[S\text{II}]\lambda 6731$ and in the $[O\text{I}]\lambda 6300$ lines, we concentrate the discussion on the structure functions derived from the $[O\text{III}]\lambda 5007$ and the $H\alpha$ lines. These show power law slopes over all scales, indicating that turbulence is being driven on scales larger than the measured ones, and an energy cascade from the largest scales to the smallest. The slopes however do not correspond to the $2/3$ Kolmogorov law. A comparison of the power law slopes with previous works shows that the MUSE data, because of a combination of lower spectral resolution, short exposure times and a low signal to noise ratio (especially for the weaker $[O\text{I}]\lambda 6300$ and $[S\text{II}]\lambda 6731$ lines), yields structure function slopes that are too shallow with respect to past papers. With high-resolution slit spectroscopy, Castaneda (1988) find a slope of $\alpha \sim 0.86$ for the $[O\text{III}]\lambda 5007$ line, which is a factor of about 2.6 steeper than $\alpha \sim 0.29$ found in this work. For the $[O\text{I}]\lambda 6300$ line, O'Dell & Wen (1992) find an almost exact Kolmogorov slope of $2/3$, while we are completely noise dominated and find $\alpha \sim 0$. What we also do not recover from the MUSE observations is a break in the power law slopes as was

[‡]We did not set a higher threshold, as this would have drastically reduced and limited the available length scales.

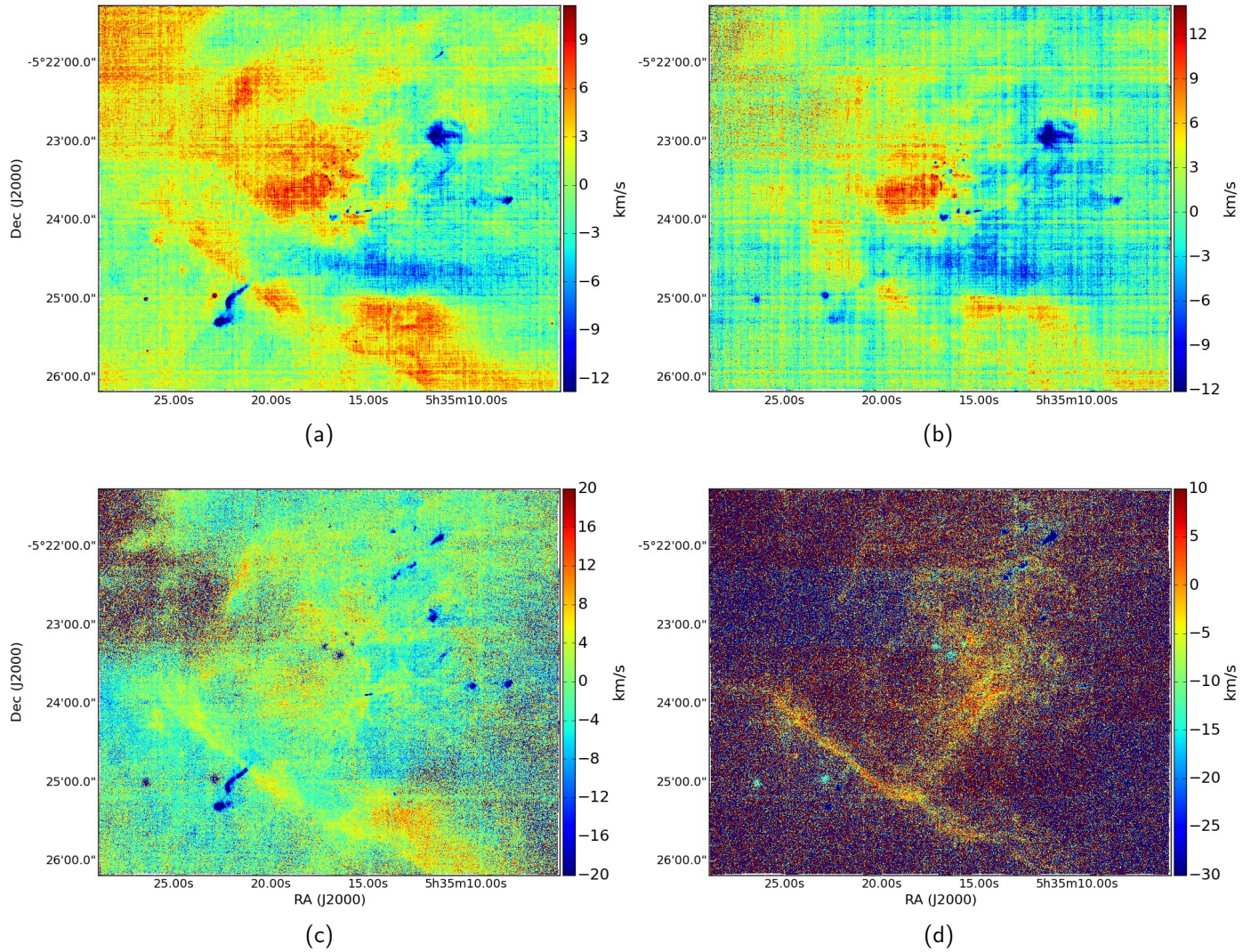


Figure 4.10: Velocity maps of $H\alpha$ (a), $[OIII]\lambda 5007$ (b), $[SII]\lambda 6731$ (c) and $[OI]\lambda 6300$ (d). The indicated velocities correspond to velocities relative to the mean velocity (see text Section 5.1).

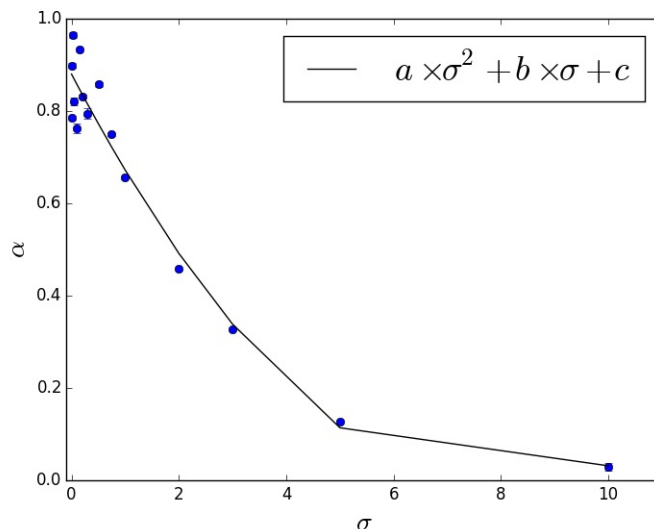


Figure 4.11: The slopes α resulting from a least-square fit to the of the structure functions computed from the [SII] maps of our simulated H II regions as a function of Gaussian noise with gradually increasing σ . The error bars correspond to the errors from the least-square fit (see text Section 4). A quadratic function was fitted with coefficients $a = 0.0143 \pm 0.0020$, $b = -0.2285 \pm 0.0193$, $c = 0.8922 \pm 0.0208$.

previously found in the above mentioned studies. We will discuss the influence of noise on simulated structure functions in further detail in McLeod et al., in preparation. It is however of importance to state the implications of these results, should they be correct: a structure function slope that does not show a break hints at a uniform injection of turbulence on all observed scales (and that turbulence is injected at larger scales than the observed), while the fact that it is shallower than Kolmogorov indicates that the injected turbulence is not sufficient to maintain a Kolmogorov-type velocity field.

4.5 Discussion of selected regions

4.5.1 The Orion bullet HH 201

The only feature that, because of its very high S_{23} values, stands out in the S_{23} map shown in Fig. 4.8a is one of the so called Orion bullets in the upper right corner of the image, in fact the only bullet covered by the MUSE field. This object corresponds to HH 201 (Graham et al., 2003), a bright shock from an outflow driven by the high-mass star forming region OMC-1 (Bally et al., 2000). To better analyse this region, we cropped the original mosaic to a $32'' \times 20''$ rectangle (centred at R.A. J2000 = 5:35:11.179, Dec J2000 = -5:21:57.22), as to cover both the bullet and a representative portion of the surrounding material. Just like the outflow detected in M 16 (see MC15), the bullet corresponds to a population in the S_{23} versus

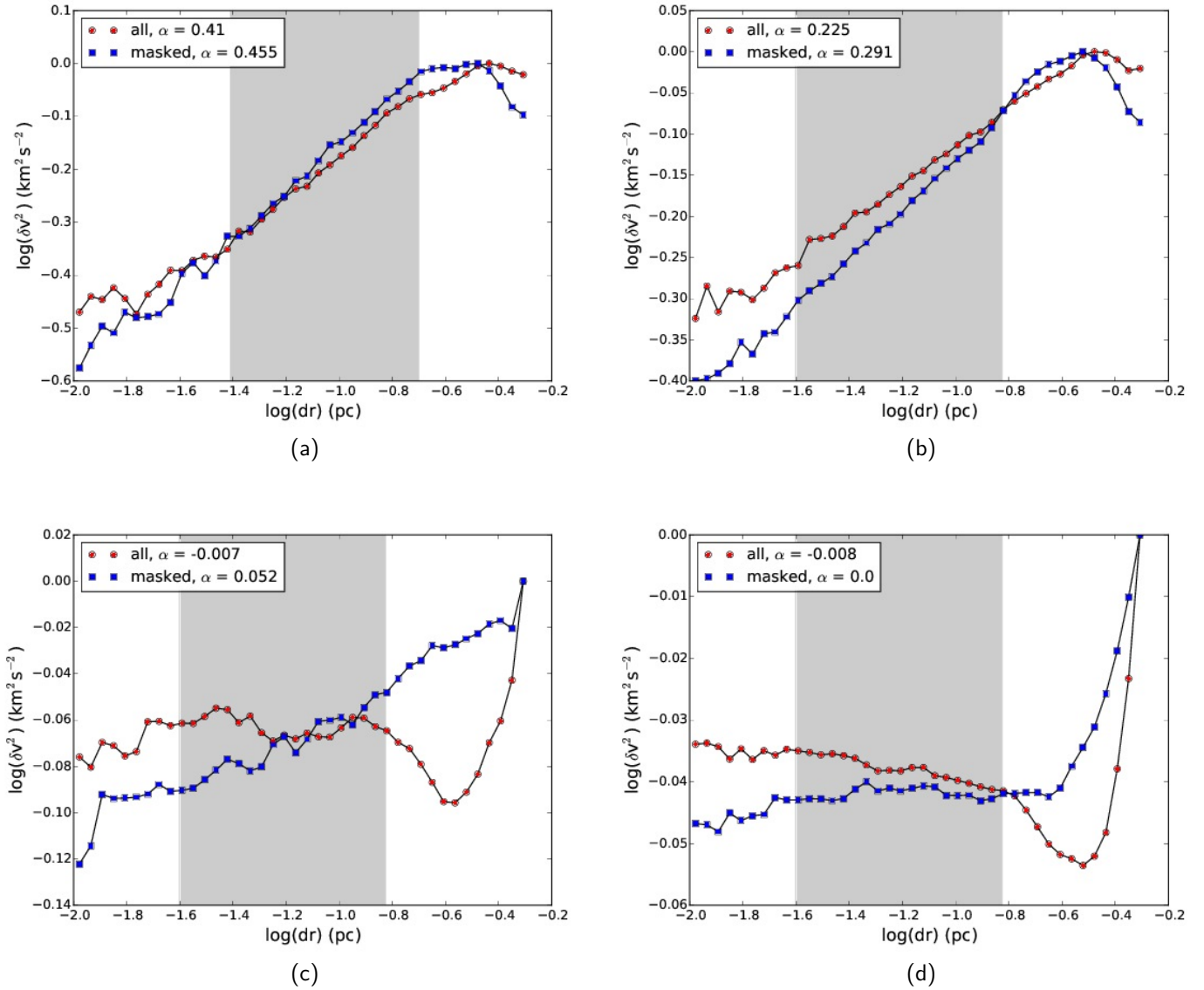
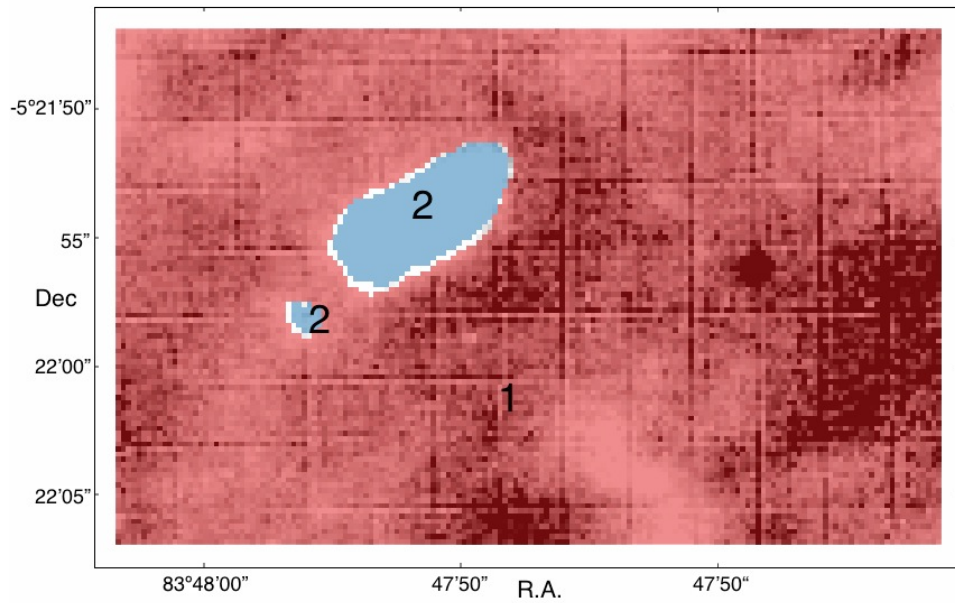


Figure 4.12: Structure functions (normalised to peak) of $\text{H}\alpha$ (a), $[\text{OIII}]\lambda 5007$ (b) and $[\text{SII}]\lambda 6731$ (c) and $[\text{OI}]\lambda 6300$ (d). The red circles are computed from the full velocity maps, the blue squares from the masked ones. The shaded areas correspond to the least-square fitting range used to compute the slope α . See text section 4.

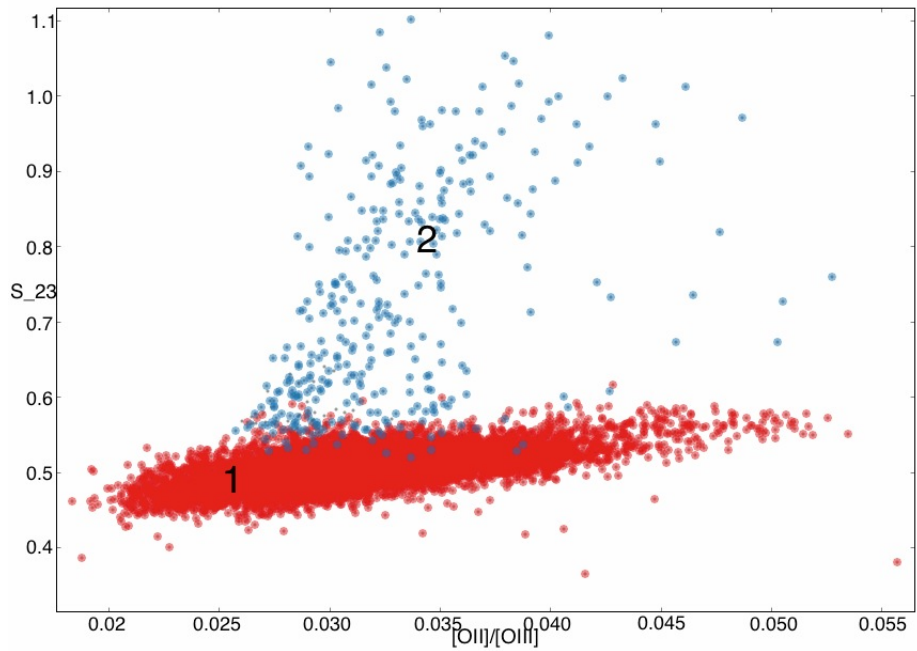
[OII]/[OIII] parameter space (Fig. 4.13b) that clearly deviates from the rest. This population, just as the M 16 outflow (red stars in Fig. 4.8c), displays very high S_{23} values, as well as a relatively high degree of ionisation, but compared to the M 16 outflow, HH 201 has S_{23} values higher by a factor of ~ 1.5 . Not only does HH 201 show higher S_{23} values than the M 16 outflow, it also shows a higher degree of ionisation. This is not surprising, as the low-velocity M 16 outflow most probably originates from a deeply embedded protostar, and the outflow itself is just now emerging from the pillar material where the driving source is embedded; HH 201 on the other hand is a high-velocity outflow travelling in a less dense medium, it originates from a highly energetic explosive event (Bally et al., 2015) rather than a protostar and it is closer (in projection) to the ionising O-star.

The integrated intensity maps of [OI] λ 6300, [SII] λ 6717, [OII] λ 7320, [NII] λ 6584, $H\alpha$ and [OIII] λ 5007 (Fig. 4.14a to f, where due to an imperfect continuum-subtraction, the residual of a star in the right side of the images is seen) show that the contrast between the bullet and the surrounding medium gets weaker as a function of the ionisation state. The sharpest contrast is seen in the neutral [OI] λ 6300 line, whereas the [OIII] λ 5007 map only shows diffuse emission. The velocity maps of the same emission lines (Fig. 4.15) show a similar behaviour: the bullet can be clearly identified in the [OI] and [SII] maps, where it assumes a blueshifted cometary shape with a head pointing away from the Trapezium cluster and a tail pointing back towards it. In the [OII] velocity map only the head can be identified as being slightly blueshifted, while the bullet cannot be seen at all in the [OIII] map. Furthermore, the [OI] and [SII] maps reveal a clear velocity difference between the head and the tail of about 50 km s^{-1} , the head showing the more negative velocities. The head-tail geometry and the velocity difference between the two could be the result of the high-velocity bullet ramming into a high-density region and being slowed down by the impact. The velocities reported here correspond to relative velocities, meaning that for each line we subtracted the mean velocity of the surrounding medium from the entire velocity map.

The Orion bullets are particularly bright in emission lines of ionised iron (Bally et al. 2015, Youngblood et al., in prep.), and the near-infrared [FeII] line (at $1.644 \mu\text{m}$) profiles of HH 201 appear to be consistent with theoretical predictions of a bow shock (Tedds et al., 1999). We inspected the line profile of the brightest of the detected iron lines, [FeII] λ 8617, and find a double component throughout the head of the bullet and along its tail. In this can be seen in Fig. 4.16, where the continuum-subtracted and Gaussian-fitted spectra for eight pixels are shown, together with the integrated [FeII] λ 8617 intensity map (central panel). Where only one component is seen (not shown in Fig. 4.16), the typically line width is $\sim 300 \text{ km s}^{-1}$, while for in case of a double-peaked line the FWHM is $\sim 30 - 45 \text{ km s}^{-1}$ for the red component and $\sim 20 - 60 \text{ km s}^{-1}$ for the blue component. The blue component is typically lower in intensity than the red one. Table 4.4 shows the best fit centroid and width values obtained with PYSPECKIT, using a two component Gaussian fit.



(a)



(b)

Figure 4.13: S_{23} map of the Orion bullet covered by MUSE (panel a), colour coded according to the S_{23} vs $[OII]/[OIII]$ plot in panel (b) H II region (red circles, number 1) and the bullet (blue circles, number 2).

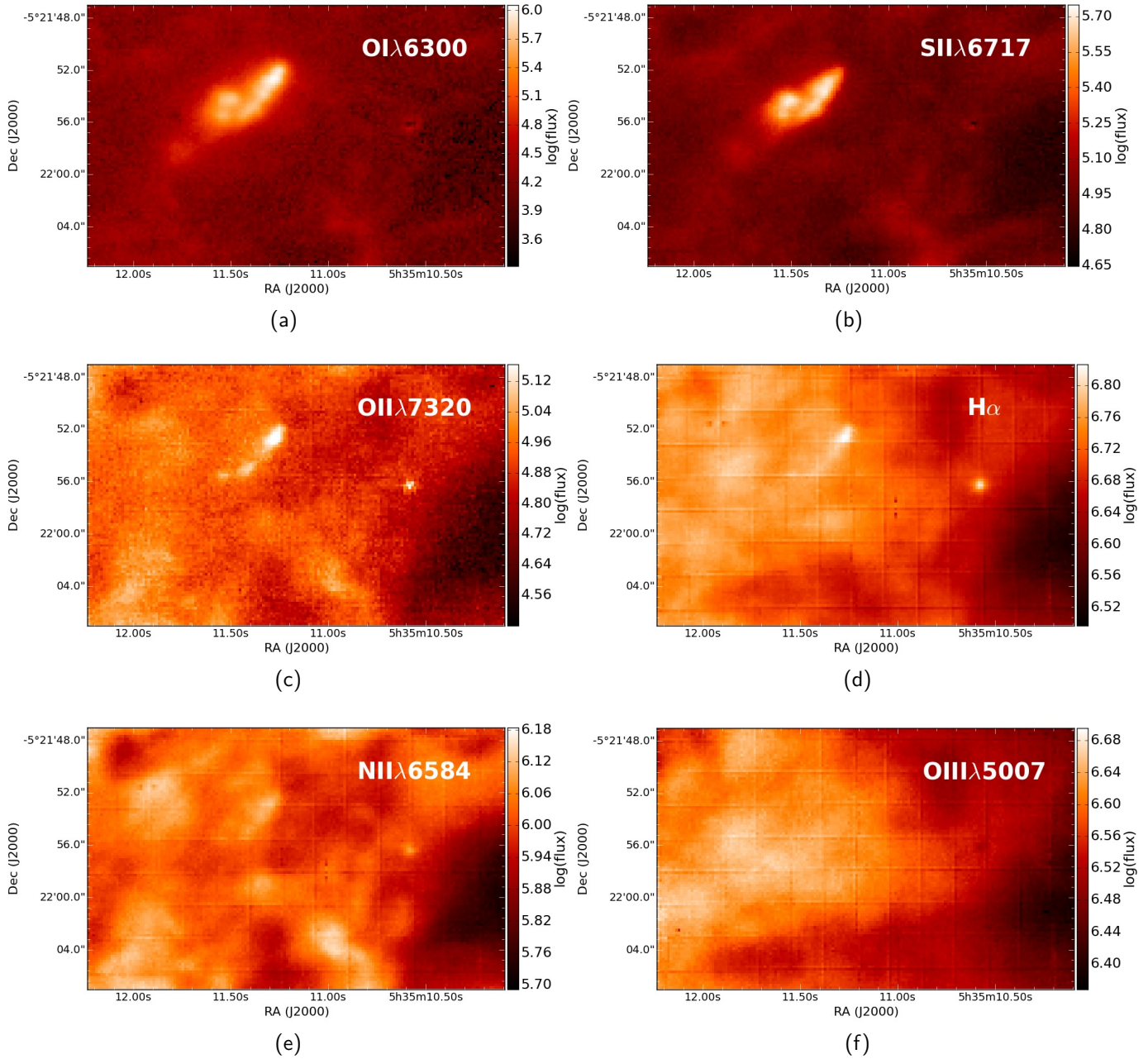


Figure 4.14: Continuum-subtracted and extinction corrected, integrated intensity maps of the Orion bullet covered by MUSE [O I] λ 6300 (a), [S II] λ 6717 (b), [O II] λ 7320, H α (d), [N II] λ 6584 (e) and [O III] λ 5007 (f). The flux is measured in 10^{-20} erg s $^{-1}$ cm $^{-2}$ pixel $^{-1}$, all maps are linearly scaled to minimum/maximum. Residual stellar emission from the continuum subtraction can be seen at R.A. 5:35:10.583, dec -5:21:56.50 (J2000).

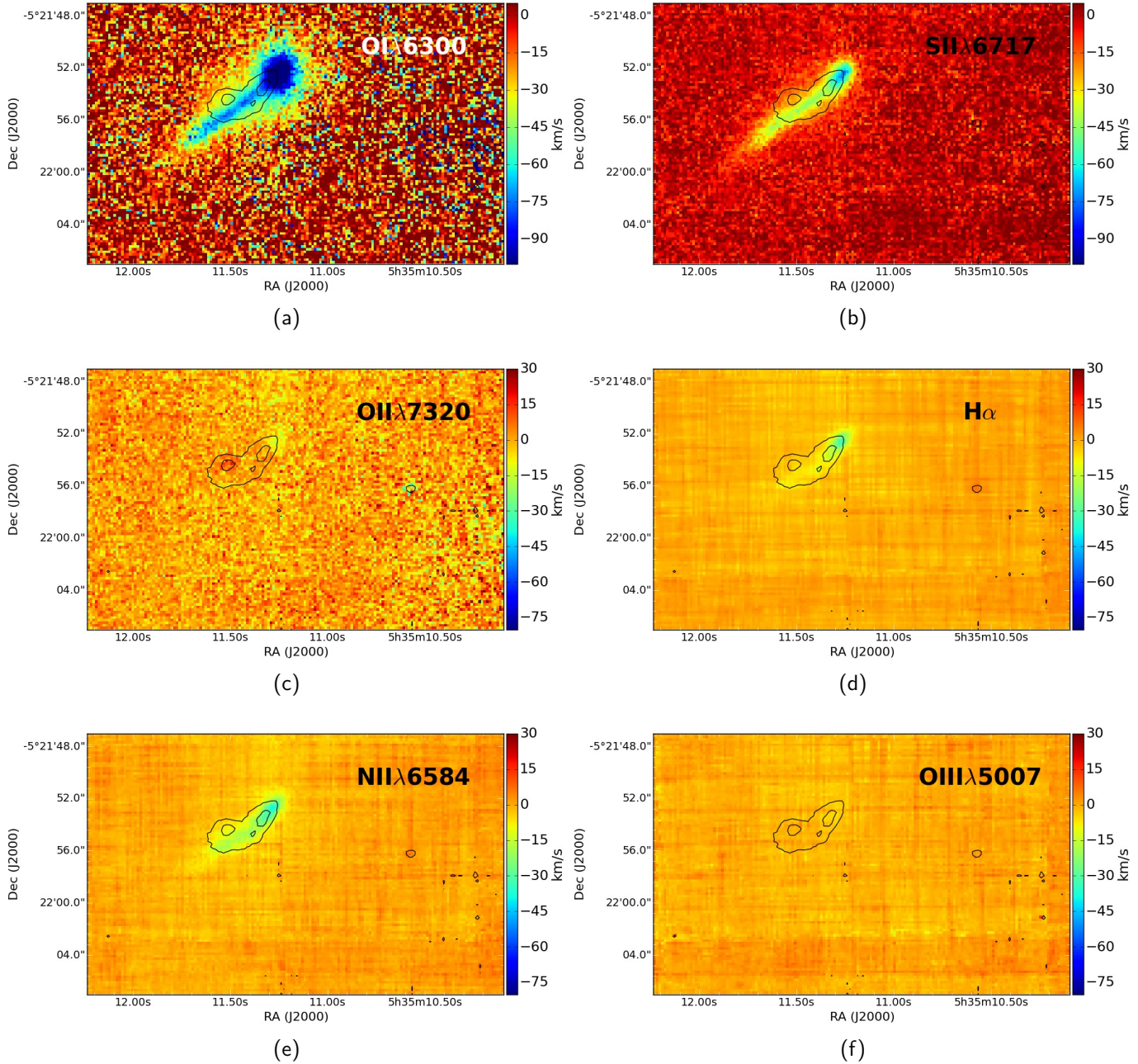


Figure 4.15: Velocity maps of the Orion bullet covered by MUSE: $[OI]\lambda 6300$ (a), $[SII]\lambda 6717$ (b), $[OII]\lambda 7320$, $H\alpha$ (d), $[NII]\lambda 6584$ (e) and $[OIII]\lambda 5007$ (f). Black contours correspond to S_{23} values (at R.A. 5:35:10.583, dec -5:21:56.50 a residual from the continuum-subtraction is seen). The indicated velocities correspond to velocities relative to the mean velocity of the surrounding medium (see text Section 5.1).

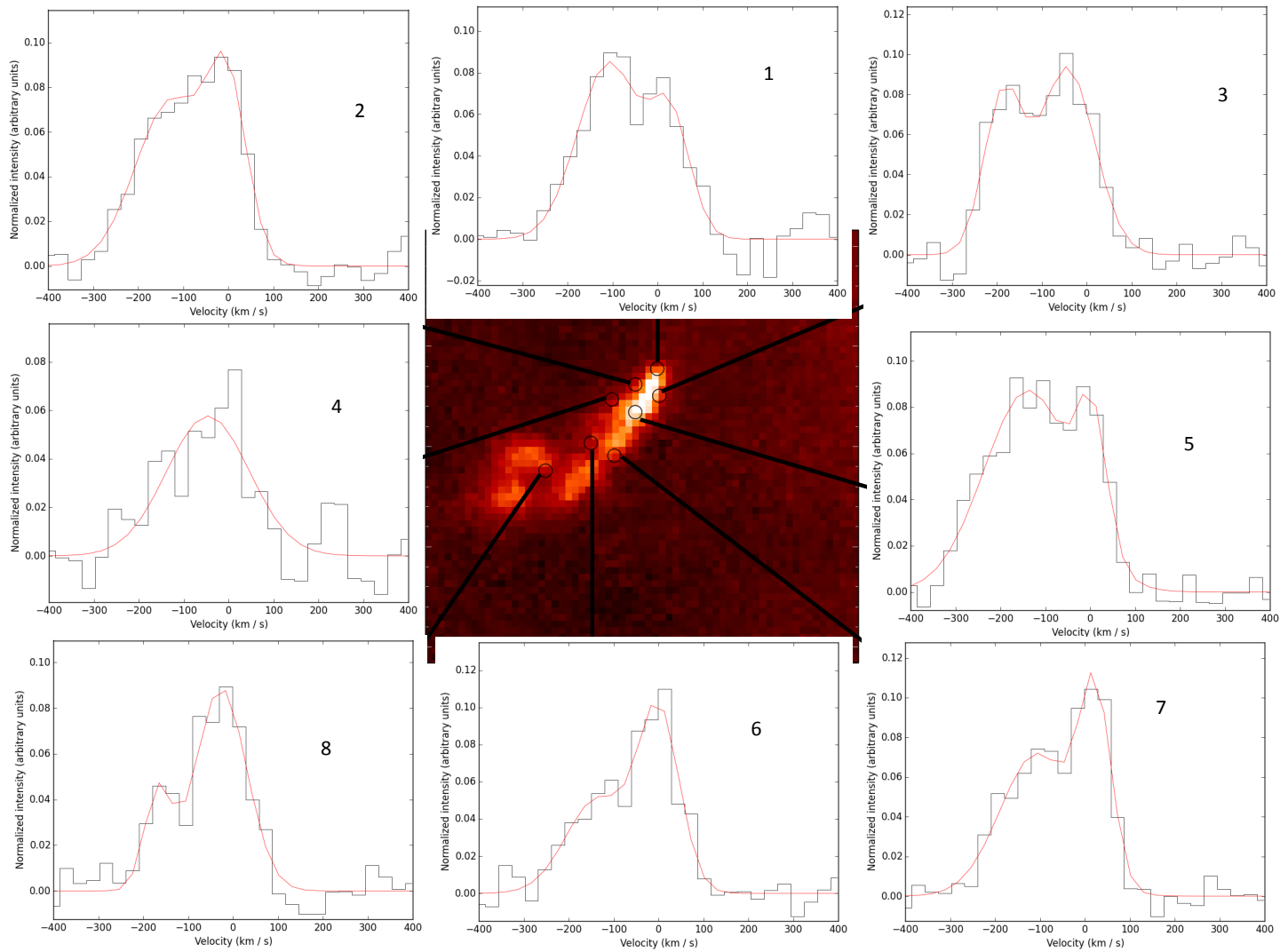


Figure 4.16: Integrated intensity map of the [FeII]λ8617 line (middle), and the spectra corresponding to the pixels marked by the centroid of the black circles. The spectra are continuum subtracted, and fitted with a two component Gaussian (the numbers correspond to the entries in Table 4.4, see also text Section 5.1 for details).

Table 4.4: Best fit parameters of the Gaussian fitting to the [FeII] λ 8617 lines shown in Fig. 4.16. Centroids and widths are measured in km s⁻¹, values are rounded to the nearest integer.

Position (J2000)	Coordinates (blue)	Centroid (blue)	Width (red)	Centroid (red)	Width
1	5 35 11.29 -5 21 52.15	-108±12	69±10	29±11	43±9
2	5 35 11.25 -5 21 52.49	-126±28	80±20	-25±10	42±11
3	5 35 11.34 -5 21 52.60	-186±10	42±8	-44±11	61±10
4	5 35 11.29 -5 21 52.98	-46±12	92±12	-	-
5	5 35 11.25 -5 21 51.68	-138±11	99±10	4±5	32±8
6	5 35 11.38 -5 21 53.90	-136±30	70±24	0±10	46±7
7	5 35 11.34 -5 21 54.28	-107±11	-30±8	-27±5	57±6
8	5 35 11.47 -5 21 54.73	-168±12	69±10	29±11	43±9

We interpret the detection of two velocity components along the line of sight as a sign of expansion. For the evolutionary scenario of this bullet we therefore suggest that it is currently being disrupted, probably because of it being a high-velocity and high-density object hydrodynamically interacting with the surrounding Orion Nebula, for example by impacting on a high-density region.

4.5.2 Outflows and proplyds

In terms of the the S_{23} vs. [OII]/[OIII] analysis, the region just south of the Bright Bar containing the HH objects 203 and 204, as well as several of the Orion proplyds including Orion 244-440, is of great interest. The proplyds on this side of the Bar occupy a completely different region in Fig. 4.8c than the proplyds that lie on the other side of the Bar and that are under the direct influence of the Trapezium stars. This is not surprising, as the physical conditions in the two regions differ in terms of ionising radiation and other feedback mechanisms (like stellar winds and outflows), which lead to the proplyds south of the Bar having higher S_{23} values and displaying lower degrees of ionisation. A $1.2' \times 1.0'$ sub-cube was generated as to analyse this region in more detail, integrated intensity maps of [OI], [SII], [OII], $H\alpha$, [NII] and [OIII] are shown in Fig. 4.17.

Fig. 4.18b shows the colour-coded S_{23} vs. [OII]/[OIII] parameter space, as well as the corresponding S_{23} map (panel a). The S_{23} vs. [OII]/[OIII] parameter space separates the various objects in this field into different populations: the Bar shows higher S_{23} values than the proplyds and HH objects, while these show a wider range of degrees of ionisation. The clear separation into different populations however is not seen when considering [SII]/ $H\beta$ (or [SII]/ $H\alpha$) as is shown in Fig. A7, where the same populations are not as clearly separated and overlapping. We interpret this as S_{23} being an indicator of the relative contribution of shocks (and photoionisation) to the excitation of the sulphur atoms, as shocks locally compress matter, reducing the ionisation parameter and therefore enhancing the emission of low- over high-ionisation species (e.g. enhancing [SII] emission with respect to [SIII]). In this scenario,

Table 4.5: Orion proplyds. The proplyd Id linking to Fig. 4.18 (column 1), the proplyd number from Ricci et al. (column 2), the coordinates (J2000, column 3), and the type (column 4, i = ionised disk seen in emission, J = jet, B = binary system, mj = microjet, $SLLI$ = S_{23} -low and low ionisation, $SLHI$ = S_{23} -low and high ionisation, $MSLI$ = medium S_{23} values and low ionisation, $SHLI$ = S_{23} -high and low ionisation).

Id	Object	Coordinates	Type*
a	250-439	5 35 25.02 -5 24 38.49	i , $SLHI$
b	247-436	5 35 24.69 -5 24 35.74	i , J , $SHLI$, mj
c	244-440	5 35 24.38 -5 24 39.74	i , $SLHI$ + $MSLI$ (out), $SLLI$ (middle), $MSLI$ (disk), mj
d	252-457	5 35 25.21 -5 24 57.34	i , $SLHI$, mj
e	245-502	5 35 24.51 -5 25 01.59	i , $SLLI$
f	231-502	5 35 23.16 -5 25 02.19	i , B , $SHLI$
g	231-460	5 35 23.05 -5 24 59.58	i , $SHLI$
h	239-510	5 35 23.98 -5 25 09.94	i , $SHLI$
i	242-519	5 35 24.22 -5 25 18.79	i , $SHLI$, mj
j	236-527	5 35 23.59 -5 25 26.54	i , $SLHI$ + $MSLI$
k [†]	221-433	5 35 22.08 -5 24 32.95	i
l	206-446	5 35 20.62 -5 24 46.45	i , $MSLI$, mj
m [†]	232-455	5 35 23.22 -5 24 52.79	i
n [‡]	224-510	5 35 22.41 -5 25 09.61	$SHLI$

*From Ricci et al. (2008), this work and Bally et al. 2000.

[†]Non-detection in this work.

[‡]New detection from this work.

the Bar shows higher S_{23} values because photoionisation from the Trapezium stars produces a larger fraction of [SIII] emission, which is not the case for the objects south of the Bar.

We cross-matched the identified sources in this field with the *HST/ACS* Atlas of Great Orion Nebula proplyds (Ricci et al., 2008), and report their main characteristics in Table 4.5, where the types are i = ionised disk seen in emission, J = jet, B = binary system (from Ricci et al. 2008), and mj = microjet (from Bally et al. 2000). All of the proplyds in this field are associated with ionised disks seen in emission, and in general the objects can be separated into 4 classes, depending on their S_{23} values and degree of ionisation:

- S_{23} -low and high ionisation ($SLHI$): proplyds a , c , d , j and outer layer of HH 204
- S_{23} -low and lower ionisation ($SLLI$): proplyds c and d
- mean S_{23} values and lower ionisation ($MSLI$): HH 204, proplyds j , c and l
- S_{23} -high and lower ionisation ($SHLI$): proplyds b , f , g , h , i and n , tip of HH 203, HH 204

The proplyd 232-455 (indicated with the letter m in Fig. 4.18a) is a non-detection in our data, as the emission is dominated by the ghost of θ^2 Ori A. Not in the Ricci et al. catalog is the object indicated with the yellow triangle (object n) in Fig. 4.18a, which is found just below HH 203. We tentatively classify this source as a candidate proplyd and assign it the identifier 224-510, as it displays similar S_{23} and [OII]/[OIII] values as the objects in the $SHLI$ category, but was not detected by Ricci et al. and we do not have the spatial resolution of *HST* to better

resolve the source and an eventual microjet/outflow. We will now briefly discuss the objects belonging to the four classes[§].

Multi-class objects: HH 204 and Orion 244-440

Both HH 204 and Orion 244-440 seem to have S_{23} -high as well as S_{23} -low components, but while 244-440 appears to have a layered structure, HH 204 shows a *head-tail* configuration. Orion 244-440 is a giant proplyd containing a YSO, or possibly even a binary system, with a one-sided microjet along the North-East axis (Bally et al., 2000). Fig. 4.18 and Fig. A8 (panels c and d) show that the outer layer of 244-440 appears to be S_{23} -low over a wide range of $[OII]/[OIII]$, while the inner part, corresponding to the star+disk component of the proplyd (magenta box marked with the letter *c* in Fig. 4.18), shows a steep rise in S_{23} values. Complementary to Henney & O'Dell (1999), we provide a sketch of Orion 244-440 in Fig. 4.19: the outer, S_{23} -low, layer of the proplyd, shows a positive $[OII]/[OIII]$ outside-in gradient, confirming the model of Henney & O'Dell where the ionised density of the outer layers is low, and increases when moving in towards the proplyd; the star+disk component seems to be aligned with the direction towards θ^2 Ori A and the direction of motion (indeed, O'Dell et al. 1993 find that some proplyds are oriented toward θ^2 Ori A, rather than θ^1 Ori C). The star+disk component itself is characterised by a S_{23} gradient that increases in the direction of motion.

The head of HH 204 (sketched in Fig. 4.20 and highlighted in Fig. A8, panels a and b), on the other hand, displays intermediate S_{23} values, and a S_{23} -low tail that shows an ionisation front in the direction of θ^2 Ori A. Also, just as 244-440, it covers a broad range of $[OII]/[OIII]$, and because of its layered structure it belongs to more than one of the four classes.

Núñez-Díaz et al. (2012) performed an thorough analysis of HH 204 with integral field data from the Potsdam Multi-Aperture Spectrograph. They find a clearly stratified ionisation structure across HH 204, and discuss the presence of a trapped ionisation front at the head of the bow-shock, due to the a high $[OI]/H\beta$ ratio at that position, on the opposite side of the source of ionisation. In their analysis, the location of the enhanced $[OI]/H\beta$ ratio is also characterised by an enhanced $[SII]/H\beta$ ratio, which is in good agreement with the enhanced S_{23} found in this work at the head of the bow-shock (marked as SHLI in Fig. 4.20).

SHLI: HH 203, proplyds 239-510, 242-519, 247-436 and the candidate proplyd 224-510

All of these objects are classified under SHLI, but they can be further separated into two sub-classes, depending on the presence of a microjet or not. The object HH 203 appears to have a different structure in terms of the S_{23} parameter than HH 204, and only its tip deviates from the general cluster of data points in Fig. 4.18b that originate from the ambient matter. Its tip classifies as SHLI, as does proplyd 239-510 and the candidate proplyd (identified as *h* and *n* respectively in Table 4.5 and Fig. 4.18a). Also classified as SHLI are the proplyds 247-436 and 242-519 (*b* and *i* respectively), but these two are associated with microjets (Bally

[§]We will not discuss proplyds 231-502, 231-460, 232-455 and 221-443, as the former three are too close to θ^2 Ori A to be properly distinguished, and the latter is confused with the emission coming from the Bright Bar.

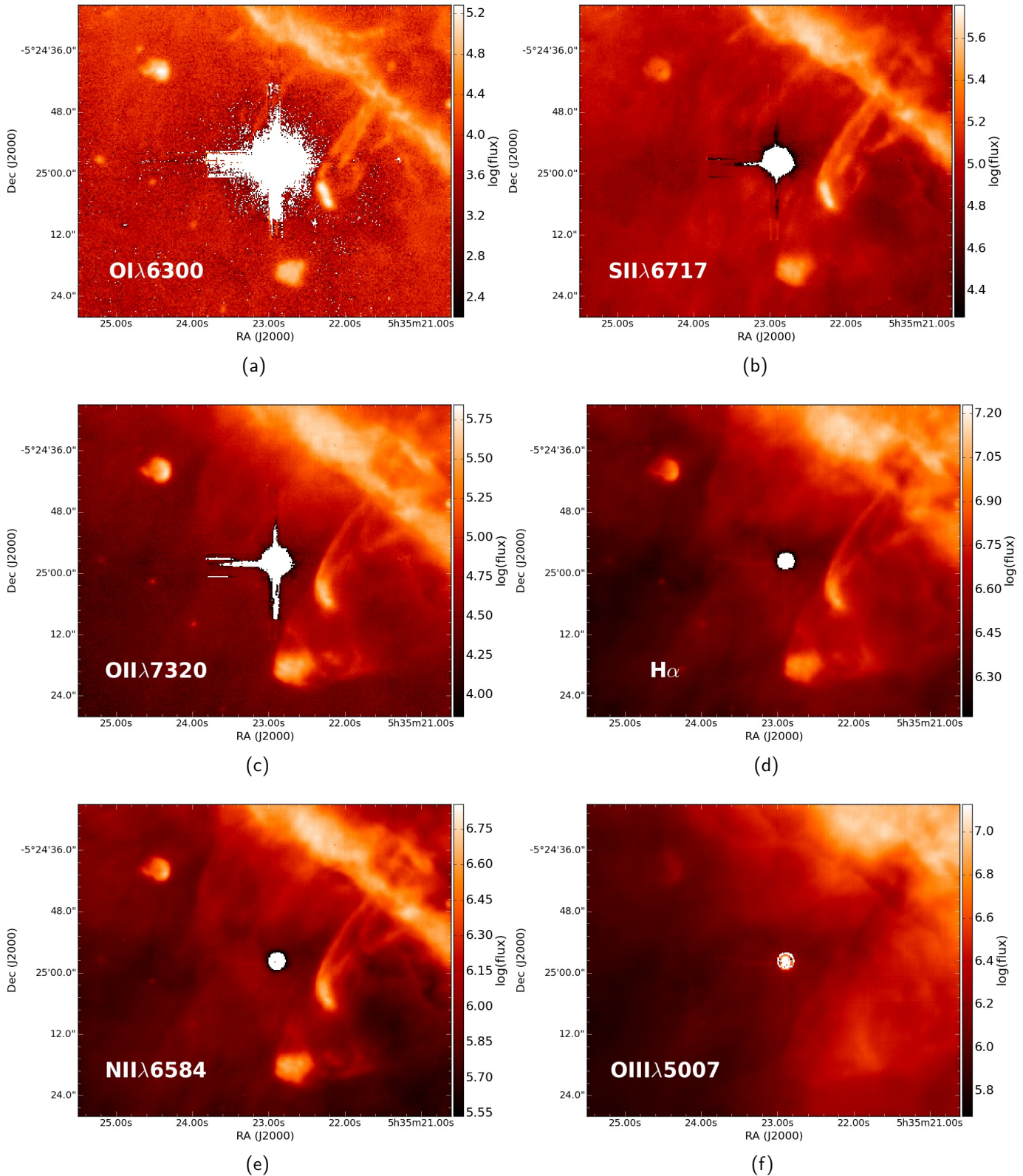


Figure 4.17: Continuum-subtracted integrated intensity maps of HH 203 and 204, as well as 244-440 $[\text{OI}] \lambda 6300$ (a), $[\text{SII}] \lambda 6717$ (b), $[\text{OII}] \lambda 7320$ (c), $\text{H}\alpha$ (d), $[\text{NII}] \lambda 6584$ (e) and $[\text{OIII}] \lambda 5007$ (f). The flux is measured in $10^{-20} \text{ erg s}^{-1} \text{ cm}^{-2} \text{ pixel}^{-1}$, all maps are linearly scaled to minimum/maximum.

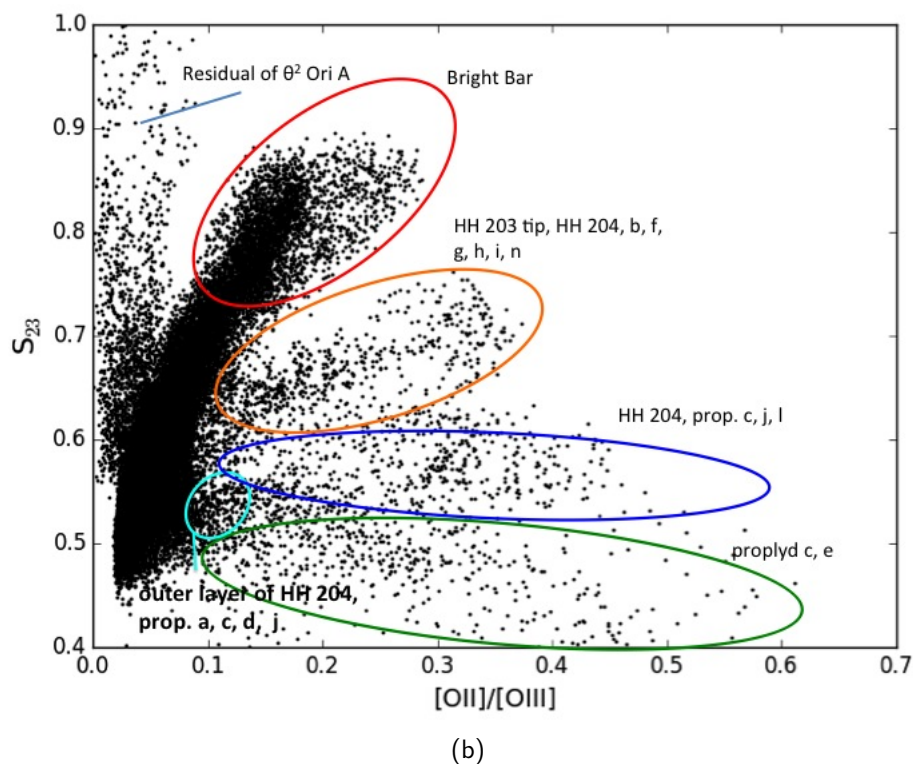
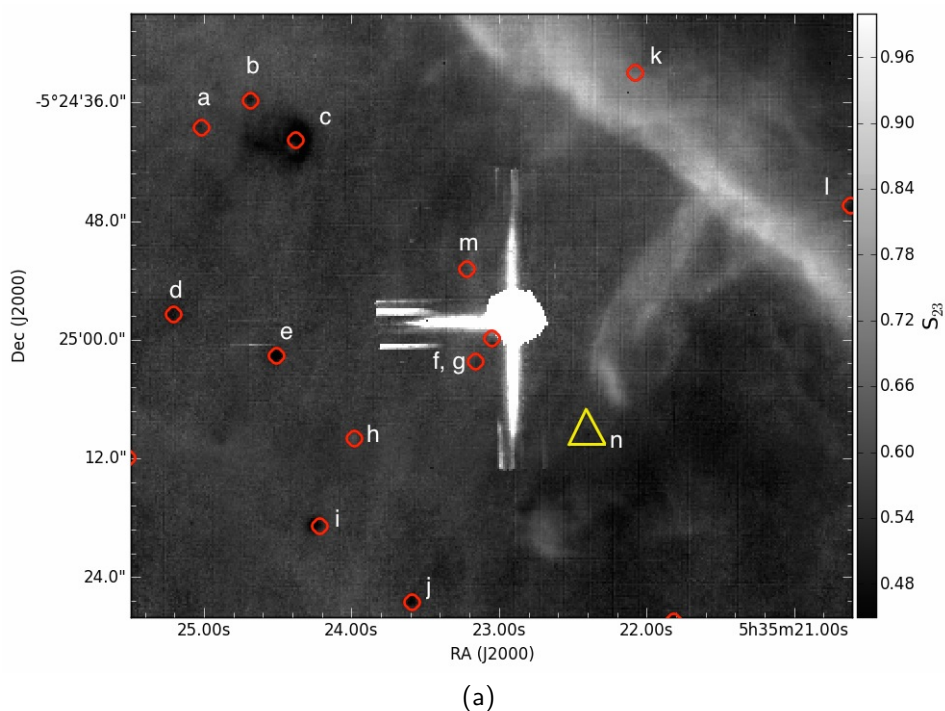


Figure 4.18: S_{23} map of the region containing the Herbig-Haro objects HH203, 204 as well as the proplyd Orion 244-440 (panel a), red circles and letters from a to m indicate the Orion proplyds in this field, the yellow triangle indicated with the letter n marks the position of a candidate proplyd (see text Section 5.2 and Table 4.5). Panel (b): S_{23} vs. $[OII]/[OIII]$ parameter space of the same region. Strong residuals of θ^2 Ori A from the continuum-subtraction are indicated in panel (b).

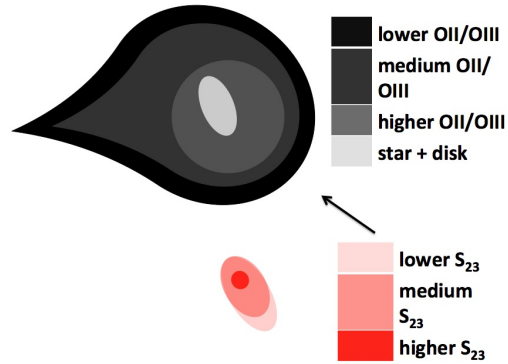


Figure 4.19: Sketch of Orion 244-440: the outer layer displays an [OII]/[OIII] gradient with decreasing ionisation from the outside in (greyscale in upper figure), the star+disk component (lower figure) shows an S₂₃ gradient which increases away from the direction of motion. The black arrow indicates the direction of θ^2 Ori A.

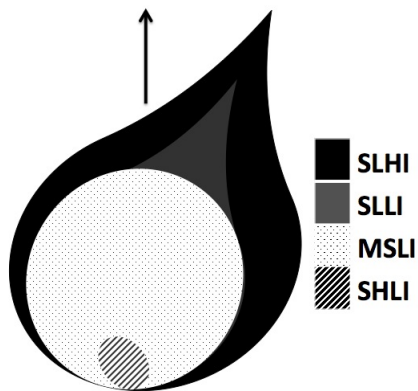


Figure 4.20: Sketch of HH 204. The black arrow indicates the direction to θ^2 Ori A, while the direction of motion is along the head-tail axis.

et al., 2000): indeed, although wSLLIe are limited by spatial resolution, we seem to be able to distinguish two components in these two proplyds, corresponding to a stellar and an outer (shell-like) component (marked in red and green respectively in Fig. A8, b and Fig. A11a, b).

SLHI: proplyds 250-439, 252-457 and 236-527

These three proplyds (identified as *a*, *d* and *j* respectively in Table 4.5) occupy the S_{23} -low but highly ionised region of the scatter plot. Of the three, only 252-457 is associated with a particularly long jet of about 15", more details are discussed in Bally et al. (2000).

SLLI and MSLI: proplyds 245-502 and 206-446

Both of these two sources are single objects in their classes, if one does not count the multi-class objects. Proplyd 245-502 (blue in Fig. A10a, b) is Proplyd 206-446 (Fig. A9c, d) is associated with a microjet perpendicular to the disk and faces θ^2 Ori A (Bally et al., 2000), and although we are again limited by spatial resolution, the MUSE data seems to hint that this proplyd might have a SLHI component.

4.6 Conclusions

An analysis of the Orion Nebula in terms of ionic and total abundances as well as kinematics of the ionised gas was presented, based on optical integral field observations with the instrument MUSE@VLT. The following points summarise the main results of this paper:

- The first 5' x 6' ionic and total abundance maps of oxygen, sulphur and nitrogen of the Orion Nebula are presented.
- The abundance maps are contaminated by a certain degree of structuring that traces the main features of M 42 (the Bright Bar, the Orion S regent, HH 203 and 204, some of the proplyds). Furthermore, the ionic abundances computed from the MUSE data do not agree with literature values. We suggest that a combination of observational limitations (e.g. high level of noise in the electron temperature and [OII] maps, strong dependence of the abundances on the physical parameters) and intrinsic properties (e.g. high-density regions with densities approaching the critical values of the species used to compute the physical parameters) lead to the described discrepancies between previously published data and this work. Within errors, the computed O and S abundances are in agreement with literature values.
- The computed structure functions (S_2) prove that this dataset lacks the depth to reproduce previous results, which showed that in the Orion Nebula, the slope of S_2 corresponds to a broken power law with a steeper index at small scales and a turnover to a shallower index at larger scales. The structure functions computed in this work are much shallower than previous results, as they are highly affected by the large number of pixels with low signal to noise in the velocity maps. We demonstrated how noise can affect the structure

function with simulated H II regions, and will discuss this issue in depth in a forthcoming paper.

- The only Herbig-Haro object that stands out from the rest is HH 201, the only one of the so called Orion Bullets covered by the MUSE mosaic. This outflow, similarly to the one identified in our analysis about the Pillars of Creation, shows very high S_{23} together with a very high degree of ionisation. From previous studies it seems that this object originates from an explosive event that occurred in the BN-KL star forming region. Based on its cometary shape in the velocity maps and on the double component seen in the [FeII] line, we speculate that this object is currently impacting in a region with high densities and that it is therefore currently being disrupted.
- We applied a method developed in our previous publication about the iconic Pillars of Creation in M 16 to the Orion dataset to analyse the outflows and proplyds. In this method, the S_{23} parameter is analysed in terms of the corresponding degree of ionisation (given by the ratio [OII]/[OIII]). We find that the proplyds can be divided into two distinct populations, in correlation with their location. The population of proplyds near the Trapezium cluster have lower S_{23} values and a higher degree of ionisation, while the population of proplyds that lie south of the Bright Bar seem to be more shielded from the intense feedback of the Trapezium stars, as they show higher S_{23} values and lower degree of ionisation. Furthermore, the proplyds and HH objects south of the Bar can be in turn divided into four classes, depending on their S_{23} vs. [OII]/[OIII] values, and we show how they can be clearly distinguished in the S_{23} vs. [OII]/[OIII] parameter space. This demonstrates that this method is very useful to pick out these kind of objects in the S_{23} vs. [OII]/[OIII] parameter space.
- We suggest that the reason for the capability of the S_{23} parameter to distinguish between the Bright Bar, the HH outflows and the proplyds is twofold: this line ratio traces both high degrees of ionisation (given by the higher S_{23} values) and the relative contribution of shocks to the excitation mechanism (in the regime of low S_{23} values).

5

Towards an observational quantification of ionising feedback

Submitted to Monthly Notices of the Royal Astronomical Society as McLeod et al. on April 28th, 2016

*“Connecting the dots: a correlation between ionising radiation and cloud mass-loss rate traced by optical integral field spectroscopy,,”**

Abstract

We present data from the integral field spectrograph MUSE mounted on the Very Large Telescope of pillar-like structures in the Carina Nebular Complex, one of the most massive star-forming regions in the Galaxy. For the observed pillars, we compute gas electron densities and temperatures, produce integrated line and velocity maps of the ionised gas, study the ionisation fronts at the pillar tips, analyse the properties of the single regions, and detect two ionised jets originating from two distinct pillar tips. For each pillar tip we determine the perceived ionising photon flux originating from the nearby massive O- and B-type stars and compute the mass-loss rate of the pillar tips due to photo-evaporation caused by the incident ionising radiation. We combine the results of the Carina data set with archival MUSE data of a pillar in NGC 3603 and with previously published MUSE data of the Pillars of Creation in M16, and with a total of 10 analysed pillars, find tight correlations between the ionising photon flux and the electron density, the electron density and the distance from the ionising sources, and the ionising photon flux and the mass-loss rate. The combined MUSE data sets of pillars in regions with different physical conditions and stellar content therefore yield an empirical quantification of the feedback effects of ionising radiation.

*This work is the result of collaborative efforts of the authors of the paper. Specifically, I was responsible for the entire data reduction, analysis and interpretation, as well as the manuscript preparation. I am also Principal Investigator of the observing proposal which lead to the data acquisition. Gritschneider provided the figures for the simulated pillar-like structures, and the other co-authors contributed with valuable insight on the interpretation of the results and in proof-reading the manuscript.

5.1 Introduction

Feedback from massive stars is a crucial factor in the baryon cycle of galaxies. It regulates how they turn their gas reservoir into stars and therefore plays a fundamental role in galaxy evolution (Sommer-Larsen et al., 2003). However, its exact role is one of the main missing ingredients to connect the observed galaxy population to Λ CDM cosmology (e.g. Vogelsberger et al. 2014, Schaye et al. 2015). On smaller, molecular cloud-scales (1-10 pc), massive stars (which generally form in a clustered environment, rather than in isolation, Beuther et al. 2007, Bressert et al. 2010) profoundly affect their immediate environment: stellar winds, photo-ionising radiation and supernova events are responsible for inflating HII regions and shell-like structures, which both halt and enhance star formation by clearing away the molecular gas but also locally compressing it to create high-density regions and therefore possible sites of new star formation (Walch, 2014).

Feedback from massive stars is also thought to be responsible for exposing pillar-like structures and globules from surrounding gas and dust (Mellema et al. 2006, Arthur et al. 2011, Tremblin et al. 2012). However, the relative importance of the different pillar formation scenarios is debated: is a pre-existing dense structure exposed by stellar feedback, or does feedback collect and compress the molecular gas to form overdensities which subsequently form pillars via instabilities (Gritschneider et al. 2010b, Tremblin et al. 2012)? Notwithstanding the contentious formation mechanism, these structures are formed throughout star forming regions, both observed (Hester et al. 1996, Klaassen et al. 2014) and simulated (Gritschneider et al. 2010b, Dale et al. 2012b), some host forming stars at their tips which are sometimes known to launch bipolar jets (Smith et al. 2010b, Reiter & Smith 2013), and they are found to photo-evaporate under the influence of the nearby massive stars (Westmoquette et al. 2013, McLeod et al. 2015). The mechanism of photo-evaporation is explained by the strong ionising radiation from the nearby O- and B-type stars impinging on the matter of the pillar tips: the pressure of the pillar material increases and it is photo-ionised, leading to a photo-evaporative flow of matter streaming away from the pillar surface (Hester et al., 1996). However, a quantitative link between the combined energy input by star cluster members and the feedback effect on the surrounding pillar-like structures has not yet been made.

In a previous study, we targeted the iconic Pillars of Creation in M 16 (McLeod et al. 2015, henceforth referred to as MC15) with the integral field unit (IFU) MUSE mounted on the Very Large Telescope (VLT). In projection, these pillars are situated ~ 2 pc south-west of the massive cluster NGC 6611, which is responsible for the radiation field which is photo-evaporating the nearby pillars. For these structures, we computed the mass-loss rate due to photo-evaporation by making use of the simultaneous imaging and spectroscopic capabilities of MUSE, which allowed us to determine both the morphology and the kinematics of the ionised gas by covering all the ionised emission lines in the 4650 Å - 9300 Å range covered by MUSE. Together with their molecular mass of about $200 M_{\odot}$ (White et al., 1999b), we estimated a lifetime of ~ 3 Myr for the pillars in M 16.

However interesting for the particular case of the M 16 region, the results obtained for the Pillars of Creation alone are not enough to analyse and quantify ionising feedback in general.

To do this, the interplay between the ionising star cluster and the affected (photo-evaporating) pillar-like structures needs to be analysed in a representative sample of regions to test for the existence of a relationship between the two. In this paper, we exploit a unique data set of pillar-like structures in the Carina star-forming region observed with the IFU MUSE. In combination with archival MUSE data of a pillar in NGC 3603 and the previously published M 16 data, we attempt a first quantitative analysis of ionising feedback in high-mass star-forming regions by comparing the photo-evaporative effect in these different regions.

The Carina Nebula Complex (CNC) is a rich, nearby (2.3 kpc, Smith 2006a) and well studied star forming region, with tens of young star clusters, O- and B-type stars and many pillar-like structures that surround the central part of the Complex (Smith & Brooks, 2008). Because of this, it is the ideal region to study the stellar populations of young, massive clusters, as well as their feedback on the surrounding molecular clouds. It hosts about 65 O-type stars as well as three WNL stars*, which together emit a total ionising photon luminosity of about 10^{51} photons s^{-1} (Smith, 2006b). Despite the high degree of feedback and the presence of already exposed star clusters, as well as the evolved massive LBV η Car, the CNC is also known to host vigorous ongoing star formation as well as a few $10^4 M_{\odot}$ in dense, cold clouds which have not yet formed stars (Preibisch et al., 2012a). The massive stellar content of the CNC is predominantly found in the three main young clusters, namely Trumpler 14, 15 and 16, which together account for $\sim 93\%$ of the total ionising flux. Tr 14 and Tr 16 are located toward the center of the giant Carina HII region and have ages of about 1-2 Myr (Hur et al., 2012). While Tr 14 hosts ~ 10 O-stars (ranging from O2 I to O6.5 V) and has a very compact spatial configuration with a core radius of just 0.15 pc and a central stellar density of the order of $10^4 M_{\odot} pc^{-2}$, Tr 16 hosts ~ 18 O-stars, a WNL star, and is a loose open cluster and consists of several subclusters (Feigelson et al. 2011, Wolk et al. 2011). By contrast, Tr 15 only hosts about 6 O-stars, none of them of spectral type earlier than O8, and is older than Tr 14 and 16, with an age between 5 and 10 Myr (Wang et al., 2011). The structure and properties of the dense, cool clouds in the CNC was recently studied in new detail by deep sub-mm mapping observations with LABOCA at the APEX telescope (Preibisch et al., 2011) and by the $70 - 500 \mu m$ far-infrared observations with the *Herschel* space observatory (Preibisch et al., 2012b; Roccatagliata et al., 2013). These observations showed that most of the dense gas in the CNC is concentrated in numerous pillar-like cloud structures, which are shaped by the irradiation of nearby high-mass stars.

The multitude of pillars, globules and outflows in the CNC have been thoroughly analysed in Hartigan et al. (2015). These authors used both broad- and narrowband near infrared (I, K, $Br\gamma$ and H_2) and optical ($H\alpha$, [SII] and [OIII]) data to detect previously unknown candidate jets (to complement and complete the already well known population of Herbig-Haro objects from Smith et al. 2010b) and identify the main irradiated surfaces between the HII region and the surrounding molecular clouds. In this exhaustive study, Hartigan et al. analyse 63 different regions within the CNC, each containing one or more pillars or irradiated globules. The MUSE CNC data set presented in this paper covers 5 of the Hartigan et al. regions and contains 5 distinct pillars as well as one irradiated globule. The regions were chosen to maximise the

*Late-type Wolf-Rayet stars with nitrogen-dominated spectra that show hydrogen lines.

number of covered pillars, sample these from a variety of different locations within the CNC, and minimise the needed amount of telescope time. This unique data set, in combination with MUSE observations of pillars in M 16 (MC15) and NGC 3603, offers for the first time the possibility of analysing both the morphology and the kinematics of the ionised gas with the unique combination of angular resolution and spectral coverage offered by MUSE. With this data, we analyse the ionising feedback from the massive stars in the CNC by computing and comparing the ionising photon flux and photo-evaporation rate for a total of 10 pillars, and we deliver an observational quantification of the effects of ionising feedback.

The observations and data reduction are discussed in Section 5.2. The analysis in this paper is divided into four main topics: a study of the behaviour of the various detected emission lines at the pillar/ambient matter interfaces (Section 5.3.1), the computation and discussion of the physical parameters of the observed regions (Section 5.3.2), the connection between the ionising massive stars and the photo-evaporation of the surrounding pillars (Section 5.3.3), and the discussion of two detected bipolar jets originating from the pillar tips (Section 5.3.4). Conclusions are present in Section 7.

5.2 Observations and data reduction

5.2.1 Carina

We observed a sample of pillar-like structures in the Carina Nebula Complex with the IFU MUSE under the program 096.C-0574(A) (PI McLeod). The observing program targeted five regions sampled from Hartigan et al. (2015), who present near-infrared images from NEWFIRM and optical images from MOSAIC observations[†] of pillars, globules and jets in the Carina star-forming region. As already mentioned, the five regions from Hartigan et al., Areas 18, 22, 37, 44 and 45 (for simplicity named R18, R22, R37, R44 and R45 henceforth in this paper) were selected based on two criteria: the presence of pillar-like structures and their different locations within the CNC (to sample different feedback environments and conditions). Only four of the five target regions are discussed in this work, as the observations of R22 showed that this region is too heavily extinguished to identify the pillars, and therefore not suited for the analysis in this work. RGB composites of the four discussed regions (R18, R37, R44 and R45) are shown in Fig. 5.1. The colours correspond to [SII] λ 6717 (red), H α (green) and [OIII] λ 5007 (blue, the images shown in this figure are not continuum-subtracted). Fig. 5.2 shows the location of the four regions with respect to the three main CNC clusters (black crosses) and the location of known O- and B-type stars from Gagne et al. (2011) (white crosses). Two O-stars (HD 303316 and HD 305518 are highlighted, as discussed in Section 5.3.3).

With these observations, we sample a total of 5 pillar-like structures (R18, R45 and three distinct pillars in R44, where we refer to the pillars as R44 P1, R44 P2 and R44 P3 as indicated by the slit positions in Fig.5.4) as well as one detached globule (R37) in the relative vicinity of

[†]the NOAO Extremely Wide-Field Infrared Imager and the NOAO/KPNO Mosaic Wide Field Imager, thus both wide-field imagers covering a much larger area than the HST and Spitzer surveys from Smith et al. (2010b), Smith et al. (2010) and Povich et al. (2011).

Table 5.1: MUSE observations of pillar-like structures in the Carina Region. Coordinates are taken from Hartigan et al. (2015).

Region	R.A. (J2000)	Dec (J2000)	Observing date	No. of mosaic pointings
R18	10:45:31.98	-59:12:23	1/2 Nov. 2015	2
R37	10:44:31.44	-59:39:21	31 Oct./1 Nov. 2015	2
R44	10:41:39.21	-59:43:33	30 Nov./1 Dec. 2015 & 10/1 Dec. 2015	10
R45	10:41:20.69	-59:48:23	15/16 Nov. 2015	2

two of the three most massive clusters in the CNC, Tr 15 and Tr 16. As will be discussed later (see Section 7), a dedicated MUSE data set covering the massive pillars around Tr 14, as well as the cluster stars themselves, has been recently observed (VLT program 097.C-0137(A), PI McLeod) and will be presented in a forthcoming publication.

The total amount of telescope time awarded to this program was 5.5 hours, and the data was taken during the period from October 31st, 2015 to January 17th, 2016. The central coordinates of each observed region, as well as the date of observation and number of mosaic pointings per region are listed in Table 5.1. The exposure time for all observations was 90 seconds, and each pointing was observed three times following a 90° dither pattern, a method generally used to minimise instrument artefacts and proven to be successful with our MUSE science verification data of pillar-like structures in M 16 (MC15). The data reduction was carried out in the ESO ESOREX environment of the MUSE pipeline (Weilbacher et al., 2012b) and using standard calibrations. Each pointing was observed in the nominal wavelength range of MUSE (4650-9300 Å, resolving power $R = 2000-4000$) and exploiting the instrument’s Wide Field Mode with a field of view of 1x1 arcminutes.

5.2.2 NGC 3603 and M 16

We compare the observations of the Carina pillars to similar structures in two other regions covered by MUSE, namely the Pillars of Creation in the Eagle Nebula (M 16), as well as a pillar south-west of the massive cluster in NGC 3603. Both the MUSE M 16 and NGC 3603 data were taken during the instrument’s science verification run in June 2014. The M 16 data set (program 60.A-9309(A), PI McLeod) is presented and analysed in MC15, which gives details of the observational setup and data reduction. The NGC 3603 and M16 pillars were included to sample pillars not only across various star-forming regions, but also in different ionising conditions.

The massive cluster in NGC 3603, in projection only about 1 pc away from the observed pillar, is one of the most massive clusters in the Milky Way with an age of 1-2 Myr (Sung & Bessell 2004, Harayama et al. 2008) and mass estimates ranging from $\sim 10^4 M_{\odot}$ (Harayama et al., 2008) to about $1.8 \times 10^4 M_{\odot}$ (Rochau et al., 2010). The exposed cluster is surrounded by molecular cloud structures, among which are two prominent pillars (e.g. Westmoquette et al.

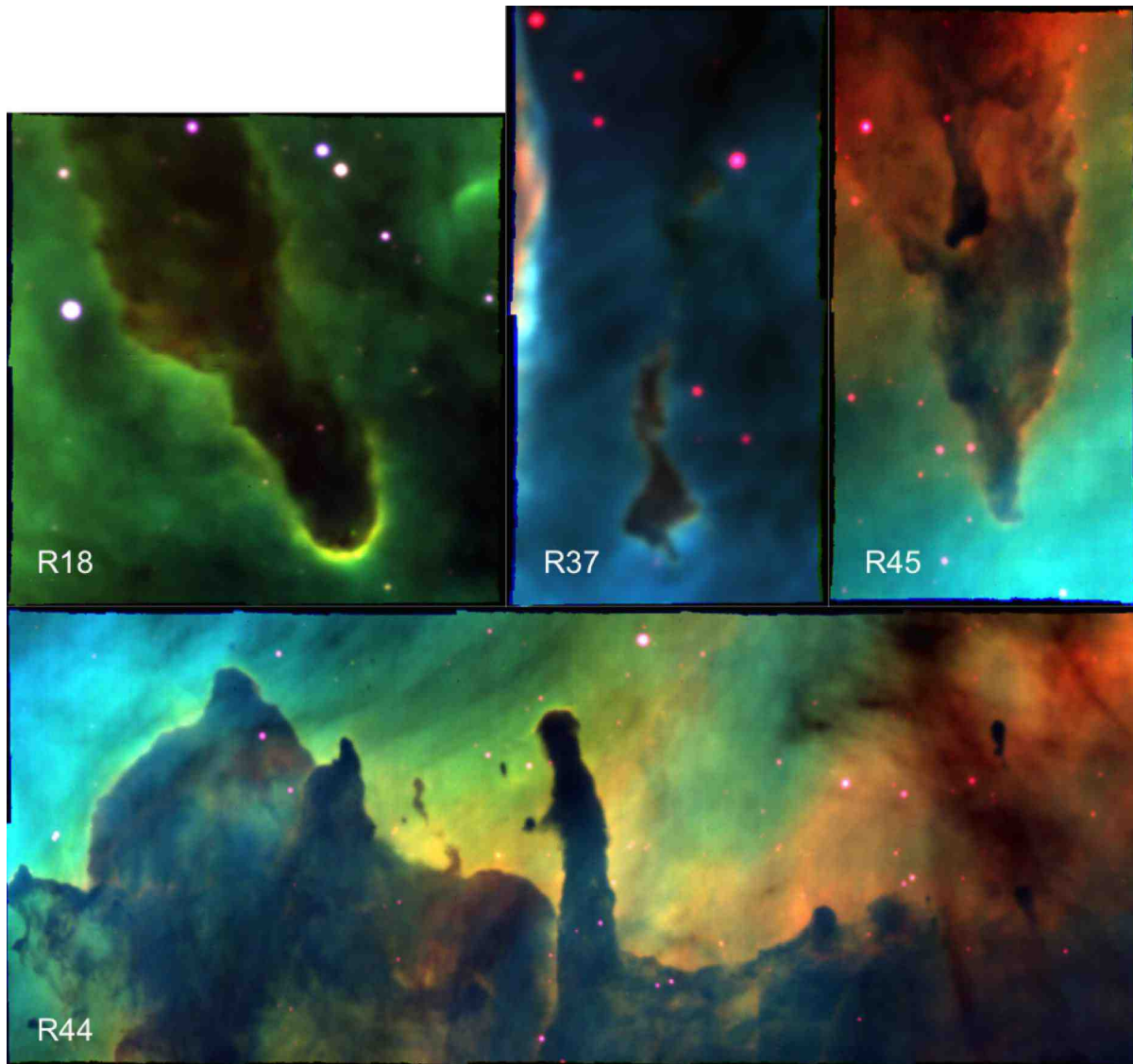


Figure 5.1: Three-color composites of integrated line maps of the four observed regions in Carina (R18, R37, R45 and R44). Red is [SII] λ 6717, green is H α and blue is [OIII] λ 5007. The images are not continuum-subtracted. See text Section 5.2 for further details.

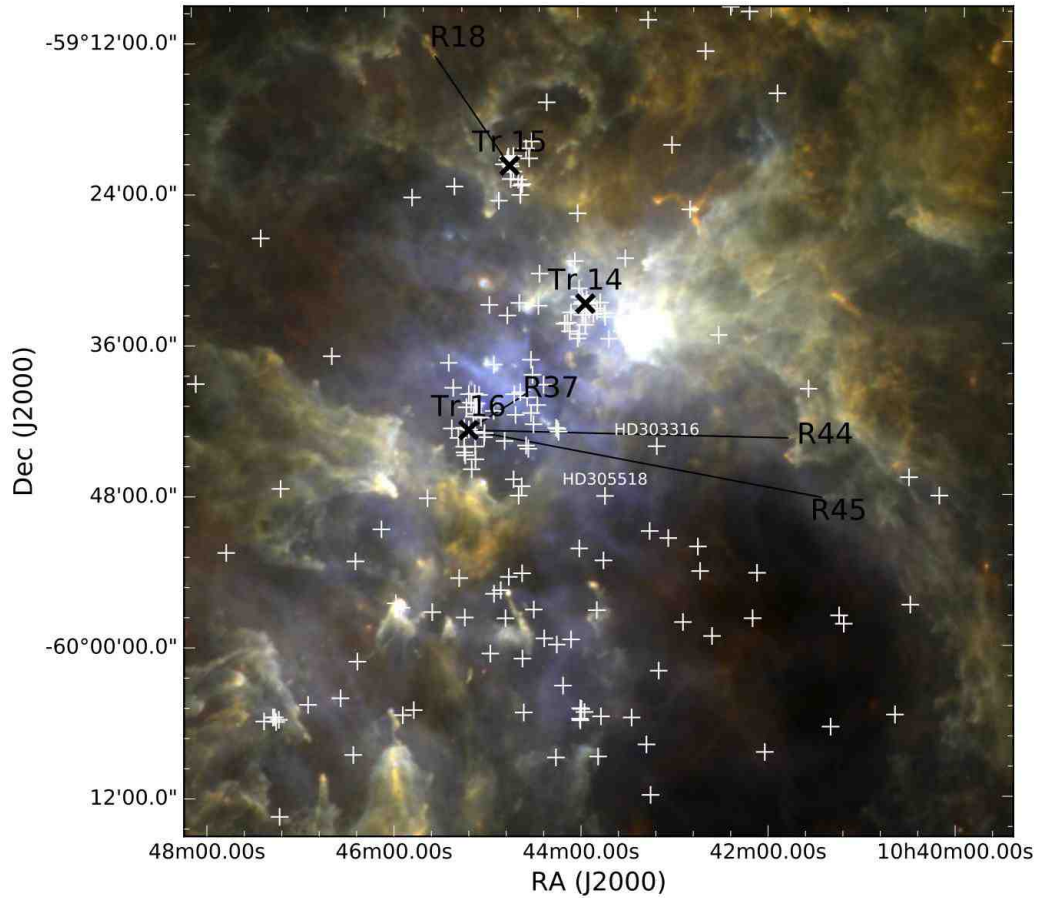


Figure 5.2: Three-color *Herschel* composite (red = 250 μm , green = 160 μm , blue = 70 μm). The 4 observed regions in Carina (R18, R37, R44 and R45) as well as the three most massive clusters (Tr 14, 15 and 16) are marked in black, O- and B-stars from Gagne et al. (2011) are marked with white crosses, the projected distances from each region to the main nearby clusters are traced with the black lines, and two O-stars (HD 303316 and HD 305518) are highlighted, see text Section 5.3.3.

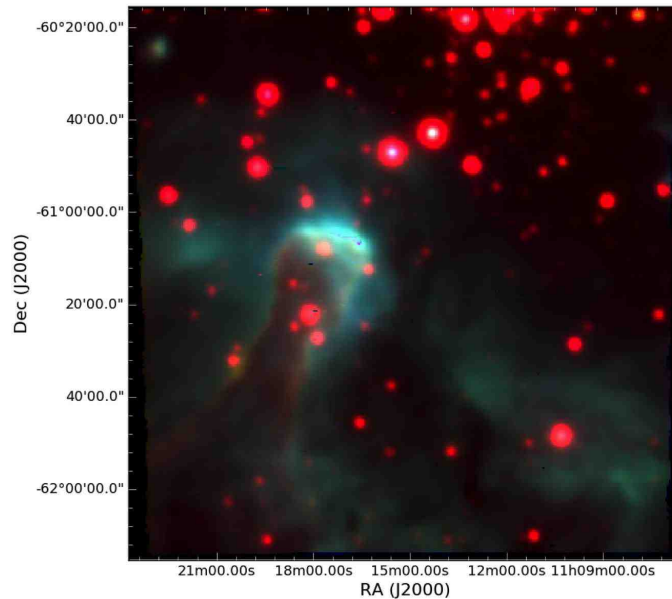


Figure 5.3: RGB composite of the pillar in NGC 3603, red is $[\text{SII}]\lambda 6717$, green is $\text{H}\alpha$ and blue is $[\text{OIII}]\lambda 5007$ (as for Fig. 5.1 the integrated emission line maps are not continuum-subtracted). See text Section 5.2.2.

2013), which are under the influence of the large number of O-type stars (> 30 , Melena et al. 2008) that dominate the feedback in the region. It is the ideal region to analyse one of the more extreme Galactic feedback environments, as the bolometric luminosity of the HD 97950 cluster[‡] is about 100 times greater than that of the Orion cluster, and about 10% that of the massive 30 Doradus cluster in the Large Magellanic Cloud. With MUSE, the pillar south-east of the cluster was covered, and an RGB composite of $[\text{SII}]$, $\text{H}\alpha$ and $[\text{OIII}]$ is shown in Fig. 5.3.

The archival NGC 3603 data set (program 60.A-9344(A)) consists of a single pointing covered with four different exposure times, namely 10, 60, 300 and 2100 seconds. For the purpose of this analysis, the 10 and 60 second exposures did not deliver the necessary S/N, and the main ionised emission lines are saturated in the 2100 seconds exposure. We therefore reduced the 300s data cube in the same manner as described in the previous subsection. Unfortunately however, the NGC 3603 data was not taken with a 90° rotation dither pattern as was done for M 16 and Carina, and the resulting images are therefore heavily contaminated by instrument artefacts, visible as a striped pattern most noticeable in the velocity maps (see e. g. Figure 5.9d).

[‡]We use HD 97950 as the designation for the massive cluster in the NGC 3603 region, although it originally refers to the star HD 97950, which could be resolved into a multiple system in the centre of a massive cluster in Melena et al. (2008).

5.3 Analysis

This work is oriented toward ionising feedback from massive stars and star clusters on the nearby pillar-like structures. The aim is to find a link between the feedback-driving stars and the feedback-affected surrounding molecular clouds by analysing the pillars pointing back towards the ionising star clusters. The analysis consists of four parts which are then combined to construct a clear picture of ionising feedback: we analyse the intensity of the ionised emission lines towards the pillars (Section 5.3.1); we determine the physical parameters for the different conditions present in each region (Section 5.3.2); we determine the mass-loss rate due to photo-evaporation of the pillars (Section 5.3.3); and we relate the presence and morphology of ionised jets at the pillar tips to the feedback conditions of the regions (Section 5.3.4).

5.3.1 Emission line intensity profiles

Figure 5.4 shows continuum-subtracted integrated $H\alpha$ line maps (all integration intervals span $\pm 3 \text{ \AA}$ around the central emission line wavelength) of all the discussed Carina pillars, while emission line maps of the other main lines used in this analysis ($H\beta$, $[\text{OIII}]\lambda 4959,5007$, $[\text{SII}]\lambda 6717,31$, $[\text{SIII}]\lambda 9069$, $[\text{NII}]\lambda 6548,84$, $[\text{OI}]\lambda 6300$, $[\text{OII}]\lambda 7320,30$) are shown in the Appendix in Figures C.1 to C.10. From the emission line maps, the ionisation fronts at the illuminated pillar tips are clearly visible, and in the case of R44-P3 and R45 the left and right sides of the pillars are also being illuminated (see Fig. 5.1), most probably by the nearby B-type stars located to the west, while the pillar tips are illuminated by two O-stars (see Section 5.3.3). However, these B-type stars are very likely not the main sources of feedback, as the pillars in R44 and R45 do not point in their direction but rather towards the two O-stars HD 303316 and HD 305518 marked in Fig. 5.2. This will be discussed in more detail in Section 5.3.3.

To analyse the structure of the ionisation fronts at the pillar tips, in Figures 5.5 and 5.6 we plot the profiles of the various emission lines along slits positioned as shown in Fig. 5.4 (from left to right, the abscissa in each plot indicates the distance along the slits, moving from the ambient matter towards the pillar tip and into the pillar material). Where more than one emission line for the same ionisation state of a given species is detected, the profile is computed from the mean value of these two (e. g. $[\text{SII}]\lambda 6717$ and $[\text{SII}]\lambda 6731$).

A general trend in order and shape of the profiles is seen in all regions: (i) the emission lines with higher ionisation energies peak first (closer to the ionising sources), followed by the emission lines with progressively lower ionisation energies (as already discussed in MC15); (ii) the emission lines originating from the higher-ionised states, which are less localised at the pillar tips but instead more diffuse ($[\text{SIII}]$, $[\text{OIII}]$ and $H\alpha, \beta$ and which predominantly originate in the HII region) show a very shallow rise when moving towards the pillar tip (for slit 3 in R44 and R37 the trend is plateau-like), followed by a steep decline after the pillar tip, while the more localised emission lines originating from the lower-ionised states show a steeper rise when moving along the slit toward the pillar tip. We therefore conclude that the ionisation fronts at the pillar tips follow the well-known stratified structure expected for expanding HII regions (e.g. Hill & Hollenbach 1978, Hester et al. 1996).

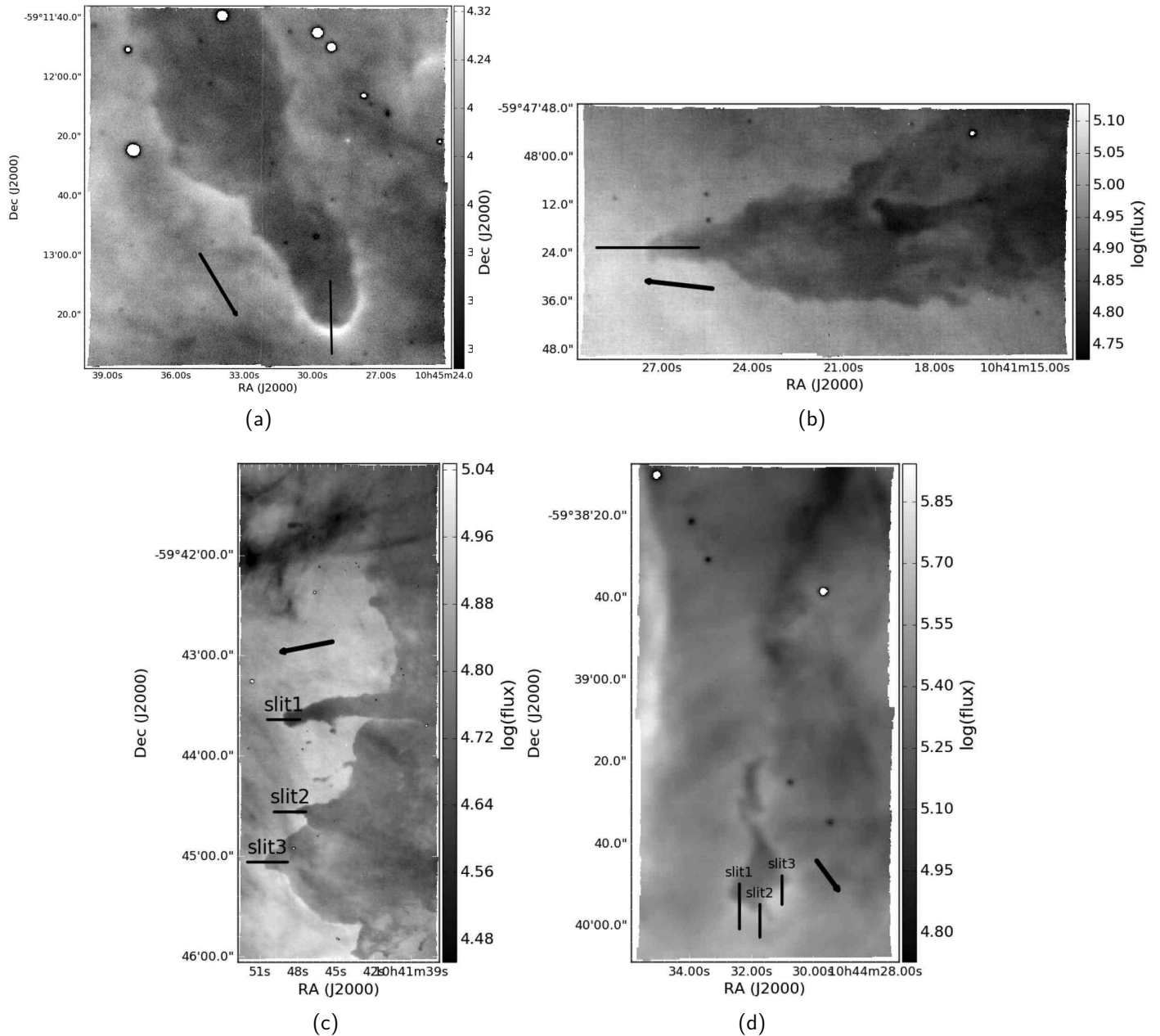


Figure 5.4: Continuum-subtracted H α integrated intensity maps of the four Carina regions: R18 (panel (a)), R45 (panel (b)), R44 (panel (c)) and R37 (panel (d)). The black lines indicate the positions of the slits used to compute the line intensity profiles (see Section 5.3.1). The flux is measured in $10^{-20} \text{ erg s}^{-1} \text{ cm}^{-2} \text{ \AA}^{-1}$. Black arrows indicate the direction towards the main ionising sources for each pillar.

Table 5.2: Location of the peaks (in 10^{-2} pc) of the emission lines with respect to the position of the [OIII] peak ($E_{\text{ion}} = 35.12$ eV) and their ionisation energy. Also reported here are the peak distances for the middle pillar in M 16 (P2, see MC15). The seeing-limited resolution of the MUSE observations is about 0.2 arcsec, which correspond to 0.002 pc at the distance of Carina.

	[SIII]	$H\alpha, \beta$	[NII]	[SII]	[OII]	[OI]
R44 slit1	1.78	1.78	2.23	2.45	2.45	3.35
R44 slit2	1.56	2.89	2.89	3.12	3.35	4.01
R44 slit3	4.68	7.58	7.81	8.03	7.81	8.92
R37 slit1	0.67	0.67	2.01	2.01	2.01	2.68
R37 slit2	0.67	0.67	2.45	2.45	2.68	2.66
R37 slit3	3.245	2.68	4.01	4.01	4.01	4.46
R18	0.000	0.67	1.12	1.34	1.34	7.14
R45	1.115	0.67	11.59	11.59	11.37	14.72
M 16 P2	0.29	0.444	0.74	0.74	0.74	1.78
E_{ion} (eV)	23.23	13.59	14.53	10.36	13.62	-

The [OIII] line (corresponding to the mean value of the $\lambda 4959$ and the $\lambda 5007$ lines) peaks first in all regions except for R18 (where its peak coincides with that of the [SIII] line), and to quantify the structure of the ionisation fronts we report the distance in parsecs of the peak of the other emission lines from the [OIII] peak in Table 5.2. The spatial resolution of MUSE does not allow a full disentanglement between emission lines from the same ionisation state. However we are able to resolve the peaks between the double ionised, single ionised and neutral lines, e.g. [OIII], [OII] and [OI]. Especially when compared to the values reported in MC15 for M 16 (comparison possible due to the relatively similar heliocentric distance of 2 and 2.3 kpc respectively[§]), it appears that the ionisation fronts in the Carina pillars are thicker (wider), as the emission line peaks appear further apart and the distance $\Delta([\text{OIII}] - [\text{OI}])$ appears, in general, greater.

This trend could be the consequence of the difference in ionising flux perceived by each pillar, which in turn is scaled to the distance from the ionising sources. The incident ionising flux is weaker on pillars further from the ionising sources, and pillars located further from the ionising sources are also less dense (see Fig. 5.8 and Section 5.3.2). Together, this allows a deeper penetration of the ionising photons in less dense pillars, and therefore increasing the size of the ionisation front, while high-density pillars do not allow the radiation to penetrate as much and therefore show narrower ionisation fronts. A further possible effect is that for denser material the extinction (and thus the shielding) rises faster per unit path length, resulting in a narrower ionisation front.

In MC15 we compared the emission line profiles along the three M 16 pillar tips to simulations of ionised pillars (Gritschneider et al., 2010b) which were post-processed with an optical

[§]For this analysis we did not include the NGC 3603 pillar, as the much greater distance to this region (about 6.9 kpc) does not allow us to resolve the emission line peaks.

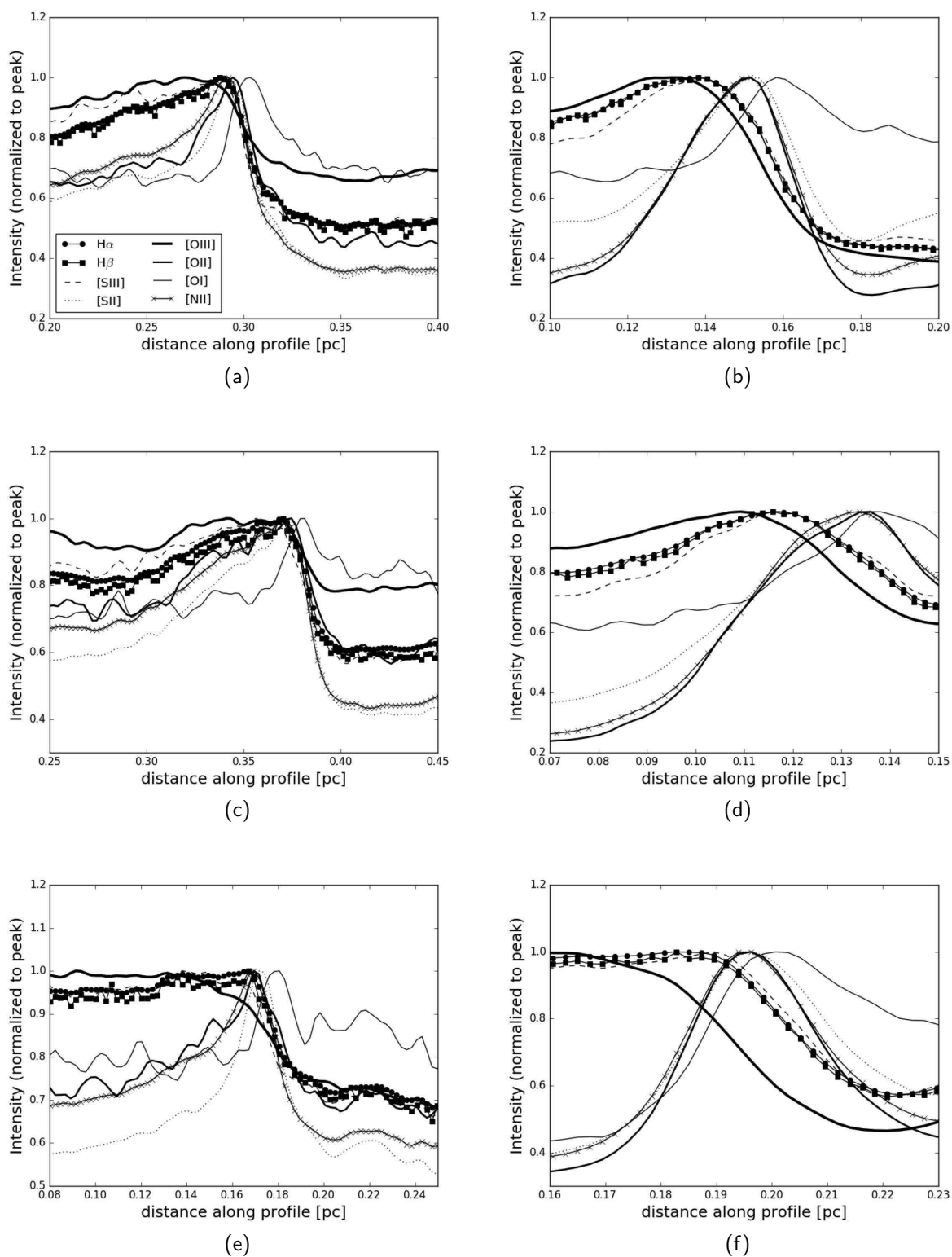


Figure 5.5: Emission line intensity profiles along the slits shown in Fig. 5.4 for R44 (left panels, slit 1, 2 and 3 in top, middle and bottom respectively) and R37 (right panels, slit 1, 2 and 3 in top, middle and bottom respectively). The legend in panel (a) applies to all other panels.

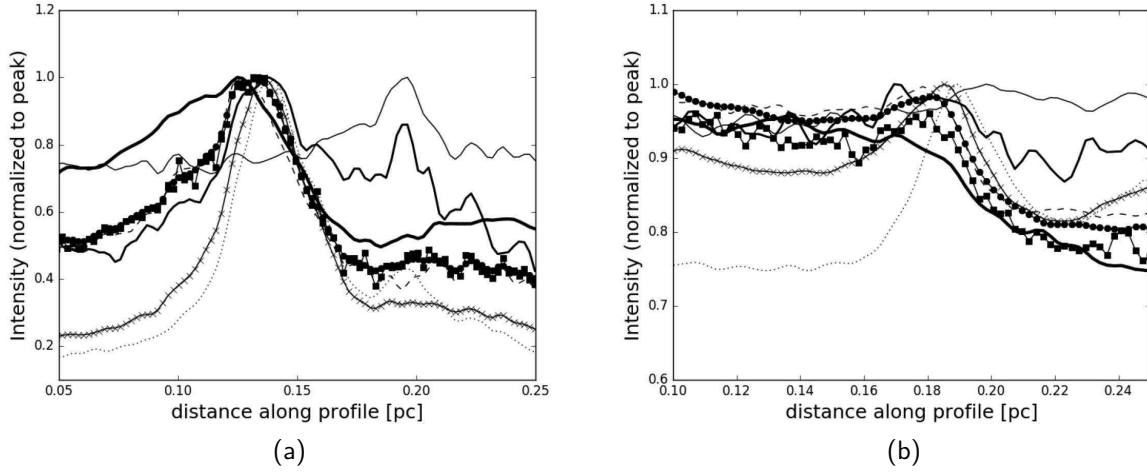


Figure 5.6: Emission line intensity profiles along the slits shown in Fig. 5.4 for R18 (panel a) and R45 (panel b). The legend is the same as in Fig. 5.5a.

radiative transfer code to obtain the simulated [OIII], $H\alpha$, [NII] and [SII] maps. This first qualitative comparison showed that the ionisation structure was recovered in the simulations. Here, we perform a preliminary analysis of theoretical ionisation front models by varying the initial conditions and processing the radiation with `CLOUDY` (Ferland et al., 2013b). We assume the conditions of the Orion photo-dissociation region calculations (Ferland et al., 2013b) but replace the ionising source with a black body at a given temperature T . The hydrogen density is assumed to be 1 cm^{-3} and changes rapidly to 5000 cm^{-3} at 0.3 pc . The resulting abundance fractions of the species [OI], [OII] and [OIII] along the pillar/ambient matter interface is shown in Fig. 5.7. The calculations confirm a general trend in which the ionisation front gets narrower with higher ionising flux, i.e. the separation between the [OIII] and the [OI] line peaks gets smaller with increasing flux. Compared to the simulated emission line profiles shown in MC15, these do not fully recover the shape of the observed lines, as in MC15 we used simulations which were post-processed with `MOCASSIN` (Ercolano et al., 2003b), a 3D radiation transfer code, while here we use a theoretical one-dimensional density profile. However, the observations in this work hint at but are not sufficient to confirm the picture in which distance from/type of ionising source determine the thickness of the ionisation front, as no clear trend in $\Delta([\text{OIII}] - [\text{OI}])$ vs d_{proj} and $\Delta([\text{OIII}] - [\text{OI}])$ vs $Q_{0,\text{pil}}$ is observed. To further test this, observations with higher angular resolution are needed, in combination with dedicated simulations in which the distance, the ionising photon flux, the pillar density as well as the geometry and the illumination of the pillar can be varied and the emission line intensity profiles carefully analysed.

5.3.2 Physical parameters

For all observed regions, the electron density and temperature was determined as in MC15. For this, a continuum subtraction was performed on every data cube, followed by an extinction cor-

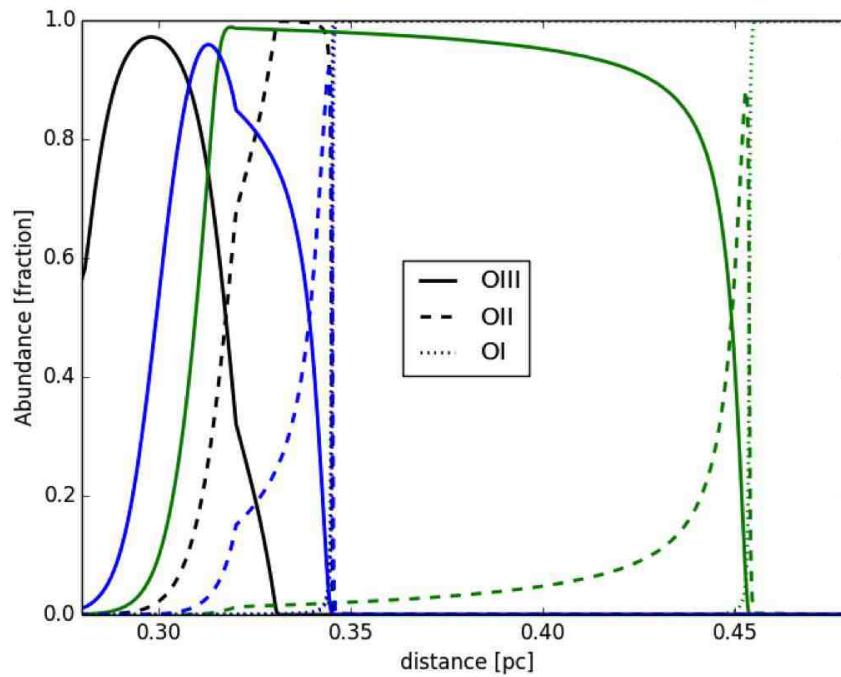


Figure 5.7: Fraction of the total species abundance of [OIII] (solid lines), [OII] (dashed lines) and [OI] (dotted lines) as a function of distance along the pillar/ambient matter interface of simulated pillar-like structures, analogous to Figures 5.5 and 5.6. The simulated pillars were exposed to three different ionising source with fluxes $\log(Q_0) = 49$ photons s^{-1} ($T = 45500$ K), $\log(Q_0) = 49$ photons s^{-1} ($T = 31500$ K) and $\log(Q_0) = 50$ photons s^{-1} (black, blue and green lines respectively). See text Section 5.3.1.

rection based on the $H\alpha/H\beta$ ratio and assuming $R_v=3.2$ (Turner & Moffat, 1979) using the nebular analysis tool `PYNEB` (Luridiana et al., 2015b). The line ratios used to compute the electron density N_e and temperature km s^{-1} are $[SII]\lambda 6731/[SII]\lambda 6717$ and $[NII]\lambda 6548+6584/[NII]\lambda 5755$ respectively, and the corresponding maps are shown in Figures C.11 to C.13. These figures also show circular regions at the pillar tips (marked with black or white circles) from which mean N_e and km s^{-1} values were extracted and reported in Table 5.3. When plotted against the ionising photon flux perceived at each pillar tip ($Q_{0,\text{pil}}$, computed by scaling the photon flux Q_0 to the subtended solid angle between pillar and ionising source, see Section 5.3.3), we find a tight correlation between the electron density and $Q_{0,\text{pil}}$. This is shown in Fig. 5.8a, where the uncertainties in N_e are the standard deviation of each circular extraction region, while for the uncertainty in $Q_{0,\text{pil}}$ (indicated by the horizontal line in the lower right corner of the figure) we assume that the pillars are projected to within $\pm 37^\circ$ and use this to provide a 25% error on the true distance. This correlation shows that pillars that are further away have lower densities, which could mean that if these low-density pillars had been further in (closer to the ionising stars), they would have probably been eroded much faster, meaning that this correlation could represent a threshold density pillars need to have in order to withstand a given ionising photon flux and be observable today. A similarly tight correlation is found between the electron density and the distance to the respective ionising sources, as is shown in Fig. 5.8b. These findings are of great importance when considering the destructive effect of ionising feedback on the pillars, as the rate at which pillars are photo-evaporated therefore not only depends on the strength of impinging ionising radiation, but also and crucially so on the density of the pillar material, as well as the distance from the ionising source. We will discuss this further in Section 5.3.3 when analysing the mass-loss rate of each pillar.

As in MC15, we normalise and stack several emission lines in each single pixel (thus assuming that all the lines in one pixel originate under one set of excitation conditions) and then fit the resulting velocity spectrum in each pixel with a gaussian function to produce a velocity map for each region[¶]. The lines used for the stacked spectrum are $H\alpha$, the two $[NII]$ lines, the two $[SII]$ lines, $[OI]\lambda 6300,6363$ and $HeI\lambda 6678$. This procedure is of great advantage for the medium spectral resolution of MUSE ($\Delta v = 150 \text{ km s}^{-1}$ at 4600 \AA and $\Delta v = 75 \text{ km s}^{-1}$ at 9300 \AA), as the line spread function is undersampled, and by applying this technique a better-sampled velocity spectrum is obtained (see MC15 for details). The velocity maps are shown in Fig. 5.9: all velocity maps show barycentric velocity, automatically corrected for by the MUSE data reduction pipeline^{||}. The black or white circles in each panel show the circular apertures used to extract the velocities of the pillar material and the surrounding ambient matter and determine the velocity of the photo-evaporative flow (values reported in Table 5.3). All maps show a certain degree of either image/instrument artefacts (such as the checked pattern visible

[¶]The `PYTHON` packages `SPECTRAL_CUBE` (spectral-cube.readthedocs.org) and `PYSPECKIT` (Ginsburg & Mirocha, 2011) were used for the fitting routine.

^{||}For the molecular gas in the Carina Complex, Yonekura et al. (2005) find LSR (local standard of rest) velocities ranging from about -26 km s^{-1} to about -12 km s^{-1} . By converting the barycentric velocities to LSR values, the MUSE data is in good agreement with these values. As an example, a barycentric velocity value of 0 km s^{-1} corresponds to approximately -12 km s^{-1} in the LSR frame.

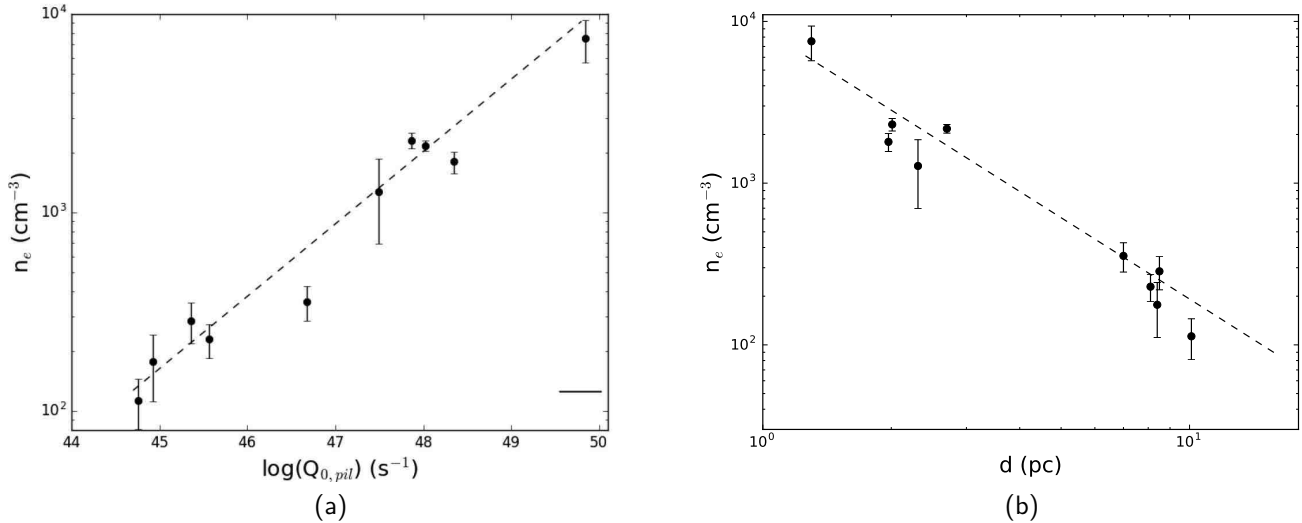


Figure 5.8: Panel (a): the electron density N_e against the ionising photon flux at the pillar tips, $Q_{0,\text{pil}}$ (circles) and the best fit power law (dashed) with index $p = 0.36 \pm 0.04$ (see text Section 5.3.2). The horizontal line indicates the average error of $\log(Q_{0,\text{pil}})$. Panel (b): N_e against the projected distance from the ionising sources (circles) and the best fit power law (dashed) with index $p = -1.66 \pm 0.19$.

in all panels except for (a)**, or the overlap regions resulting from mosaicking the various pointings for each region), low S/N (e. g. R18), or both (e. g. R45). However, each pillar is clearly distinguishable from the surrounding ambient matter (making a confident estimate of the photo-evaporation flow velocity possible), being typically blueshifted with respect to the latter. The blueshift of the pillar material traces the photo-evaporative flow, as this flows out perpendicular to the pillar surface (Hester et al. 1996, MC15) and results in the pillar surfaces pointing towards the observer being blueshifted along the line of sight. The velocity of the photo-evaporative flow is smaller than c_s ($\sim 10 \text{ km s}^{-1}$, the sound speed of ionised gas) in all regions, c_s being the sound speed of ionised gas. This fact reflects that the matter is being accelerated along a density-gradient, the densest gas is slower than the less dense gas, and the matter already moving at the sound speed of ionised gas is already merging with the HII region.

**The checked pattern is particularly visible in the velocity map of NGC 3603 (panel (d)), as the 90° rotation dither pattern implemented in the Carina observations was not used.

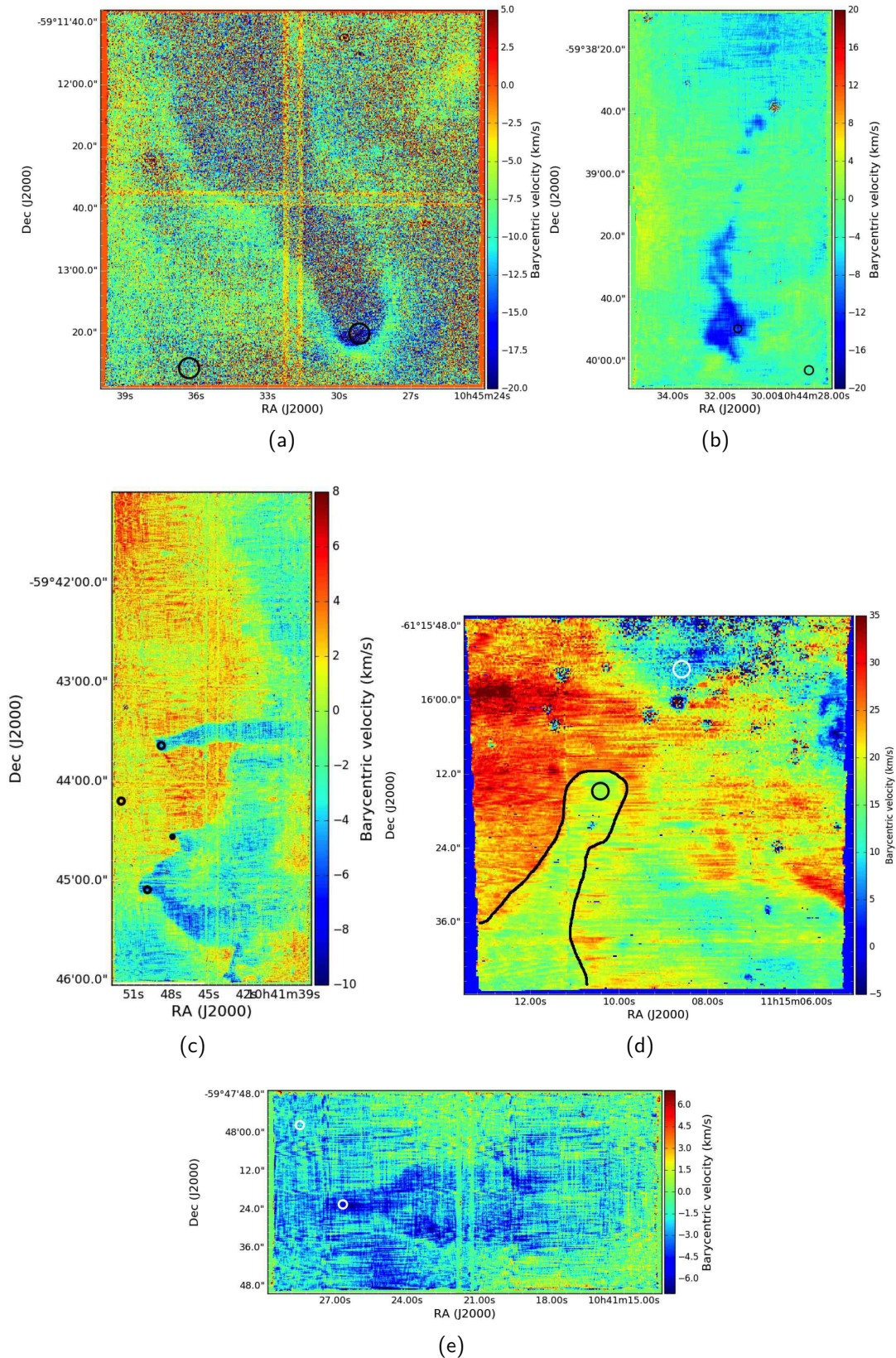


Figure 5.9: Velocity maps of the four Carina regions (R18, R37, R44 and R45 in panels a, b, c and e respectively) and NGC 3603 (panel d). Circles (black or white depending on visibility) mark the regions used to extract velocity values of the pillar material and the surrounding interstellar medium (see text Section 5.3.2 and Table 5.3). To better highlight the pillar in NGC 3603, a black contour tracing the pillar was added.

5.3.3 Quantifying ionising feedback: relating the ionising photon flux to the photo-evaporation rate

Ionisation from the nearby massive star clusters

To determine the impact of ionising feedback from the nearby massive clusters, a first assumption of which cluster is acting on which region needs to be made. The cases of NGC 3603 and M 16 are relatively simple, as in both regions there is only one massive nearby star cluster (the HD 97950 star cluster and NGC 6611 respectively). The case of Carina however is less simple, due to the complex nature of this massive and large star-forming region. We therefore compute the projected distances from the observed pillars to the three most massive clusters, Tr 14, 15 and 16, and relate this to the direction the pillars point back to, therefore assuming that the direction of the pillars is indicative for the origin of the dominating impinging radiation. We use the SIMBAD coordinates for each of these clusters: 10:43:56.0 -59:33:00 for Tr 14, 10:44:43.0 -59:22:00 for Tr 15 and 10:45:10.0 -59:43:00 for Tr 16 (all coordinates are in J2000). The location of the pillars with respect to the central coordinates of the three star clusters, as well as the known O- and B-stars in the Carina region (Gagne et al., 2011) are shown in Fig. 5.2. Based on the orientation of the pillars and their distance to the nearby clusters, we assume the following for each region:

- R18: the pillar is located at $\sim 10.5'$ (7.0 pc) north-east of Tr 15, and points directly toward the central coordinates of this cluster; we therefore assume that Tr 15 is the feedback-driving cluster acting on this region.
- R37: this ionised globule lies at $\sim 6.1'$ (4.1 pc) south-east of Tr 16. Smith et al. (2004) propose that the dominant ionising sources might be either the O4 I star Tr16-244, the WNL star WR25 (HD 93162), or both, since the main ionisation fronts point in that direction. Indeed (as shown by the black arrow in Fig. 5.4), the globule and its main ionisation front do not point back towards the central coordinates of Tr 16, but rather towards Tr16-244 and HD 93162, and together with the fact that it is also closer in projection to these two stars (2.7 pc) we therefore assume that these are the main ionising sources.
- R44 and R45: these pillars lie closer in projection to Tr 14 than Tr 16 (12.9 vs. 16.9 pc and 16.1 pc vs. 19.1 pc respectively). However, they do not point back towards the central coordinates of these two clusters, but rather towards an O6- and an O9.5-star (HD303316 and HD305518) at about 2.7 pc north-east. Given the large projected distance and the weak emission from these pillars, we therefore assume that it is the combined flux of the two above mentioned O-type stars acting on these regions, rather than Tr 16 or Tr 14. To simplify the discussion, we will refer to the combination of these two O-stars as HD30 henceforth.

For NGC 3603 there is no full census of B-type stars, and for Carina we see that the B-type stars only contribute a few percent of the ionising flux (see below), and to estimate the energy

input in terms of photons s^{-1} from the massive clusters, we assume that the O-type stellar population of each cluster is dominating the energy input. We convert the spectral type of the known O stars to a flux Q_0 by using the values given in Martins et al. (2005). For Tr 14, 15 and 16 this was done in Smith (2006a), however these authors also include B-type stars in their estimate of the total flux for each cluster. Here, we therefore use the list of O-stars in Smith (2006a) as well as their reported values for $\log(Q_0)$ (also taken from Martins et al. 2005) and find $\log(Q_0)=49.49 s^{-1}$ for Tr 15 and $\log(Q_0)=50.92 s^{-1}$ for Tr 16. The comparison between these two values for $\log(Q_0)$ and those obtained by including the B-stars reveals that the contribution to the ionising flux of the B-stars is only 15% for Tr 15 and 8% for Tr 16.

As mentioned above, we assume that R37 is mainly affected by Tr16-244 and HD 93162, which correspond to an O4 I star and a WN6 star respectively, and their ionising fluxes add up to $\log(Q_0)=48.02 s^{-1}$ (henceforth we will refer to the combination of these two stars as O4/WNL). For R44 and R45 the combined fluxes of HD303316 and HD305518 (HD30) amount to $\log(Q_0)=49.02 s^{-1}$.

For NGC 3603, Moffat (1983) and Drissen et al. (1995) derived spectra for 13 and 14 objects respectively, of which 11 were classified as early-type O-stars. However, neither of these studies could resolve the central part of the cluster, which was classified as a Trapezium-like WR system (Walborn, 1973). It was not until Melena et al. (2008) and a combination of optical spectroscopy and high-resolution *HST* imaging that the classification of a total number of 38 cluster stars was possible. These authors find a large number of O- and B-type stars with spectral types as early as O3, and high-mass objects with $M \sim 120 M_\odot$ and Wolf-Rayet features. They discuss that the highest mass stars seem to be slightly younger than the 1-4 Myr old population with $M \sim 40 M_\odot$, having ages between 1 and 2 Myr. We derive the integrated ionising flux Q_0 of each O-type star in Table 1 of Melena et al. (2008) by comparing their spectral type to the one derived from simulations in Martins et al. (2005). For the 33 O-type stars in this table, we find a total ionising photon flux of $\log(Q_0) \sim 50.98 s^{-1}$. For the number and spectral type of O-stars in M 16 we refer to Table 11 in Evans et al. (2005), and compute $\log(Q_0) \sim 49.87 s^{-1}$ for the 13 O-stars of this cluster.

We then scale the integrated ionising fluxes Q_0 of each cluster to the distance of each pillar to determine the ionising fluxes perceived by each pillar, $Q_{0,pil}$. For this we measure the radius of the pillar tips to determine the exposed pillar area and derive the solid angle which each pillar subtends with the respective cluster as $\Omega = 2\pi r^2/d_{proj}^2$, where d_{proj} is the projected pillar-cluster distance. All values are reported in Table 5.3.

Mass-loss rate due to photo-evaporation

In MC15 the mass-loss rate was computed with the optically thin [SII] $\lambda 6731$ line. In this method, the luminosity of the [SII] line is used to compute the mass of the line-emitting matter, which is then used to compute the mass-loss rate as $\dot{M} = Mv/l$ (where v is the velocity of the photo-evaporative flow and l the size of the line-emitting region). However, this method is only valid if the density of the line-emitting matter is $N \gtrsim N_c$, with N_c the critical density of the [SII] $\lambda 6731$ line ($N_c \sim 3.9 \times 10^3 \text{ cm}^{-3}$). With this method $M \propto (1 + N_c/N_e)$, so in the low-density regime the computed mass M would not be representative of the line-emitting

Pillar	Cluster	d_{proj} (pc)	r_{surf} (pc)	Ω (sr)	$\log(Q_0)$ (photons s^{-1})	$\log(Q_{0,\text{pil}})$ (photons s^{-1})	N_e (cm^{-3})	T_e (K)	v (km s^{-1})	\dot{M} ($M_\odot \text{Myr}^{-1}$)
R18	Tr 15	7.0	0.11	1.55×10^{-3}	49.49	46.68	355 ± 73	9832 ± 2663	6.3 ± 4.8	3.1 ± 0.8
R37	O4/WNL	2.7	0.09	6.98×10^{-3}	50.18	48.02	2171 ± 133	9738 ± 274	8.9 ± 0.1	17.7 ± 0.1
R44 P1	HD30	8.5	0.05	2.17×10^{-4}	49.02	45.36	285 ± 66	8418 ± 1224	6.4 ± 0.3	0.5 ± 0.2
R44 P2	HD30	8.4	0.03	8.01×10^{-5}	49.02	44.92	177 ± 66	7746 ± 1422	3.3 ± 0.1	0.07 ± 0.37
R44 P3	HD30	8.1	0.06	3.45×10^{-4}	49.02	45.56	229 ± 44	8189 ± 1209	6.6 ± 0.1	0.6 ± 0.2
R45	HD30	10.1	0.03	5.54×10^{-5}	49.02	44.76	113 ± 32	7453 ± 1262	3.4 ± 0.1	0.04 ± 0.28
M16 P1	NGC 6611	1.97	0.14	31.73×10^{-3}	49.87	48.35	1800 ± 230	8777 ± 749	4.5 ± 0.3	17.9 ± 0.1
M16 P2	NGC 6611	2.01	0.08	9.95×10^{-3}	49.87	47.87	2306 ± 205	8792 ± 601	5.3 ± 0.3	8.9 ± 0.1
M16 P3	NGC 6611	2.31	0.06	4.24×10^{-3}	49.87	47.49	1277 ± 579	8823 ± 1905	8.8 ± 11.8	4.6 ± 1.4
NGC 3603	HD97950	1.30	0.14	72.87×10^{-3}	50.92	49.84	7536 ± 1824	11347 ± 809	9.2 ± 2.4	150.0 ± 0.4

Table 5.3: Properties and physical parameters of the considered pillars (column 1): feedback-driving cluster (column 2), projected distance from cluster (column 3), radius of pillar tip (column 4), subtended solid angle pillar-cluster (column 5), integrated ionising photon flux of the cluster (column 6), photon flux at pillar tip (column 7), electron density (column 8), electron temperature (column 9), velocity of the photo-evaporative flow (column 10) and mass loss rate of the pillar tip (column 11). HD30 stands for the combination of HD303316 and HD305518, while O4/WNL stands for the combination of Tr16-244 and HD 93162 (see text Section 5.3.3).

matter. As the densities computed for the Carina pillars are in general much lower than this (see Table 5.3), we use the expression given in Smith et al. (2004) to compute the mass loss rate,

$$\dot{M} \simeq \pi r^2 m_{\text{H}} n_{\text{H}} v \quad (\text{kg/s}) \quad (5.1)$$

where r is the curvature radius of the pillar tip, v the velocity of the photo-evaporative flow and n_{H} the matter density. As in Smith et al. (2004), we adopt $n_{\text{e}} \simeq 0.7n_{\text{H}}$ (Sankrit & Hester, 2000), and we position circular apertures at the ionisation fronts, i.e. the pillar tips, to extract values for v and N_{e} . The positions of the circular extraction regions are marked in Figures 5.9, C.11 and C.12, and the extracted values are reported in Table 5.3. The errors on the v , N_{e} and km s^{-1} measurements correspond to the standard deviation of the values of included pixel values. The uncertainty for \dot{M} is then computed by propagating the uncertainties in velocity and electron density. For R37 we find $\dot{M} \sim 18 M_{\odot} \text{ Myr}^{-1}$, which agrees with the value of $\dot{M} \sim 20 M_{\odot} \text{ Myr}^{-1}$ found by Smith et al. (2004). For M16, in MC15 we report a mass-loss rate of $\dot{M} \sim 70 M_{\odot} \text{ Myr}^{-1}$, while here the combined mass-loss rate of the three pillars (Table 5.3) is about $\dot{M} \sim 20 M_{\odot} \text{ Myr}^{-1}$. The difference of these two values comes from the fact that in MC15 we determined the mass-loss rate of the the combined three pillars by computing the total mass of the [SII]-emitting matter of the three pillars, while here we only consider the ionisation fronts of the pillar tips.

Since the mass-loss rate of the pillars is due to photo-evaporation caused by the impinging ionising photons, we investigate the presence of a correlation between the ionising photon flux perceived by the pillar tips, $\log(Q_0)$, and the mass-loss rate \dot{M} . The resulting plot is shown in Fig. 5.10, where the data points are best fit with a power law of index $p = 0.56$. Together with the correlation between N_{e} and $\log(Q_{0,\text{pil}})$, and N_{e} and the projected distance, we find as expected that pillars with lower densities are further away from the ionising stars/star clusters, and these also show lower mass-loss rates. The photo-evaporative effect of ionising radiation therefore depends on the relative flux perceived at the pillar tip, the density, as well as the distance of the pillar from the massive stars.

This result might be challenged by the fact that the assumptions made for the ionising sources of R37, R44 and R45. However, even if both R37 and R44/45 are under the full influence of Tr 16 instead of O4/WNL and HD30, the correlations would still hold, as in that case $\log(Q_{0,\text{pil}}) = 48.40$ for R37, $\log(Q_{0,\text{pil}}) = 46.11$ for R45 and $\log(Q_{0,\text{pil}}) = 46.67, 46.22, 46.82$ for the three pillars in R44. Furthermore, geometrical effects need to be considered when interpreting this correlation, as it depends on projected distances instead of real distances. However, pillars are only identified as such with a favourable spatial orientation and illumination (i. e. if viewed edge-on), and the consequence of this is that for projection angles up to 60 degrees, the true distance is no more than a factor of 2 greater than the projected distance to the ionising sources. A further note on this is that photo-evaporation is certainly not the only mechanism able to destroy pillar-like structures in these kind of regions, as the massive stellar content implies strong stellar winds, as well as supernova events which will occur at some point during the evolution of the star-forming region. These events will contribute to a more rapid disruption of the pillars.

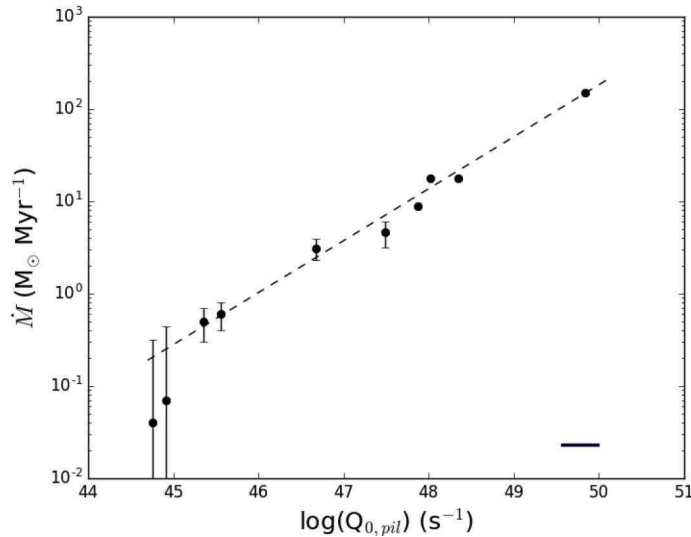


Figure 5.10: The mass-loss rate \dot{M} against the ionising photon flux at the pillar tips, $Q_{0,pil}$ (circles) and the best fit linear (dashed) relation. The power law index is $p = 0.56 \pm 0.02$. The horizontal line indicates the average uncertainty of $\log(Q_{0,pil})$. See text Section 5.3.3.

A natural expansion of this analysis would be to compute the (remaining) lifetime of each pillar and analyse the presence of a correlation with $\log(Q_{0,pil})$. With a CO-derived mass of 10-20 M_{\odot} from Cox & Bronfman (1995), Smith et al. (2004) determined a remaining lifetime of about $10^{5.3-6}$ yr for the globule in R37, while for the M 16 pillars a remaining lifetime of about $10^{6.47}$ yr is computed (MC15). With molecular line data (e. g. ^{12}CO), or alternative via SED fitting of in-house *Herschel* images available for the CNC (Preibisch et al., 2012a), one could attempt a mass computation of all the pillars in the MUSE Carina data set and consequently determine their lifetimes.

5.3.4 Ionised jets

In MC15, we developed a novel method to detect jets from young stars that have not yet had time to fully emerge from the embedding material. This method uses the so-called S_{23} parameter ($([\text{SII}] + [\text{SIII}])/\text{H}\beta$, Vilchez & Esteban 1996b) to detect a jet that is only now starting to emerge from the pillar. The S_{23} parameter detection needs to be complemented with a line-of-sight velocity map, derived via a pixel-by-pixel gaussian fitting routine to the stacked spectrum of several lines in the 600-700 nm range, as was done to compute the velocity maps of the pillars discussed here. In the case of M 16, the well studied pillars were not previously known to host jets, and it was only due to a careful analysis of the MUSE data that such a detection could be made. We inspected the Carina pillars in terms of the S_{23} parameter, but no jet could be identified in the pillars with this parameter. However, we identified two jets in the Carina data set nonetheless: these are jets protruding for several arcseconds from the pillar tips that host their sources, and they are detected as ionised jets predominantly visible in the

$H\alpha$ and [SII] lines. In McLeod et al. (2016), we propose the utility of the S_{23} parameter as an indicator of the shock contribution to the excitation of line-emitting atoms, meaning that if a jet is traced by this parameter, it is because it is interacting with the host pillar material from which it is emerging by creating a layer of shocked material at the ionised pillar surface. From the fact that the two jets are not identified with the S_{23} parameter map, we conclude that these jets are more evolved than the M16 case, as in the latter the jet is not yet detected beyond the pillar boundaries. The R44 and the R18 jets however are seen to extend well beyond the pillars which host their sources. In the following two subsections, we will discuss the R18 and R44 jets separately.

The two detected jets are in regions R18 and R44, and are comparable to the *HST*-detected jets in Smith et al. (2010b). In the case of R44, the jet corresponds to the known Herbig-Haro object HH 1010. With this data set however, because of the spectral coverage of MUSE, we are not only able to identify the ionised jets in emission lines such as $H\alpha$ and [SII], but we are also able to distinguish their kinematics. This is because the two detected jets are only seen in the emission line wings, and we can therefore split them into a red- and a blue-shifted component respectively. In the case of R18, this is the first reported detection of the ionised jet.

HH 1124 in R18

The R18 pillar and the sources at its tip are discussed in Hartigan et al. (2015), and the main features presented by these authors are reported in Fig. 5.11: four emission line knots (A to D), two infrared sources (IRS1 and IRS2), and two young stellar objects (PCYC 884 and 889, for simplicity referred to as 884 and 889). These authors attribute all emission line knots to a jet (HH 1124) originating from the tip of the pillar that is being bent north by the O-stars responsible for the formation of the pillar. In Fig. 5.11 a fifth knot is marked with *E*, which (as will be discussed below), is a faint knot belonging to the blue lobe of the jet and was not detected by Hartigan et al. (2015) but only in this work.

The presence of a jet becomes clear when inspecting the wavelength slices of the data cube around the bright single-ionised emission lines such as $H\alpha$, [SII] and [NII]: when moving through the cube around the central wavelength of these lines, the two jet lobes become visible in the blue and red slices before and after the central frame (see coloured contours in Fig. 5.11). The ionised jet does not, however, follow the direction of the jet proposed in Hartigan et al. (2015), where emission line knot D is discussed to be part of it and it is proposed that the jet is being bent north by the feedback of the nearby massive stars of Tr 15. Here, we find a P.A. of $\sim 123^\circ$ for the red counterpart, and a P.A. of $\sim 113^\circ$ for the blue counterpart. The pillar itself is at P.A. $\sim 210^\circ$, meaning that the jet is approximately perpendicular to the pillar (the angle of the pillar being 97° and 87° with the red and the blue counterparts respectively), and that there is an indication for the red jet-lobe being bent $\sim 10^\circ$ north with respect to the blue lobe due to the high-mass stellar feedback (in the form of stellar winds or outflowing material from the inner parts of the nebula, Bally & Reipurth 2001). When compared to the conclusion reached in Hartigan et al. that there is evidence for strong jet bending due to stellar winds (because these authors include emission knot D as being part of the jet), the jet bending seen in this work is minimal.

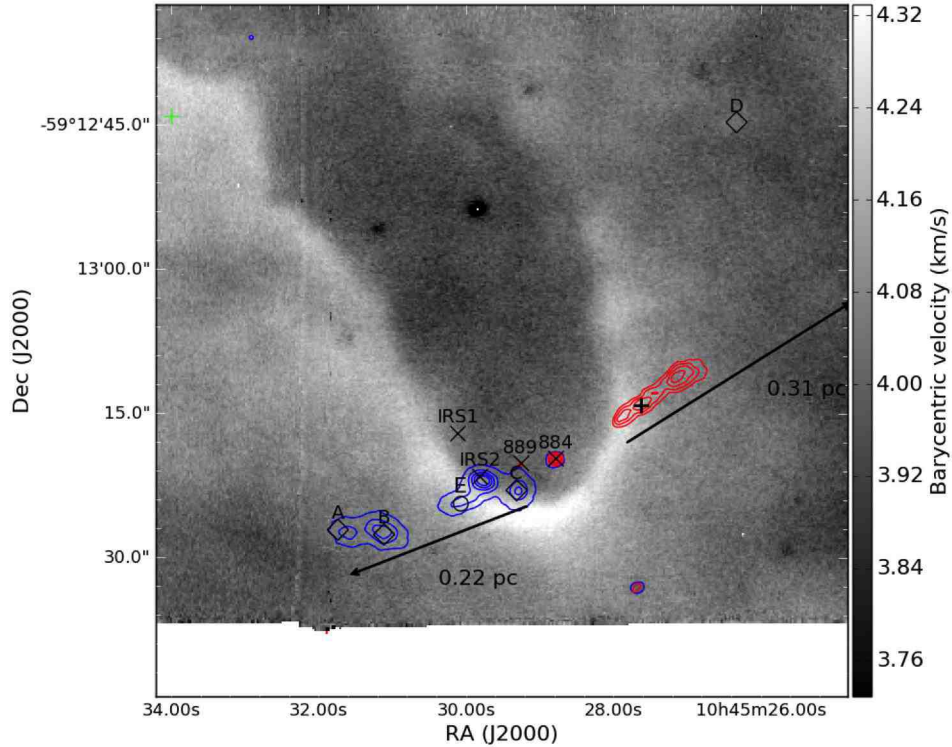


Figure 5.11: Continuum-subtracted $H\alpha$ intensity map of the tip of pillar R18 and HH 1124. Blue and red contours mark the location of the red and blue lobes of the bipolar jet originating from the pillar tip. The contours are extracted from the corresponding two slices of the data cube at red = 6566.43 \AA and blue = 6558.93 \AA . The emission line knots A-D as well as IRS1/2, 884 and 889 are the sources discussed in Hartigan et al. (2015), while the region marked with E is only detected here as part of the blue counterpart of the jet (see text Section 5.3.4). The black arrows indicate the extent of the jet, best compared with the RGB composite of the pillar tip shown in fig. C.14, and the black cross indicated the position of aperture used to determine the jet velocity of the red lobe (see text Section 5.3.4).

Compared to the blue, the red lobe of the jet is more continuous, and it can be traced up to $\sim 0.46'$ ($\sim 0.31 \text{ pc}$) from the pillar surface into the surrounding medium. The blue lobe on the other hand consists of at least 5 knots, out of which 4 correspond to emission line knots A, B, C and IRS2, as is shown in Fig. 5.11. If measured from knot C to knot A, the spatial extent of the blue lobe is $\sim 0.33'$ ($\sim 0.22 \text{ pc}$). From this data we conclude that emission line knot D is not part of the jet, but there is a fifth detectable knot, marked as E in Fig. 5.11.

In terms of velocity, emission line knots A, B, C, as well as IRS2 and 889 are blueshifted with respect to both the pillar and the ambient matter. This is shown in Fig. 5.12, where the discussed emission line knots and young stellar objects are overlaid on the $[SII]\lambda 6717$ velocity map^{††}. However, by inspecting the emission line profiles for the sources/knots in Fig. 5.11,

^{††}We show the $[SII]\lambda 6717$ velocity map instead of that of the $H\alpha$ line, because the latter is contaminated by

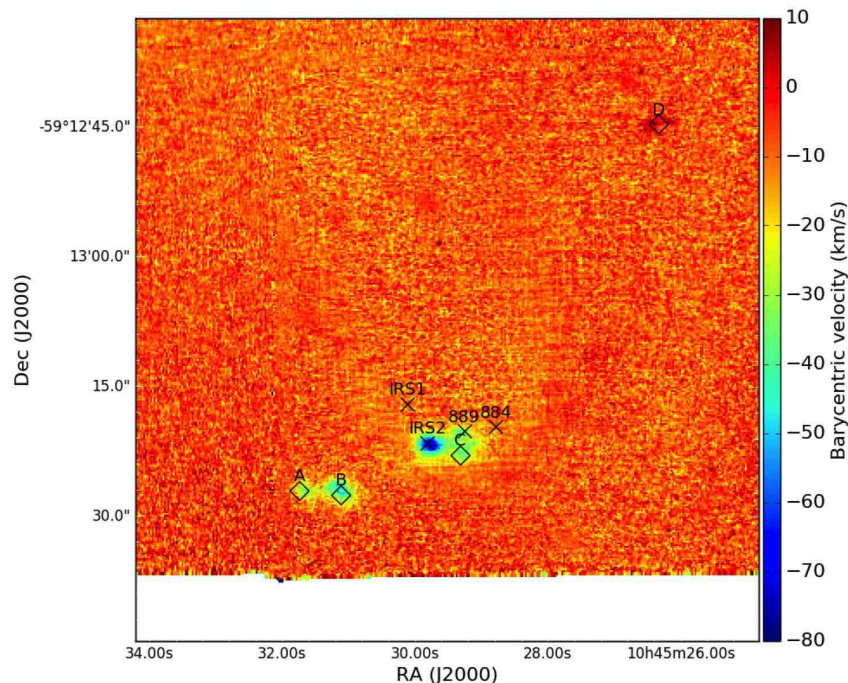


Figure 5.12: Velocity map of the [SII] λ 6717 line zoomed on the pillar tip and the emission line knots/sources located at the tip (see text Section 5.3.4).

we detect double components in the low-ionization emission lines ([OI], [SII], [NII], and $H\alpha$) towards knots B and E as well as IRS2, but not towards knots A, C, D and 889. In both IRS2 and knot B, the blue component is $\sim 50\%$ weaker in intensity than the red component, the two are separated by about 200 km s^{-1} (as is shown in Fig. 5.12 and Table 5.4 for the [SII] λ 6717 line), the blue component being at $\sim -200 \text{ km s}^{-1}$ and the red at $\sim -35 \text{ km s}^{-1}$. In emission line knot E the brightness of the blue component is only about 15% that of the red component, so that a two-component gaussian fit was not possible. One possible scenario for this peculiar configuration is that the blue component of the double-peaked line profile is tracing the $\sim 200 \text{ km s}^{-1}$ jet, while the red component is tracing a $\sim 30 \text{ km s}^{-1}$ stellar wind.

To determine the dynamical age t_{dyn} of the jet, we assume that the jet velocity of the blue lobe is $\sim 200 \text{ km s}^{-1}$, while a velocity of $\sim -8 \text{ km s}^{-1}$ for the red lobe is obtained by fitting the spectrum of a 3-pixel aperture centred on the black cross marked in Fig. 5.11. With a total spatial extent of $\sim 0.5 \text{ pc}$, we obtain $t_{\text{dyn}} \approx 10^{3.4} \text{ yr}$. This age is much younger than the age of Tr 15, indicating that the jet-driving source must have formed after the formation of the cluster. Whether the formation of the jet source was triggered by the feedback of Tr 15 cannot be determined from this data.

The determination of the source of the jet and wind is not trivial. In Hartigan et al. (2015), IRS2 is mentioned to be a possible sub-arcsecond binary, however, the MUSE data does not

instrument artefacts in the form of a checked pattern as is shown in Fig. 5.9. Other than being unpleasant to the eye, this pattern does not influence our analysis.

Table 5.4: Best fit parameters of the 2-component gaussian fitting performed on the [SII] λ 6717 spectra of emission line knot B and IRS2 (see Fig. 5.11). All values are in km s^{-1} .

Source	Centroid (blue)	Width (blue)	Centroid (red)	Width (red)
IRS2	-228.7 ± 10.8	86.1 ± 10.2	-31.7 ± 3.6	60.8 ± 2.9
Knot B	-208.5 ± 28.0	102.6 ± 26.9	-2.5 ± 8.3	69.4 ± 7.1

allow a verification of this. A source at the approximate location of YSO 884 is discussed and analysed in Ohlendorf et al. (2012): with multi-wavelength photometric data ranging from the near- to the far-infrared, these authors obtain an estimate of $2.6 M_{\odot}$ for the stellar mass of this source. However, the angular resolution of the data used by these authors does not allow them to distinguish between YSOs 884 and 889, and indeed it is treated as a single compact green object. The question whether IRS2 or one of the two YSOs is responsible for driving the jet could be tackled with high angular resolution molecular data, e.g. with CO or a shock tracer like SiO, as to trace the jet directly back to its source.

HH 1010 in R44

The highly collimated jet HH 1010 at the tip of pillar 44-P1 was identified with *HST* $H\alpha$ imaging in Smith et al. (2010b), where a PA of about 216° and an extent of 60 arcseconds are reported. These values for extent and position angle are confirmed with the MUSE data, where the jet can again be separated into a red and a blue component by extracting slices on either side of the central $H\alpha$ wavelength from the data cube. Fig. 5.13 shows the continuum-subtracted $H\alpha$ map with contours extracted from the 6566.43 \AA and 6558.93 \AA slices for red and blue respectively. The red lobe of the jet is composed of a series of knots (*A* to *G* in Fig. 5.13) which extend over almost $40''$ (0.45 pc), knot *A* being at the tip of the dark host pillar approximately where Smith et al. (2010b) report the presence of a faint optical source, and knot *G* being close to the rim of a small globule south-west of the pillar. There is a very shallow S-shaped wiggle in the red lobe, which might be an indication for jet precession (Reipurth & Bally, 2001). The blue lobe is fainter than the red one, more collimated, and spans over $\sim 20''$ (0.22 pc) north-east. Unlike HH 1124 in R18, none of the knots of the red lobe show remarkable line profiles. However, the velocity of the two lobes can be determined from the stacked velocity map shown in Fig. 5.9c, of which a close-up is shown in Fig. 5.14: the blue lobe emerges from the pillar with $v \approx -2 \text{ km s}^{-1}$, and the red lobe with $v \approx 6 \text{ km s}^{-1}$, yielding a jet (radial) velocity of $\sim 8 \text{ km s}^{-1}$. Together with a total spatial extent of $\sim 0.7 \text{ pc}$, this yield a dynamical age of $\sim 10^{4.9} \text{ yr}$. As for HH 1124, this age is much smaller than the age of the nearby clusters, indicating that the driving source formed after the formation of the clusters. As for R18, there is no indication for a feedback-bent jet, as the lobes (except for the slight S-shape of the red lobe) are not seen to bend away from the direction of the incident radiation. This could be an indication either for the fact that the jet has enough mass to resist being bent by the feedback from the nearby massive stars, or for the fact that, compared to HH 1124 in R18, HH 1010 is exposed to a weaker radiation field, which is less likely to bend jets.

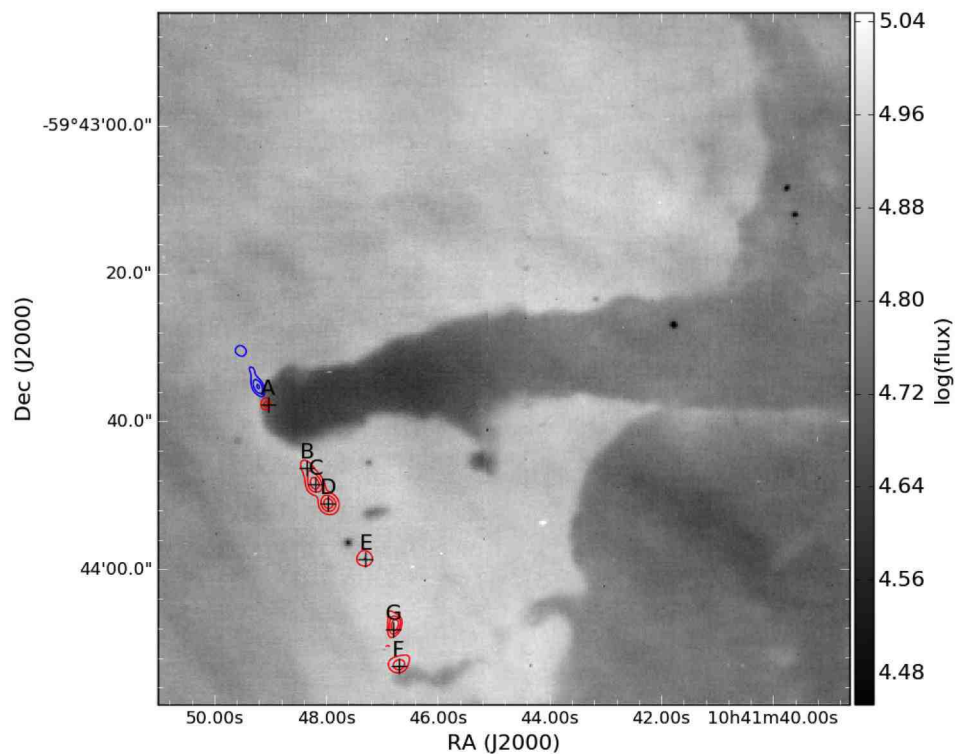


Figure 5.13: Continuum-subtracted $H\alpha$ intensity map of the tip of pillar R44. Blue and red contours mark the location of the red and blue lobes of the bipolar jet originating from the pillar tip. The contours are extracted from the corresponding two slices of the data cube at red = 6566.43 \AA and blue = 6558.93 \AA . The knots of the red lobe are marked with the white diamonds and letters from *A* to *G*. See text Section 5.3.4.

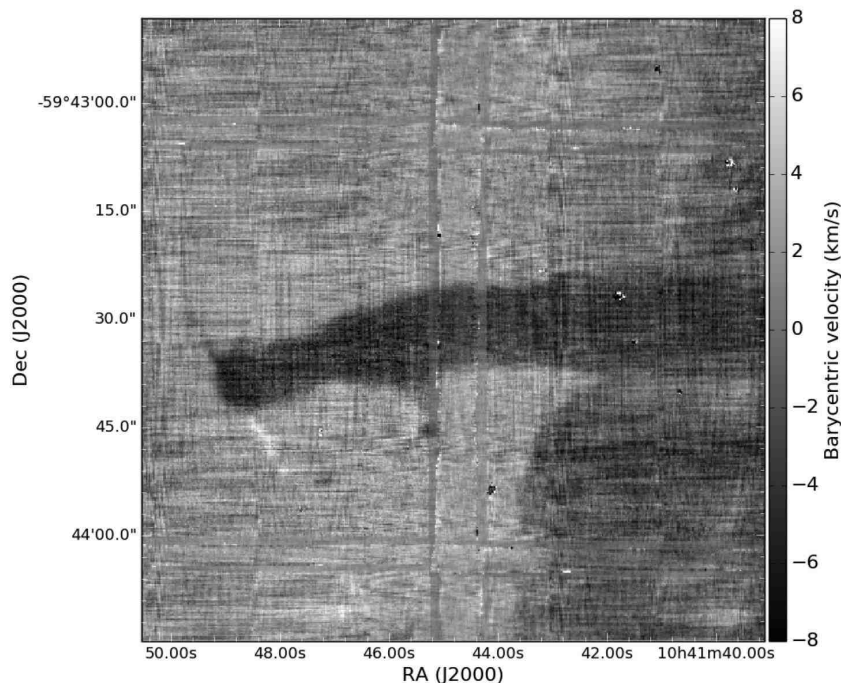


Figure 5.14: Velocity map of P1 in R44 showing the red and blue lobes of the jet (see text Section 5.3.4).

With multi-wavelength near-infrared data, Povich et al. (2011) report the presence of a $1.8 M_{\odot}$ YSO at J2000 10:41:48.670 -59:43:38.10 (PCYC55), which is just south of knot *A*. We conclude that this object is most likely the source of the jet.

5.4 Conclusions

In this paper, we presented MUSE optical integral field data of pillar-like structures in the Carina Nebula Complex. We exploit the unprecedented spectral and spatial coverage of this instrument to analyse the morphology and kinematics of the ionised gas component in the observed regions by producing integrated line maps of the main ionised and neutral emission lines covered by MUSE ($H\alpha$, $H\beta$, [OI], [OII], [OIII], [SII], [SIII] and [NII]), as well as velocity maps and maps of the electron temperature and density. The analysis performed in this paper is oriented towards understanding the link between the feedback-driving massive stars and the pillar-like structures in their vicinity. The main results are:

- The behaviour of the various emission lines along slits positioned across the pillar/ambient matter interface was derived. The pillar tips present the expected ionisation stratification, where the line-emitting species with higher ionisation energy peak first and further away from the pillar, followed by the species with lower and lower ionisation energy. By comparing the separation between the [OIII] and the [OI] lines ([OIII] having the highest ionisation energy, and [OI] tracing the neutral material), we find a slight trend in which the separation between the highly

ionised and the neutral material gets larger with distance from/ weaker intensity of the ionising sources. We include a preliminary comparison with analytical density profiles under the influence of three different types of ionising sources, and find that the ionisation front gets narrower with increasing photon flux. This however needs to be thoroughly tested with higher angular resolution imaging, as well as dedicated simulations in which a full parameter space of pillars under varying ionising conditions can be performed.

- For each region, we compute the electron density, electron temperature and velocity maps. A tight correlation between the electron density, N_e and the ionising photon flux at each pillar tip, $\log(Q_{0,\text{pil}})$, is found, as well as a correlation between the electron density and the projected distance from the ionising sources, yielding a lower limit for the density a pillar must have at a certain distance not to be destroyed in a region with given ionising conditions.

- We compute the mass-loss rate \dot{M} due to the photo-evaporative effect of the nearby ionising stars, and find that \dot{M} strongly depends on the perceived photon flux $\log(Q_{0,\text{pil}})$. This empirical correlation is the first observational quantification of the effect of ionising feedback, and will need to be thoroughly investigated with further observations, as well as numerical simulations. A very interesting perspective for future analyses is to test the presence of a correlation between the lifetime of pillars and the ionising photon flux acting on them. This could be achieved with either molecular line data or via multi-wavelength SED fitting to dust-emission maps in order to obtain a mass estimate for each pillar.

- With the spectrally resolved MUSE data, we identify two jets at the tips of R18 and R44 P1, where HH 1010 in R44 is a previously detected and discussed jet, while the morphology and extent of HH 1124 in R18 is seen and discussed for the first time in this work. Only HH 1124 shows signs of being bent away from the direction of the incoming radiation from the massive stars, while this is not the case for HH 1010, where no jet-bending is observed, which could indicate either that it has sufficient mass to resist the jet bending, or that the radiation field is not strong enough to cause jet-bending. Also, both jets are younger than the clusters in their vicinity, indicating that the formation of their driving sources occurred after the formation of the massive clusters. HH 1124 presents a rather peculiar morphology in terms of velocity, which we attribute to the presence of both a jet and a wind, possibly originating from the same source. The red lobe of HH 1010 displays a slight S-shape, hinting at jet precession.

To summarise, we demonstrate that MUSE optical integral field data can yield valuable information when analysing the effect of ionising feedback from massive stars and star clusters, as it offers a unique combination of simultaneous large spatial and spectral coverage. Not only was the effect of ionising feedback analysed through a correlation between the ionising photon flux (originating from nearby massive stars) and the mass-loss rate due to photo-evaporation of pillar-like structures, but the same data set was used to understand the effect of ionisation on the size (width) of the ionisation fronts at the pillar tips, but also to look for signs of jet bending via the detection of two ionised jets originating from the pillar tips. These results set the scene for further investigations to better understand feedback from massive stars, which can be achieved by combining the results from more IFU data sets and simulations of star-forming regions which include feedback recipes.

6

Outlook

As mentioned in the introduction, trying to understand the global effect of FB from massive stars and its dependencies on galactic environments and properties is a long-term project which cannot possibly be undertaken by a single researcher. The task of answering the open questions of Section 1.4.1 has to be instead split into different steps, approached with large data sets and tackled on different fronts, i.e. simulations and observations need to work hand in hand and the effect of the single FB mechanisms has to be understood first.

Because the different FB mechanisms act on the surrounding clouds (or host galaxies) at different stages in the evolution of massive stars, to fully sample massive star formation FB it is of great importance to cover all of these stages. Together with a first application, this will be described in Section 6.1. Furthermore, the dependency of the effect of FB on the properties of the considered star-forming regions and even host galaxies cannot be tackled with observations of the Milky Way only: to sample star-forming regions throughout entire galaxies at a reasonable cost in telescope time, extragalactic observations are crucial. This will be discussed in Section 6.2. Last but not least, answering the open questions requires a twofold comparison: the comparison of FB observations in a statistically representative number of different star-forming regions and the comparison between observations, and simulations that include different FB mechanisms, which will be described in Section 6.3.

As will become clear throughout this chapter, several observational campaigns based on the work of this thesis have already started, or proposals for these have been submitted. These ongoing and future projects will build and expand on the work here presented. As a consequence, the work done for this thesis served to build connections with new collaborators, expand already existing networks, and bring together researchers from the numerical and observational communities.

6.1 Constructing evolutionary timelines from a multi-wavelength approach

Massive stars and star clusters form in dense cores and clumps of GMC complexes. In a scenario of competitive accretion, their evolution begins in high-mass cores devoid of star formation,

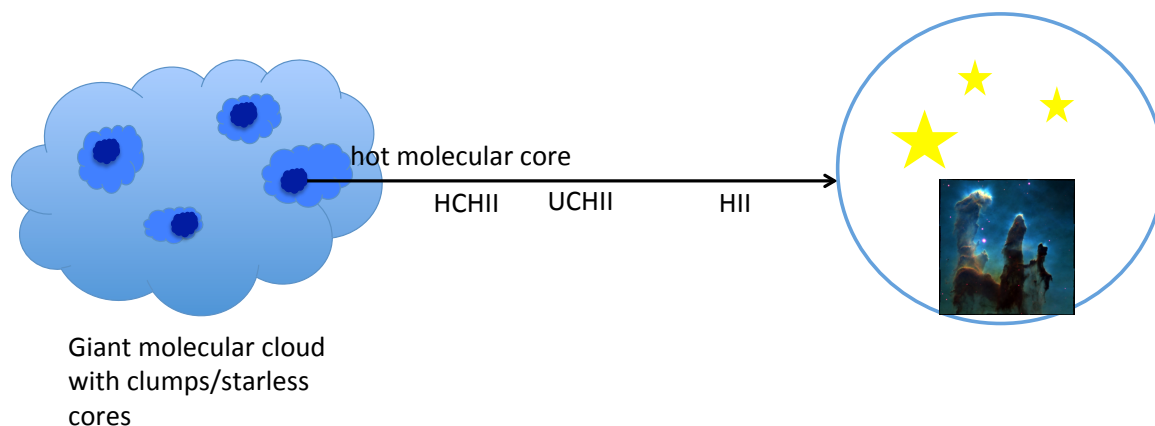


Figure 6.1: Time evolution of a molecular cloud core from starless core to HII region via the hot molecular core stage, hyper-compact and ultra-compact HII regions (HCHII and UCHII respectively).

which will eventually collapse and form low- and intermediate-mass protostars. These will evolve into high-mass protostellar objects and finally into massive stars (Beuther et al., 2007). Because of the early onset of FB via protostellar outflows, stellar winds and radiation, massive stars influence their immediate surroundings already when still deeply embedded in their native material. The dense surrounding matter, affected by the FB, will be heated, it will expand and disperse on an evolutionary sequence that starts from massive starless cores and ends with fully evolved HII regions. The intermediary steps are so-called *hot molecular core phase*, *hyper-compact* and *ultra-compact* HII regions, as is sketched in Fig. 6.1.

The evolution of the molecular cloud cores is traced by their chemical composition which goes hand in hand with the evolution of the forming stars: as these affect the surrounding matter, more and more molecules will be liberated from the surfaces of the dust grains they were previously frozen onto. These hot molecular cores are heavily extinguished by very high column densities, and are observed in the radio regime. As the forming massive stars evolve and start emitting UV radiation, hyper-compact (size < 0.01 pc) and ultra-compact (size < 0.1 pc) HII regions are formed, which start to become visible via free-free and maser emission in the radio and evolve towards the infrared regime (Hoare et al., 2007), until the FB from the massive stars has cleared away the gas sufficiently and HII regions become visible at near-infrared and optical wavelengths. A detailed description of HCHII and UCHII and observations of these is beyond this thesis, and the interested reader is referred to Beuther et al. (2007), Hoare et al. (2007) and references therein.

In order to observe massive star formation FB from the very early stages up until supernova events occur (and to understand the contribution of outflows and radiation FB during the very early HCHII and UCHII stages to star formation), it is therefore necessary to fully sample the evolutionary sequence, from massive protostellar cores to HII regions. This requires a *multi-*

wavelength approach: young, collapsing clouds/cloud cores are observed toward the radio/mm regime, exposed star clusters and HII regions in the optical and shorter wavelengths. **This opens the door to a whole range of projects starting from the work present in this thesis**, and is oriented towards answering question (1) in Section 1.4.1.

6.1.1 An infrared study of three Galactic cloud clumps with *KMOS* and *Herschel*

As a first application, in a forthcoming publication (McLeod et al., in prep.) we will analyse three Galactic molecular cloud clumps in the mass range $10^3 - 10^5 M_{\odot}$ with a multi-wavelength approach, using near-infrared *KMOS* integral field data in combination with mid- to far-infrared *Herschel* Hi-GAL data. The analysis is divided into two components: (i) we first derive the physical parameters of the three sources (column density, temperature and mass from the HiGAL data; excitation temperature and gas kinematics from the *KMOS* data) and analyse the kinematics of the ionised (for the $\text{Br}\gamma$ 2.1655 μm line) and molecular gas (for the H_2 (1-0) and H_2 (2-1) lines at 2.122 μm and 2.247 μm respectively), analysis ongoing; and (ii) compare the same physical parameters obtained from synthetic observations of three simulated star-forming molecular clouds with matching sizes and masses that include feedback in the form of winds and ionisation (see also Section 6.3).

The targets were selected from the SIMBA survey of southern high mass star forming regions (Faúndez et al., 2004) and the Bolocam Galactic Plane Survey sources discussed in Ginsburg et al. (2012) based on the detection of H_2 emission towards them, which makes them observable with *KMOS*. Because these three regions are forming massive stars but still have enough gas and dust for further potential star formation, and based on the fact that we see a luminosity spread from 10^4 to $10^6 L_{\odot}$, our target selection also contains an age selection criterion. All three targets host both forming and already formed massive O- and B-type stars, which makes them ideal laboratories to trace the warm and ionised gas components and study the feedback from several massive stars as well as possible triggered star formation. BYF73 (Barnes et al., 2010) hosts an early stage of feedback from at least two embedded (and possibly accreting) young stellar objects (Ohlendorf et al., 2013) and an already exposed cluster just north of it is irradiating the clump's edge. G012.809-00.200 (aka W33 Main) is associated with an HII region driven by a central star cluster with several O- and B-type stars (Immer et al., 2013). IRAS19078+0901 (aka W49A) consists of several optically-obscured compact HII regions and hot cores heated by deeply embedded young and massive stellar objects (Wilner et al., 2001), as well as a central cluster of about 30 O stars (Conti & Blum, 2002). The three targets are listed in Table 6.1 (the indicated masses were computed in this work, while the other listed parameters are from the above cited papers), together with the simulated cloud selected to match the observed ones (simulations extracted from the numerical library compiled by Dale et al.).

The *KMOS* observations are part of the project 095.C-0530 (PI McLeod), carried out in service mode in the period from April 6th to May 30th, 2015. Each target was covered with a 129.8"x86.6" mosaic in the K band, corresponding to 4x16 telescope pointings per object,

Table 6.1: KMOS target selection

Clump name	Mass ($10^4 M_\odot$)	Radius (pc)	$n(\text{H}_2) 10^4 \text{ cm}^{-3}$	Distance (kpc)	Luminosity ($10^5 L_\odot$)	$\log(N_{\text{lim}})$
BYF73	0.25	1.3	19	2.3	0.2 - 0.3	21.89
Run BTOP	0.23	2	-	-	-	-
W33	1.5	1	3.8	3.6	3	22.75
Run UP	1	2.5	0.91	-	-	-
W49	17	1.9	4	11.8	56	22.562
Run F	10	10	1.4	-	-	-

with an exposure time of 90s and by taking one offset sky frame every two science frames. The *Herschel* infrared Galactic Plane Survey (Hi-GAL, Molinari et al. 2010) is a 5 band survey in the latitude range $-1^\circ < b < +1^\circ$ aimed at a full dust census of the entire Galactic Plane. The survey exploits simultaneous *PACS* and *SPIRE* observations at 70, 160, 250, 350 and 500 μm with an angular resolution ranging from 6" to 36". For this work we use the fully reduced data products, courtesy of Sergio Molinari.

The column densities and temperatures were obtained by fitting a fixed β pixel-by-pixel modified black body model to the spectral energy distribution (SED) using the HiGAL 160, 250, 350 and 500 μm maps, according to

$$S_\nu = \frac{2h\nu^3}{c^2} \frac{1}{e^{h\nu/kT} - 1} (1 - e^{-\tau_\nu}) \quad (6.1)$$

where $\tau_\nu \propto (\nu/\nu_0)^\beta$ and $\beta = 1.75$.

Assuming optically thin emission and only considering the emission within the column density contour levels tracing the clumps (see Table 6.1), masses were derived via the following expression (Hildebrand, 1983)

$$M = \frac{S_\nu D^2}{B_\nu(T) \kappa_\nu} \quad (6.2)$$

where D is the distance to the source, B_ν is the Planck function and κ_ν the dust mass absorption coefficient set to $\kappa_\nu = \kappa_0 (\frac{\nu}{\nu_0})^\beta$, with $\beta = 1.75$, $\nu_0 = 505 \text{ GHz}$ and the dust opacity $\kappa_0 = 4 \text{ cm}^2 \text{ g}^{-1}$ as in Battersby et al. (2011). The mass computation was performed on the background-subtracted column density maps, where the background was obtained by convolving the column density maps with a Gaussian kernel. An example fit to one of the pixels of BYF 73 is shown in Fig. 6.2, while Fig.6.3 shows the resulting column density and temperature maps of W49. Where the *Herschel* data is saturated, resulting in invalid pixels, the column density and temperatures are obtained by interpolating over the bad pixels. The computed masses are listed in Table 6.1.

We will determine both the rotational and vibrational excitation temperatures T_{rot} and T_{vib} , according to the methods described in Burton et al. (1989) and Ramsay et al. (1993):

$$\frac{I_1}{I_2} = \frac{A_1 \nu_1 g_1}{A_2 \nu_2 g_2} \exp\left(\frac{E_2 - E_1}{k_B T_{\text{vib}}}\right) \exp(\Delta\tau) \quad (6.3)$$

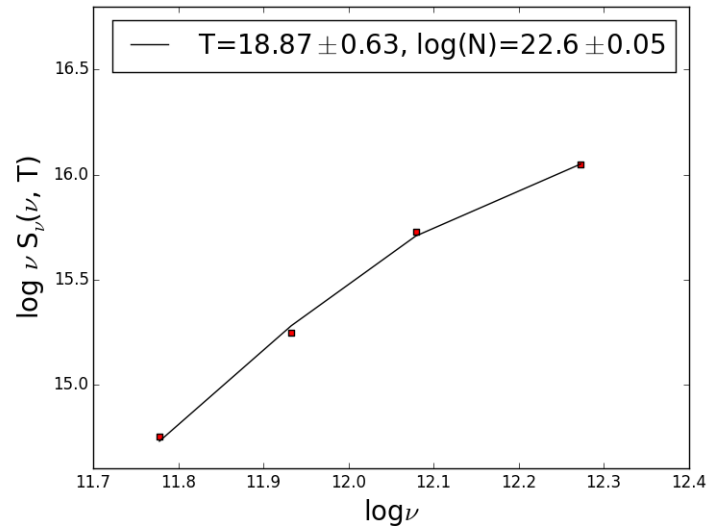


Figure 6.2: Example SED fit of BYF 73. The Herschel data points are marked with red squares (160, 250, 350 and 500 μm), the black line is the best fit black body.

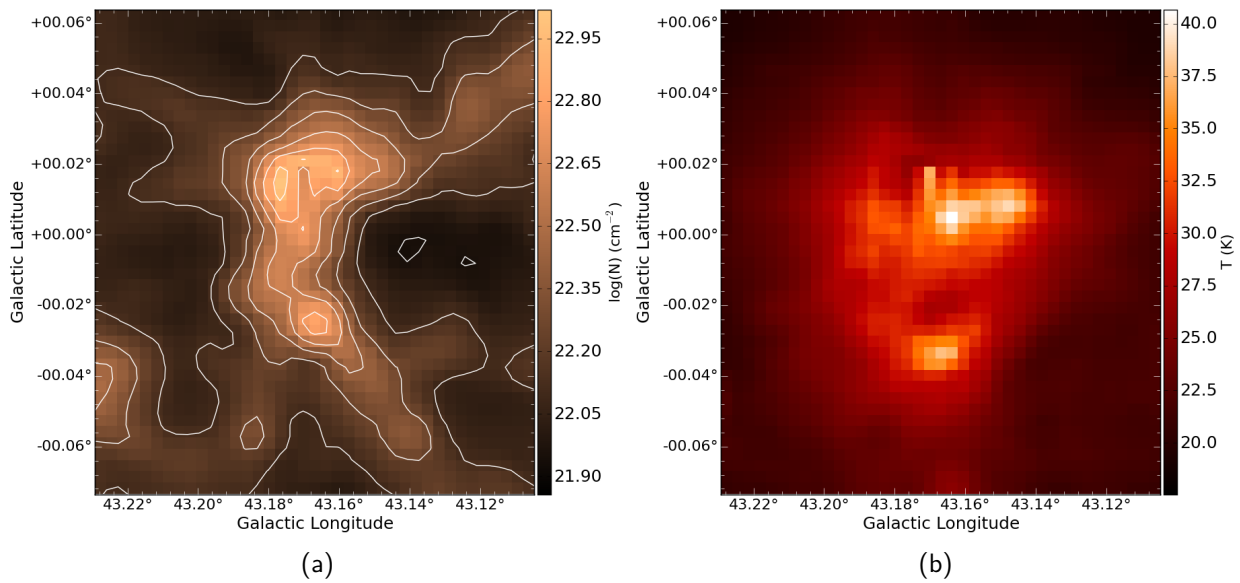


Figure 6.3: Column density (left) and temperature (right) maps of W49 derived from the HiGAL data. Column density contour levels are $\log(N) = 21.95, 22.11, 22.27, 22.43, 22.59, 22.75, 22.91$.

Line	λ (μm)	g_j	A (10^{-7} s^{-1})	Energy level (K)
1-0 S(0)	2.2233	5	2.53	6472
1-0 S(1)	2.1218	21	3.47	6952
1-0 S(2)	2.0338	9	3.98	7585
1-0 S(3)	1.9576	33	4.21	8365
1-0 Q(1)	2.4066	9	4.29	6149
1-0 Q(2)	2.4134	5	3.03	6471
1-0 Q(3)	2.4237	21	2.078	6956
2-1 S(0)	2.3556	5	3.68	12097
2-1 S(1)	2.2477	21	4.98	12552
2-1 S(2)	2.1542	9	5.6	13152
2-1 S(3)	2.0735	33	5.77	13892

Table 6.2: H₂ lines identified in the KMOS K-band spectra. g_j is the statistical weight of the upper level and A is the transition probability.

$$\frac{I_o}{I_p} = \frac{A_o g_o}{A_p g_p} \exp\left(\frac{E_p - E_o}{k_B T_{\text{rot}}}\right) \quad (6.4)$$

where A is the decay rate, g is the statistical weight of the energy level, ν is the frequency of the emission line and E is the energy of the level. In this analysis, vibrational temperatures were computed from the H₂ 1-0 S(1) and the H₂ 2-1 S(1) lines (I_1 and I_2 respectively), while the rotational temperatures were computed using the 2-1 S(1) and 2-1 S(2) (ortho and para respectively) lines. We assume homogeneity of the extinction between the 1-0 S(1) and the 2-1 S(1) lines, and therefore neglect the $\Delta\tau$ term (which takes into account differential optical depth of the extinction between the wavelengths of two lines). A list of the molecular and ionised emission lines detected with KMOS is given in Table 6.2.

The analysis of the KMOS data sets for the first part of this analysis is still ongoing, and it will be followed by a comparison with the simulations via the tools described in Section 6.3. However, a few preliminary results in terms of massive star formation FB can be summarised as follows.

W49

The W49A region is certainly among the most massive ($M_{\text{gas}} \sim 10^6 M_{\odot}$, Simon et al. 2001) and luminous ($L \sim 10^{7.2} L_{\odot}$, Sievers et al. 1991, at a distance of ~ 11.1 kpc, Zhang et al. 2013) star forming regions in the Milky Way. It hosts three sites of massive star formation: W49N, W49S and W49SW, of which W49N is the most luminous one. The entire region of W49A is very embedded, containing over 40 ultra compact HII regions (De Pree et al., 1997) associated with massive stars or young stellar objects. Peng et al. (2010) find evidence for two expanding shells as well as two gas ejections using Spitzer mid-infrared and molecular line data, and these authors hypothesize that these are responsible for triggering the remarkable starburst in W49A.

More recently, Galván-Madrid et al. (2013) performed a multi-scale analysis of the region that cover scales from ~ 110 pc down to ~ 10 pc with CO molecular line as well as radio continuum data, and found a total gas mass of about $1.1 \times 10^6 M_{\odot}$ for the entire W49 GMC spanning 60 pc, and that the layout of this mass corresponds to a hierarchical network of filaments that converge toward W49N. These authors conclude that the starburst if this region is probably the result of a global collapse along filaments.

With KMOS we targeted the luminous W49N clump of the W49A molecular cloud, and find this region to host several feedback-tracing structures. This is shown in Fig. 6.4, where two sub regions from the $\text{Br}\gamma$ velocity map, enlarged from the $\text{Br}\gamma$ integrated intensity map in the upper left panel, are shown in the two right panels. The upper one corresponds to a bubble-shaped structure with a diameter of ~ 0.5 pc, it hosts a candidate massive young stellar object (Saral et al., 2015), and presents a layered, shell-like structure in velocity space. The lower one is of a similar size-scale (~ 0.4 pc) and also hosts a candidate massive YSO, but instead of a shell-like structure, it shows a velocity gradient along the NE/SW direction, possibly tracing an outflow or a stellar wind. The bottom left panel shows the capability of KMOS of identifying and classifying massive stars, which is of extreme importance for the arguments in this thesis as it demonstrated that IFS allows the identification of the FB-driving massive stars and the tracing of the FB-affected gas with the same data set.

W33

W33 Main is one of three large molecular cloud clumps in the W33 complex, which comprises W33 Main, W33 A and W33 B and lies in the Scutum spiral arm at a distance of 2.4 kpc (Immer et al., 2013). Fig. 6.5 shows the main features of the W33 complex, together with the KMOS field-of-view (white box), as well as the detected water and methanol maser emission (white crosses from Immer et al. 2014 and white diamond from Menten et al. 1986 respectively) and the positions of an embedded star cluster (EC) and an open cluster (OC) from Morales et al. (2013) (red x) in the KMOS field (inset in upper right corner). With APEX 280 GHz and SMA 230 GHz data, Immer et al. (2014) conclude that the evolutionary stage of W33 Main corresponds to the HII region phase, as it shows strong radio emission, it lacks the emission from complex molecules typical for hot cores, and the $\text{H}30\alpha$ radio recombination line tracing ionised gas is detected.

Fig. 6.6 shows the KMOS $\text{Br}\gamma$ integrated intensity and velocity maps of W33 Main. In the velocity map, a bipolar velocity field of the ionised gas in the region with a NE/SW velocity gradient is clearly identified, the two lobes being separated by an gap in the emission (due to high extinction) of the size of about 0.4 pc in which the central water maser from Fig. 6.5 is located, hinting at a site of ongoing massive star formation. This outflow is therefore likely to be driven by a massive star or star cluster being formed in the central part of the image. The total scale of the KOMS-traced outflow is of ~ 1 pc.

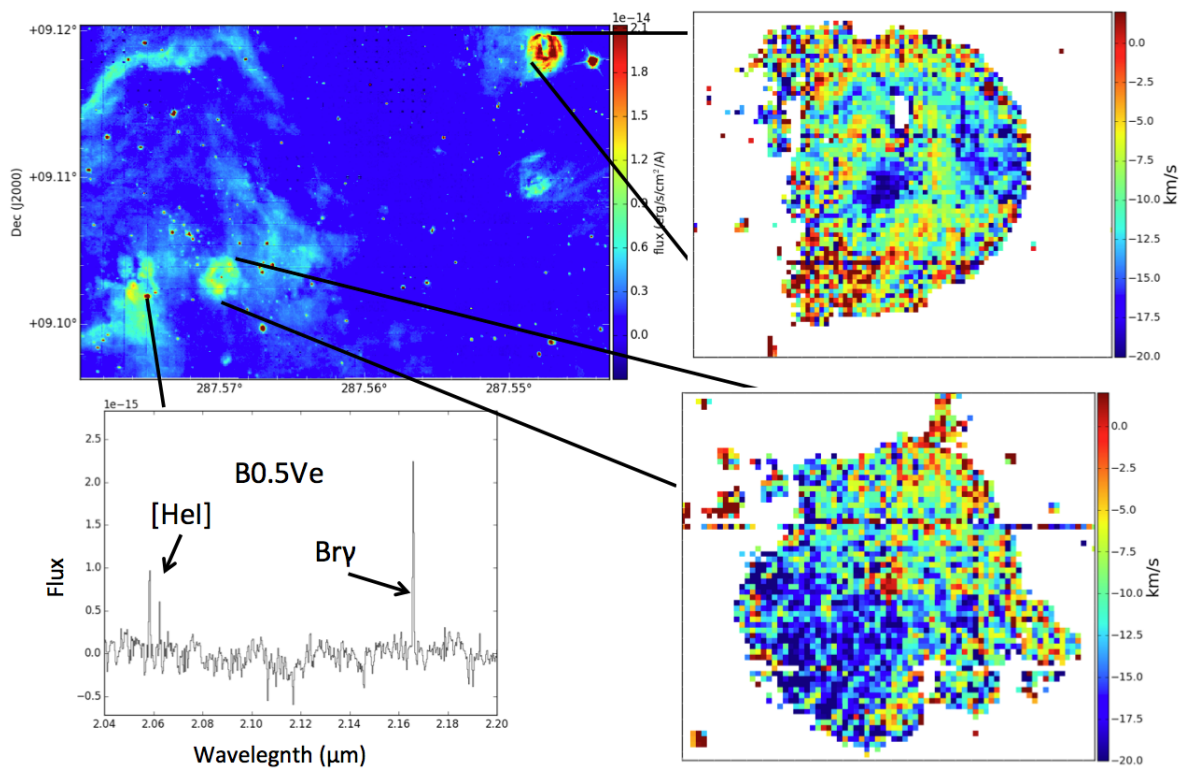


Figure 6.4: Feedback-driven structures in W49 traced by KMOS. The upper left panel shows an integrated intensity map of the ionised $\text{Br}\gamma$ line, while the two right panels show enlarged regions of the $\text{Br}\gamma$ velocity map. The lower left panel shows the spectrum of a star in the KMOS data, preliminarily classified as a B-type star.

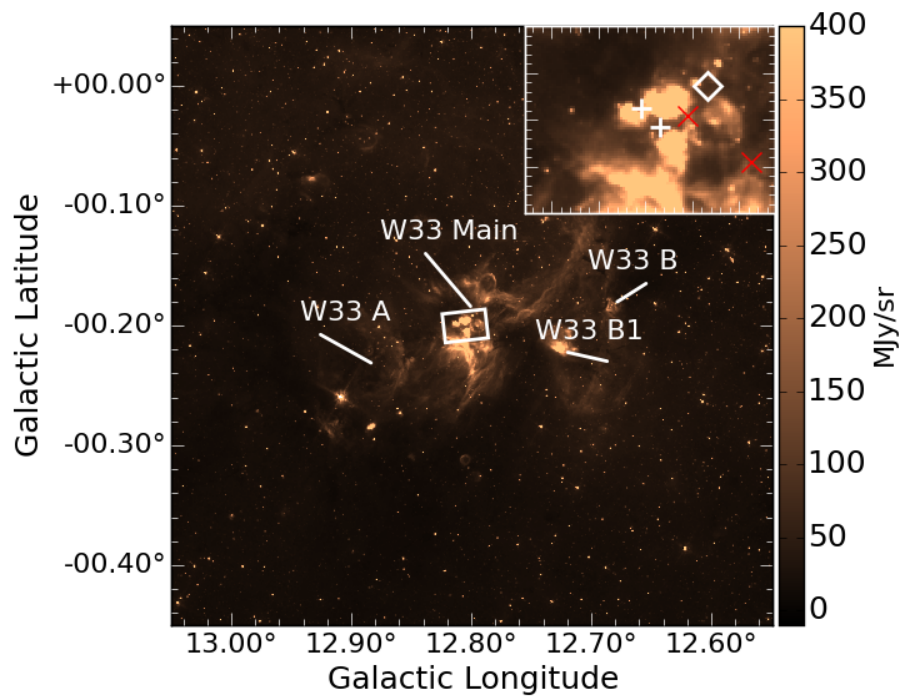


Figure 6.5: Spitzer/GLIMPSE 5.8 μm image showing the main features of W33 (for more details, see Immer et al. (2014)). The white box indicates the KMOS field of view, a zoom-in is shown in the upper right corner: water and methanol masers are marked with the white crosses and the white diamond, the positions of two young star clusters are marked in red.

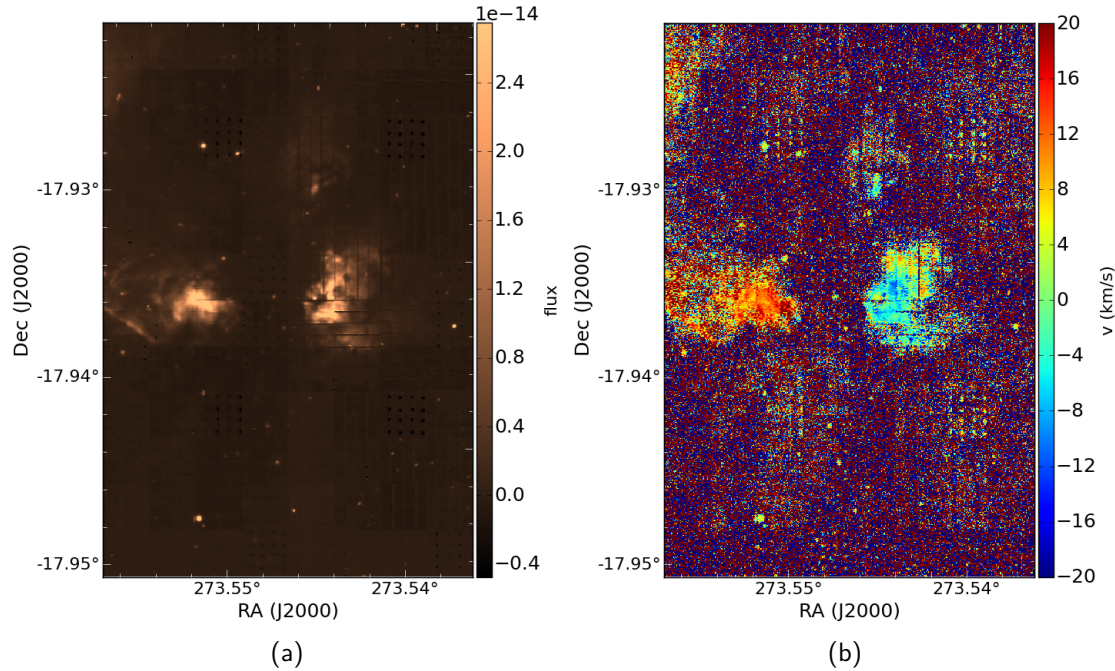


Figure 6.6: Integrated intensity (left) and velocity map of the Br γ line in W33 Main.

BYF 73

The cloud clump BYF 73 (Barnes et al. 2011, aka G286.21+0.17, [DBS2003] 127) is situated in the northern outskirts of the Carina Complex, about 12' north of Gum 31. BYF 73 is known to host at least one young stellar object, and a young cluster with about 45 YSOs (Ohlendorf et al., 2013) is found in its immediate north-western vicinity. Because of this particular setup, BYF 73 is the perfect object where young stellar feedback from both in- and outside the molecular cloud clump can be analysed.

Barnes et al. (2010) (henceforth referred to as B10) extensively studied this object with Mopra molecular line data, as well as K-band photometric data from the Anglo-Australian Telescope. Based on the density of the line-emitting matter, these authors find a mass of $\sim 2 \times 10^4 M_\odot$, which is a factor of about 40 times the $470 M_\odot$ derived via SED fitting by Faúndez et al. (2004), and ten times the $2105 M_\odot$ derived by Ohlendorf et al. (2013). Together with an infall rate of $\sim 3.4 \times 10^{-2} M_\odot \text{ yr}^{-1}$ derived via radiative transfer modeling, B10 report that BYF 73 might be the molecular cloud clump with the highest known infall rate to date. From the SED fit and Eq. 2 we find a mass of $\sim 2500 M_\odot$, which is about a factor of 8 smaller than what B10 find, and in good agreement with the Ohlendorf et al. (2013) estimate.

The near- and far-infrared data, in combination with the derived column density and temperatures, yield a very interesting picture of this cloud clump. Three are the YSOs identified to date towards BYF 73: G286.2086+00.1694 (Mottram et al., 2007), and the two in Ohlendorf et al. 2013 IRAC-identified sources at $l = 286.21^\circ$, $b = 0.18^\circ$ and $l = 286.21^\circ$, $b = 0.16^\circ$. These are marked with a green cross, a red diamond and a cyan circle respectively in Fig. 6.7a,

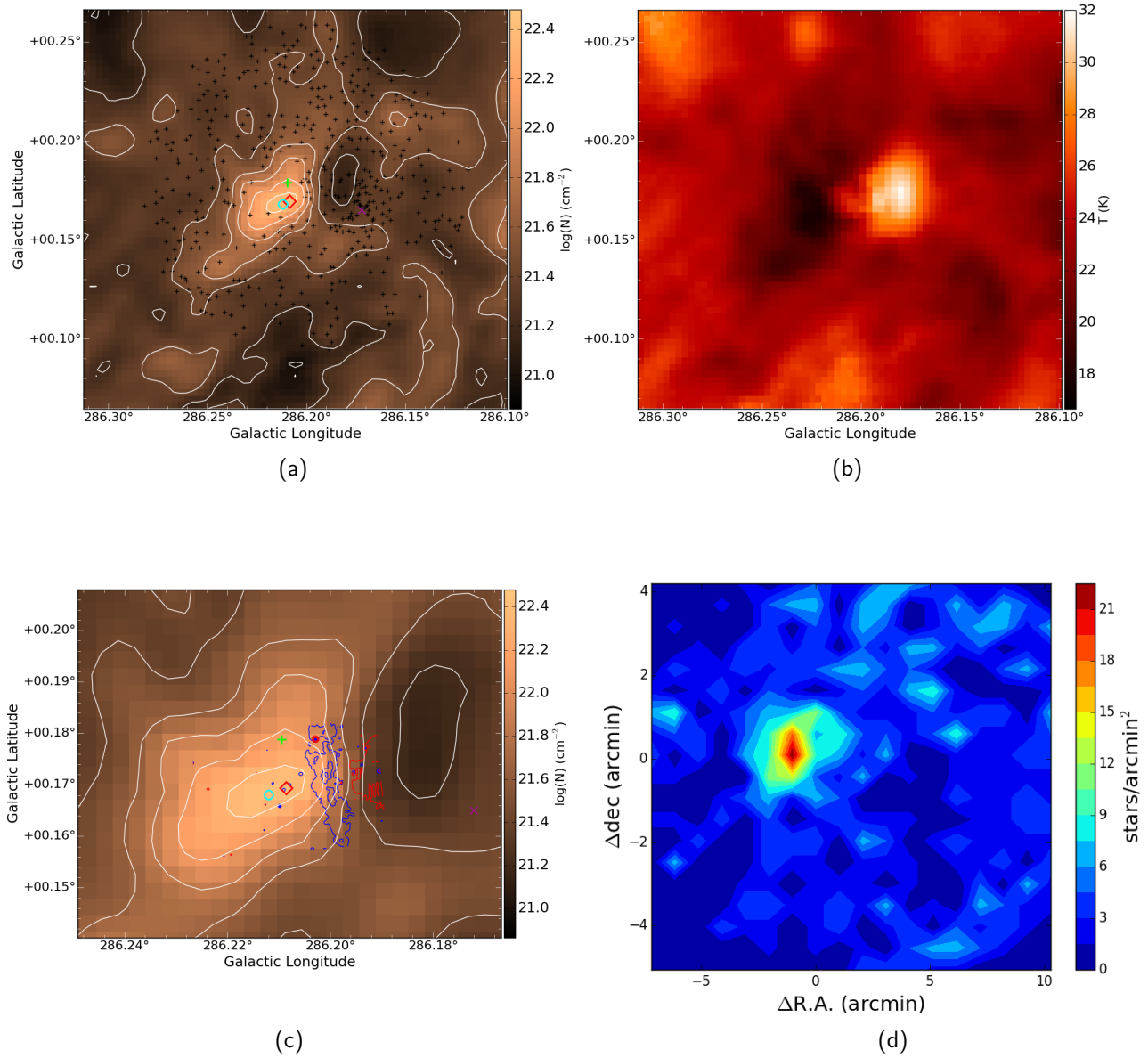


Figure 6.7: Column density (a) and temperature (b) maps of BYF 73 derived from the HiGAL data. (a) Column density contour levels are $\log(N) = 20.99, 21.22, 21.44, 21.67, 21.88, 22.11, 22.33$. Black crosses mark the positions of the WISE sources in a 5 arcmin cone selection around $l = 286.18^\circ$ and $b = 0.17^\circ$, the red diamond, green cross and cyan circle indicate the positions of three candidate young stellar object, while the magenta x indicates the coordinates of the stellar over-density in panel (d). Panel (c) is a zoom-in of panel (a), blue and red contours correspond to the KMOS H_2 (1-0) and $\text{Br}\gamma$ emission respectively. Stellar surface density plot (d) for the WISE catalog sources.

c. The positions of the latter two coincide with the highest column density values of the cloud clump. The central coordinates of the cluster (identified via its over-density seen in the stellar surface density plot shown in Fig. 6.7 d) are marked with the magenta x and correspond to $l = 286.172^\circ$, $b = 0.165^\circ$. In panel (c) of Fig. 6.7, the elongated H_2 and concentrated $Br\gamma$ emission are traced by the blue and red contours respectively. This, together with Fig. 7(a) in B10, shows that the bubble-shaped HII region and the cloud clump BYF 73 are separated by a slab-like photo-dissociation region (PDR), traced by the $Br\gamma - H_2$ emission. The PDR - i.e. the part of the molecular cloud clump facing the nearby star cluster - reveals the mechanical feedback from the cluster on BYF 73, shaping it into a slab-like structure. Unfortunately, we cannot perform a kinematical analysis of BYF 73 from the KMOS data, as the signal-to-noise ratio does not allow it.

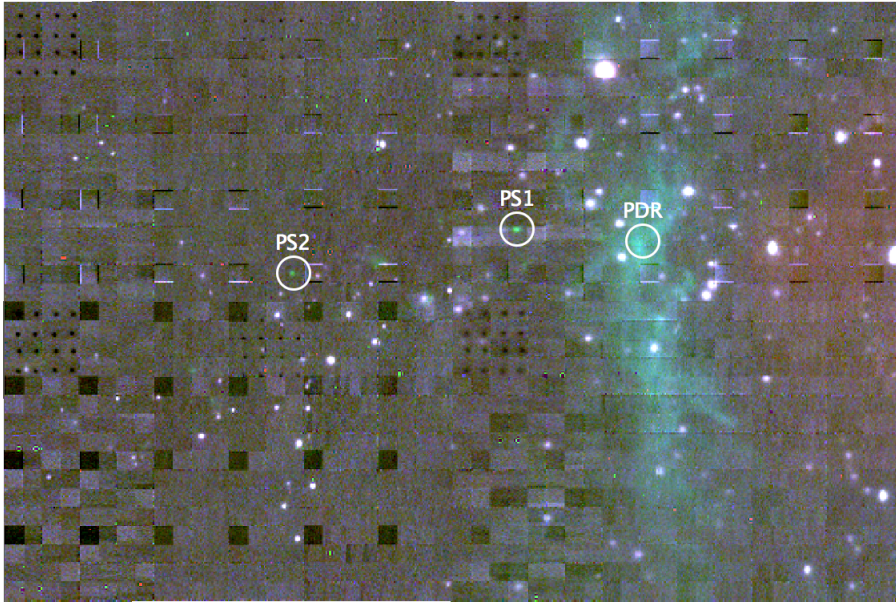


Figure 6.8: RGB colour composite of $Br\gamma$ (red), H_2 1-0 S(1) (green) and H_2 2-1 S(1) (blue). The white regions mark the positions of the H_2 point sources PS1 and PS2 (see text Section 6.1.1) and the location of the circular extraction of the PDR emission. Minimum/maximum scale values are $-1.15 \times 10^{-15} / 2.95 \times 10^{-15}$ (red), $-1.22 \times 10^{-15} / 3.16 \times 10^{-15}$ (green), $-5.00 \times 10^{-15} / 1.50 \times 10^{-15}$ $\text{erg s}^{-1} \text{cm}^{-2}$.

With our KMOS data we furthermore trace feedback from within the cloud clump. The 3-colour composite shown in Fig. 6.8, together with the PDR (driven by the nearby cluster to the south-east) marked with the transition from the ionised ($Br\gamma$, red) to the molecular gas components (H_2 , coincident blue and green), also shows two point sources with excess H_2 1-0 S(1) emission (PS1 and PS2) in the high-density region of the cloud clump. PS1 ($b = 286.2056^\circ$, $l = 0.1722^\circ$) lies, in projection, $\sim 0.2'$ (0.13 pc), while PS2 ($b = 286.2144^\circ$, $l = 0.1695^\circ$) is at about $0.7'$ (0.47 pc) west of the PDR. For these, we will extract co-added spectra (the example of PS1 is shown in Fig. 6.9), compute excitation diagrams and compare

these to the same diagram obtained for the PDR to distinguish between collisionally-excited and fluorescent emission lines to determine the presence of shocks.

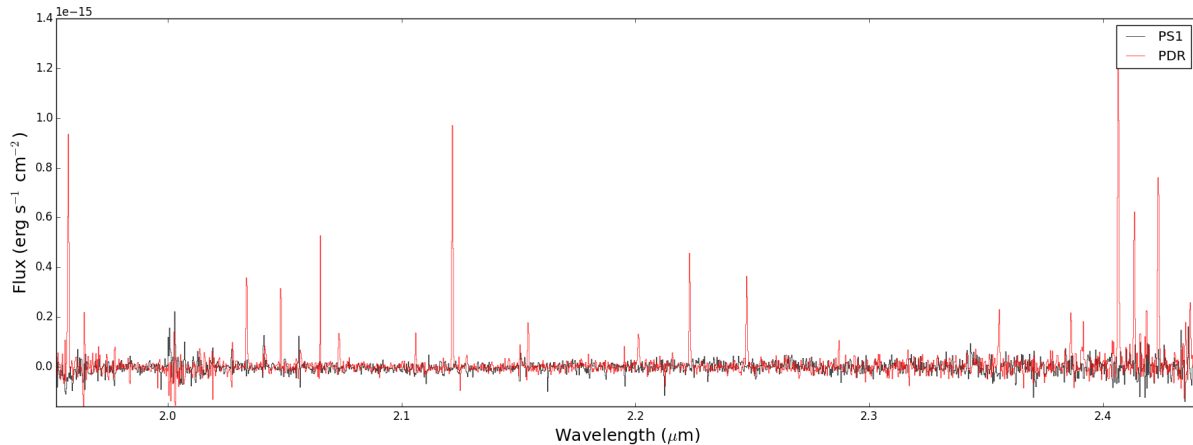


Figure 6.9: Co-added spectrum of a circular extraction of 0.4'' around PS1 and for a region of the same size of the PDR.

6.2 Taking things beyond the Milky Way

Observations of the different evolutionary stages of the evolution of massive stars are needed to study in detail the different FB mechanisms throughout the evolution of massive stars and their environment. However, in order to tackle questions (2), (3) and (4) posed in Section 1.4.1, it is necessary to extend the observational campaigns to galaxies beyond the Milky Way. The main reason for this is that the combination of our position in the Galaxy and the vicinity of Galactic star forming regions makes it quite difficult to observationally sample a large enough number of entire star-forming/HII regions. Therefore, to analyse the dependency of FB on environment as well as size-scale, and to test the role of massive star-formation FB on the regulation of star formation in galaxies, the work of this thesis will be expanded with extragalactic observations.

A pilot study of two HII regions in our nearest neighbour, the Large Magellanic Cloud (LMC), as well as a MUSE large program to sample more of these is discussed in Section 6.2.1, and the project of observing the nearby star-forming galaxy NGC 300 is described in Section 6.2.2.

6.2.1 A MUSE view of feedback in HII regions in the Large Magellanic Cloud

In Period 96, we submitted a successful MUSE proposal (PI McLeod) to image two HII regions in the LMC (program 096.C-0137(A)), with the goal to test the capability of MUSE in detecting and classifying FB-driving O- and B-type stars, derive FB-driven quantities such as the expansion

velocities of the HII regions or photo-evaporation from the ionisation fronts at the distance of the LMC, and compare the results to simulations of FB-driven, star-forming molecular clouds (see Section 6.3). The LMC is an ideal laboratory to study the feedback of massive star formation as it is nearly face-on and close enough that single stars can be resolved, indeed the star cluster population in the LMC is well studied, and its stellar, gaseous and dusty components have been targeted in many multi-wavelength surveys over the past decades.

The targets for this proposal were selected from the HII region sample presented in Slater et al. (2011), based on the spectral class of the hottest ionising star and the number of stars in the HII region that contribute to the total bolometric luminosity. Thus we selected the HII regions N180 and N44: both have formed O-type stars, but the distribution of their stellar content is very different, N44 hosting 3 distinct OB associations with their respective HII regions and embedded young stellar objects (Chen et al., 2009) and N180 hosting one central cluster of several early O-type stars, more than 50 stars with $M > 10\text{--}15 M_{\odot}$ and a population of young stellar objects (Caulet et al., 2008). Furthermore, the different stellar populations and injected energetics of the two sources match the different masses, evolutionary stages and feedback effects of the simulations described in Section 6.3, and for the two targets, we will aim at determining physical parameters such as density, temperature, expansion velocities of the bubbles, kinematics of the ionised gas. We will explicitly compare these parameters with those extracted from the numerical simulations.

For this proposal, the immediate objectives (based on the techniques developed in McLeod et al. 2015) were:

- analyse the structure of the ionised gas by computing line intensity maps for different emission lines
- exploit emission line ratios of the [NII] and [SII] duplets to compute electron densities and temperatures
- compute velocity maps via our gaussian line fitting algorithm, trace and analyse the kinematics of the ionised gas and the expanding HII bubbles and compare these with the energies injected by the stars
- compute line ratios of collisionally excited lines (i.e. [OIII] λ 5007, [NII] λ 6583 and [SII] λ 6717) to hydrogen recombination lines such as $H\alpha$ and $H\beta$ to distinguish between shocks and photo-ionisation

The two H II regions were observed with 8x8 arcmin mosaics (thus 64 pointings per target) with an exposure time of 90 seconds per pointing as a filler program between October 2015 and February 2016. The data reduction of the first HII region, N44, was carried out soon after, and a first analysis is shown in Fig. 6.10. The RGB-composite (left panel) shows the main HII bubble surrounded by 4 smaller and younger bubbles. The younger bubbles are smaller in size, they host fewer stars, and show a relatively large degree of emission from matter in their centres. An $H\alpha$ velocity map is shown in the right panel: the main bubble can be clearly distinguished from the background matter, and an expansion velocity of $\sim 40 \text{ km s}^{-1}$ is computed from the MUSE data, in very good agreement with previously found values (e.g. Meaburn & Laspias 1991). Further analysis will be carried out after the reduction of the N180 data set: we will compare the stellar contents of the various bubbles and their expansion velocities, correlate

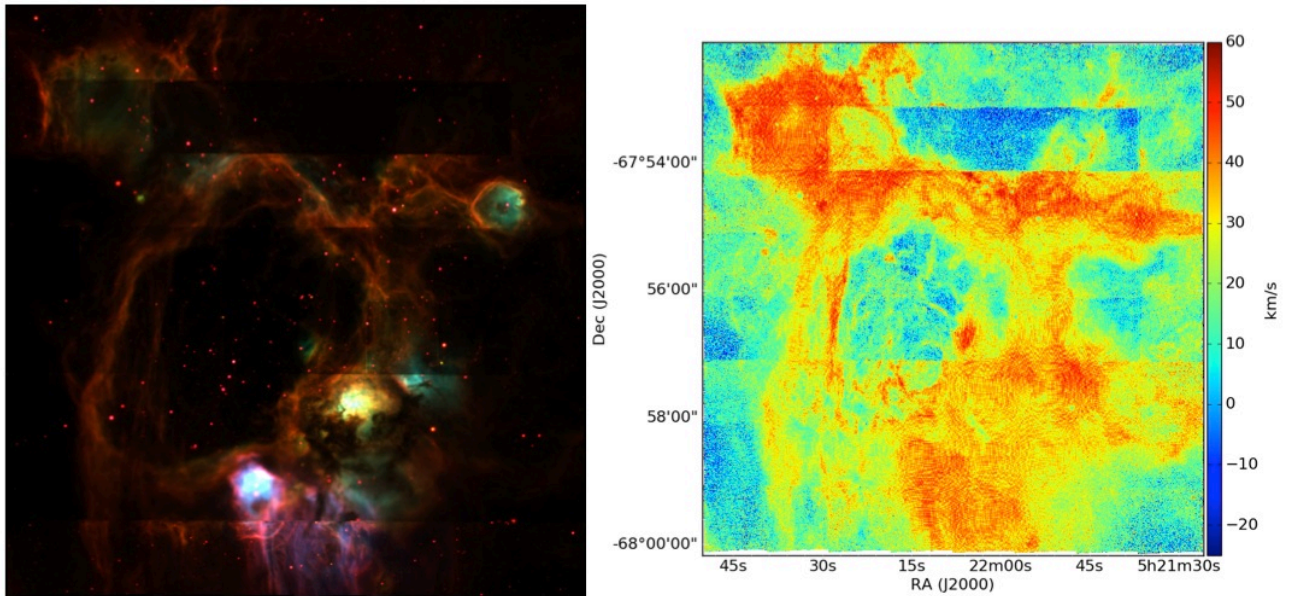


Figure 6.10: MUSE observations of the HII region N44 in the LMC, from program 096.C-0137(A) (PI McLeod). Left panel: an RGB-composite of [SII] (red), $H\alpha$ (green) and [OIII] (blue). Right panel: the $H\alpha$ velocity map.

this with the presence (or absence) of supernovae, and compare the different derived physical parameters to understand how FB differs in these two regions.

These observations served as a pilot for a MUSE large program submitted for Period 98 (PI McLeod). For this, we proposed to derive the physics of feedback with a unique legacy MUSE dataset of HII regions in LMC with a survey named I-MAGiCS (the MUSE Integral field Magellanic Cloud Survey). By covering a total of 10 HII regions in the LMC with MUSE (9 regions from this large program and including N44*), we will be able to cover all the FB mechanisms which can be traced by an optical integral field unit: stellar winds, ionising radiation and supernovae (SN). The targets (as well as their number) have been carefully selected to cover the entire observed LMC HII region $H\alpha$ luminosity range, different representative locations within the galaxy, sizes, and presence of supernovae (Table 6.3, Fig. 6.11). With the data from this large program, we will tackle FB with different topics: together with the (1) FB analysis as main science goal, we will exploit the data set to (2) derive a complete census of massive stars for the covered regions, (3) determine elemental abundances across a representative part of the LMC disk, (4) link the optical MUSE dataset to existing infrared and (sub)millimetre observations to connect the dust, the neutral ISM and the ionised medium, and (5) exploit planetary

*The HII region N180, observed in the same project as N44, is not in the LMC disk, and will therefore not be included in the I-MAGiCS survey.

Table 6.3: MUSE LMC large program target selection. Values for the integrated $H\alpha$ luminosity (column 3), the size (column 4), exposure time (column 9) and total telescope time (column 10) are given, as well as the presence of known supernova remnants (SNR, column 6), planetary nebulae (PN, column 7) and the size of the proposed mosaic (column 8). The already observed region N44 is included for completeness.

Target	RA	Dec	$\log(L)$ (L_{\odot})	r (arcmin)	SNR	PN	Mosaic	t_{exp} (s)	t (h)
N75	05:55:53.5	-68:14:00.9	35.76	3.5	no	no	7'x6'	180	7.35
N206	05:31:05.3	-71:03:59.5	36.83	7	yes	no	14'x11'	180	27
N55	05:32:17.1	-66:26:33.9	36.9	4.6	no	no	8'x8'	180	11.24
N113	05:13:28.9	-69:22:09.4	37.1	3	no	no	5'x4'	120	2.92
N70	05:43:17.5	-67:50:48.0	37.84	4.4	no	no	9'x9'	120	11.28
NGC 1850	05:08:38.2	-68:45:27.7	37.86	4.5	yes	yes	composite	120	12.5
N 44	05:22:06.9	-67:56:46.0	38.19	3	yes	no	8'x8'	90	
N144	05:26:42.5	-68:49:34.0	38.36	3.9	no	no	9'x9'	90	9.84
N51	05:26:13.1	-67:29:56.0	38.52	11	no	yes	composite	90	39.2
N11	04:56:47.4	-66:25:48.4	39.01	11.3	yes	no	24'x20'	90	57.6

nebulae in the target fields to determine the chemical enrichment of previous generations of stars. If granted, the I-MAGiCS data set will greatly improve on previous legacy data sets of the LMC (e.g. HST, Spitzer, Herschel), as only MUSE has the unprecedented combination of large spectral and spatial coverage in a single instrument to carry out all the above analyses simultaneously.

6.2.2 Constraining the physics of high-mass stellar feedback in NGC 300

As already discussed throughout this thesis, the physics of star formation and the (re)distribution of mass, energy, and metals by stellar FB are the missing ingredients required to understand galaxy evolution. Progress in the field requires a systematic observational census of the small (cloud-)scale quantities describing star formation and FB, i.e. the cloud lifetime, the star formation efficiency, the FB ejection velocity and heating rate, the mass loading factor (outflow rate in units of the star formation rate), and the coupling efficiency of FB to the surrounding ISM. Until recently, it was not possible to obtain these quantities outside of the limited sample of Galactic star-forming regions. Thanks to the arrival of MUSE and ALMA, as well as our recent development of novel analysis techniques, we can now systematically characterise the above quantities describing star formation and FB for large samples of star-forming regions across the nearby Universe. As a first key contribution of MUSE, in P98 we submitted a proposal to derive the physics of star formation and FB in the nearby star-forming galaxy NGC 300 (PI McLeod).

If granted the time, we will combine the FB analysis methods and results from this thesis with a further novel analysis technique developed by Kruijssen & Longmore (2014) (KL14 hereafter). These authors developed a new, fundamental statistical model explaining why the tight, galaxy-scale relations between gas and/or star formation tracers break down on small

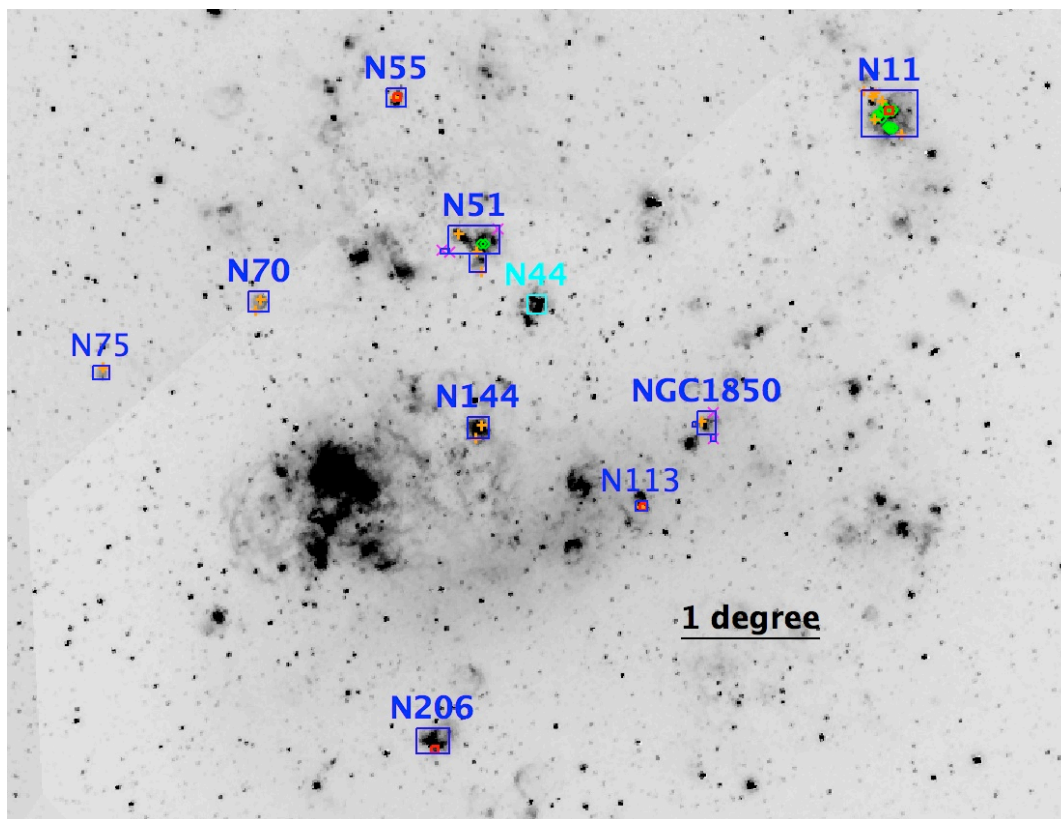


Figure 6.11: SHASSA (Southern H-Alpha Sky Survey Atlas) $H\alpha$ image showing the location across the LMC of the I-MAGiCS target HII regions (blue), centres of complementary archival ALMA programs (red squares), the location of the planned PNe (magenta crosses), NANTEN molecular clouds (orange crosses, from Kawamura et al. 2009) and HST-identified young stellar objects (green diamonds, from Vaidya et al. 2009). The already observed HII region, N44 (see Fig. 6.10) is marked in cyan. The sizes of all blue squares correspond to the planned mosaics.

spatial scales (Schruba et al. 2010 Leroy et al. 2013). It was shown that this breakdown can be used to robustly derive the lifetimes of these tracers, because the relative occurrence of two tracers on small scales is a simple function of their relative lifetimes, see Fig. 6.12b. As detailed in KL14, the shape of the curves in Fig. 6.12b is uniquely set by the duration for which the gas (t_{CO}) and stellar (t_{FUV}) tracers are visible, as well as their overlap t_{FB} . Obtaining the time-axis of astrophysical processes is often a challenge, but is crucial for deriving the FB energy and momentum deposition rates and efficiencies. With this new method, we can derive the timeline of emission for any set of gas and star formation/FB tracer, throughout the cloud-scale star formation and FB process.

We therefore proposed to cover a representative part of the star-forming optical disk of NGC 300, a nearby, gas-rich ($M_{\text{HI}} = 1.5 \times 10^9 M_{\odot}$), star-forming ($\text{SFR} = 0.1 M_{\odot} \text{ yr}^{-1}$), near-solar metallicity flocculent spiral galaxy that is the near twin of M33 but easily accessible from the southern hemisphere. At NGC 300's distance of $d = 1.9 \text{ Mpc}$, MUSE offers a resolution of $\sim 10 \text{ pc}$, allowing the detection of HII regions and the coverage of a relatively large field ($7' \times 5'$) in just over 30 hours of telescope time and without any particular constraints on observing conditions. Our selected region covers the galactic center and reaches out to $R_{\text{gal}} = 2.5 \text{ kpc}$ (where most of the star formation takes place, see Fig. 6.12a). The chosen fields complement our unique ALMA CO(1-0) data – the largest field-of-view (300 pointings), highest-resolution (20 pc), highest-sensitivity ($1\sigma \approx 3000 M_{\odot}$) extragalactic CO data obtained by ALMA (Cycle 2 delivered and Cycle 3 nearing completion) – and contains a large-enough (≥ 70) number of HII regions (~ 100 , Pietrzyński et al. 2001) to perform our planned analysis (see Fig. 6.12b).

6.3 The next necessary step: comparing observations and simulations

As discussed so far, to answer the open questions of Section 1.4.1, both Galactic and extragalactic observations are essential, and the observational approach has to be a multi-wavelength one. Large observational data sets spanning over wide mass-, age- and size-ranges are needed, but to fully understand and characterise massive star formation FB also from a numerical and theoretical perspective, the observations need to be compared to simulations of star-forming molecular clouds that include FB recipes. A complete picture of FB from massive stars can then be obtained with analytical tools specifically designed to compare the observations to each other and to the same parameter space in mass, size and evolutionary stage available from simulations (a schematic view of this is shown in Fig. 6.13). Furthermore, from simulations of massive star-forming molecular clouds that include FB recipes (Gritschneider et al. 2010b, Walch et al. 2015, Dale et al. 2013) a quantification of the star formation FB mechanisms is possible, and their qualitative morphological predictions are in agreement with observations. But, while the simulations become more realistic, they still fail to reproduce the observed star formation efficiencies and rates, and to date no simulation includes all the fundamental physics of star formation. Therefore, a comparison between simulations and observations is needed to better constrain the FB physics used as recipes in the simulations.

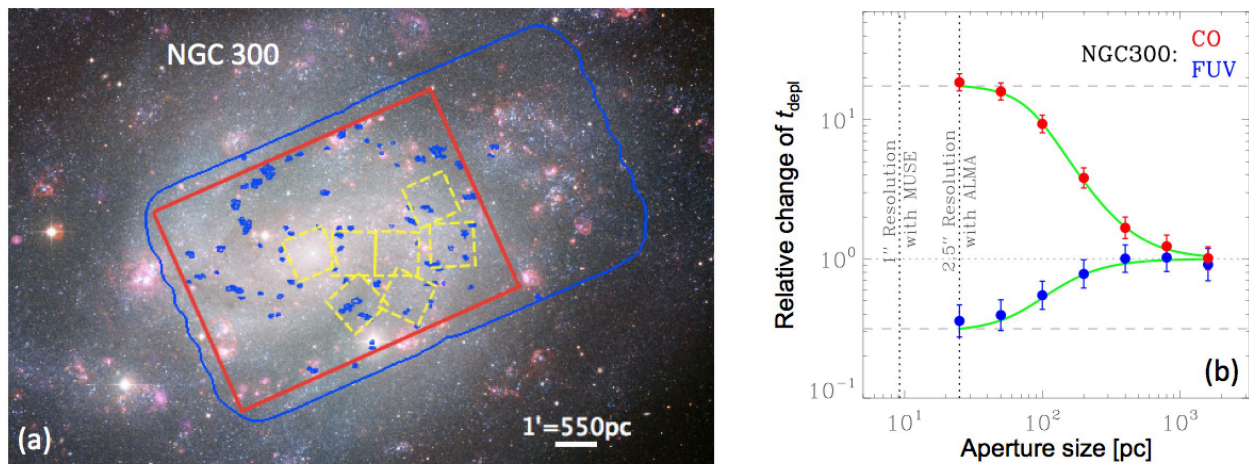


Figure 6.12: Planned observations (panel a): NGC 300 with the proposed MUSE field (red), our ALMA field (blue) with the location of the detected molecular clouds (blue contours), and the 7 MUSE pointings observed in program 094.D-0116 (dashed yellow squares). KL14 analysis (panel b): Relative change of the gas depletion time ($t_{\text{depl}} = M_{\text{gas}}/SFR$) as a function of aperture size when focusing on gas peaks (top branch) or stellar peaks (bottom branch). Red and blue points with error bars show our ALMA Cycle 2/3 CO (1-0) and far-UV (young stars) observations of NGC 300. Green curves show the best-fitting model of KL14.

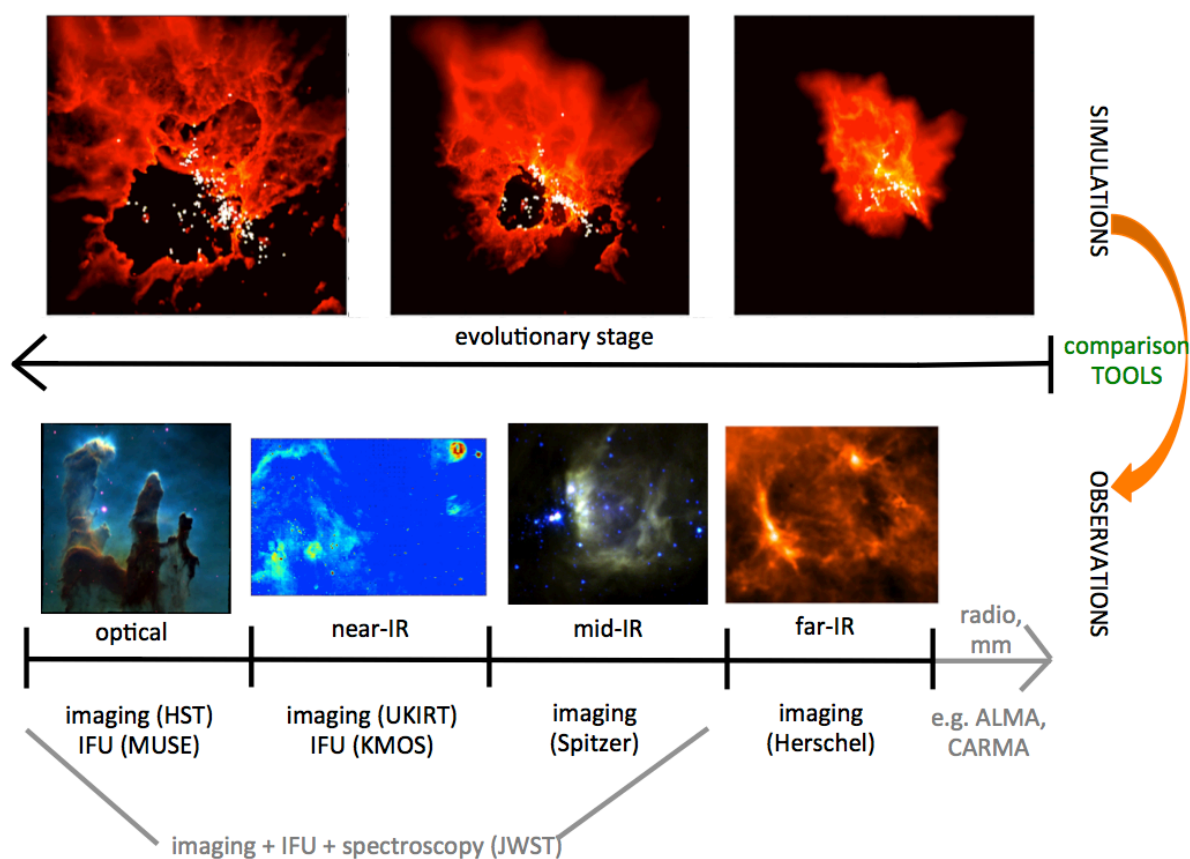


Figure 6.13: A schematic view of the outlook: (i) the time evolution of star forming molecular clouds under the influence of radiative and mechanical feedback is analysed to extract observable parameters (SIMULATIONS); (ii) statistical tools to compare these to observations are developed (TOOLS); (iii) to fully sample the age/mass/size/structure range of the simulations, observations from the optical to the radio regime are used (OBSERVATIONS). Observations already at hand (archival or still under proprietary time) are marked in black, planned data (proposals submitted/to be submitted) as well obtainable through collaborators are marked in grey. The three upper panels correspond to column density maps of three different time steps of a simulated molecular cloud including radiative feedback (courtesy of J. Dale). The images in the lower panels are (from left to right): the Pillars of Creation as imaged by MUSE (McLeod et al., 2015); KMOS Brackett γ image of W49 main ([9]); Spitzer 3 colour image of BYF 73 (courtesy of P. Barnes); column density map of IRAS17220-3609 obtained from Herschel HiGAL data (McLeod et al., in prep.).

The computational base of this project is given by the Smoothed Particle Hydrodynamics (SPH) simulations presented and described in Dale et al. (2012b) (see also Dale et al. 2013b, Dale et al. 2013), which simulate the evolution of star-forming molecular clouds under the influence of ionisation and stellar winds, soon to be augmented to comprise magnetic fields and supernovae. From these simulations, we already extracted physical parameters (e.g. kinematics of the ionised and cold gas components, expansion velocities of bubbles, gas densities and temperatures, etc.) for entire clouds as well as selected regions (pillars, ionisation fronts, expanding HII bubbles), and demonstrated a first qualitative comparison with observations (McLeod et al. 2015 and soon quantitatively in McLeod et al., in prep.). The library of GMCs from Dale et al. will be expanded with more simulations that include other types of feedback (such as outflows and supernovae) and cover larger (galactic) scales, for example by exploiting the publicly available SILCC (Simulating the Life-Cycle of molecular Clouds) data sets (Walch et al., 2015).

The link between the simulations and the observations is given by statistical tools specifically designed for this purpose. These include:

- (i) **Dendrograms**, a hierarchical tree-representation of structures which is applied to column density and temperature maps of specific structures. As a star-forming molecular cloud evolves under the feedback of the stars forming within it, the complexity of the dendrogram increases. The complexity (number of independent branches) is therefore a good indicator of the evolutionary stage, and a preliminary comparison with observations shows very satisfying results.
- (ii) **Correlation functions**. A simple approach to star formation dictates that stars form in high-density gas clumps, which can be identified and isolated with dendrograms. The spatial correlation between signs of star formation and dense clumps will be tested in both simulations and observations.
- (iii) **Radial profiles**. A further indicator of the evolutionary stage of star forming molecular clouds is the shape of the radial density and mass profiles, which from the simulations show shallower slopes with increasing age. A model to describe this behaviour will be developed and tested on the observations.
- (iv) **Velocity probability distribution functions (vPDFs)**. The simulations show a clear dependence of the width and symmetry of their vPDFs on both the included feedback mechanism and their virial parameter α . We will test this with the kinematics extracted from the observations.

For this, the output of the simulations needs to be brought as close as possible to the observations. This can be achieved by e.g. post-processing the simulated clouds with radiation transfer codes to obtain maps of the relevant emission lines also obtained from the observations (as was done in McLeod et al. 2015, see Chapter 3) or by producing synthetic observations (e.g. synthetic *Herschel* maps as in Koepferl et al. 2016) and subsequently applying the same analysis techniques on both simulations and observations.

7

Summary and conclusions

The work presented in this thesis is concerned with the effect of the feedback from massive stars on their environment. Specifically, massive star formation feedback was analysed from an observational perspective, by exploiting data from integral field spectrographs. These instruments produce spatially and spectrally resolved data cubes, in which for every pixel of the field of view there is a spectrum across the wavelength range covered by the instrument. The integral field spectrograph exploited here is the Multi Unit Spectrographic Explorer MUSE mounted on the Very Large Telescope in Chile, which operates in the optical regime, covering a wavelength range from about 4800 Å to about 9300 Å with a field of view of 1×1 arcminutes. The unique large spectral and spatial coverage of MUSE is ideal to analyse feedback in HII regions inflated by massive stars, as it covers all the nebular emission lines necessary to derive the main physical quantities (such as electron densities and temperatures, as well as ionic and elemental abundances), and it also delivers the kinematics of the feedback-affected matter. Furthermore, it can be also used to identify and classify the feedback-driving massive stars with the same data set.

In this thesis, the effect of ionising feedback was analysed in a 3-step project, with the main driving question being: is it possible, with unprecedented spatial and spectral coverage of integral field spectroscopy, to quantify the effects of ionising feedback and therefore deliver an observational quantification of high-mass stellar feedback? A first observational set up was used to image ionised pillar-like structures in M 16, to test the applicability of MUSE in analysing ionising feedback and to develop the analysis methods and techniques needed for the project. These were then tested with one of the best-studied HII regions in the Milky Way, the central Orion Nebula. Finally, the observational setup and analysis methods and techniques were then applied to derive an observational quantification of ionising feedback from massive stars and star clusters with observations of a sample of ionised pillar-like structures in the Carina Nebula Complex.

In the first part of the analysis, MUSE was used to image the Pillars of Creation in the Eagle Nebula (M 16) with a 9-pointing mosaic, an exposure time of 90 seconds per pointing, and a 90° rotation dither pattern. With this observational setup, it was possible to analyse the spatial distribution of the pillars along the line of sight as well as their orientation with respect to the observer. The MUSE data also allowed to identify a previously unknown outflow at the tip of

the middle pillar originating from a young star forming in the pillar material, through a novel analysis technique which exploits the so-called S_{23} parameter tracing the excited matter as the outflow emerges from the pillar material, together with a velocity map tracing the kinematics of the outflow. Furthermore, the mass-loss rate of the pillars due to ionisation-induced photo-evaporation was computed, and, together with the total mass of the pillars, a lifetime of 3 Myr was estimated for these objects.

The analysis methods developed for the M 16 pillars was then applied to study analyse the structures the Orion Nebula, one of the best-studied HII regions in the Galaxy. Specifically, the S_{23} parameter was used, in combination with $[\text{OII}]/[\text{OIII}]$ as an indicator for the degree of ionisation, to distinguish between different populations of the outflows and protoplanetary disks (short 'proplyds') present in the region. It is concluded that the proplyds found closer to the ionising massive stars of the central Trapezium star cluster are clearly distinguishable from those that are further away, as they show lower S_{23} values and higher degrees of ionisation. Together with the fact that the outflows and proplyds further away from the ionising sources can be further divided into four classes, depending on their S_{23} vs $[\text{OII}]/[\text{OIII}]$ values, it is argued that the S_{23} parameter traces the relative contribution of shocks and ionising feedback to the excitation of sulphur. Future analyses of the S_{23} parameter are needed to fully disentangle the contribution of the two feedback mechanisms.

The observational setup and analysis techniques developed and tested for the previous two studies were then applied to a sample of ionised pillars in the Carina Nebula Complex, one of the most massive and active star-forming regions of the Milky Way, which hosts several different massive star clusters. For these pillars, the S_{23} parameter analysis did not yield the detection of jets from young stars at the tip of the pillars, however two of these could nonetheless be identified. It is concluded that the S_{23} parameter traces jets from stars that are still deeply embedded in the pillar and that are only just emerging from (and therefore exciting) the pillar material, while the two jets detected in the Carina pillars seem to be more evolved as they are detected as ionised jets and extend well beyond the pillar surfaces. More importantly though, this data set was combined with the M 16 data and MUSE observations of a pillar in the massive star-forming region NGC 3603 to derive a correlation between the ionising photon flux from the feedback-driving nearby massive stars and the mass-loss rate due to photo evaporation of the pillar tips. It is found that pillars exposed to higher photon fluxes display higher mass-loss rates.

The analysis of this thesis therefore led to the answer to the main question it was aimed at: indeed, integral field spectroscopy, because of its capability of simultaneously delivering spatially and spectrally resolved morphological and kinematical information, is ideal to analyse the effect of ionising feedback in high-mass star-forming regions. As will be demonstrated with already ongoing further analyses, integral field spectroscopic data can also be used to identify and classify the massive stars with the same data set, therefore delivering the perfect observational tool to connect the feedback-driving stars to the feedback-affected gas.

Future projects, planned and already ongoing, are aimed at (1) extending these methods to longer wavelengths (e.g. with the near-infrared integral field spectrograph KMOS) to sample earlier evolutionary stages as well as other feedback mechanisms, and therefore analyse feedback throughout the evolution of massive stars and their feedback-driven environments; (2) extending

the methods to nearby resolved and unresolved HII regions to understand how the different feedback mechanisms depend on the galactic environment, which mechanisms are dominant on which scales, and how they affect star formation on large (galactic) scales; (3) compare the parameters obtained from the observations with their analogues extracted from simulations of feedback-driven star-forming molecular clouds to better constrain the physics of the simulations and better interpret the observations.

A

Appendix A

Here we show the extinction corrected integrated line maps of the detected emission lines (Fig. A.1 to Fig. A.8a, linearly scaled to minimum/maximum, the flux is in units of 10^{-20} erg s⁻¹ cm⁻² pixel⁻¹), the S_{23} parameter as well as a disk-like structure in one of our simulated pillars (Fig. A.9) and a zoom-in of the velocity map onto the tip of P1 where the candidate outflow is located (Fig. A.10).

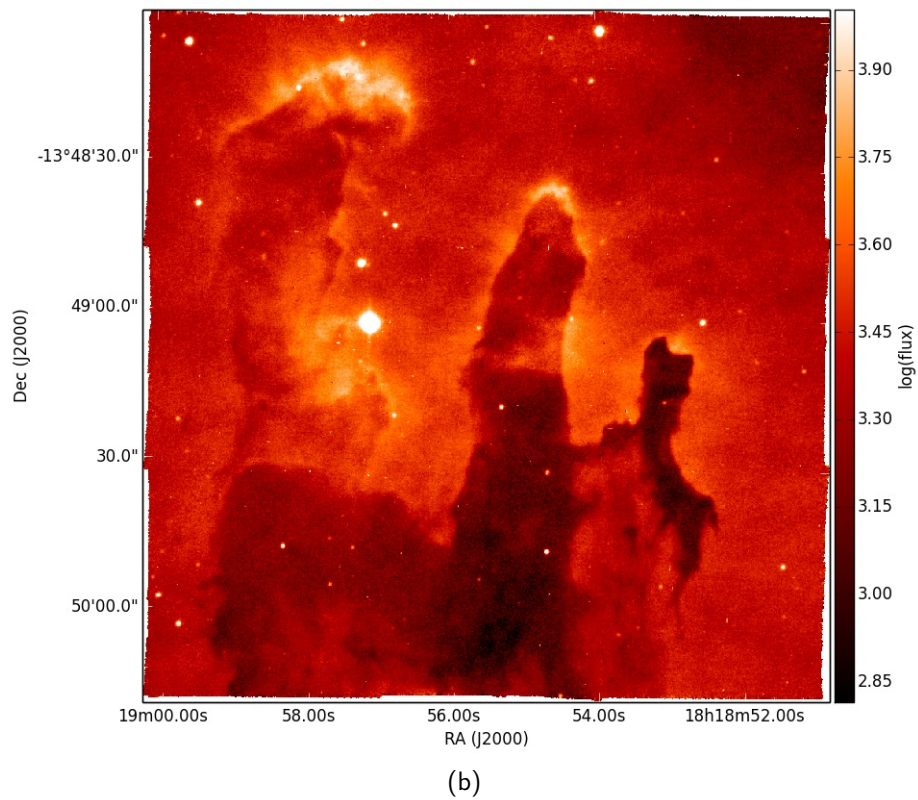
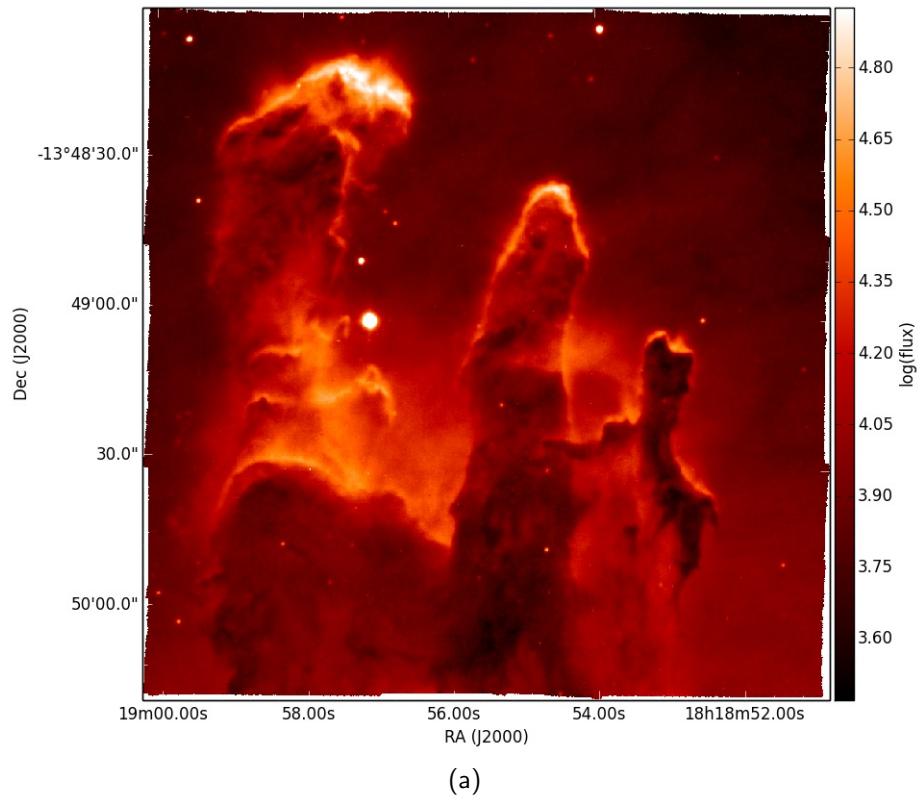


Figure A.1: Extinction corrected integrated line maps of [NII] $\lambda 6584$, [SIII] $\lambda 9068$.

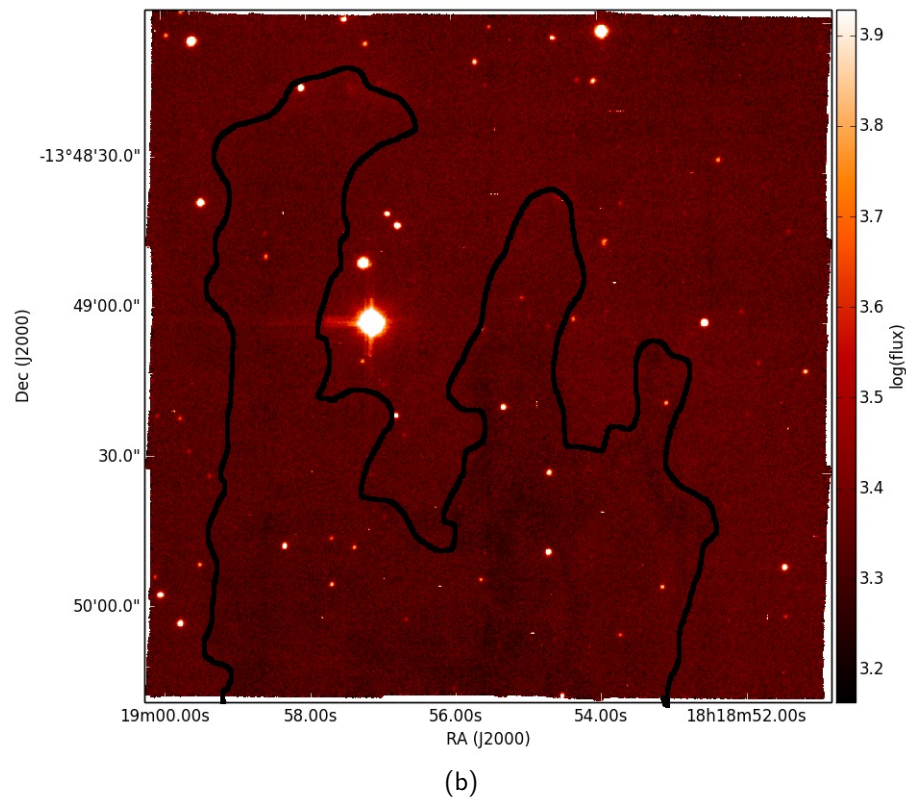
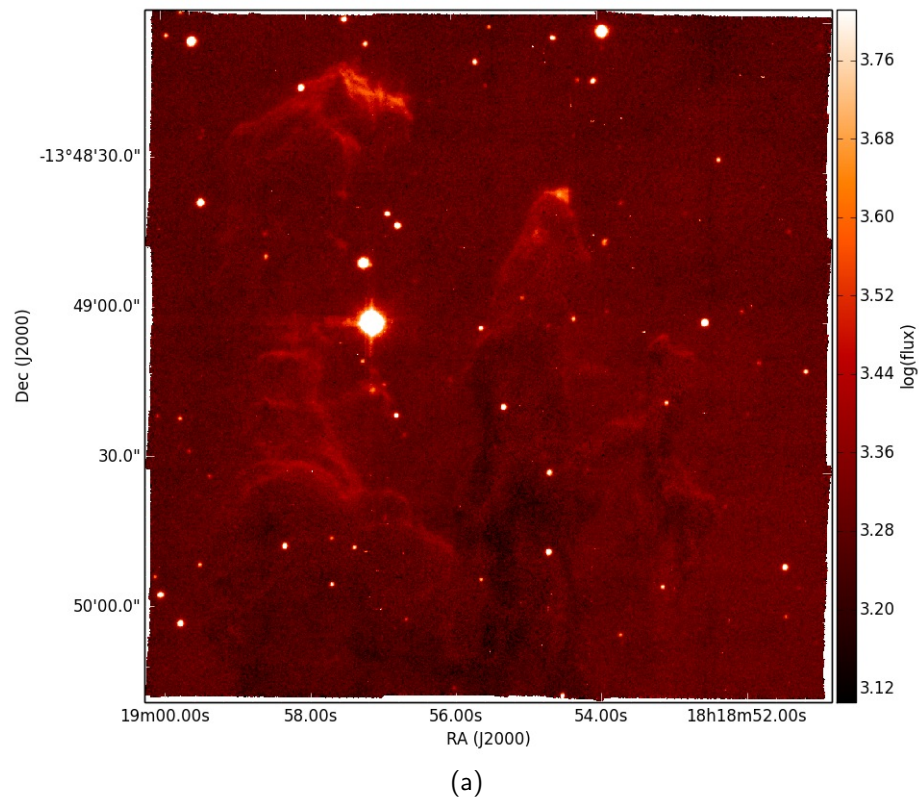


Figure A.2: Extinction corrected integrated line maps of $[\text{O I}]\lambda 6300$, $[\text{O I}]\lambda 5577$. To help the reader identify the location of the Pillars has been marked with a schematic black contour.

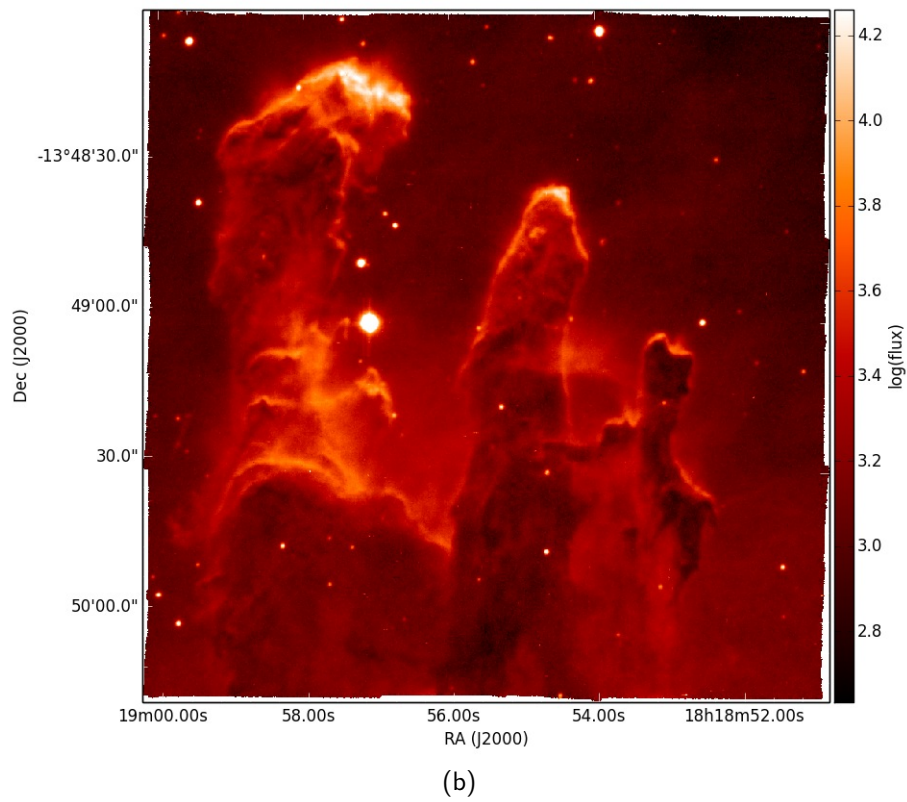
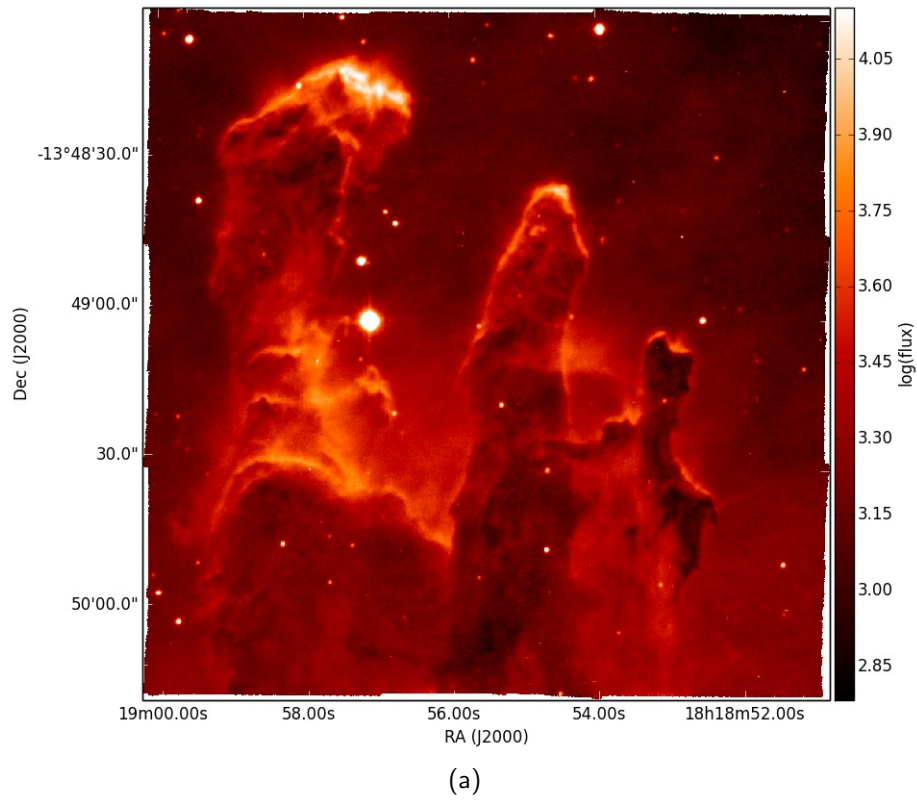


Figure A.3: Extinction corrected integrated line maps of [SII]λ6717, [SII]λ6731.

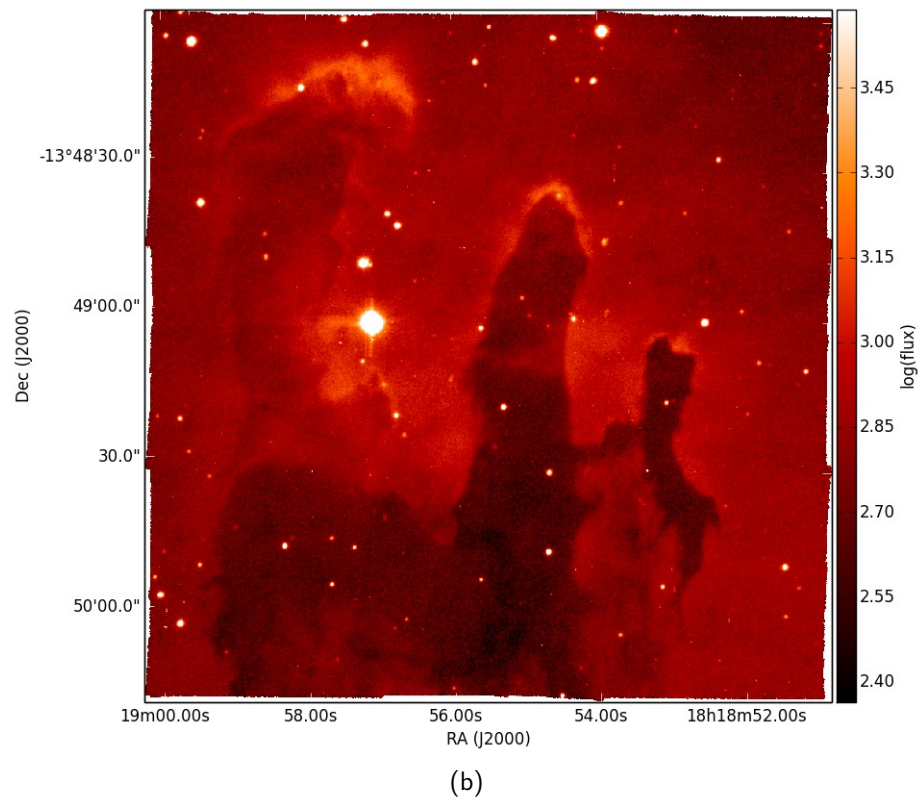
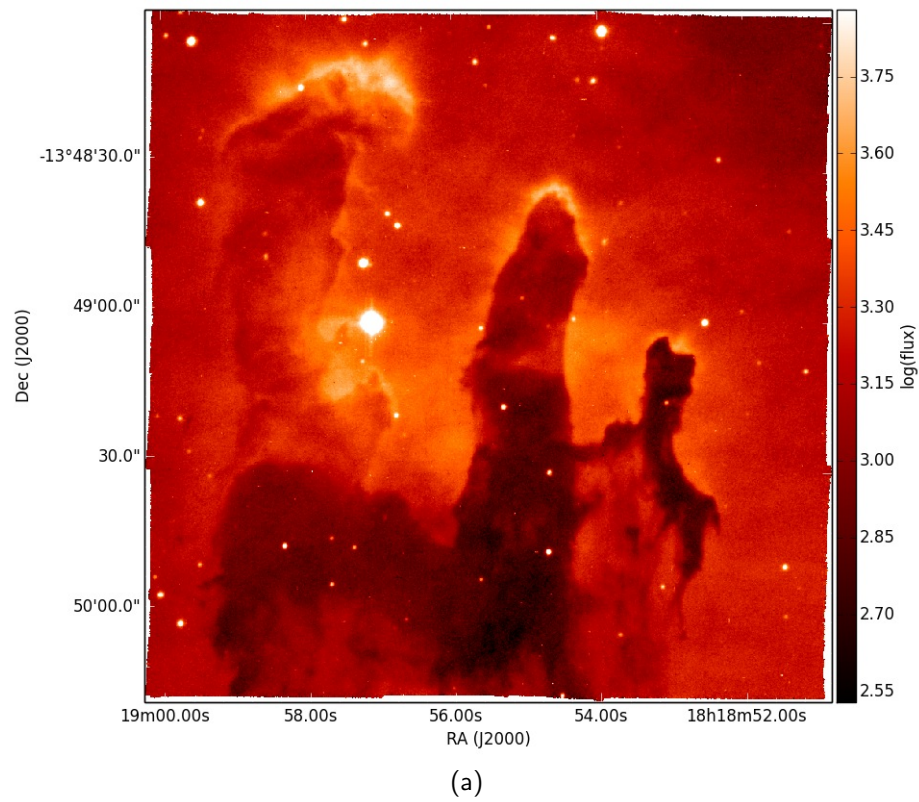


Figure A.4: Extinction corrected integrated line maps of [ArIII]λ7135, [ArIII]λ7751.

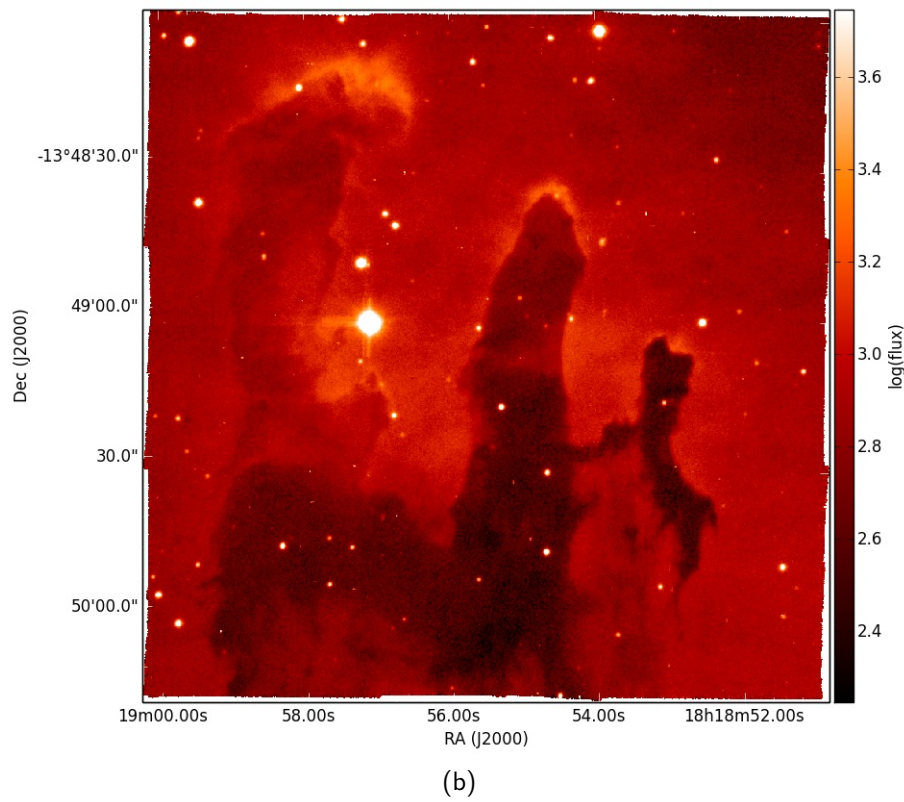
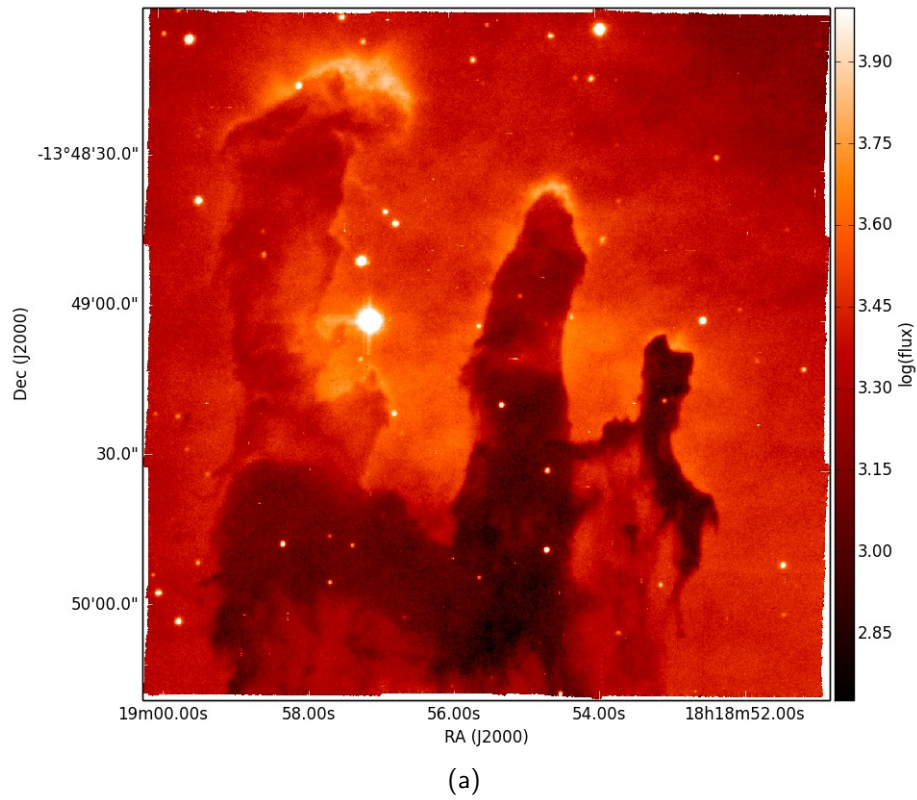
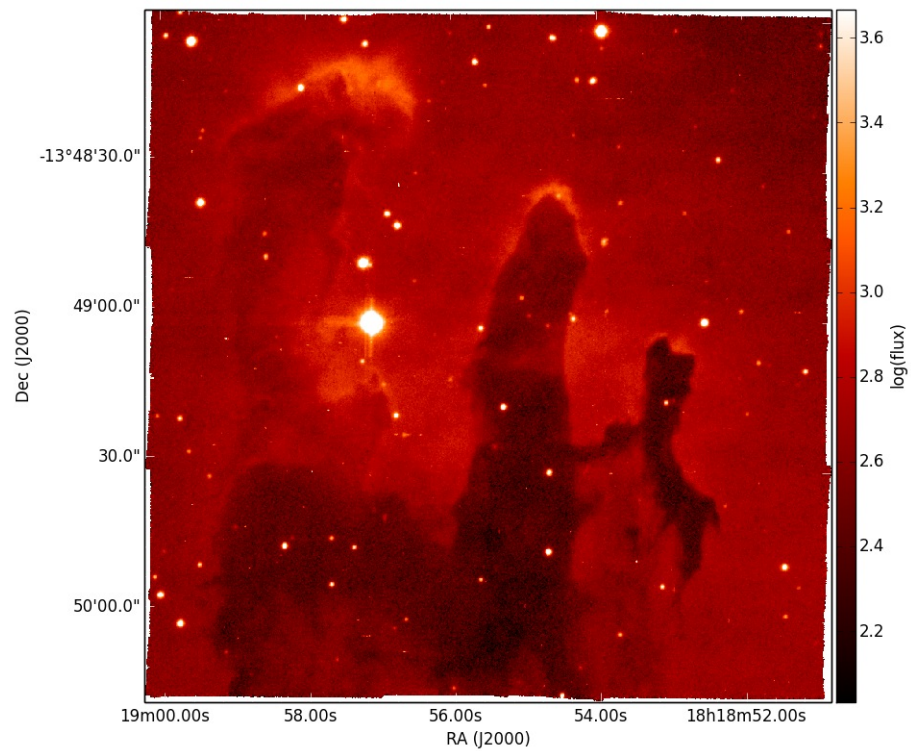
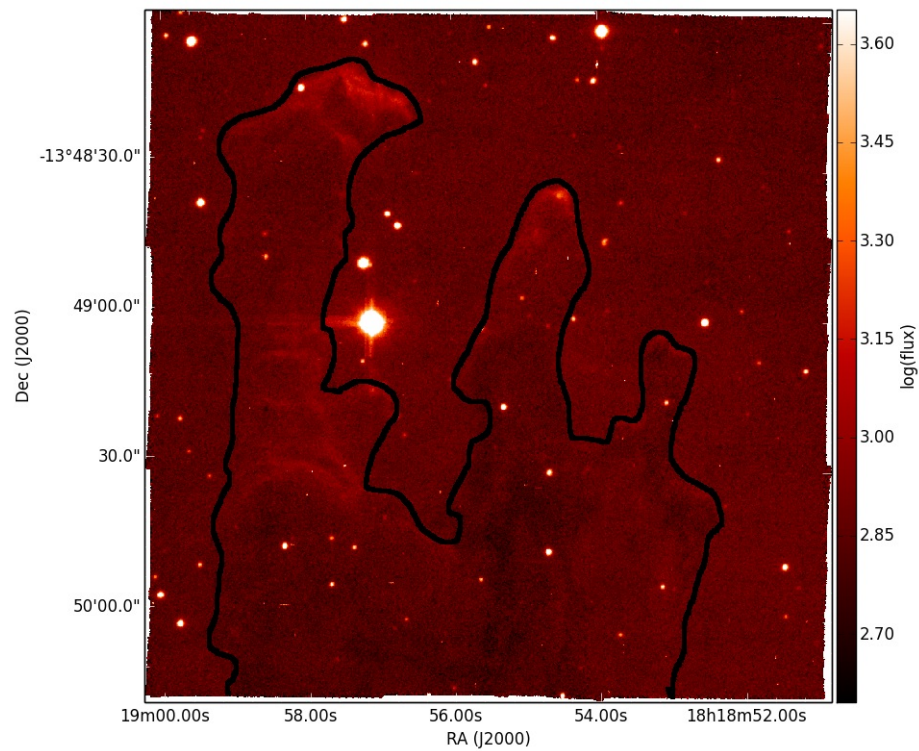


Figure A.5: Extinction corrected integrated line maps of [He I] $\lambda 5876$, [He I] $\lambda 6678$.

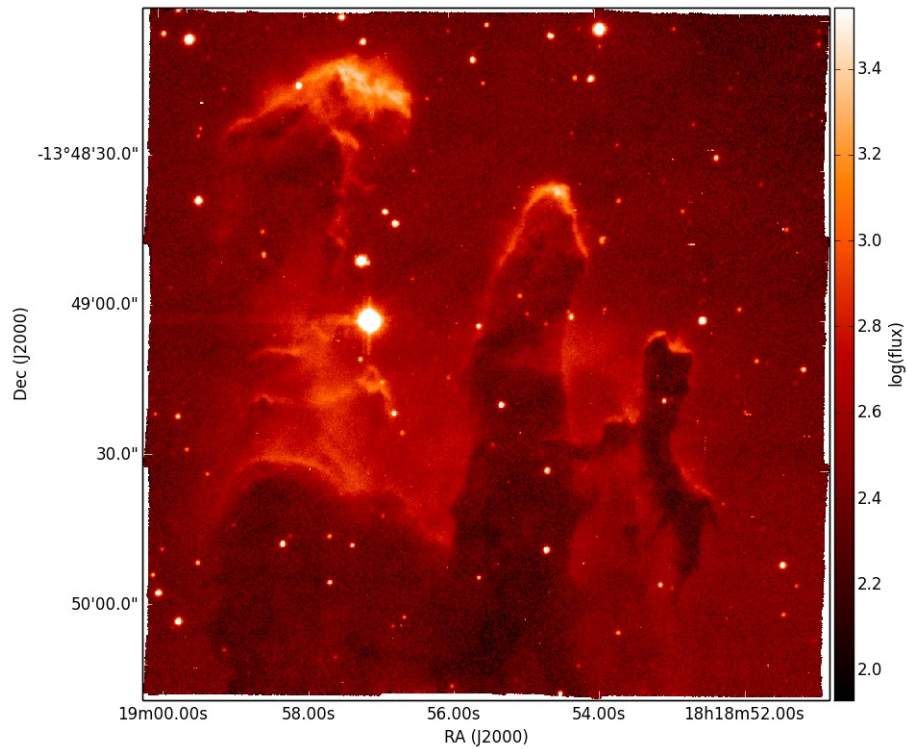


(a)

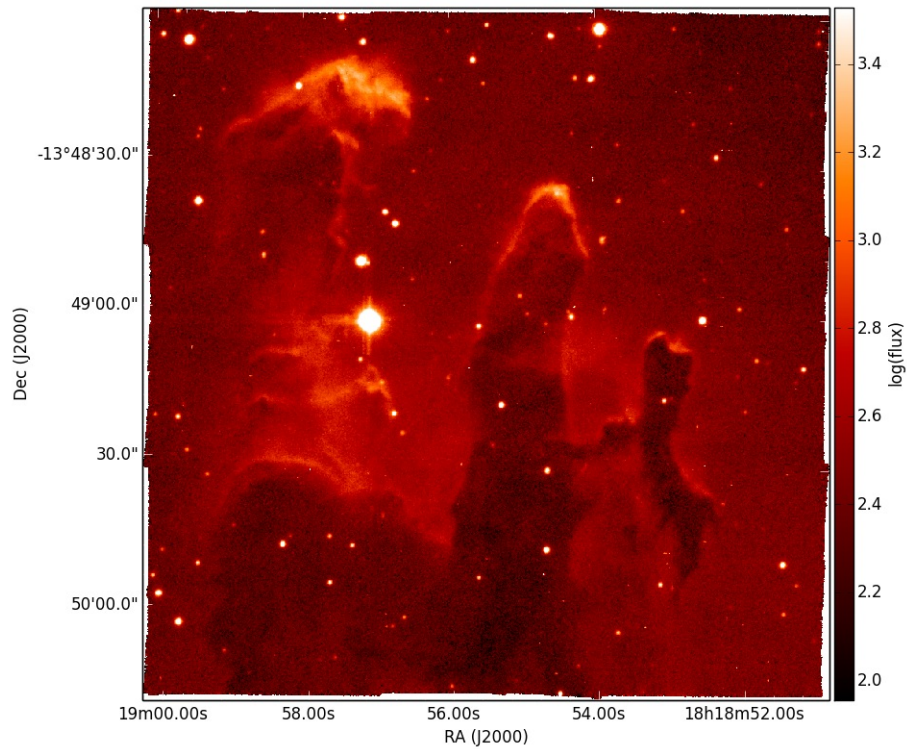


(b)

Figure A.6: Extinction corrected integrated line maps of [HeI] $\lambda 7065$, [O I] $\lambda 6363$. To help the reader identify the location of the Pillars has been marked with a schematic black contour.

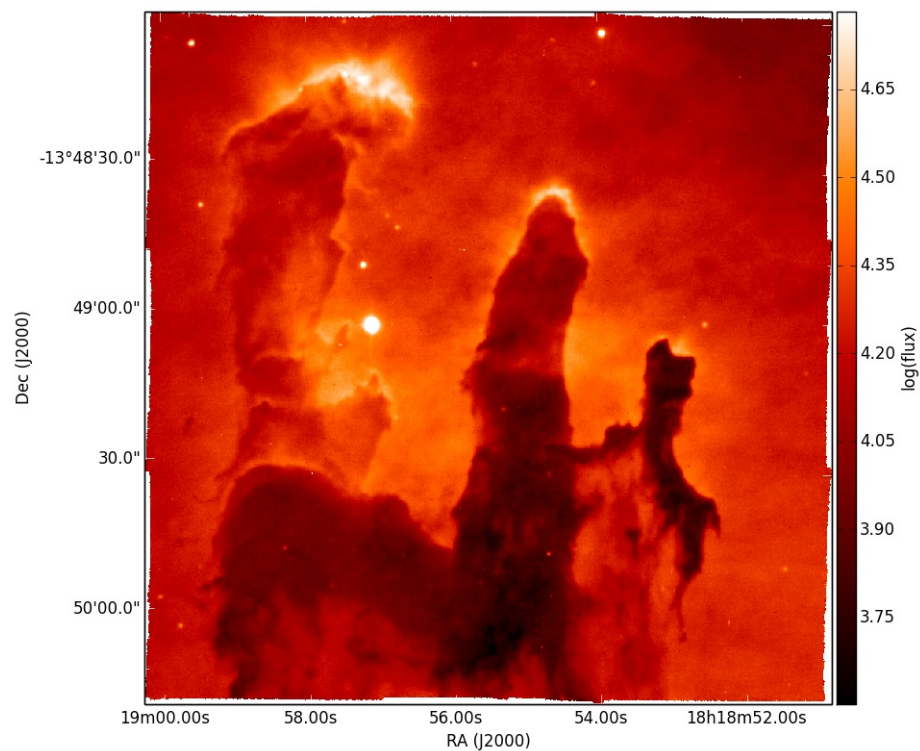


(a)

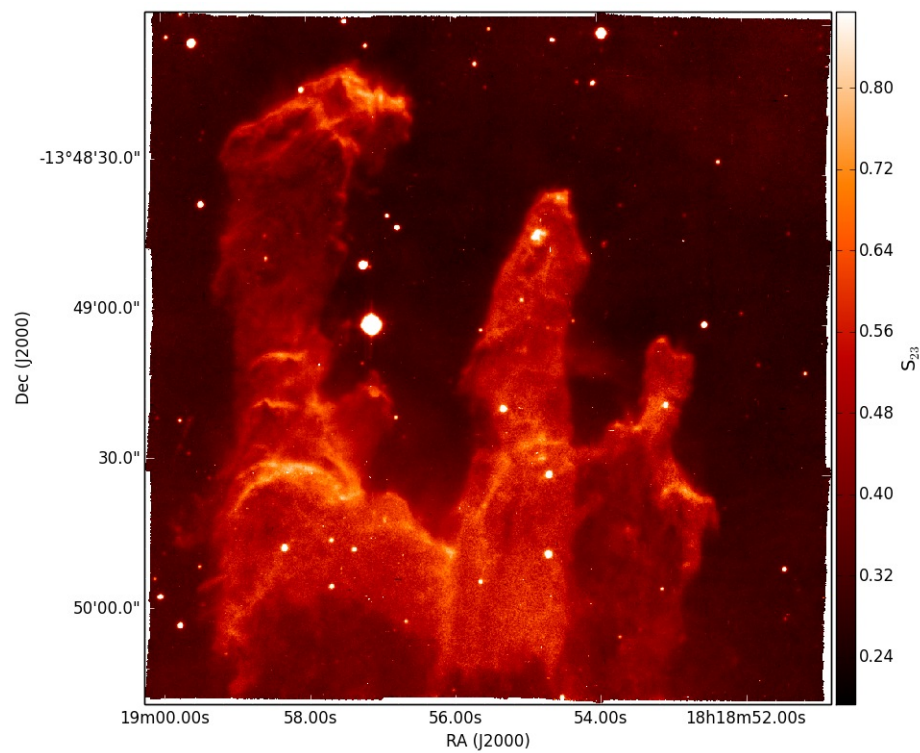


(b)

Figure A.7: Extinction corrected integrated line maps of [OII]λ7320, [OII]λ7330.



(a)



(b)

Figure A.8: H β , S_{23} parameter (see text for explanation).

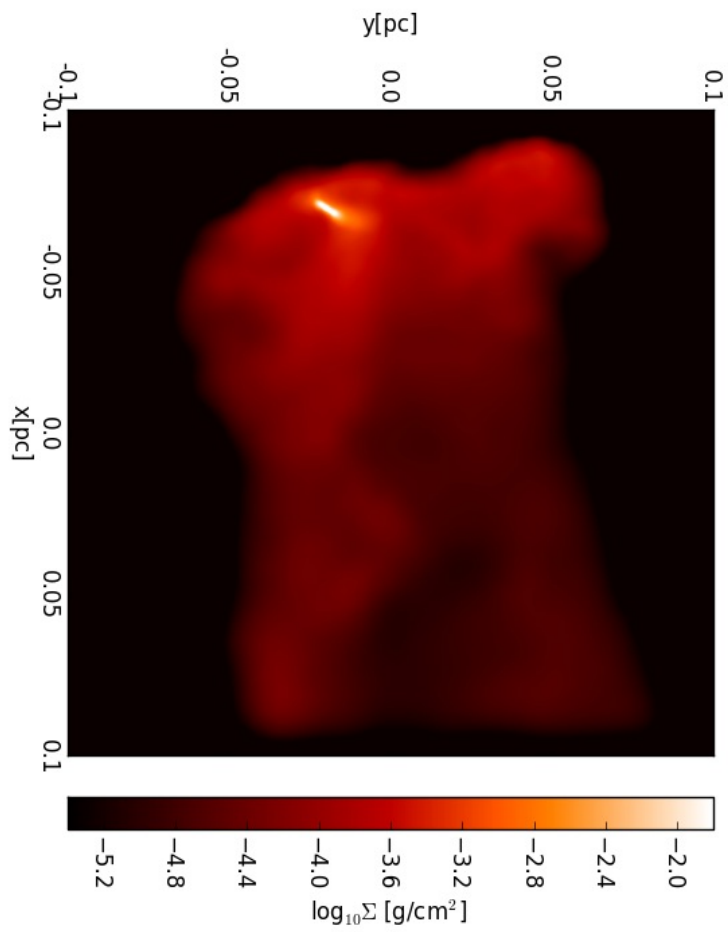


Figure A.9: Zoom-in onto one of the simulated pillars: a disk-like structure is seen tracing a forming stellar object at the tip of the pillar (see text Section 4.1).

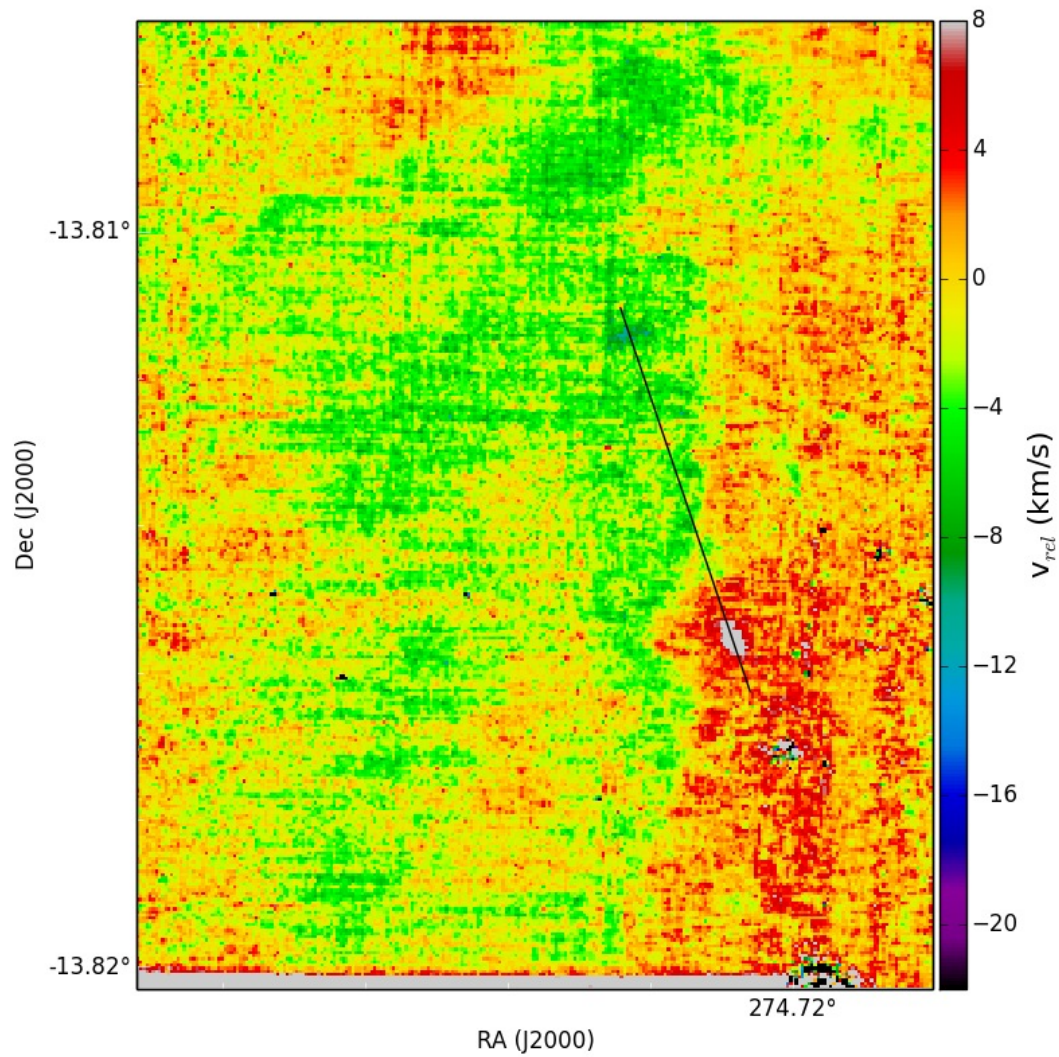


Figure A.10: Zoom-in of the velocity map shown in Fig. 16a onto P2. The black line shows the orientation of the outflow candidate discussed in Section 4.1.

B

Appendix B

Fig. B.1 shows the velocity maps masked according to the $[\text{OI}]\lambda 6300$ intensity threshold of $\sim 10^{-16} \text{ erg s}^{-1} \text{ cm}^{-2} \text{ pixel}^{-1}$ used to compute the second order structure function S_2 . The effect of adding Gaussian noise to the synthetic velocity maps (Fig. B.2 and B.3) of a simulated HII region (Fig. B.6) is shown in Fig. B.4 and B.5, where the structure functions for different values of the standard deviation σ are shown. See text Chapter 4.

Figure B.7 shows the equivalent of Fig. 4.18b, but for $[\text{SII}]/\text{H}\beta$ (see text Section 4.5.2). Figures from B.8 to B.11 show the S_{23} maps (left panels) and their corresponding location in the S_{23} vs. $[\text{OII}]/[\text{OIII}]$ parameter space of the Orion proplyds listed in Table 4.5 and discussed in Section 4.5.2. Figures from B.8 to B.11 are intentionally not continuum-subtracted (a version of continuum-subtracted S_{23} vs $[\text{OII}]/[\text{OIII}]$ parameter space is shown in Fig. 4.18) to highlight the stellar components of the proplyds (244-440, 242-519, 247-436).

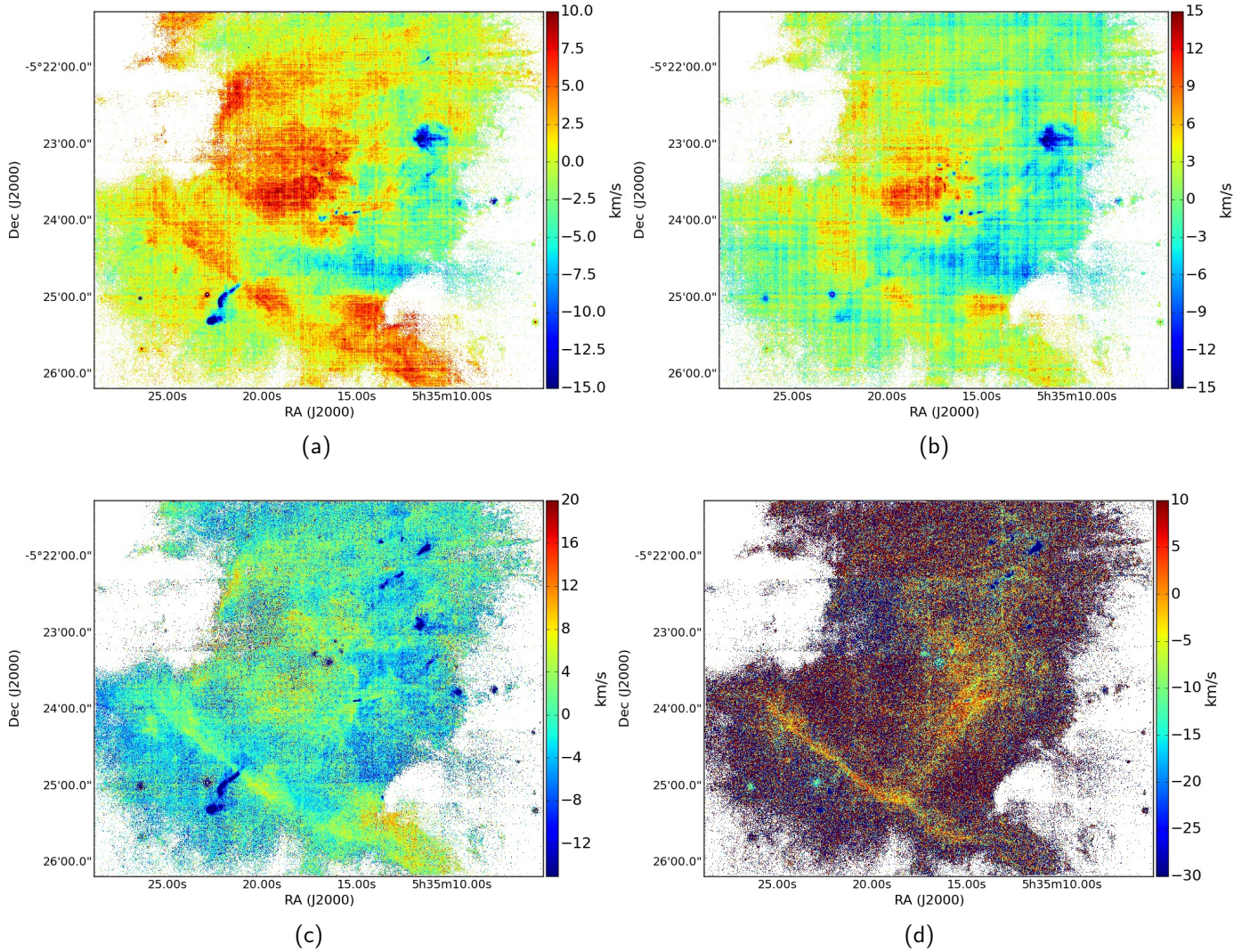


Figure B.1: Velocity maps of $H\alpha$ (a), $[OIII]\lambda 5007$ (b) and $[SII]\lambda 6731$ (c) and $[OI]\lambda 6300$ (d) masked based on the mean value of the $[OI]$ line. The indicated velocities correspond to velocities relative to the mean velocity of the surrounding medium (see text Section 4.4).

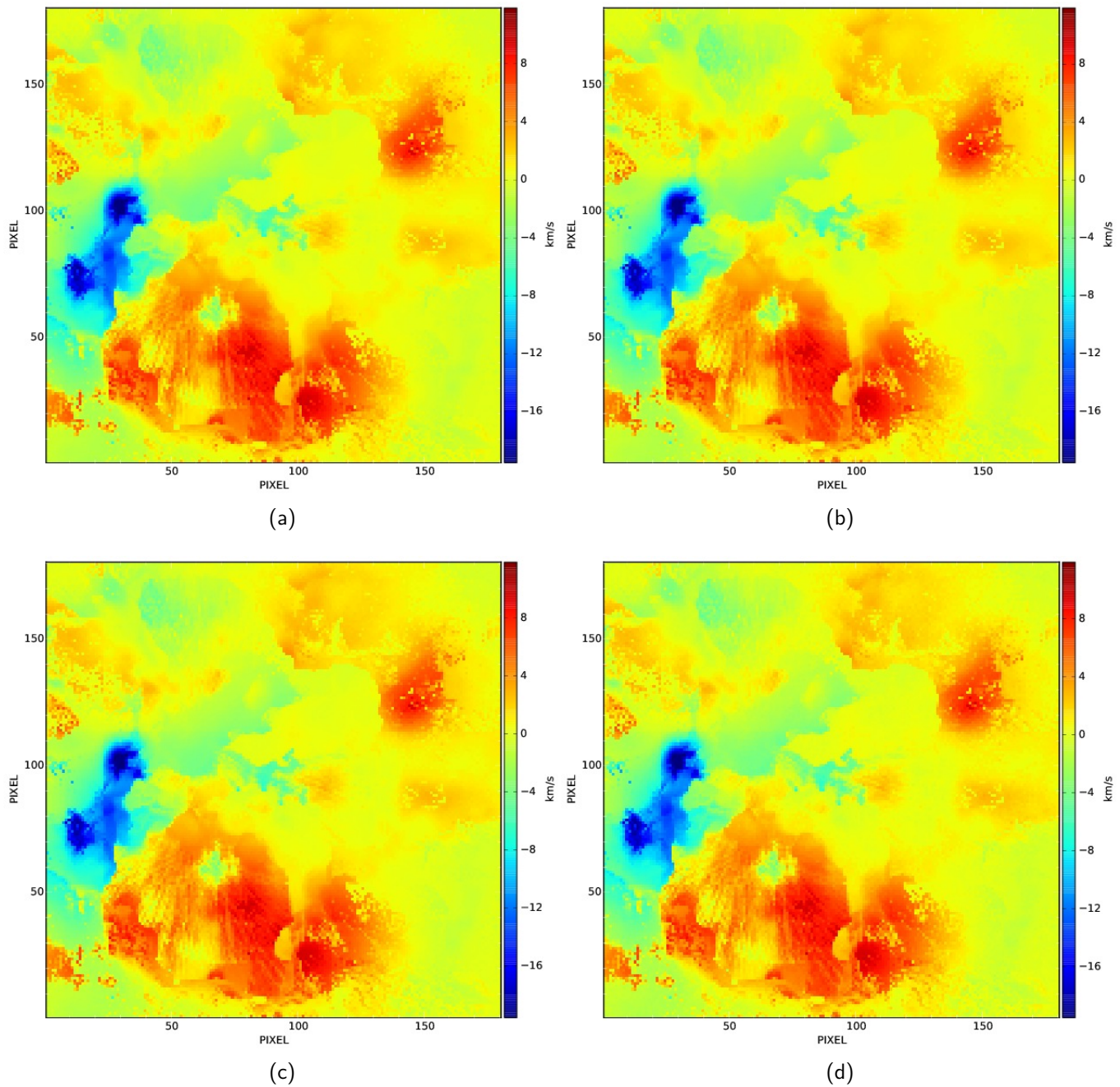


Figure B.2: [SII] velocity map of our simulated HII region (panel a), post-processed with the ionisation radiative transfer code MOCASSIN. The pixel scale is 0.028 pc. To this we gradually add Gaussian noise by increasing the standard deviation σ from 0.01 km/s (panel b) to 10 (panel d in Fig. B.3).

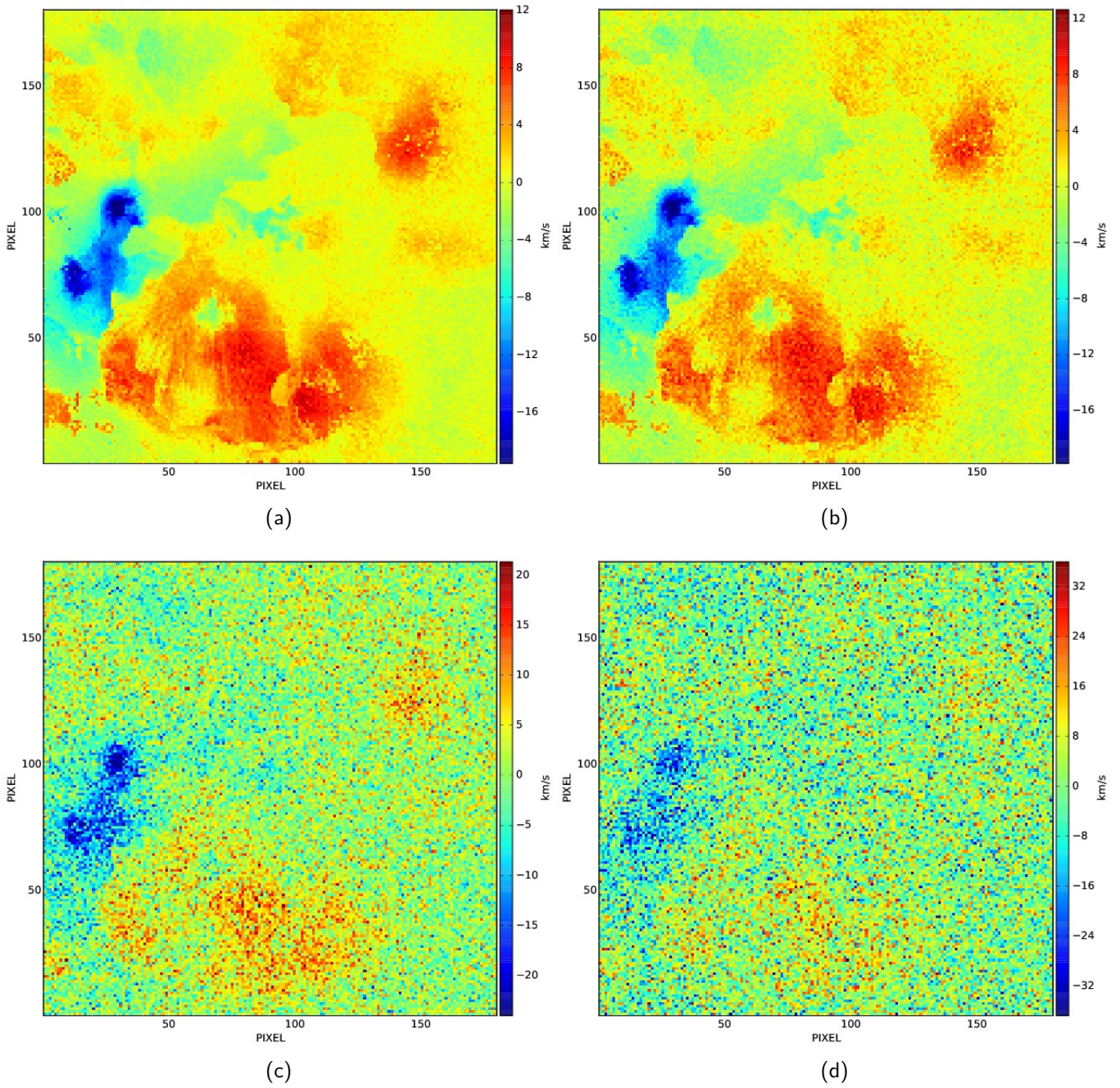


Figure B.3: See Fig. B.2.

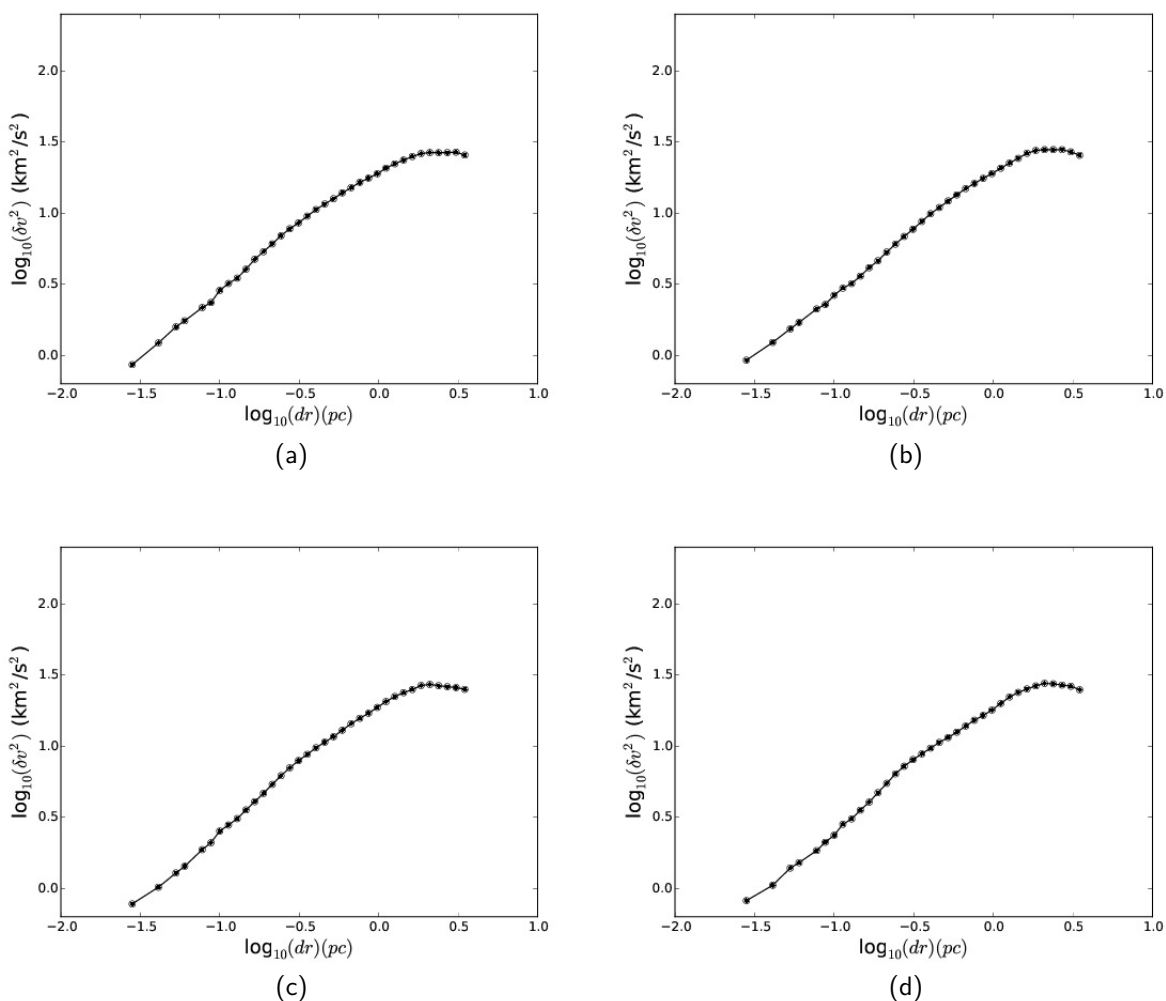


Figure B.4: Structure function corresponding to the [SII] velocity map of our simulated HII region (panel a). To this we gradually add Gaussian noise by increasing the standard deviation σ from 0.01 km/s (panel b) to 10 (panel d in Fig. B.5). To show the flattening of the structure function, all plots share the same scaling.

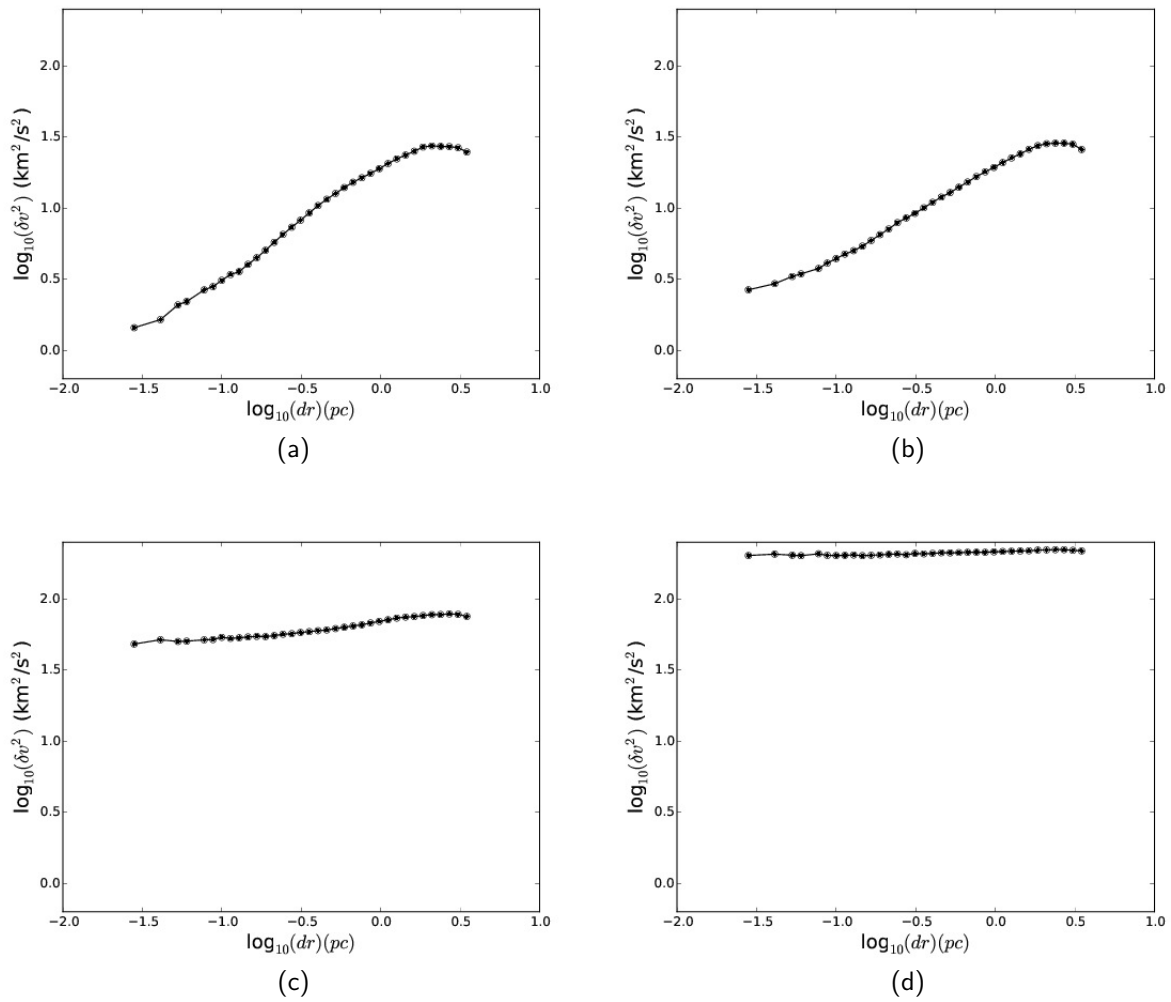


Figure B.5: See Fig. B.4.

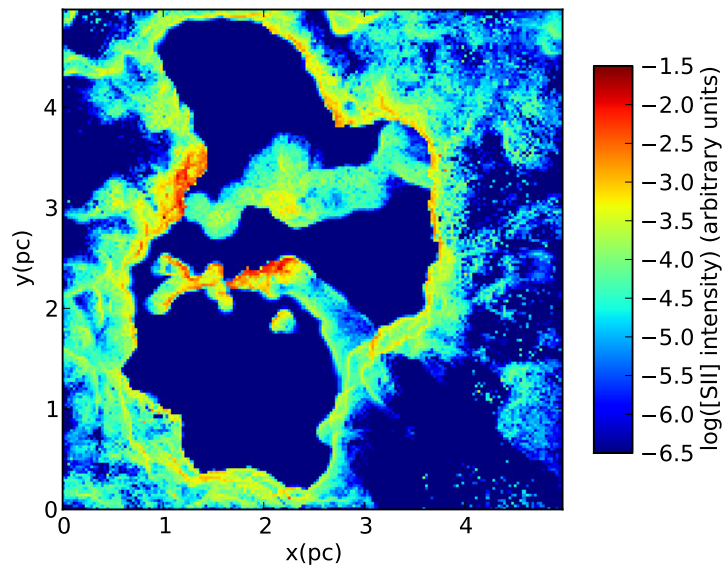


Figure B.6: Integrated [SII] intensity map of the synthetic star forming molecular cloud, post-processed with MOCASSIN. See text Section 4.4.

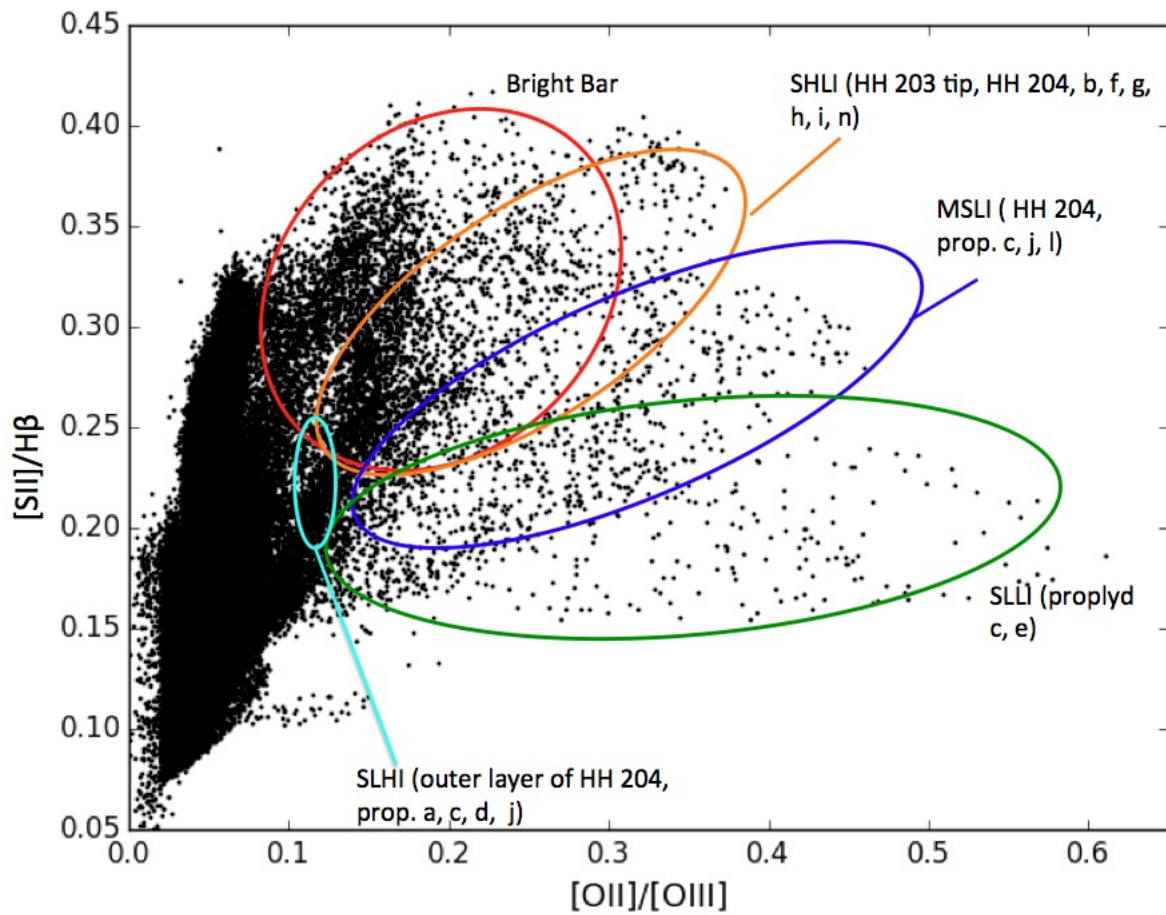


Figure B.7: $[SII]/H\beta$ vs. $[OII]/[OIII]$ scatter plot, with the same regions as indicated in Fig. 4.18b. See text Section 4.5.2.

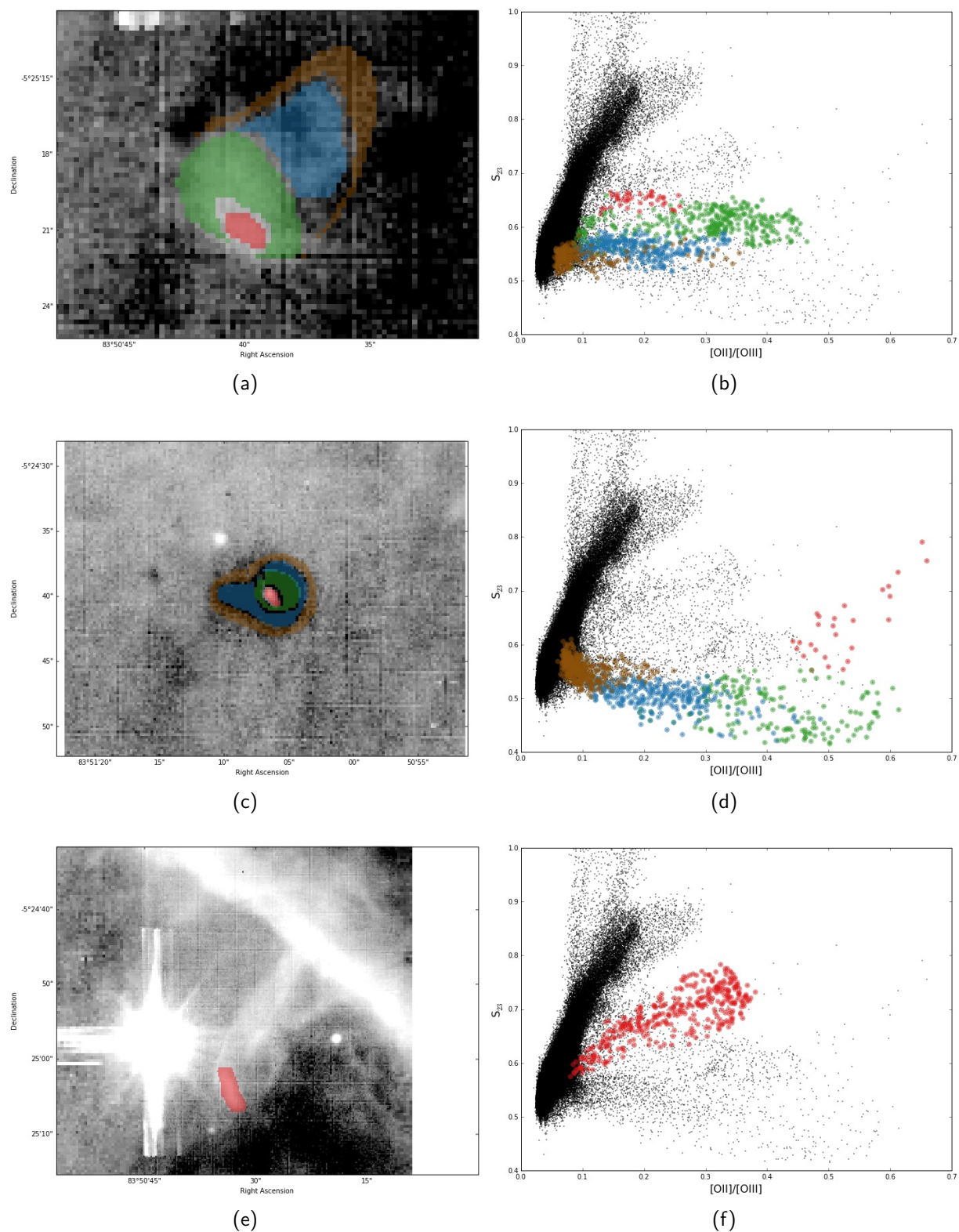


Figure B.8: S_{23} maps (left panels) and S_{23} vs. $[OII]/[OIII]$ scatter plots (right panels) of HH 204 (panels a and b), proplyd 244-440 (panels c and d) and HH 203 (panels e and f). Scales and coordinates are the same as in Fig. 4.18.

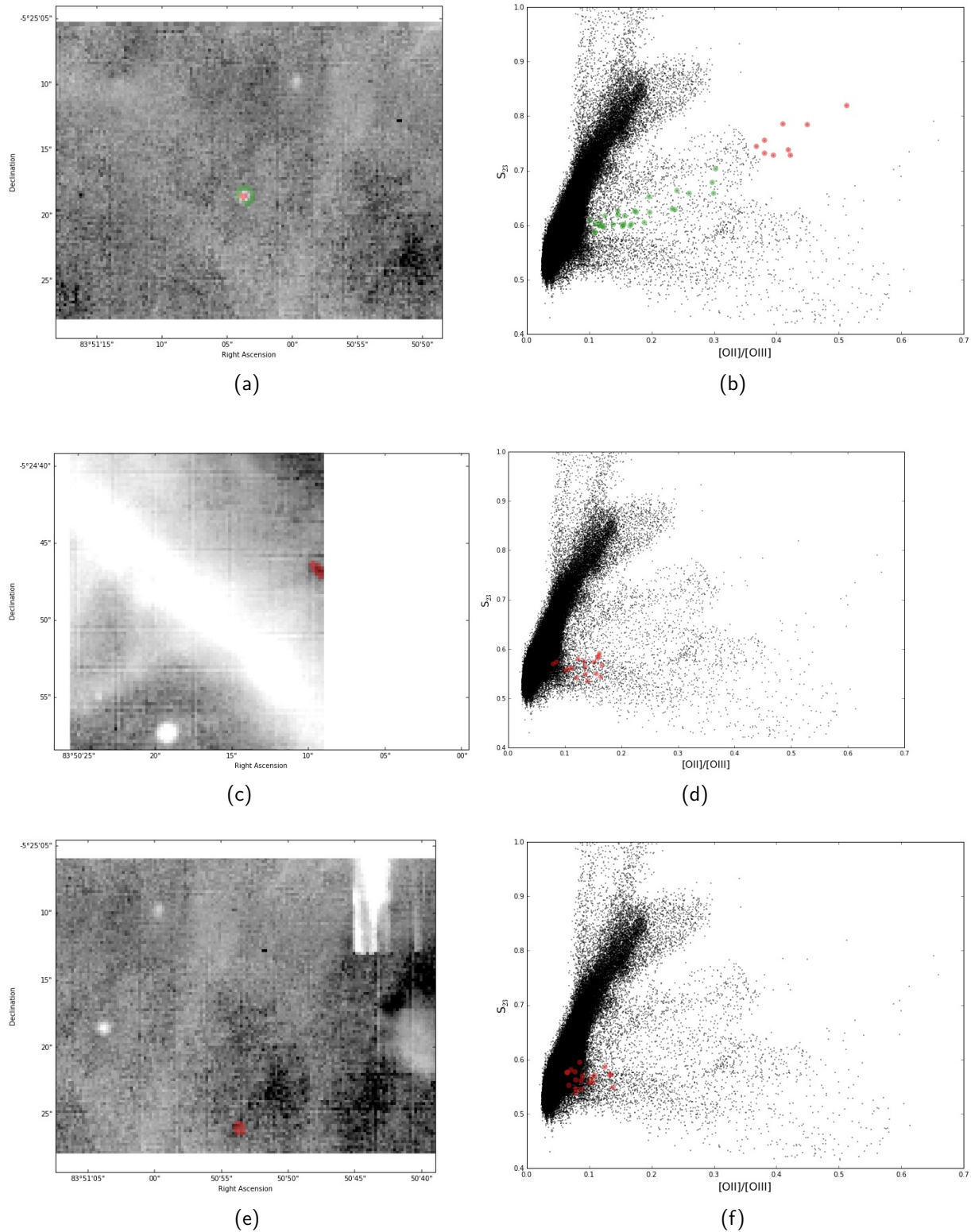


Figure B.9: Same as Fig. B.8, but for proplyds 242-519 (panels a and b), 206-446 (panels c and d) and 236-527 (panels e and f).

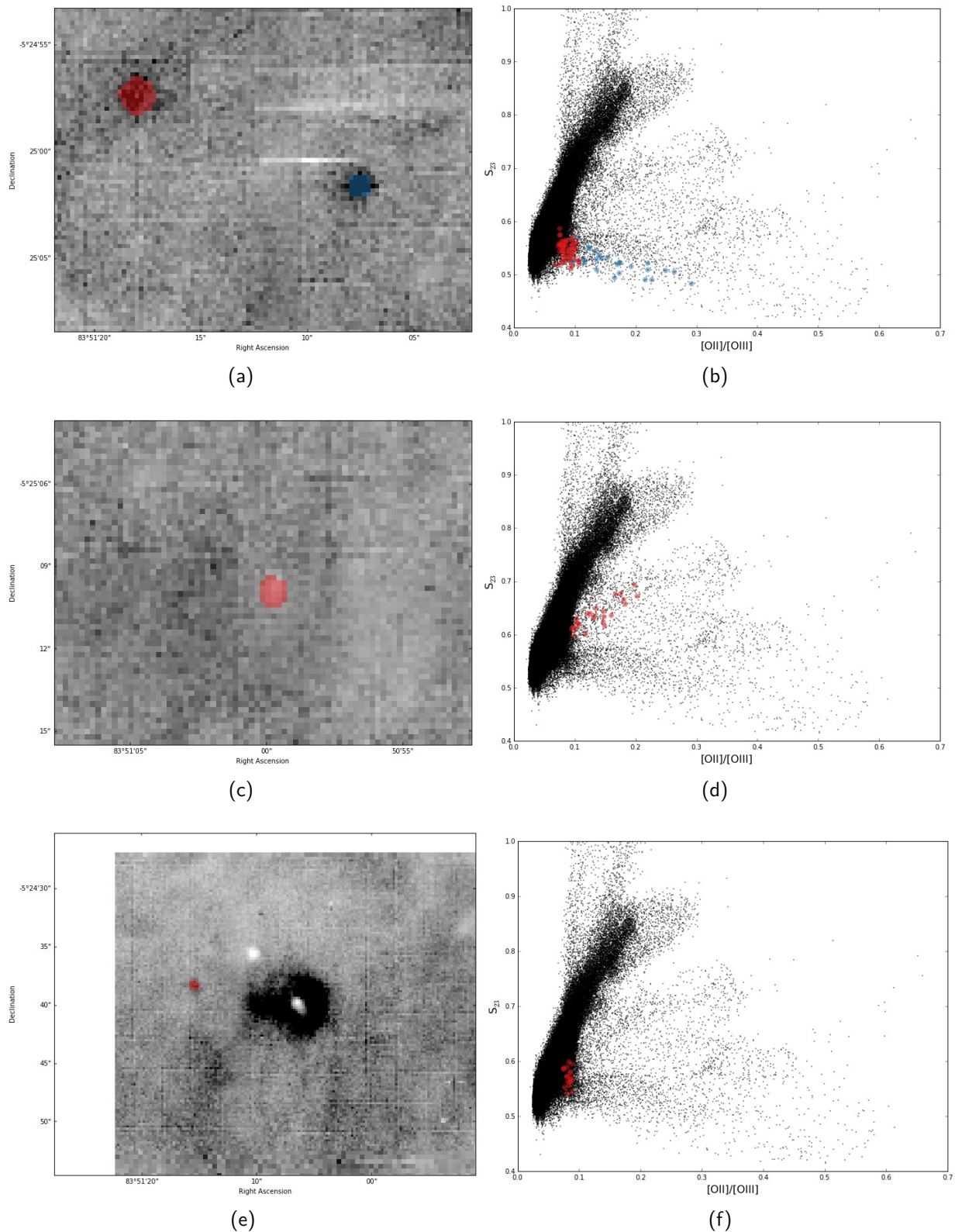


Figure B.10: Same as Fig. B.8, but for the proplyds 252-457 and 245-502 (red and blue respectively in panels a and b), 239-510 (panels c and d) and 250-439 (panels e and f).

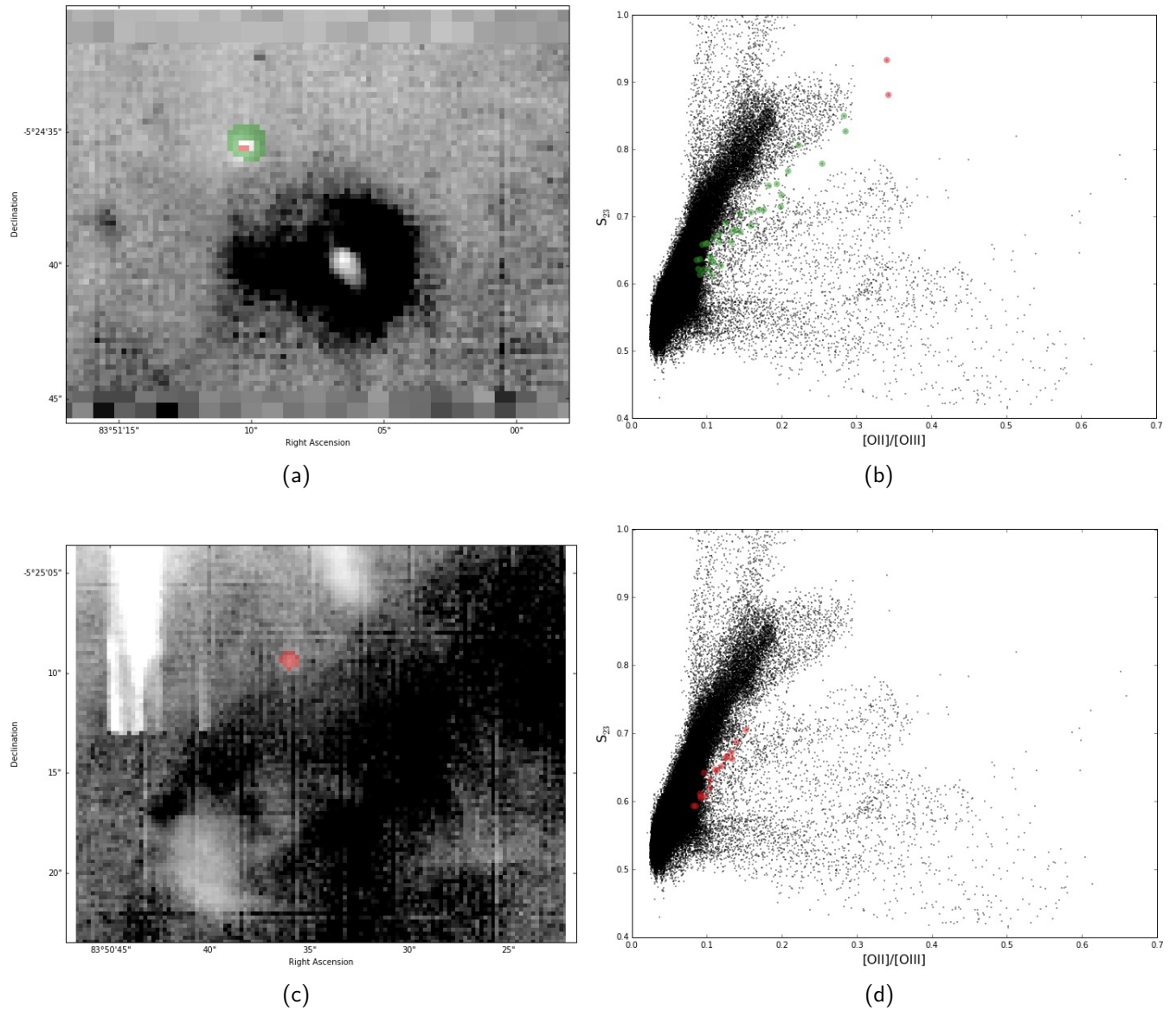


Figure B.11: Same as Fig. B.8, but for the proplyd 247-436 (panels a and b), the candidate proplyd (224-510, letter *n* in Fig. 4.18a, panels c and d).

C

Appendix C

Figures C.1 to C.10 show continuum-subtracted integrated line maps of the main emission lines analysed in this work. Figures C.11 to C.12 show the electron temperature and density maps of the various regions, while Figure C.14 shows a three-colour composite of the outflow HH 1124 in R18.

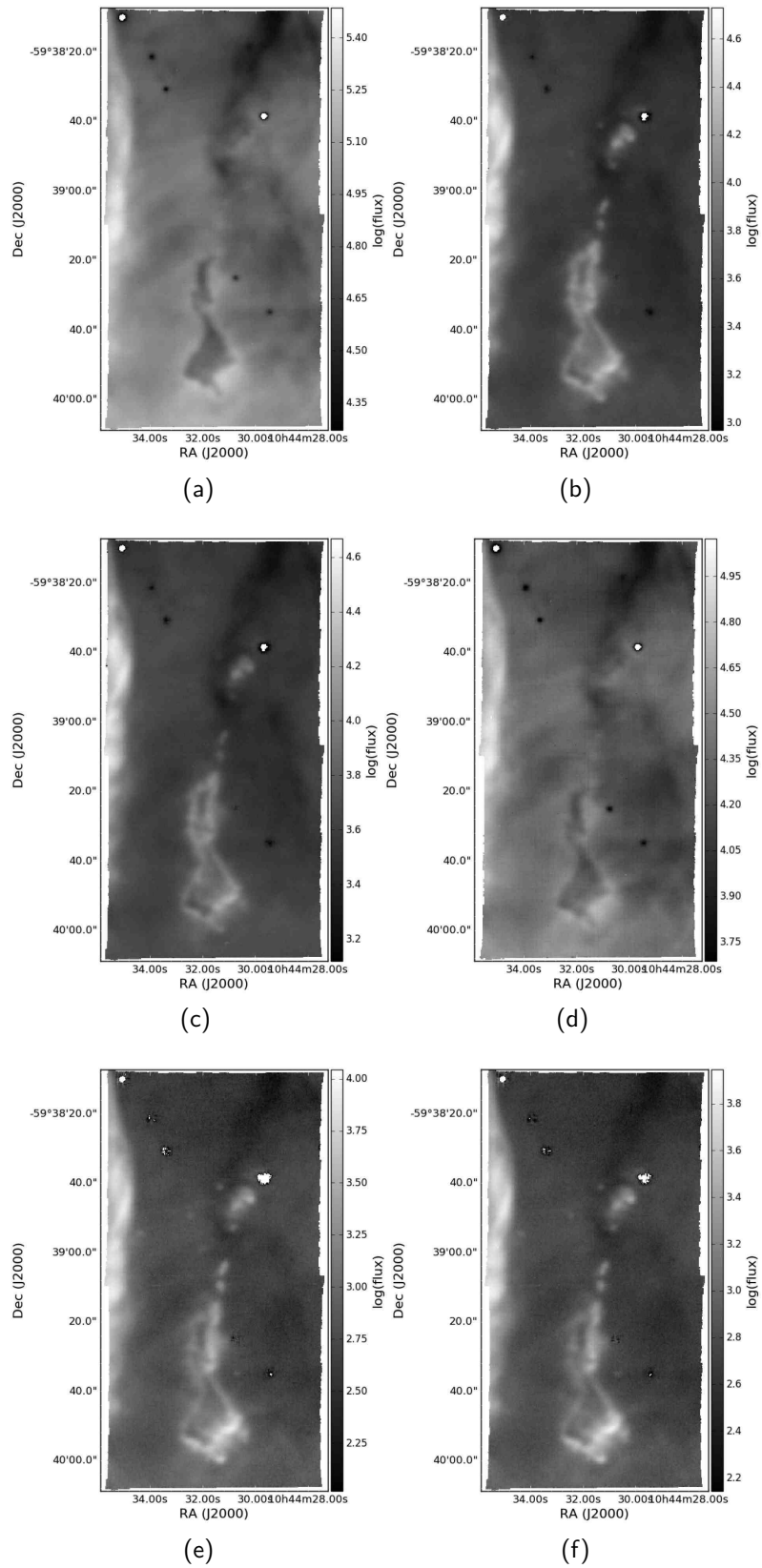


Figure C.1: Continuum-subtracted integrated emission line intensity maps of R37, from (a) to (f): $H\beta$, $[\text{SII}]\lambda 6731$, $[\text{SII}]\lambda 6717$, $[\text{SIII}]\lambda 9068$, $[\text{OII}]\lambda 7320$, $[\text{OII}]\lambda 7330$.

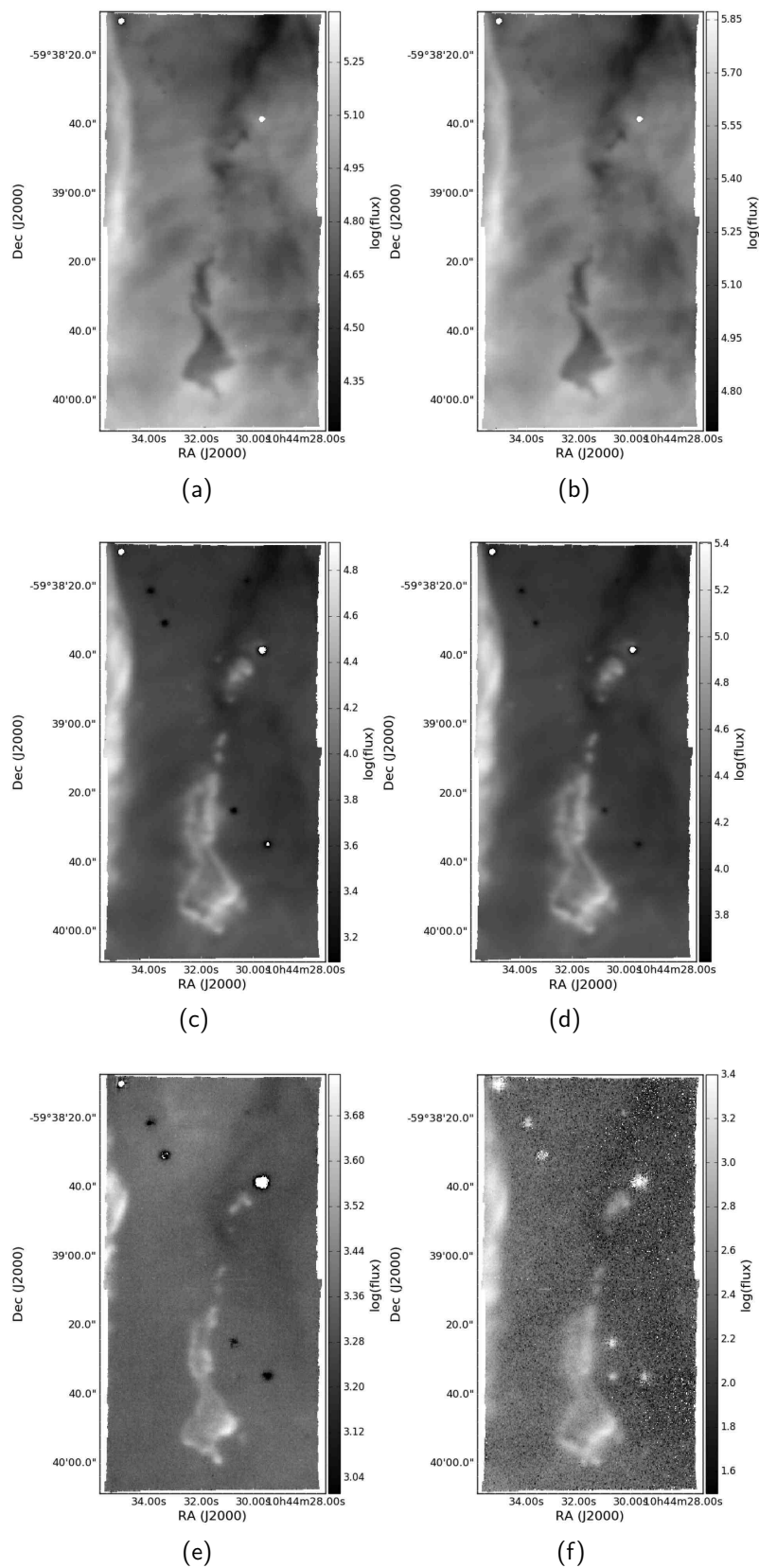


Figure C.2: Same as Fig. A1 , (a) to (e): $[\text{OIII}]\lambda 4959$, $[\text{OIII}]\lambda 5007$, $[\text{NII}]\lambda 6548$, $[\text{NII}]\lambda 6584$, $[\text{OI}]\lambda 6300$, $[\text{NII}]\lambda 5755$.

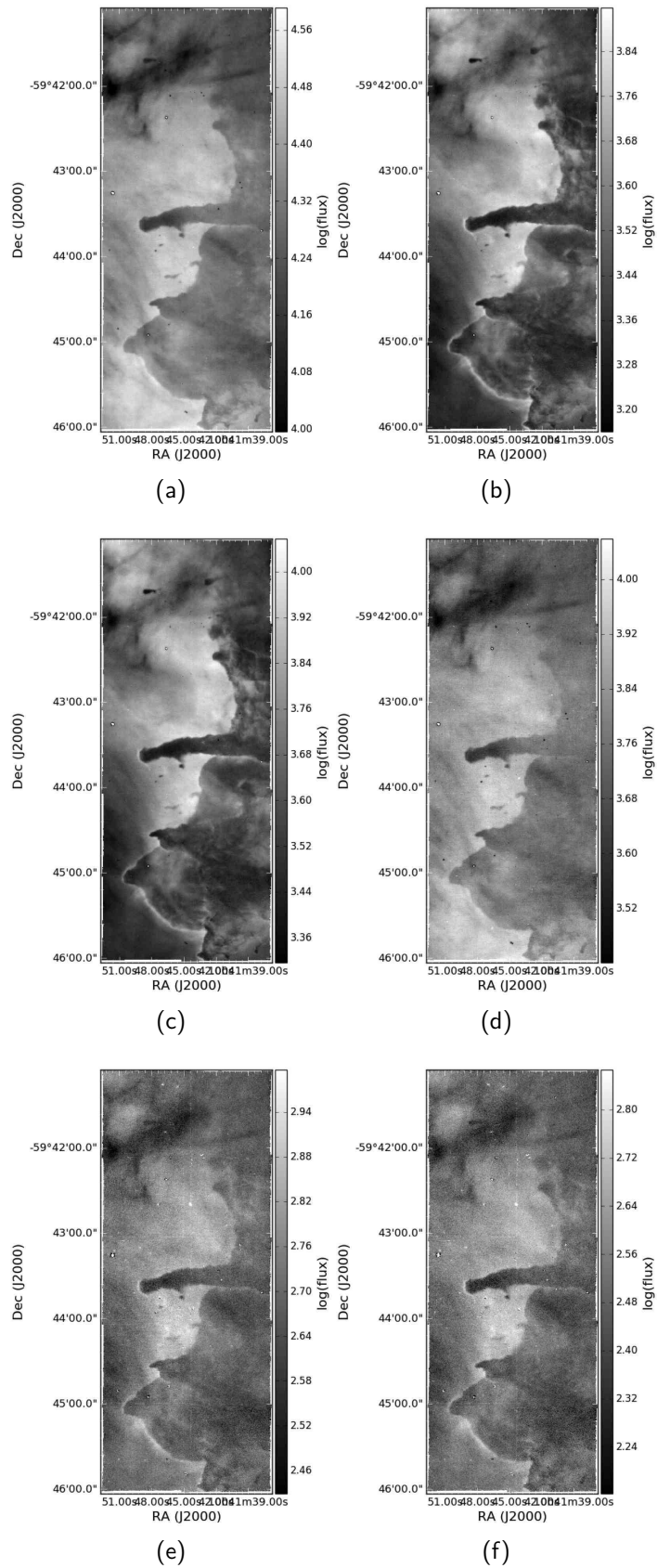


Figure C.3: Same as Fig. A1 for R44.

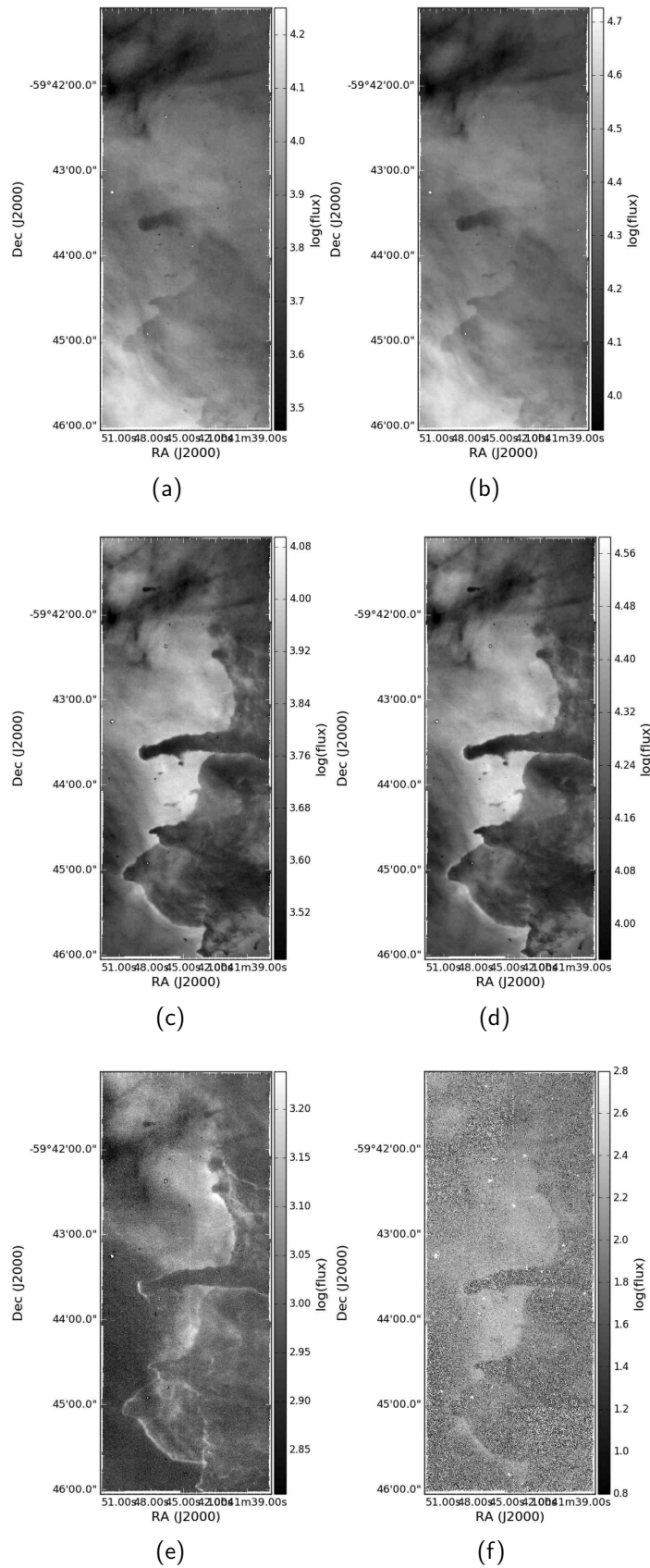


Figure C.4: Same as Fig. A2 for R44.

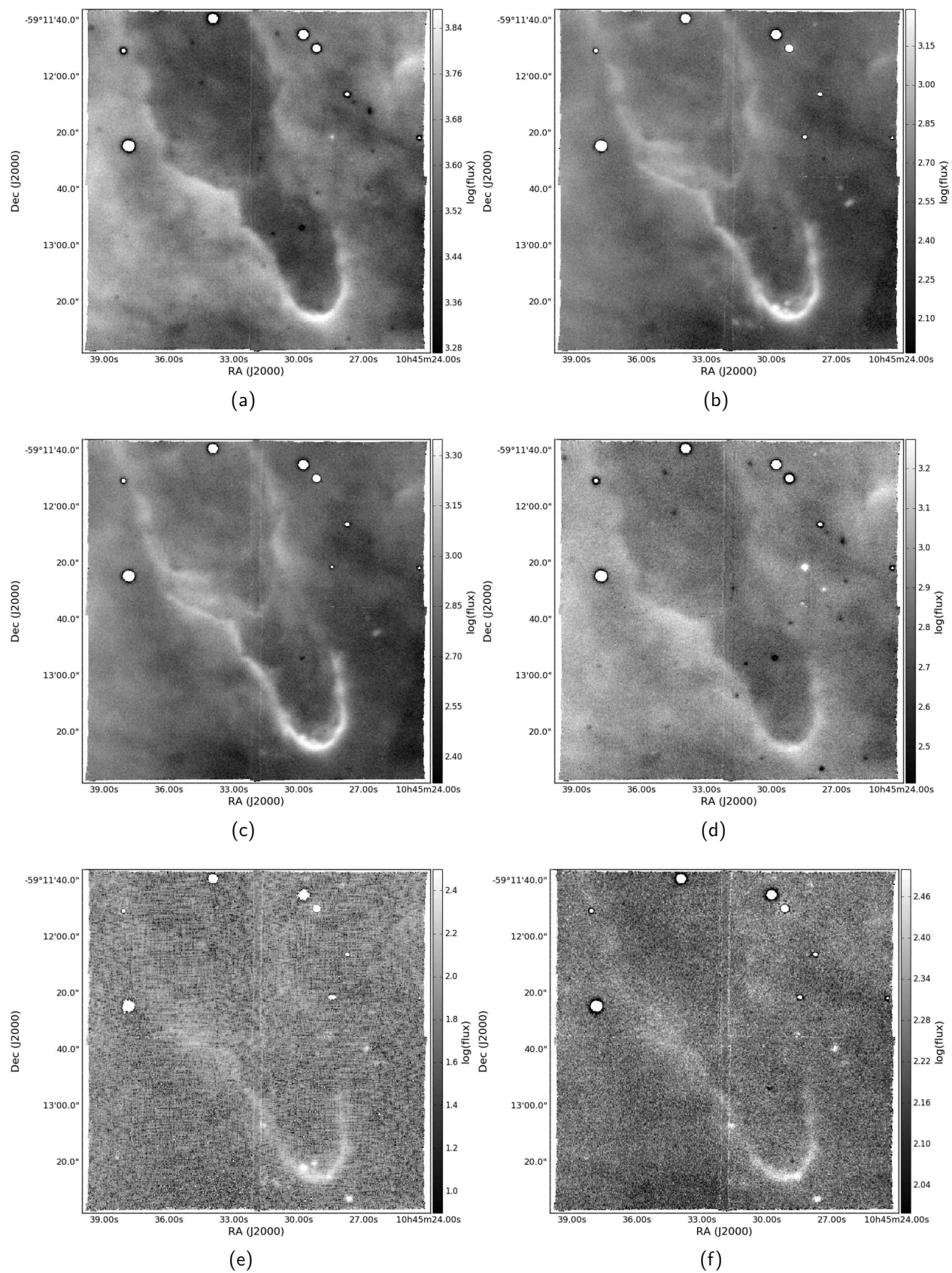


Figure C.5: Same as Fig. A1 for R18.

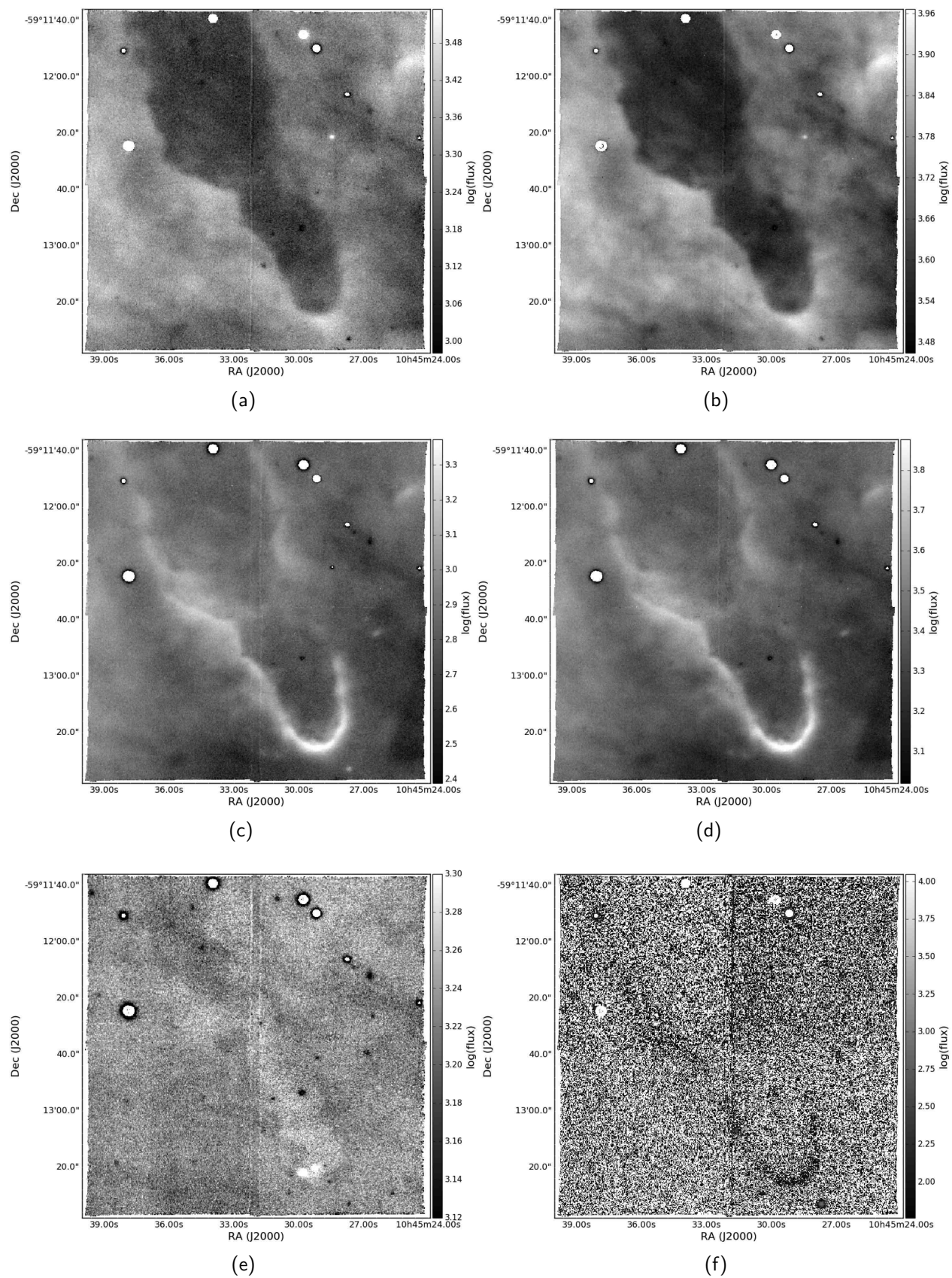


Figure C.6: Same as Fig. A2 for R18.

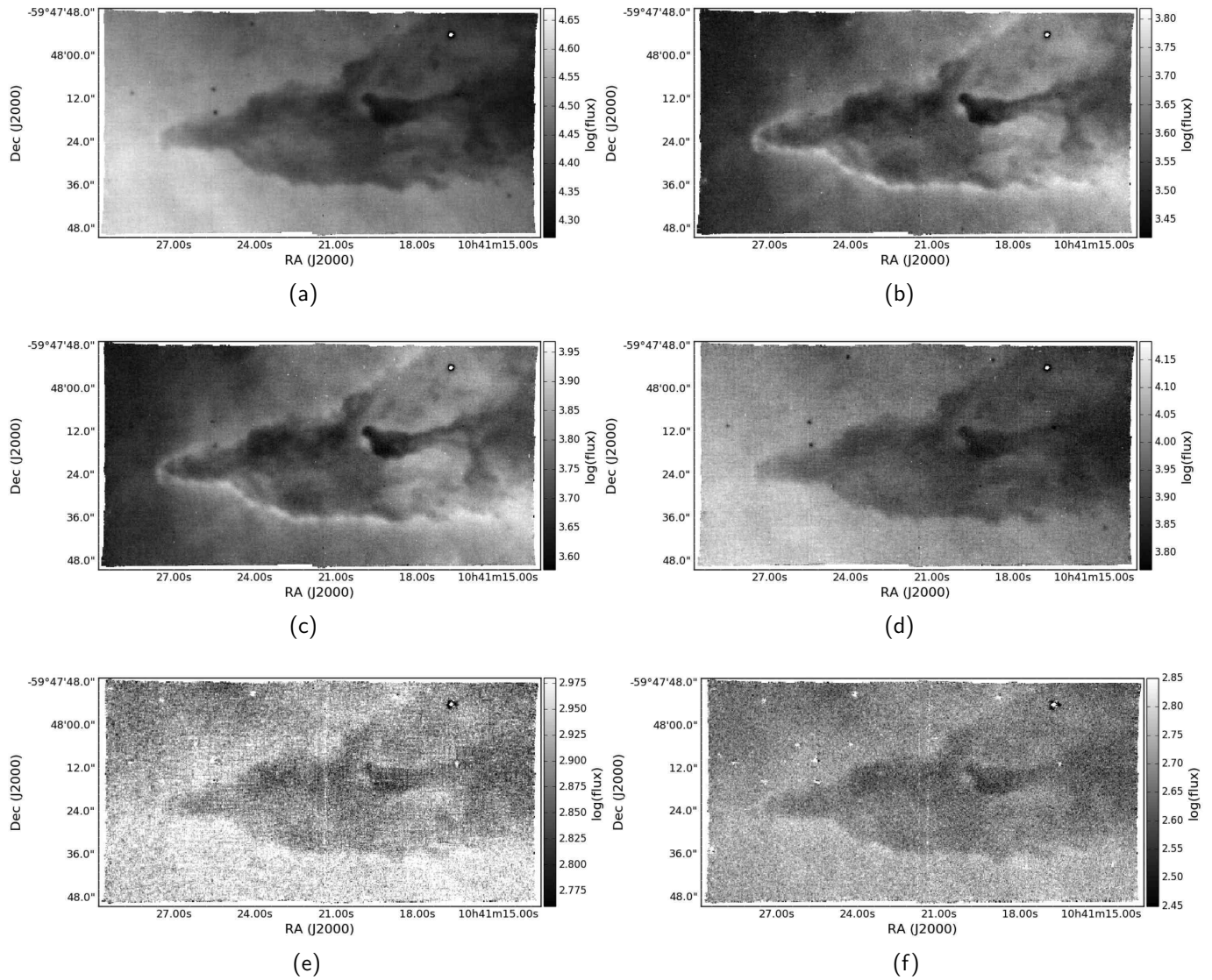


Figure C.7: Same as Fig. A1 for R45.

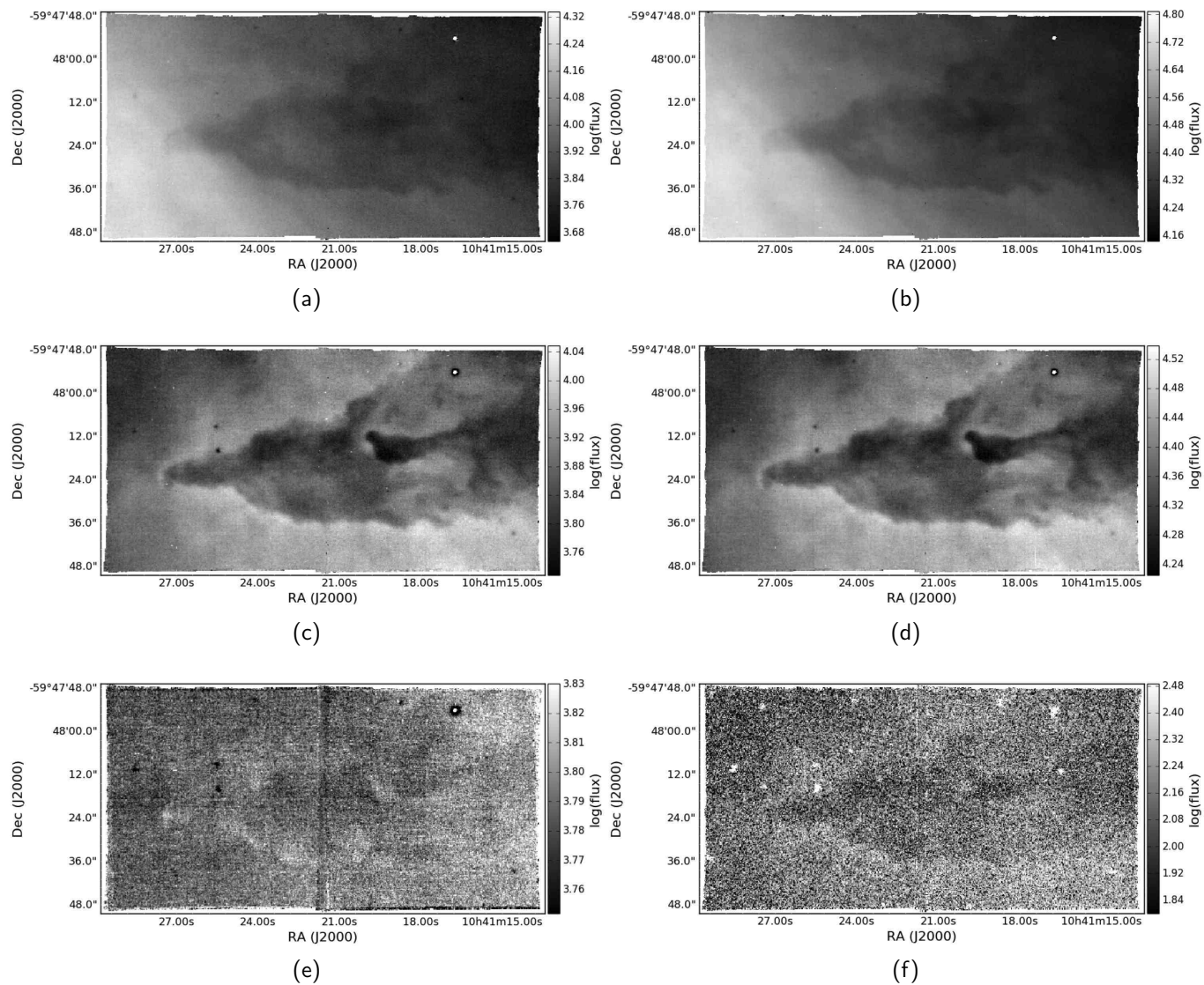


Figure C.8: Same as Fig. A2 for R45.

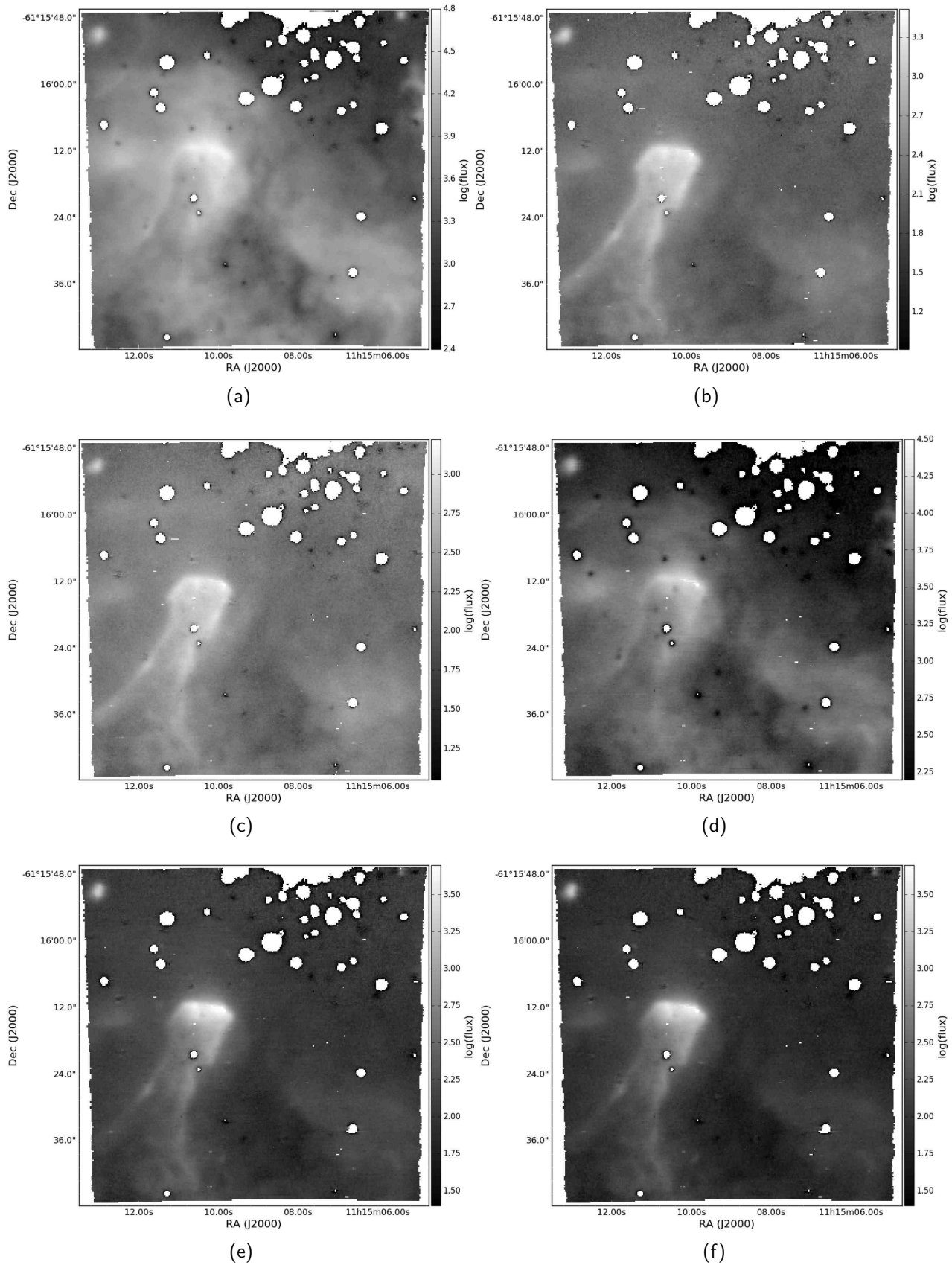


Figure C.9: Same as Fig. A1 for NGC 3603.

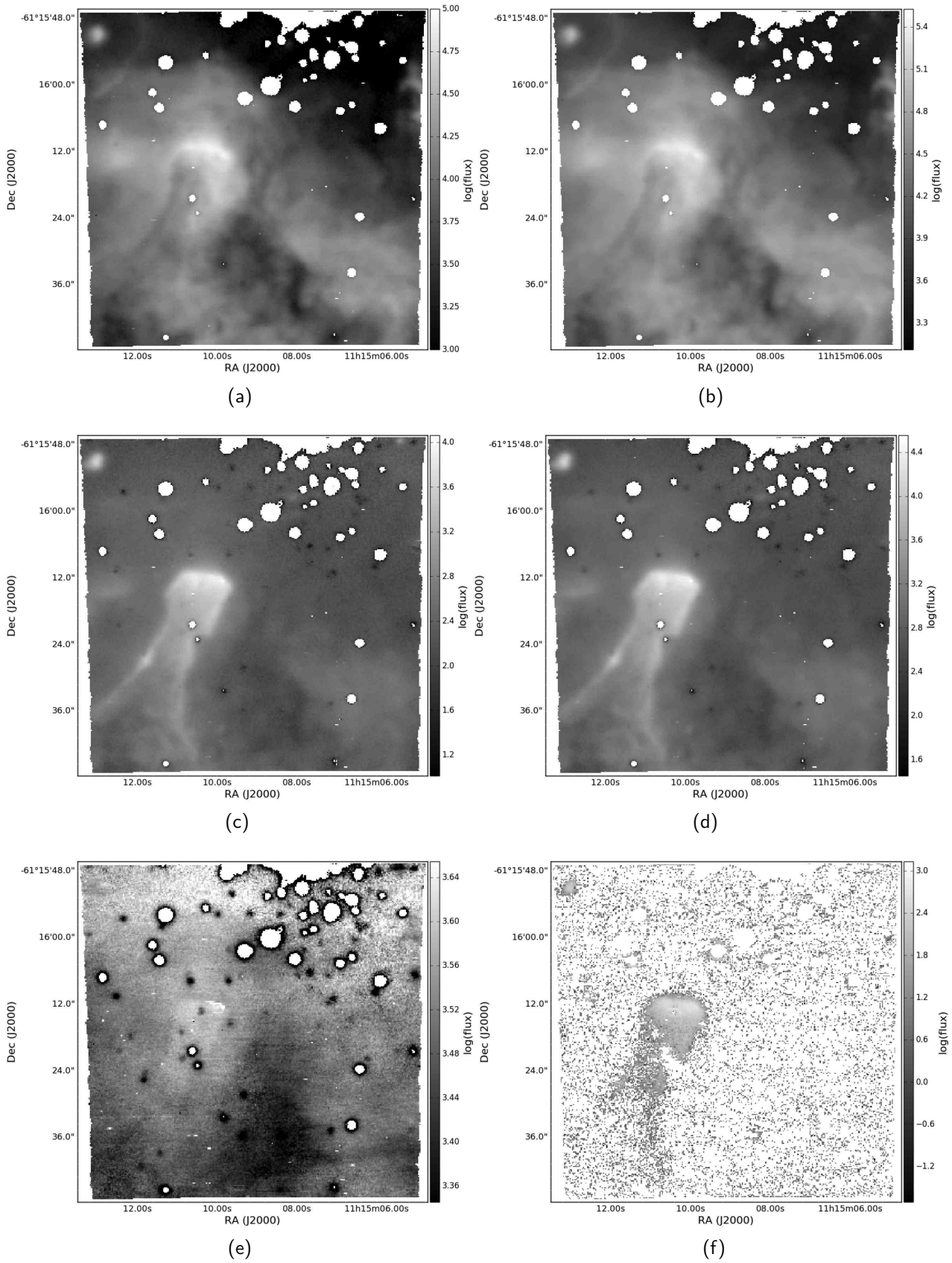


Figure C.10: Same as Fig. A2 for NGC 3603.

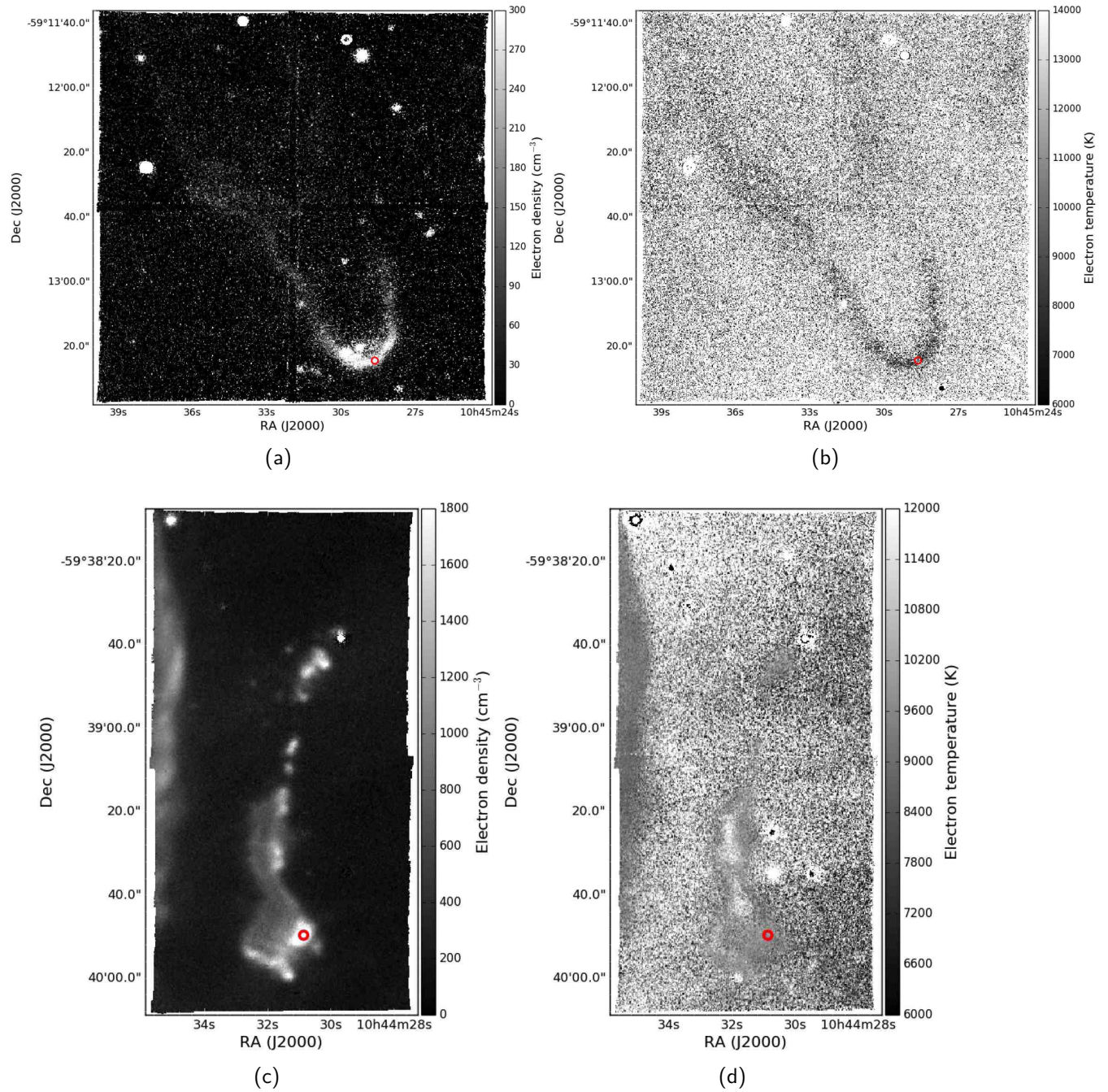


Figure C.11: Electron density and temperature maps of R18 (top panels) and R37 (bottom panels). Black circles indicate the regions used to extract values reported in Table 5.3.

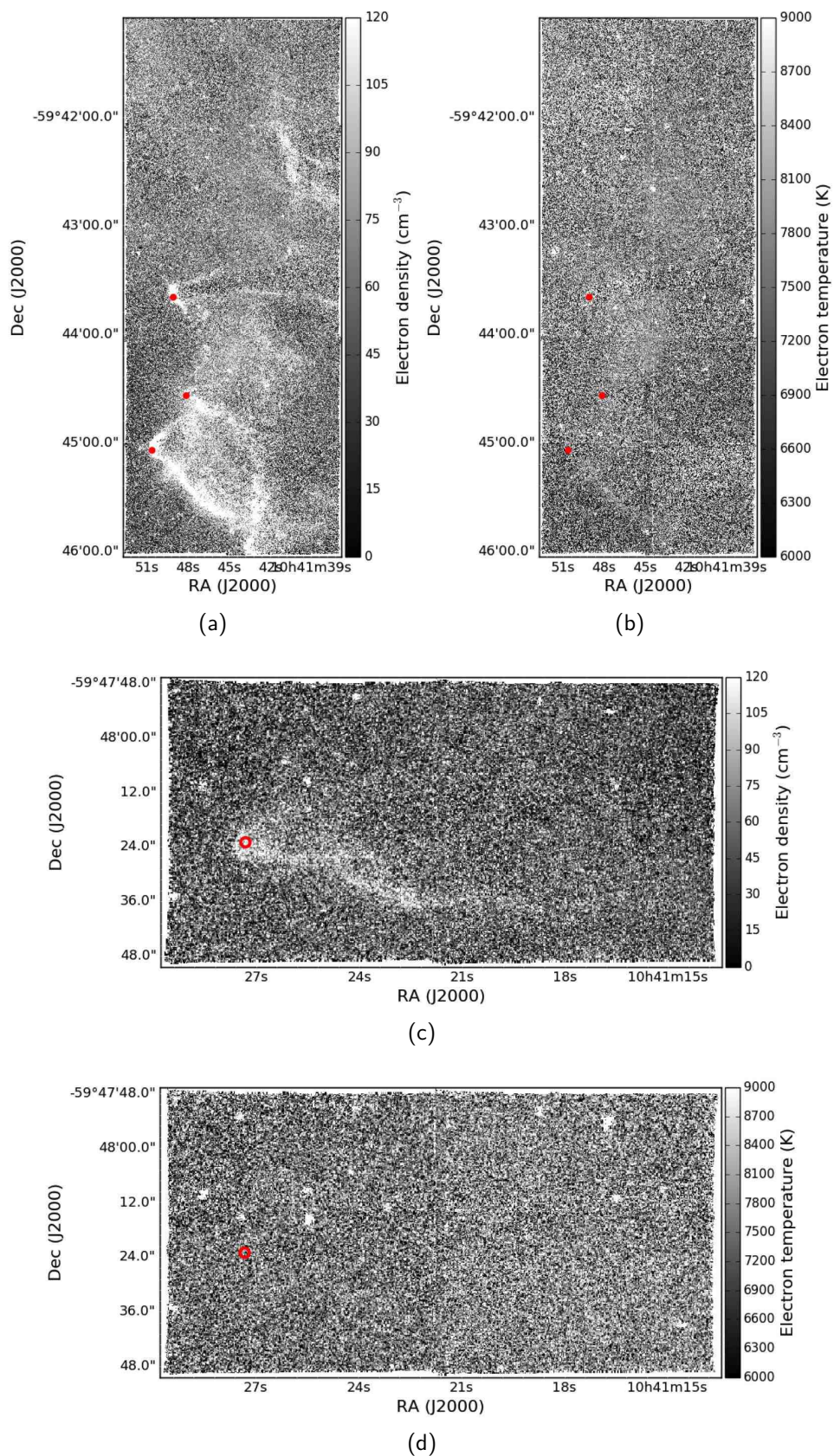
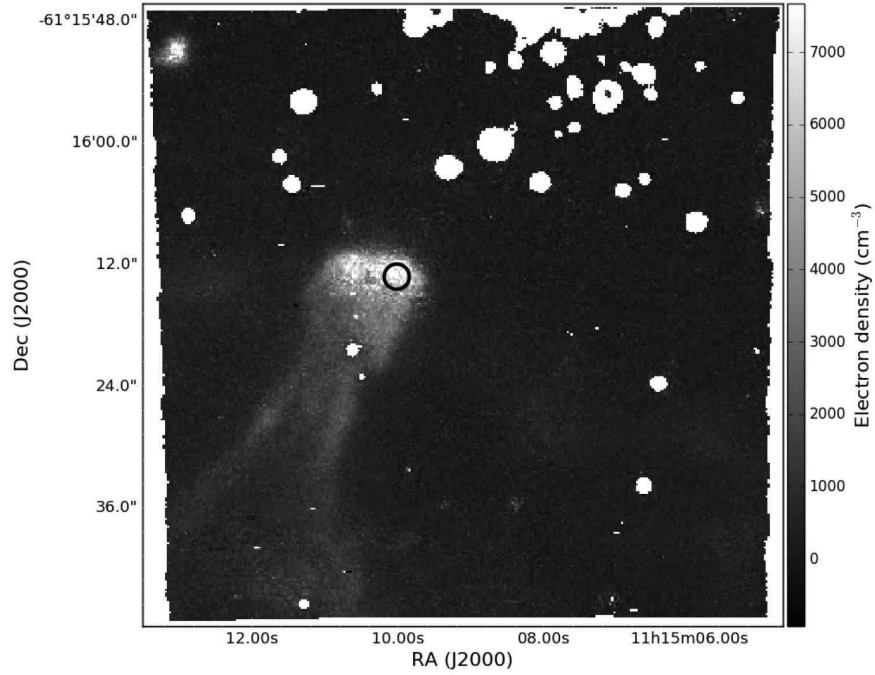
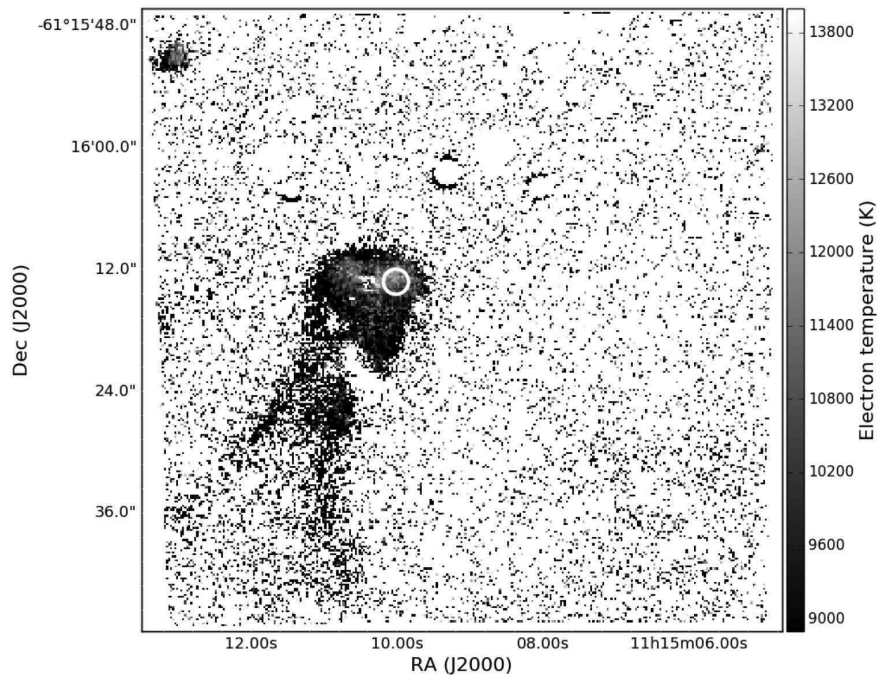


Figure C.12: Same as Fig. C.11, but for R44 (top panels), and R45 (bottom panels).



(a)



(b)

Figure C.13: Same as Fig. C.11, but for NGC 3603.

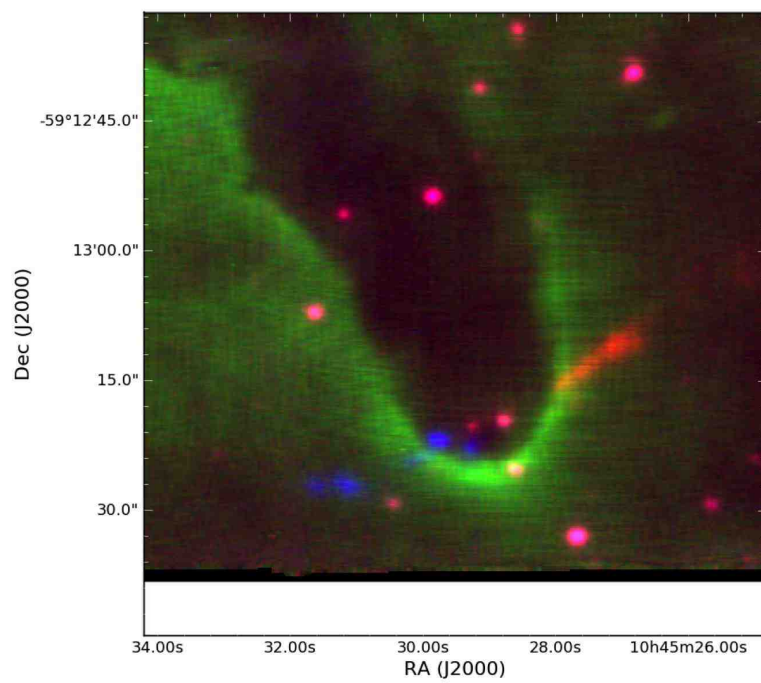


Figure C.14: RGB composite of three slices around the H α line showing the outflow HH 1124 in R18. See text Section 5.3.4.

Bibliography

- Aggarwal K. M., Keenan F. P., 1999, *ApJS*, 123, 311
- Allen C. W., 1973, *Astrophysical quantities*. University of London, Athlone Press, 3rd ed.
- Allen M. G., Groves B. A., Dopita M. A., Sutherland R. S., Kewley L. J., 2008, *ApJS*, 178, 20
- Allington-Smith J., Content R., 1998, *PASP*, 110, 1216
- Anderson L. D., Bania T. M., Balser D. S., Rood R. T., 2011, *ApJS*, 194, 32
- Arce H. G., Borkin M. A., Goodman A. A., Pineda J. E., Halle M. W., 2010, *ApJ*, 715, 1170
- Arribas S., Mediavilla E., García-Lorenzo B., del Burgo C., Fuensalida J. J., 1999, *AAPS*, 136, 189
- Arthur S. J., Henney W. J., Mellema G., de Colle F., Vázquez-Semadeni E., 2011, *MNRAS*, 414, 1747
- Bacon R., Adam G., Baranne A., Courtes G., Dubet D., Dubois J. P., Emsellem E., Ferruit P., Georgelin Y., Monnet G., Pecontal E., Rousset A., Say F., 1995, *AAPS*, 113, 347
- Bacon R., Copin Y., Monnet G., Miller B. W., Allington-Smith J. R., Bureau M., Carollo C. M., Davies R. L., Emsellem E., Kuntschner H., Peletier R. F., Verolme E. K., de Zeeuw P. T., 2001, *MNRAS*, 326, 23
- Bacon R., et al., 2010, in *Society of Photo-Optical Instrumentation Engineers (SPIE) Conference Series Vol. 7735 of Society of Photo-Optical Instrumentation Engineers (SPIE) Conference Series*, The MUSE second-generation VLT instrument. p. 8
- Bacon R., et al., 2015, *A&A*, 575, A75
- Bacon R., Vernet J., et al. B., 2014, *The Messenger*, 157, 13
- Baldwin J. A., Ferland G. J., Martin P. G., Corbin M. R., Cota S. A., Peterson B. M., Slettebak A., 1991, *ApJ*, 374, 580
- Baldwin J. A., Phillips M. M., Terlevich R., 1981, *PASP*, 93, 5

- Bally J., 2011, in Alves J., Elmegreen B. G., Girart J. M., Trimble V., eds, Computational Star Formation Vol. 270 of IAU Symposium, Observations of Winds, Jets, and Turbulence Generation in GMCs. pp 247–254
- Bally J., Ginsburg A., Silvia D., Youngblood A., 2015, *A&A*, 579, A130
- Bally J., O'Dell C. R., McCaughrean M. J., 2000, *AJ*, 119, 2919
- Bally J., Reipurth B., 2001, *ApJ*, 546, 299
- Bally J., Reipurth B., Davis C. J., 2007, *Protostars and Planets V*, pp 215–230
- Barnes P. J., Yonekura Y., Fukui Y., Miller A. T., Mühlegger M., Agars L. C., Miyamoto Y., Furukawa N., Papadopoulos G., Jones S. L., Hernandez A. K., O'Dougherty S. N., Tan J. C., 2011, *ApJS*, 196, 12
- Barnes P. J., Yonekura Y., Ryder S. D., Hopkins A. M., Miyamoto Y., Furukawa N., Fukui Y., 2010, *MNRAS*, 402, 73
- Bate M. R., 2009, *MNRAS*, 392, 1363
- Bate M. R., Bonnell I. A., Bromm V., 2003, *MNRAS*, 339, 577
- Battersby C., Bally J., Ginsburg A., Bernard J.-P., Brunt C., Fuller G. A., Martin P., Molinari S., Mottram J., Peretto N., Testi L., Thompson M. A., 2011, *A&A*, 535, A128
- Bertoldi F., 1989, *ApJ*, 346, 735
- Bertoldi F., McKee C. F., 1990, *ApJ*, 354, 529
- Beuther H., Churchwell E. B., McKee C. F., Tan J. C., 2007, *Protostars and Planets V*, pp 165–180
- Bisbas T. G., Wunsch R., Whitworth A. P., Hubber D. A., Walch S., 2011, *ApJ*, 736, 142
- Blagrove K. P. M., Martin P. G., Baldwin J. A., 2006, *ApJ*, 644, 1006
- Boneberg D. M., Dale J. E., Girichidis P., Ercolano B., 2015, *MNRAS*, 447, 1341
- Bonnell I. A., Bate M. R., Vine S. G., 2003, *MNRAS*, 343, 413
- Bressert E., Bastian N., Gutermuth R., Megeath S. T., Allen L., Evans II N. J., Rebull L. M., Hatchell J., Johnstone D., Bourke T. L., Cieza L. A., Harvey P. M., Merin B., Ray T. P., Tothill N. F. H., 2010, *MNRAS*, 409, L54
- Burton M. G., Brand P. W. J. L., Geballe T. R., Webster A. S., 1989, *MNRAS*, 236, 409
- Cardelli J. A., Clayton G. C., Mathis J. S., 1989, *ApJ*, 345, 245

- Carroll J. J., Frank A., Blackman E. G., Cunningham A. J., Quillen A. C., 2009, *ApJ*, 695, 1376
- Castaneda H. O., 1988, *ApJS*, 67, 93
- Castor J. I., Abbott D. C., Klein R. I., 1975, *ApJ*, 195, 157
- Caulet A., Gruendl R. A., Chu Y.-H., 2008, *ApJ*, 678, 200
- Chakraborty A., Anandarao B. G., 1999, *A&A*, 346, 947
- Chen C.-H. R., Chu Y.-H., Gruendl R. A., Gordon K. D., Heitsch F., 2009, *ApJ*, 695, 511
- Chini R., Wargau W. F., 1990, *A&A*, 227, 213
- Conti P. S., Blum R. D., 2002, *ApJ*, 564, 827
- Cox P., Bronfman L., 1995, *A&A*, 299, 583
- Cresci G., et al., 2015, *A&A*, 582, A63
- Cunningham A. J., Frank A., Carroll J., Blackman E. G., Quillen A. C., 2009, *ApJ*, 692, 816
- Curtis E. I., Richer J. S., Swift J. J., Williams J. P., 2010, *MNRAS*, 408, 1516
- Dale J. E., Bonnell I. A., 2008, *MNRAS*, 391, 2
- Dale J. E., Ercolano B., Bonnell I. A., 2012a, *MNRAS*, 427, 2852
- Dale J. E., Ercolano B., Bonnell I. A., 2012b, *MNRAS*, 427, 2852
- Dale J. E., Ercolano B., Bonnell I. A., 2013a, *MNRAS*, 431, 1062
- Dale J. E., Ercolano B., Bonnell I. A., 2013b, *MNRAS*, 431, 1062
- Dale J. E., Ercolano B., Bonnell I. A., 2013c, *MNRAS*, 430, 234
- Dale J. E., Ngoumou J., Ercolano B., Bonnell I. A., 2013, *MNRAS*, 436, 3430
- Dale J. E., Ngoumou J., Ercolano B., Bonnell I. A., 2014, *MNRAS*, 442, 694
- de Avillez M. A., Breitschwerdt D., 2004, *A&A*, 425, 899
- de Jager C., Nieuwenhuijzen H., van der Hucht K. A., 1988, *AAPS*, 72, 259
- De Pree C. G., Mehringer D. M., Goss W. M., 1997, *ApJ*, 482, 307
- Drissen L., Moffat A. F. J., Walborn N. R., Shara M. M., 1995, *AJ*, 110, 2235
- Duarte-Cabral A., Chrysostomou A., Peretto N., Fuller G. A., Matthews B., Schieven G., Davis G. R., 2012, *A&A*, 543, A140

- Eisenhauer F. o., 2003, in Iye M., Moorwood A. F. M., eds, Instrument Design and Performance for Optical/Infrared Ground-based Telescopes Vol. 4841 of SPIE conference proceedings, SINFONI - Integral field spectroscopy at 50 milli-arcsecond resolution with the ESO VLT. pp 1548–1561
- Ercolano B., Barlow M. J., Storey P. J., 2005, MNRAS, 362, 1038
- Ercolano B., Barlow M. J., Storey P. J., Liu X.-W., 2003a, MNRAS, 340, 1136
- Ercolano B., Barlow M. J., Storey P. J., Liu X.-W., 2003b, MNRAS, 340, 1136
- Ercolano B., Dale J. E., Gritschneider M., Westmoquette M., 2012, MNRAS, 420, 141
- Ercolano B., Gritschneider M., 2011, MNRAS, 413, 401
- Ercolano B., Young P. R., Drake J. J., Raymond J. C., 2008, ApJS, 175, 534
- Esteban C., Peimbert M., García-Rojas J., Ruiz M. T., Peimbert A., Rodríguez M., 2004, MNRAS, 355, 229
- Esteban C., Peimbert M., Torres-Peimbert S., Escalante V., 1998, MNRAS, 295, 401
- Evans C. J., et al., 2005, A&A, 437, 467
- Fall S. M., Chandar R., 2012, ApJ, 752, 96
- Faúndez S., Bronfman L., Garay G., Chini R., Nyman L.-Å., May J., 2004, A&A, 426, 97
- Feigelson E. D., Getman K. V., Townsley L. K., Broos P. S., Povich M. S., Garmire G. P., King R. R., Montmerle T., Preibisch T., Smith N., Stassun K. G., Wang J., Wolk S., Zinnecker H., 2011, ApJS, 194, 9
- Feldmeier-Krause A., Neumayer N., Schödel R., Seth A., Hilker M., de Zeeuw P. T., Kuntschner H., Walcher C. J., Lützgendorf N., Kissler-Patig M., 2015, A&A, 584, A2
- Ferland G. J., Porter R. L., van Hoof P. A. M., Williams R. J. R., Abel N. P., Lykins M. L., Shaw G., Henney W. J., Stancil P. C., 2013a, RevMexAA, 49, 137
- Ferland G. J., Porter R. L., van Hoof P. A. M., Williams R. J. R., Abel N. P., Lykins M. L., Shaw G., Henney W. J., Stancil P. C., 2013b, RevMexAA, 49, 137
- Fukuda N., Hanawa T., Sugitani K., 2002, ApJL, 568, L127
- Fumagalli M., Fossati M., Hau G. K. T., Gavazzi G., Bower R., Sun M., Boselli A., 2014, MNRAS, 445, 4335
- Gagne M., Fehon G., Savoy M. R., Cohen D. H., Townsley L. K., Broos P. S., Povich M. S., Corcoran M. F., Walborn N. R., Evans N. R., Moffat A. F. J., Naze Y., Oskinova L. M., 2011, VizieR Online Data Catalog, 219

- Galavis M. E., Mendoza C., Zeppen C. J., 1997, AAPS, 123, 159
- Galván-Madrid R., Liu H. B., Zhang Z.-Y., Pineda J. E., Peng T.-C., Zhang Q., Keto E. R., Ho P. T. P., Rodríguez L. F., Zapata L., Peters T., De Pree C. G., 2013, ApJ, 779, 121
- García-Benito R., Díaz A., Hägele G. F., Pérez-Montero E., López J., Vílchez J. M., Pérez E., Terlevich E., Terlevich R., Rosa-González D., 2010, MNRAS, 408, 2234
- García-Lorenzo B., Arribas S., Mediavilla E., 2000, The Newsletter of the Isaac Newton Group of Telescopes, 3, 25
- Gatto A., Walch S., Low M.-M. M., Naab T., Girichidis P., Glover S. C. O., Wunsch R., Klessen R. S., Clark P. C., Baczynski C., Peters T., Ostriker J. P., Ibáñez-Mejía J. C., Haid S., 2015, MNRAS, 449, 1057
- Gazak J. Z., Kudritzki R., Evans C., Patrick L., Davies B., Bergemann M., Plez B., Bresolin F., Bender R., Wegner M., Bonanos A. Z., Williams S. J., 2015, ApJ, 805, 182
- Gent F. A., Shukurov A., Fletcher A., Sarson G. R., Mantere M. J., 2013, MNRAS, 432, 1396
- Ginsburg A., Bressert E., Bally J., Battersby C., 2012, ApJL, 758, L29
- Ginsburg A., Mirocha J., , 2011, PySpecKit: Python Spectroscopic Toolkit, Astrophysics Source Code Library
- Gorti U., Hollenbach D., 2002, ApJ, 573, 215
- Graham M. F., Meaburn J., Redman M. P., 2003, MNRAS, 343, 419
- Gritschneider M., Burkert A., Naab T., Walch S., 2010a, ApJ, 723, 971
- Gritschneider M., Burkert A., Naab T., Walch S., 2010b, ApJ, 723, 971
- Gritschneider M., Naab T., Burkert A., Walch S., Heitsch F., Wetzstein M., 2009, MNRAS, 393, 21
- Guarcello M. G., Micela G., Peres G., Prisinzano L., Sciortino S., 2010, A&A, 521, A61
- Gutermuth R. A., Myers P. C., Megeath S. T., Allen L. E., Pipher J. L., Muzerolle J., Porras A., Winston E., Fazio G., 2008, ApJ, 674, 336
- Hägele G. F., Díaz Á. I., Terlevich E., Terlevich R., Pérez-Montero E., Cardaci M. V., 2008, MNRAS, 383, 209
- Harayama Y., Eisenhauer F., Martins F., 2008, ApJ, 675, 1319
- Hartigan P., Edwards S., Ghandour L., 1995, ApJ, 452, 736
- Hartigan P., Reiter M., Smith N., Bally J., 2015, AJ, 149, 101

- Healy K. R., Hester J. J., Claussen M. J., 2004, *ApJ*, 610, 835
- Hennebelle P., Commerçon B., 2014, *Astrophysics and Space Science Proceedings*, 36, 365
- Hennebelle P., Iffrig O., 2014, *A&A*, 570, A81
- Henney W. J., O'Dell C. R., 1999, *AJ*, 118, 2350
- Hester J. J., 1991, *PASP*, 103, 853
- Hester J. J., et al., 1996, *AJ*, 111, 2349
- Hester J. J., Gilmozzi R., O'dell C. R., Faber S. M., Campbell B., Code A., Currie D. G., Danielson G. E., Ewald S. P., Groth E. J., Holtzman J. A., Kelsall T., Lauer T. R., Light R. M., Lynds R., O'Neil Jr. E. J., Shaya E. J., Westphal J. A., 1991, *ApJL*, 369, L75
- Hildebrand R. H., 1983, *Quarterly Journal of the Royal Astronomical Society*, 24, 267
- Hill A. S., Reynolds R. J., Benjamin R. A., Haffner L. M., 2007, in Haverkorn M., Goss W. M., eds, *SINS - Small Ionized and Neutral Structures in the Diffuse Interstellar Medium Vol. 365 of Astronomical Society of the Pacific Conference Series, Density Distribution of the Warm Ionized Medium*. p. 250
- Hill J. K., Hollenbach D. J., 1978, *ApJ*, 225, 390
- Hillenbrand L. A., Massey P., Strom S. E., Merrill K. M., 1993, *AJ*, 106, 1906
- Hoare M. G., Kurtz S. E., Lizano S., Keto E., Hofner P., 2007, *Protostars and Planets V*, pp 181–196
- Hook I. M., Jørgensen I., Allington-Smith J. R., Davies R. L., Metcalfe N., Murowinski R. G., Crampton D., 2004, *PASP*, 116, 425
- Hur H., Sung H., Bessell M. S., 2012, *AJ*, 143, 41
- Icke V., 1979, *A&A*, 78, 352
- Iffrig O., Hennebelle P., 2015, *A&A*, 576, A95
- Immer K., Galván-Madrid R., König C., Liu H. B., Menten K. M., 2014, *A&A*, 572, A63
- Immer K., Reid M. J., Menten K. M., Brunthaler A., Dame T. M., 2013, *A&A*, 553, A117
- Indebetouw R., Robitaille T. P., Whitney B. A., Churchwell E., Babler B., Meade M., Watson C., Wolfire M., 2007, *ApJ*, 666, 321
- Joung M. K. R., Mac Low M.-M., 2006, *ApJ*, 653, 1266

- Kauffmann G., Heckman T. M., Tremonti C., Brinchmann J., Charlot S., White S. D. M., Ridgway S. E., Brinkmann J., Fukugita M., Hall P. B., Ivezić Ž., Richards G. T., Schneider D. P., 2003, MNRAS, 346, 1055
- Kawamura A., Mizuno Y., Minamidani T., Filipović M. D., Staveley-Smith L., Kim S., Mizuno N., Onishi T., Mizuno A., Fukui Y., 2009, ApJS, 184, 1
- Kewley L. J., Dopita M. A., Sutherland R. S., Heisler C. A., Trevena J., 2001, ApJ, 556, 121
- Kippenhahn R., Weigert A., 1990, Stellar Structure and Evolution
- Klaassen P. D., Mottram J. C., Dale J. E., Juhasz A., 2014, MNRAS, 441, 656
- Klessen R. S., Burkert A., 2000, ApJS, 128, 287
- Klessen R. S., Burkert A., 2001, ApJ, 549, 386
- Koepferl C. M., Robitaille T. P., Dale J. E., Biscani F., 2016, ArXiv e-prints
- Kolmogorov A., 1941, Akademiia Nauk SSSR Doklady, 30, 301
- Kruijssen J. M. D., Longmore S. N., 2014, MNRAS, 439, 3239
- Krumholz M. R., Bate M. R., Arce H. G., Dale J. E., Gutermuth R., Klein R. I., Li Z.-Y., Nakamura F., Zhang Q., 2014, Protostars and Planets VI, pp 243–266
- Krumholz M. R., Cunningham A. J., Klein R. I., McKee C. F., 2010, ApJ, 713, 1120
- Krumholz M. R., Klein R. I., McKee C. F., 2007, ApJ, 656, 959
- Krumholz M. R., Klein R. I., McKee C. F., Offner S. S. R., Cunningham A. J., 2009, Science, 323, 754
- Krumholz M. R., McKee C. F., Klein R. I., 2005, ApJL, 618, L33
- Krumholz M. R., Thompson T. A., 2012, ApJ, 760, 155
- Kuiper R., Klahr H., Beuther H., Henning T., 2011, ApJ, 732, 20
- Kuiper R., Klahr H., Beuther H., Henning T., 2012, A&A, 537, A122
- Kuiper R., Yorke H. W., 2013, ApJ, 763, 104
- Lada C. J., Lada E. A., 2003, ARA&A, 41, 57
- Lagrois D., Joncas G., 2011, MNRAS, 413, 721
- Larson R. B., Starrfield S., 1971, A&A, 13, 190

- Le Fèvre O., Saisse M., Mancini D., Brau-Nogue S., Caputi O., Castinel L., D'Odorico S., Garilli B., Kissler-Patig M., Lucuix C., Mancini G., Pauget A., Sciarretta G., Scodreggio M., Tresse L., Vettolani G., 2003, in Iye M., Moorwood A. F. M., eds, Instrument Design and Performance for Optical/Infrared Ground-based Telescopes Vol. 4841 of SPIE conference proceedings, Commissioning and performances of the VLT-VIMOS instrument. pp 1670–1681
- Lefloch B., Lazareff B., 1994, *A&A*, 289, 559
- Leitherer C., Robert C., Drissen L., 1992, *ApJ*, 401, 596
- Leroy A. K., Walter F., Sandstrom K., Schrubba A., Munoz-Mateos J.-C., Bigiel F., Bolatto A., Brinks E., de Blok W. J. G., Meidt S., Rix H.-W., Rosolowsky E., Schinnerer E., Schuster K.-F., Usero A., 2013, *AJ*, 146, 19
- Li Z.-Y., Nakamura F., 2006, *ApJL*, 640, L187
- Linsky J. L., Gagné M., Mytyk A., McCaughrean M., Andersen M., 2007, *ApJ*, 654, 347
- Longmore S. N., Pillai T., Keto E., Zhang Q., Qiu K., 2011, *ApJ*, 726, 97
- Lopez L. A., Krumholz M. R., Bolatto A. D., Prochaska J. X., Ramirez-Ruiz E., 2011, *ApJ*, 731, 91
- Luridiana V., Morisset C., Shaw R. A., 2015a, *A&A*, 573, A42
- Luridiana V., Morisset C., Shaw R. A., 2015b, *A&A*, 573, A42
- Maeder A., Meynet G., 2010, *NewAR*, 54, 32
- Martins F., Schaerer D., Hillier D. J., 2005, *A&A*, 436, 1049
- Massey R., et al., 2015, *MNRAS*, 449, 3393
- Mathis J. S., Rumpl W., Nordsieck K. H., 1977, *ApJ*, 217, 425
- Matzner C. D., 2007, *ApJ*, 659, 1394
- Maury A. J., André P., Li Z.-Y., 2009, *A&A*, 499, 175
- McCall M. L., 1984, *MNRAS*, 208, 253
- McCaughrean M. J., Andersen M., 2002, *A&A*, 389, 513
- McGregor P. J., Hart J., Conroy P. G., Pfitzner M. L., Bloxham G. J., Jones D. J., Downing M. D., Dawson M., Young P., Jarnyk M., Van Harmelen J., 2003, in Iye M., Moorwood A. F. M., eds, Instrument Design and Performance for Optical/Infrared Ground-based Telescopes Vol. 4841 of SPIE conference proceedings, Gemini near-infrared integral field spectrograph (NIFS). pp 1581–1591

- McKee C. F., Ostriker E. C., 2007, *ARA&A*, 45, 565
- McKee C. F., Ostriker J. P., 1977, *ApJ*, 218, 148
- McLeod A. F., Dale J. E., Ginsburg A., Ercolano B., Gritschneider M., Ramsay S., Testi L., 2015, *MNRAS*, 450, 1057
- McLeod A. F., Weilbacher P. M., Ginsburg A., Dale J. E., Ramsay S., Testi L., 2016, *MNRAS*, 455, 4057
- Meaburn J., Laspas V. N., 1991, *A&A*, 245, 635
- Medina Tanco G. A., Sabalisk N., Jatenco-Pereira V., Opher R., 1997, *ApJ*, 487, 163
- Melena N. W., Massey P., Morrell N. I., Zangari A. M., 2008, *AJ*, 135, 878
- Mellema G., Arthur S. J., Henney W. J., Iliev I. T., Shapiro P. R., 2006, *ApJ*, 647, 397
- Menten K. M., Walmsley C. M., Henkel C., Wilson T. L., 1986, *A&A*, 157, 318
- Mesa-Delgado A., Esteban C., García-Rojas J., 2008, *ApJ*, 675, 389
- Mesa-Delgado A., Núñez-Díaz M., Esteban C., López-Martín L., García-Rojas J., 2011, *MNRAS*, 417, 420
- Miao J., White G. J., Nelson R., Thompson M., Morgan L., 2006, *MNRAS*, 369, 143
- Miville-Deschenes M.-A., Joncas G., Durand D., 1995, *ApJ*, 454, 316
- Mizuta A., Kane J. O., Pound M. W., Remington B. A., Ryutov D. D., Takabe H., 2006, *ApJ*, 647, 1151
- Moffat A. F. J., 1983, *A&A*, 124, 273
- Molinari S., et al., 2010, *A&A*, 518, L100
- Monreal-Ibero A., Relaño M., Kehrig C., Pérez-Montero E., Vílchez J. M., Kelz A., Roth M. M., Streicher O., 2011, *MNRAS*, 413, 2242
- Morales E. F. E., Wyrowski F., Schuller F., Menten K. M., 2013, *A&A*, 560, A76
- Mottram J. C., Hoare M. G., Lumsden S. L., Oudmaijer R. D., Urquhart J. S., Sheret T. L., Clarke A. J., Allsopp J., 2007, *A&A*, 476, 1019
- Muno M. P., Law C., Clark J. S., Dougherty S. M., de Grijs R., Portegies Zwart S., Yusef-Zadeh F., 2006, *ApJ*, 650, 203
- Nakamura F., et al., 2011, *ApJ*, 726, 46
- Nakamura F., Li Z.-Y., 2007, *ApJ*, 662, 395

- Nakamura F., Sugitani K., Shimajiri Y., Tsukagoshi T., Higuchi A., Nishiyama S., Kawabe R., Takami M., Karr J. L., Gutermuth R. A., Wilson G., 2011, *ApJ*, 737, 56
- Narayanan G., Snell R., Bemis A., 2012, *MNRAS*, 425, 2641
- Ngoumou J., Hubber D., Dale J. E., Burkert A., 2015, *ApJ*, 798, 32
- Norman C. A., Ferrara A., 1996, *ApJ*, 467, 280
- Núñez-Díaz M., Mesa-Delgado A., Esteban C., López-Martín L., García-Rojas J., Luridiana V., 2012, *MNRAS*, 421, 3399
- O'Dell C. R., 1986, *ApJ*, 304, 767
- O'Dell C. R., 2001, *ARA&A*, 39, 99
- O'Dell C. R., Ferland G. J., Henney W. J., 2001, *ApJ*, 556, 203
- O'Dell C. R., Wen Z., 1992, *ApJ*, 387, 229
- O'Dell C. R., Wen Z., 1994, *ApJ*, 436, 194
- O'Dell C. R., Wen Z., Hu X., 1993, *ApJ*, 410, 696
- Offner S. S. R., Klein R. I., McKee C. F., Krumholz M. R., 2009, *ApJ*, 703, 131
- Ohlendorf H., Preibisch T., Gaczkowski B., Ratzka T., Grellmann R., McLeod A. F., 2012, *A&A*, 540, A81
- Ohlendorf H., Preibisch T., Gaczkowski B., Ratzka T., Ngoumou J., Roccatagliata V., Grellmann R., 2013, *A&A*, 552, A14
- Oliveira J. M., 2008, *Star Formation in the Eagle Nebula. Handbook of Star Forming Regions, Volume II*, p. 599
- Oort J. H., Spitzer Jr. L., 1955, *ApJ*, 121, 6
- Orsatti A. M., Vega E. I., Marraco H. G., 2006, *AJ*, 132, 1783
- Osterbrock D. E., 1989, *Astrophysics of gaseous nebulae and active galactic nuclei*
- Osterbrock D. E., Ferland G. J., 2006, *Astrophysics of gaseous nebulae and active galactic nuclei*. University Science Books, 2nd ed.
- Osterbrock D. E., Tran H. D., Veilleux S., 1992, *ApJ*, 389, 305
- Pagel B. E. J., Edmunds M. G., Blackwell D. E., Chun M. S., Smith G., 1979, *MNRAS*, 189, 95
- Parenago P. P., 1954, *Trudy Gosudarstvennogo Astronomicheskogo Instituta*, 25, 1

- Peimbert M., 1967, *ApJ*, 150, 825
- Peimbert M., Torres-Peimbert S., 1977, *MNRAS*, 179, 217
- Pellegrini E. W., Baldwin J. A., Ferland G. J., 2011, *ApJ*, 738, 34
- Peng T.-C., Wyrowski F., van der Tak F. F. S., Menten K. M., Walmsley C. M., 2010, *A&A*, 520, A84
- Peters T., Banerjee R., Klessen R. S., Mac Low M.-M., 2011, *ApJ*, 729, 72
- Plunkett A. L., Arce H. G., Corder S. A., Mardones D., Sargent A. I., Schnee S. L., 2013, *ApJ*, 774, 22
- Podobedova L. I., Keller D. E., Wiese W. L., 2009, *JPCRD*, 38
- Pound M. W., 1998, *ApJL*, 493, L113
- Povich M. S., Smith N., Majewski S. R., Getman K. V., Townsley L. K., Babler B. L., Broos P. S., Indebetouw R., Meade M. R., Robitaille T. P., Stassun K. G., Whitney B. A., Yonekura Y., Fukui Y., 2011, *ApJS*, 194, 14
- Pradhan A. K., Montenegro M., Nahar S. N., Eissner W., 2006, *MNRAS*, 366, L6
- Preibisch T., Roccatagliata V., Gaczkowski B., Ratzka T., 2012a, *A&A*, 541, A132
- Preibisch T., Roccatagliata V., Gaczkowski B., Ratzka T., 2012b, *A&A*, 541, A132
- Preibisch T., Schuller F., Ohlendorf H., Pekruhl S., Menten K. M., Zinnecker H., 2011, *A&A*, 525, A92
- Raga A. C., Lora V., Smith N., 2010, *RevMexAA*, 46, 179
- Ramsay S. K., Chrysostomou A., Geballe T. R., Brand P. W. J. L., Mountain M., 1993, *MNRAS*, 263, 695
- Redfield S., Falcon R. E., 2008, *ApJ*, 683, 207
- Reipurth B., Bally J., 2001, *ARA&A*, 39, 403
- Reiter M., Smith N., 2013, *MNRAS*, 433, 2226
- Ricci L., Robberto M., Soderblom D. R., 2008, *AJ*, 136, 2136
- Roccatagliata V., Preibisch T., Ratzka T., Gaczkowski B., 2013, *A&A*, 554, A6
- Rochau B., Brandner W., Stolte A., Gennaro M., Gouliermis D., Da Rio N., Dzyurkevich N., Henning T., 2010, *ApJL*, 716, L90
- Rogers H., Pittard J. M., 2013, *MNRAS*, 431, 1337

- Rubin R. H., Dufour R. J., Walter D. K., 1993, *ApJ*, 413, 242
- Sánchez et al., 2015, *A&A*, 573, A105
- Sánchez S. F., Cardiel N., Verheijen M. A. W., Martín-Gordón D., Vilchez J. M., Alves J., 2007, *A&A*, 465, 207
- Sankrit R., Hester J. J., 2000, *ApJ*, 535, 847
- Saral G., Hora J. L., Willis S. E., Koenig X. P., Gutermuth R. A., Saygac A. T., 2015, *ApJ*, 813, 25
- Schaye J., et al., 2015, *MNRAS*, 446, 521
- Schlafly E. F., Green G., Finkbeiner D. P., Rix H.-W., Bell E. F., Burgett W. S., Chambers K. C., Draper P. W., Hodapp K. W., Kaiser N., Magnier E. A., Martin N. F., Metcalfe N., Price P. A., Tonry J. L., 2014, *ApJ*, 786, 29
- Schruba A., Leroy A. K., Walter F., Sandstrom K., Rosolowsky E., 2010, *ApJ*, 722, 1699
- Scowen P. A., Hester J. J., Sankrit R., Gallagher J. S., Ballester G. E., Burrows C. J., Clarke J. T., Crisp D., Evans R. W., Griffiths R. E., Hoessel J. G., Holtzman J. A., Krist J., Mould J. R., Stapelfeldt K. R., Trauger J. T., Watson A. M., Westphal J. A., 1998, *AJ*, 116, 163
- Seaton M. J., 1979, *MNRAS*, 187, 73P
- Shu F. H., Adams F. C., Lizano S., 1987, *ARA&A*, 25, 23
- Sievers A. W., Mezger P. G., Bordeon M. A., Kreysa E., Haslam C. G. T., Lemke R., 1991, *A&A*, 251, 231
- Silva-Villa E., Larsen S. S., 2011, *A&A*, 529, A25
- Simon R., Jackson J. M., Clemens D. P., Bania T. M., Heyer M. H., 2001, *ApJ*, 551, 747
- Slater C. T., Oey M. S., Li A., Bernard J.-P., Churchwell E., Gordon K. D., Indebetouw R., Lawton B., Meixner M., Paradis D., Reach W. T., 2011, *ApJ*, 732, 98
- Smith N., 2006a, *MNRAS*, 367, 763
- Smith N., 2006b, *ApJ*, 644, 1151
- Smith N., Bally J., Walborn N. R., 2010a, *MNRAS*, 405, 1153
- Smith N., Bally J., Walborn N. R., 2010b, *MNRAS*, 405, 1153
- Smith N., Barbá R. H., Walborn N. R., 2004, *MNRAS*, 351, 1457
- Smith N., Brooks K. J., 2008, *The Carina Nebula: A Laboratory for Feedback and Triggered Star Formation*. p. 138

- Smith N., et al., 2010, MNRAS, 406, 952
- Sommer-Larsen J., Götz M., Portinari L., 2003, ApJ, 596, 47
- Storey P. J., Zeppen C. J., 2000, MNRAS, 312, 813
- Sugitani K., Tamura M., Nakajima Y., Nagashima C., Nagayama T., Nakaya H., Pickles A. J., Nagata T., Sato S., Fukuda N., Ogura K., 2002, ApJL, 565, L25
- Sugitani K., Watanabe M., Tamura M., Kandori R., Hough J. H., Nishiyama S., Nakajima Y., Kusakabe N., Hashimoto J., Nagayama T., Nagashima C., Kato D., Fukuda N., 2007, PASJ, 59, 507
- Sung H., Bessell M. S., 2004, AJ, 127, 1014
- Tamburro D., Rix H.-W., Leroy A. K., Mac Low M.-M., Walter F., Kennicutt R. C., Brinks E., de Blok W. J. G., 2009, AJ, 137, 4424
- Tan J. C., Beltrán M. T., Caselli P., Fontani F., Fuente A., Krumholz M. R., McKee C. F., Stolte A., 2014, Protostars and Planets VI, pp 149–172
- Tayal S. S., 2007, ApJS, 171, 331
- Tayal S. S., 2011, ApJS, 195, 12
- Tayal S. S., Gupta G. P., 1999, ApJ, 526, 544
- Tayal S. S., Zatsarinny O., 2010, ApJS, 188, 32
- Tedds J. A., Brand P. W. J. L., Burton M. G., 1999, MNRAS, 307, 337
- Tenorio-Tagle G., 1979, A&A, 71, 59
- Thompson R. I., Smith B. A., Hester J. J., 2002, ApJ, 570, 749
- Tielens A. G. G. M., 2010, The Physics and Chemistry of the Interstellar Medium
- Townsley L. K., Feigelson E. D., Montmerle T., Broos P. S., Chu Y.-H., Garmire G. P., 2003, ApJ, 593, 874
- Tremblin P., Audit E., Minier V., Schmidt W., Schneider N., 2012, A&A, 546, A33
- Tremblin P., Audit E., Minier V., Schneider N., 2012, A&A, 538, A31
- Turner D. G., Moffat A. F. J., 1979, Journal of the Royal Astronomical Society of Canada, 73, 301
- Urban A., Martel H., Evans II N. J., 2010, ApJ, 710, 1343
- Vaidya K., Chu Y.-H., Gruendl R. A., Chen C.-H. R., Looney L. W., 2009, ApJ, 707, 1417

- Vallee J. P., 1987, *A&A*, 178, 237
- van Altena W. F., Lee J. T., Lee J.-F., Lu P. K., Upgren A. R., 1988, *AJ*, 95, 1744
- Verdolini S., Yeh S. C. C., Krumholz M. R., Matzner C. D., Tielens A. G. G. M., 2013, *ApJ*, 769, 12
- Vilchez J. M., Esteban C., 1996a, *MNRAS*, 280, 720
- Vilchez J. M., Esteban C., 1996b, *MNRAS*, 280, 720
- Vink J. S., de Koter A., Lamers H. J. G. L. M., 2000, *A&A*, 362, 295
- Vogelsberger M., Genel S., Springel V., Torrey P., Sijacki D., Xu D., Snyder G., Bird S., Nelson D., Hernquist L., 2014, *Nature*, 509, 177
- von Hoerner S., 1951, *ZfA*, 30, 17
- Walborn N. R., 1973, *ApJL*, 182, L21
- Walch S., Girichidis P., Naab T., Gatto A., Glover S. C. O., Wünsch R., Klessen R. S., Clark P. C., Peters T., Derigs D., Baczynski C., 2015, *MNRAS*, 454, 238
- Walch S., Whitworth A. P., Bisbas T. G., Wünsch R., Hubber D. A., 2013, *MNRAS*, 435, 917
- Walch S. K., 2014, *Astrophysics and Space Science Proceedings*, 36, 173
- Wang J., Feigelson E. D., Townsley L. K., Broos P. S., Getman K. V., Wolk S. J., Preibisch T., Stassun K. G., Moffat A. F. J., Garmire G., King R. R., McCaughrean M. J., Zinnecker H., 2011, *ApJS*, 194, 11
- Weaver R., McCray R., Castor J., Shapiro P., Moore R., 1977, *ApJ*, 218, 377
- Weilbacher P. M., Monreal-Ibero A., Kollatschny W., Ginsburg A., McLeod A. F., et al., 2015, *A&A*, 582, A114
- Weilbacher P. M., Streicher O., Urrutia T., Jarno A., Pécontal-Rousset A., Bacon R., Böhm P., 2012a, in *Society of Photo-Optical Instrumentation Engineers (SPIE) Conference Series Vol. 8451 of Society of Photo-Optical Instrumentation Engineers (SPIE) Conference Series, Design and capabilities of the MUSE data reduction software and pipeline.* p. 0
- Weilbacher P. M., Streicher O., Urrutia T., Jarno A., Pécontal-Rousset A., Bacon R., Böhm P., 2012b, in *Society of Photo-Optical Instrumentation Engineers (SPIE) Conference Series Vol. 8451 of Society of Photo-Optical Instrumentation Engineers (SPIE) Conference Series, Design and capabilities of the MUSE data reduction software and pipeline.* p. 0
- Wen Z., O'Dell C. R., 1993, *ApJ*, 409, 262
- Westmoquette M. S., Dale J. E., Ercolano B., Smith L. J., 2013, *MNRAS*, 435, 30

- Whalen D., van Veelen B., O'Shea B. W., Norman M. L., 2008, *ApJ*, 682, 49
- White G. J., Nelson R. P., Holland W. S., Robson E. I., Greaves J. S., McCaughrean M. J., Pilbratt G. L., Balser D. S., Oka T., Sakamoto S., Hasegawa T., McCutcheon W. H., Matthews H. E., Fridlund C. V. M., Tohill N. F. H., Hultgren M., Deane J. R., 1999a, *A&A*, 342, 233
- White G. J., Nelson R. P., Holland W. S., Robson E. I., Greaves J. S., McCaughrean M. J., Pilbratt G. L., Balser D. S., Oka T., Sakamoto S., Hasegawa T., McCutcheon W. H., Matthews H. E., Fridlund C. V. M., Tohill N. F. H., Hultgren M., Deane J. R., 1999b, *A&A*, 342, 233
- Wiese W. L., Fuhr J. R., Deters T. M., 1996, Atomic transition probabilities of carbon, nitrogen, and oxygen : a critical data compilation
- Williams J. P., Blitz L., McKee C. F., 2000, *Protostars and Planets IV*, p. 97
- Williams J. P., McKee C. F., 1997, *ApJ*, 476, 166
- Williams J. P., Plambeck R. L., Heyer M. H., 2003, *ApJ*, 591, 1025
- Wilner D. J., De Pree C. G., Welch W. J., Goss W. M., 2001, *ApJL*, 550, L81
- Wolfire M. G., Cassinelli J. P., 1987, *ApJ*, 319, 850
- Wolk S. J., Broos P. S., Getman K. V., Feigelson E. D., Preibisch T., Townsley L. K., Wang J., Stassun K. G., King R. R., McCaughrean M. J., Moffat A. F. J., Zinnecker H., 2011, *ApJS*, 194, 12
- Wuyts S., et al., 2016, ArXiv e-prints
- Yeh S. C. C., Matzner C. D., 2012, *ApJ*, 757, 108
- Yonekura Y., Asayama S., Kimura K., Ogawa H., Kanai Y., Yamaguchi N., Barnes P. J., Fukui Y., 2005, *ApJ*, 634, 476
- Yorke H. W., Sonnhalter C., 2002, *ApJ*, 569, 846
- Zeppen C. J., 1982, *MNRAS*, 198, 111
- Zhang B., Reid M. J., Menten K. M., Zheng X. W., Brunthaler A., Dame T. M., Xu Y., 2013, *ApJ*, 775, 79
- Zinnecker H., Yorke H. W., 2007, *ARA&A*, 45, 481
- Zuckerman B., Evans II N. J., 1974, *ApJL*, 192, L149

Acknowledgments

As so many clever people said before me, the road is the goal, and the journey the reward. I would like to thank all of the supervisors, colleagues, family and friends who stood beside me and accompanied me along the way.

Thank you Leonardo for your trust, wisdom and guidance, but especially for letting me pave my way while supporting my ideas and letting these run freely, and for giving me the freedom a PhD student seldom gets. Thank you Suzie, Jim and Adam for being splendid co-supervisors, for your help and support, for the not so weekly meetings, the brainstorming sessions and the best conference trips so far. Thank you Thomas for the help and clarity you never failed to give. Thank you Diederik for believing in me, for pushing and supporting me, and for sharing the passion for my ideas and help developing them.

Thank you Simone, for listening to (and not running away from) my endless rants, worries and complaints, for supporting me, pulling me back up whenever I felt I was falling, and for being the wonderful husband that you are. Thank you Mom, Dad, Paolo and Laura, because of who you are and what you mean to me, more words are, I believe, not necessary.

Thank you Bitten, Maud, Katha, Gergo, Anke, Wolfgang, Kate, Claudia, Carlo, Anna, Marco & Marco, Adrian, Alexis, Emin, Laura, Izaskun. You are the best of friends, without you 3 years at ESO would never have been so much fun. Thank you for the hikes, BBQs, skiing and non-skiing trips, dinners, sushi, beers, laughs, hugs. To many more of all of these!

Because in the end, we are all cosmic mud (Prof. Dr. Harald Lesch).